University of Nottingham
UK | CHINA | MALAYSIA

Development of Encapsulated Air Microparticles using Spray Drying and Sessile Single Droplet Drying

by

Tengku Farizan Izzi Che Ku Jusoh

Thesis submitted to the University of Nottingham for the Degree of Doctor of Philosophy

Division of Food, Nutrition and Dietetics
School of Biosciences
University of Nottingham

October 2020

Acknowledgements

I would like to praise and thank Allah, the Almighty, for giving me the opportunity, determination and strength to undertake this research study. Without His blessings, this achievement would not have been completed successfully.

"If you are grateful, I will surely increase you (in favour)."
[Holy Quran 14:7]

Deepest gratitude and appreciation to my supervisors, academic and non-academic staffs from the Division of Food, Nutrition and Dietetics and from other organisations, colleagues, friends and family.

Foremost, I sincerely thank my supervisory team, Prof Bettina Wolf (School of Chemical Engineering, University of Birmingham), Dr Joanne Gould (Division of Food, Nutrition and Dietetics, University of Nottingham), Dr David Fairhurst (School of Science and Technology, Nottingham Trent University) and Prof Serafim Bakalis (Department of Chemical and Environmental Engineering, University of Nottingham) for their tremendous support, guidance and encouragement throughout this PhD journey. I would have got lost without them. I also wish to extend my appreciation to my internal assessor Prof Tim Foster for his valuable inputs and comments on my research work.

I would like to acknowledge Nottingham Trent University for accepting me as a visiting student and gave me permission to do single droplet drying experiments in their laboratory. I also wish to acknowledge use of facilities in the Nanoscale and Microscale Research Centre (NMRC), University of Nottingham and a special thank you to Dr Elisabeth Steer for the SEM imaging, Dr Chris Parmenter for the FIB-SEM imaging and Dr Emily Smith for acquiring the XPS spectra and data interpretation. I am grateful to Craig Sturrock from Hounsfield Facility, University of Nottingham and Dr Patricia Andreu Cabedo from School of Chemical Engineering, University of Birmingham for access to the X-ray micro-computed tomography (micro-CT).

My appreciation also goes to all technicians and staff in the Division especially Khatija Nawaz Husain, Steven Johnson, Bill Macnaughtan and Elizabeth Starr for assistance with technical issues. I am also very thankful to members in my research group (Meetawee Anawachkul, Xinxin Li, Liling Zhang, Ruth Price, Holly Cuthill, James Huscroft, Omran Elkwil, Hui Zhang and Dr Miroslaw Kasprzak), EPSRC Centre for Innovative Manufacturing for Food, University of Nottingham and all other friends especially Syamila, Jutarat, Yangyi, Yi Ren, Charfeddine, Syah, Vincenzo, Filippo, Gedi, Mostafa and Book, for making my experience at the University of Nottingham unforgettable. 2020 has been a tough year for all of us. Covid-19 please go away!

I gratefully acknowledge the Ministry of Higher Education Malaysia and Universiti Sultan Zainal Abidin (UniSZA), Malaysia for the financial support during my PhD studies.

My special thanks go to my big family in the UK especially Hanis, Suryani and family, Elis and husband, Ammar and family, Isma and family, Mazlina and family, Suhaiza and family, Aishah and family, Aini and family, Asilah and family, Hairul & family, Fitri and family, Farah and family, Dayah and family, Erik and family, for their unique friendship, help and motivation during this study.

Finally, I would like to dedicate my profound gratitude to my wonderful husband Khairul Amiruddin, my lovely kids Safiyah Irdina Amani and Shafi Izzul Ayman, my dear parents Nafisah Daud and Che Ku Jusoh Che Ku Ismail, parents-in-law and siblings for their unconditional love, prayers, support and patience throughout my research.

Tengku Farizan Izzi Che Ku Jusoh
22nd October 2020

List of Presentations

Oral presentations:

1. **Tengku Farizan Izzi, C. K. J.**, Fairhurst, D., Gould, J. & Wolf, B. *Development of encapsulated air microparticles using spray drying.* **Postgraduate Student Symposium 2017**, 16 - 17 May 2017, Nottingham, UK.
2. **Tengku Farizan Izzi, C. K. J.**, Gould, J., D. Fairhurst, & Wolf, B. *Gum Arabic as an amphiphilic functional hydrocolloid in the development of encapsulated air microparticles*. **EPSRC CIM in Food Conference**, 26 March - 27 March 2018, Nottingham, UK.
3. **Tengku Farizan Izzi, C. K. J.**, Fairhurst, D., Gould, J. & Wolf, B. *Development of encapsulated air microparticles: Morphology of particles obtained by spray drying and single droplet drying*. **PARTEC International Congress on Particle Technology**, 9 - 11 April 2019, Nuremberg, Germany.

Poster presentations:

1. **Tengku Farizan Izzi, C. K. J.**, Johnson, S., Gould, J. & Wolf, B. *Hydrocolloid based encapsulated air micro particles for innovative food manufacture*. **EPSRC CIM in Food Conference**, 30 - 31 March 2017, Birmingham, UK.
2. **Tengku Farizan Izzi, C. K. J.**, Johnson, S., Gould, J. & Wolf, B. *Hydrocolloid based encapsulated air micro particles for innovative food manufacture*. 3. **19th Gums & Stabilisers for the Food Industry Conference: Hydrocolloid multifunctionality**, 27 - 30 June 2017, Berlin, Germany.
3. **Tengku Farizan Izzi, C. K. J.**, Johnson, S., Gould, J. & Wolf, B. *Hydrocolloid based encapsulated air micro particles for innovative food manufacture*. **3rd UK Hydrocolloids Symposium: Hydrocolloids**

structures determining functionality, 13 September 2017, Nottingham, UK.

4. **Tengku Farizan Izzi, C. K. J.**, Johnson, S., Fairhurst, D., Gould, J. & Wolf, B. *Gum Arabic as an amphiphilic functional hydrocolloid in the development of encapsulated air microparticles*. **31st EFFoST International Conference: Challenges for the 21st century research for progress society**, 13 - 16 November 2017, Sitges, Spain.
5. **Tengku Farizan Izzi, C. K. J.**, Fairhurst, D., Gould, J. & Wolf, B. *Particle formation during single droplet drying of mixed maltodextrin and gum Arabic solutions*. **Postgraduate Student Symposium 2018**, 19 - 20 April 2018, Nottingham, UK.
6. **Tengku Farizan Izzi, C. K. J.**, Fairhurst, D., Gould, J. & Wolf, B. *Development of encapsulated air microparticles: Morphology of particles obtained by spray drying and single droplet drying*. **32nd EFFoST International Conference: Developing innovative food structures and functionalities through process and reformulation to satisfy consumer needs and expectations**, 6 - 8 November 2018, Nantes, France.

Abstract

The aim of this research was to produce spray dried particles with one large vacuole and controlled surface wettability, also known as encapsulated air microparticles, to be potentially applied as the dispersed gas phase in foam-based processed foods. Droplets containing a mixture of the slightly hydrophobic and thus surface active gum Arabic (GA) and the hydrophilic maltodextrin (MD) was selected for the development of encapsulated air microparticles based on literature reports of hollow spray dried particles[1, 2]. A sessile single droplet drying (SDD) on a hydrophobic surface and spray drying with a two-fluid atomiser were employed to evaluate the impact of droplet compositions (ratio of GA:MD, solids concentration and DE-value of MD) and processing conditions (drying temperature and droplet size) on the particle formation and the wetting properties of the particles.

The sessile SDD study revealed that the mechanical strength of the skin and the drying rate were the key determining factors for the development of particles with one large vacuole. These particles were also characterised by a smooth surface appearance. The formation of one large vacuole (and a smooth surface) required the droplet to withstand surface collapse during drying. These conditions were fulfilled for droplets containing a higher proportion of GA than MD, for a higher solids concentration (40% w/v) and for the MD with the lowest dextrose equivalent (DE 7) of two MDs included in this research. A high drying rate constant at higher drying temperature (120 °C) and smaller initial droplet volume (1 µl) resulted in an earlier onset of bubble nucleation, and thus were more likely to lead to the formation of a large vacuole.

Particle morphologies produced by spray drying were comparable to those produced in the SDD experiments. The highest fraction of smooth-surface hollow particles (15%) was achieved by spray drying the feed that contained

[1] Paramita et al., (2010)
[2] Porras-Saavedra et al., (2015)

high solids (40% w/v) at high inlet temperature (220 °C) and slow feed rate (300 ml/h), whereas the opposite conditions resulted in the lowest percentage of hollow particles (2%). The wetting behaviour of spray dried powders was found to be identical to SDD particles, wherein particles higher in GA showed poorer wetting (by water) due to the enrichment of the more hydrophobic GA at the surface of the particles. Likewise, the dissolution time increased with an increasing amount of GA in the particles due to the ability to hold higher amount of water (swelling) before the onset of collapse. The increasing dissolution time is advantageous in certain applications such as ice cream manufacture.

Overall, this research has provided insight into fundamental aspects of encapsulated air microparticles, whereby GA has demonstrated convincing encapsulating material for the development of hollow particles, as well as in the control of particle wettability. The re-design SDD set-up developed in this research can be used as a design tool to achieve specific particle morphology and thus particle functionality for processing using spray drying.

Table of Contents

List of Figures

List of Tables

Nomenclature

Abbreviations

ANOVA	Analysis of variance
APCA	Apparent projected contact angle
Aw	Water activity
BS	Backscattering light
C	Carbon
CCD	Charged-couple device
CFD	Computational fluid dynamics
CI	Carr index
CLSM	Confocal laser scanning microscopy
CRM	Confocal Raman microscopy
DE	Dextrose equivalent
DLS	Dynamic light scattering
DVS	Dynamic vapour sorption
EDX	Energy dispersive X-ray spectroscopy
FIB	Focused ion beam
GA	Gum Arabic
He	Helium
HR	Hausner ratio
MD	Maltodextrin
MD7	Maltodextrin DE 7.5-9.9
MD12	Maltodextrin DE 12-15
micro-CT	X-ray micro-computed tomography
N	Nitrogen
Ne	Neon
O	Oxygen
Pe	Peclet
RH	Relative humidity
SEC-MALS	Size exclusion chromatography couple with a multi angle laser-light scattering
SEM	Scanning electron microscopy

SDD	Single droplet drying
T	Transmission light
ToF-SIMS	Time of light secondary ion mass spectroscopy
XPS	X-ray photoelectron spectroscopy

Latin Symbols

d_{10}	Particle diameter at 10% volume distribution
d_{50}	Particle diameter at 50% volume distribution
d_{90}	Particle diameter at 90% volume distribution
D	Diffusion coefficient
k_B	Boltzmann's constant
M*n*	Number average molecular weight
M*w*	Molecular weight
Pe	Peclet number
R	Radius
R_0	Initial droplet radius
R*h*	Hydrodynamic radius
t	Time
t_{dry}	Drying time
T	Temperature

Greek Symbols

κ	Drying rate
η	Apparent viscosity
[η]	Intrinsic viscosity

CHAPTER 1

Introduction

1.1 Research Topic

This PhD research is concerned with the formulation of encapsulated air microparticles by spray drying technology to create a new food ingredient, particularly aimed at the manufacture of foam-based products. As such air would be added as an ingredient, cutting out conventional whipping processes enabling process minimisation and novel product development. For application as a dispersible food ingredient, partial surface hydrophobicity is required to control the particle wetting, so the air does not escape and the particles collapse before they have been kinetically trapped in the food matrix. It is hypothesised that the particle wettability is controllable through surface active components in the formulation, for example gum Arabic (GA).

A mixture of GA and maltodextrin (MD) was chosen as the encapsulating material for particle manufacture based on literature reports by Paramita et al. (2010) and Porras-Saavedra et al. (2015) who found that 81% and 26% respectively of their spray dried particles were hollow. GA is of amphiphilic character and known to absorb at the air-water interface of droplets during spray drying (Munoz-Ibanez et al., 2016). MD, on the other hand, is a hydrophilic biopolymer produced from acid and/or enzymatic hydrolysis of starch and classified by dextrose equivalent (DE) value (Castro et al., 2016; Pycia et al., 2016).

The main question of this research was how the mixing ratio of GA:MD and the drying conditions influence the formation of a hollow particle and the functional properties of the spray dried particles, especially wettability. Firstly, an experiment was conducted to evaluate the potential of producing encapsulated air microparticles by spray drying a mixture of GA and MD. However, it is challenging to study particle morphology development on an actual spray dryer because of the polydispersity of the droplet size spectrum formed at the nozzle, the short residence time together with the fast drying kinetics, the variability in temperature history of each droplet depending on the flight path, the complexity of the drying operation and the difficulty of monitoring the drying parameters in situ (Adhikari et al., 2000; Sadek et al., 2015b). To overcome these difficulties, single droplet drying (SDD) under well-controlled conditions is often used as a technique to study drying at a particle level (Both et al., 2018b; Bouman et al., 2016; Nuzzo et al., 2017).

In this PhD research, a sessile single droplet was deposited on a flat hydrophobic membrane to monitor the evolution of drying as a function of time. It was hypothesised that the feed composition (ratio of GA:MD, solids concentration and DE-value of MD) and the processing parameters (temperature and droplet size) influence the morphology of the final particle. In fact, these relationships have been reported in number of publications (Alamilla-Beltrán et al., 2005; Caliskan and Dirim, 2016; Daza et al., 2016; Elversson et al., 2003; Fernandes et al., 2014; Jafari et al., 2017; Mishra et al., 2014; Negrão-Murakami et al., 2017; Porowska et al., 2015; Sadek et al., 2014; Tontul and Topuz, 2017; Zhang et al., 2019). However, there is no report on the impact of composition and/or processing parameters on the development of hollow spray

dried particles from GA and MD mixtures. Finally, three conditions leading to hollow particles at the single droplet drying level were selected and applied in a laboratory-scale spray drier for validation.

1.2 Research Objectives

The following research objectives were identified following the literature review, presented in Chapter 2:

1. To investigate the impact of droplet compositions (ratio of GA:MD, solids concentration and DE-value of MD) and processing parameters (drying temperature and droplet size) on the development of encapsulated air microparticles in sessile SDD and spray drying experiments.
2. To evaluate the wetting and dissolution properties of encapsulated air microparticles dried individually and by spray drying.

1.3 Thesis Outline

Following on from this introductory Chapter 1, this thesis consists of a further 5 chapters. The results and discussion chapters 3, 4 and 5 are presented in the style of research manuscripts. An overview of the chapter content follows:

- In Chapter 2 a literature review on spray drying, the use of GA and MD as encapsulating materials in the production of spray dried powders, factors that affect powder properties, mechanisms for the development of encapsulated air microparticles, drying kinetics of droplets in spray drying and an overview of single droplet drying techniques is provided.

- In Chapter 3 the results of an investigation into the influence of the ratio of GA:MD on the microstructure and physicochemical properties of the spray dried powders, as well as the particle surface composition, are presented. Optical microscopy, scanning electron microscopy (SEM) and focused ion beam (FIB)-SEM were used to obtain information on the morphology of the particles. Measurements of water activity, moisture content, hygroscopicity, particle size, water solubility, wetting and dissolution time, density and flowability of the powders are presented. The distribution of elements at the surface of the particles was obtained by X-ray photoelectron spectroscopy (XPS).

- In Chapter 4 the effects of the droplet solutions (ratio of GA:MD, solids concentration and DE-value of MD) and the drying conditions (temperature and droplet volume) on the particle morphology development during sessile SDD are discussed. The reported morphological development from droplet to particle during drying was recorded with a camera, and the dried particles were imaged by X-ray micro-computed tomography (micro-CT) and SEM to visualise their surface and internal structure. The molecular characteristics of materials and the properties of the droplet solutions (miscibility of mixed solutions, viscosity and diffusion coefficient) were also evaluated. Finally, the results of wettability, dissolution and water absorption of the dried particles are reported.

- In Chapter 5 the efforts to validate some of the results obtained in Chapter 4 at laboratory scale spray drier are reported. The feed of varied

solids concentrations was spray dried at two different drying temperatures and feed rates. The morphology and physicochemical properties of the resultant powders were evaluated.

- In the final Chapter 6 the overall conclusions drawn from this PhD research are presented together with recommendations for future work.

CHAPTER 2

Literature Review

2.1 Introduction

The present chapter is organised into four main sections. Section 2.2 provides an overview of the spray drying process, the use of GA and MD as encapsulating materials in the production of spray dried powders and factors that affect powder properties. The concept of encapsulated air microparticles has briefly been described in the introduction of this thesis and the mechanisms underlying the development of these particles will be elaborated in more detail in Section 2.3. In Section 2.4, drying kinetics of the spray drying process is also discussed. At the end of the chapter (Section 2.5), a brief overview of single droplet drying as a complementary approach to spray drying is presented.

2.2 Spray Drying

Microencapsulation is a process in which one substance (either liquid, solid or gas) is coated within another substance (Esfanjani et al., 2015; Nedovic et al., 2011; Rajabi et al., 2015). The encapsulated substance is often called the core, fill, active, internal or payload phase, whereas the substance that is encapsulating is referred to as the coating, membrane, shell, wall material, capsule, carrier material, external phase, or matrix (Fang and Bhandari, 2010; Gharsallaoui et al., 2007). Microcapsules are small (1-1000 μm) and can have

many morphologies. The most commonly seen morphologies are mononuclear capsules, which have a single core enveloped by a wall material, and aggregates, which have many cores embedded in a matrix (Figure 2.1). The wall or matrix materials are usually polymers (Schrooyen et al., 2001). There are a number of techniques available for the encapsulation of food compounds such as spray drying, spray cooling/chilling, extrusion, fluidised bed coating, liposome entrapment, coacervation, inclusion complexation, centrifugal suspension separation, lyophilisation/freeze drying (Gibbs et al., 1999; Ray et al., 2016).

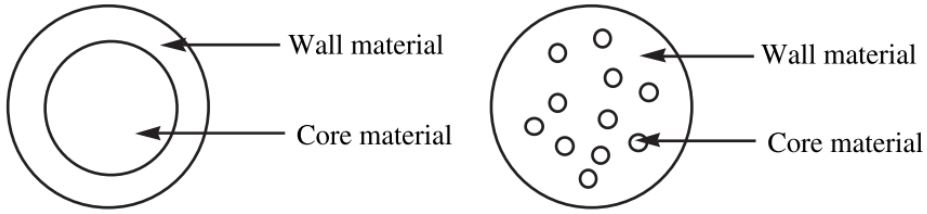

Figure 2.1 Encapsulation morphologies: mononuclear capsule (left) and aggregate (right) (Fang and Bhandari, 2010).

Among microencapsulation techniques, spray drying is the most widely used in the food industry. The reason for utilising spray drying is the possibility of a continuous process, the relatively low production cost and the relatively short exposure time to heat in combination with evaporation cooling allowing processing of heat sensitive materials (Flores et al., 2014; Gharsallaoui et al., 2007; Madene et al., 2006; Sansone et al., 2011). Microencapsulation by spray drying is the process of converting a liquid mixture of an encapsulating material with/without a core material into a dry powder by rapid drying in a hot gas. The feeding liquid can be a solution, an emulsion, or a suspension. Figure 2.2 shows a schematic of the conventional spray drying process. Generally, the spray

drying process involves four elementary steps (Anandharamakrishnan and Ishwarya, 2015; Gharsallaoui et al., 2007):

1. Atomisation of the liquid feed into fine droplets by an atomiser or a nozzle that can be a two-fluid nozzle (pneumatic atomisation), a rotary atomiser, a pressure nozzle (hydraulic atomisation) or an ultrasonic atomiser into a hot drying chamber. The larger surface area results in a more efficient heat and mass transfers, thus promoting rapid drying of droplets in the spray drying chamber.
2. Contact of small droplets with the hot gas in either co-current flow or counter-current flow. In co-current flow, both the heated air and sprayed liquid flowing in the same direction, whereas the hot air flows against the flow from the atomiser in the counter-current configuration.
3. The small droplets are subjected to fast water evaporation that eventually leads to the formation of dry particles.
4. The dried particles are separated from the drying medium by a cyclone or bag filter and collected in a collector at the bottom of the dryer.

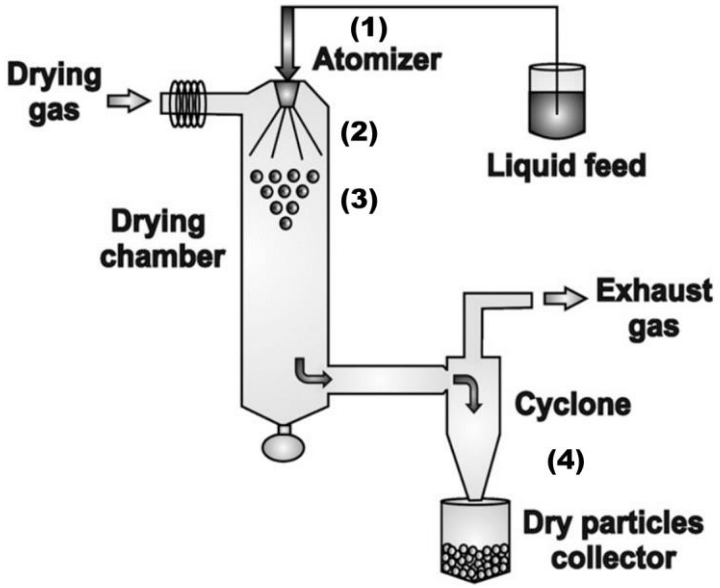

Figure 2.2 Process steps of spray drying: (1) atomisation of the feed, (2) contact of droplets with the hot gas, (3) evaporation of moisture and (4) dry product/humid air separation. Adapted from Sosnik & Seremeta (2015).

In the context of traditional food and beverage products, the primary objective of spray drying is to protect the core material from environmental factors such as light, moisture and oxygen, thereby reducing deterioration and increasing the shelf life of the products (Shahidi and Han, 1993). The process also allows for easier handling, transportation and storage, masks unwanted flavours and aromas, improves the nutritional value and the appearance of the microencapsulated agent (Desai and Park, 2005; Porras-Saavedra et al., 2015). Typical examples of spray dried products are fruit and vegetable juices (Shishir and Chen, 2017; Tontul and Topuz, 2017), aromas and flavours (Madene et al., 2006; Sanchez-Reinoso et al., 2017; Sultana et al., 2017), oils (Botrel et al., 2014; Encina et al., 2016; Fuchs et al., 2006), antioxidants (Ballesteros et al., 2017; Fang and Bhandari, 2010), vitamins (Estevinho et al., 2013; Gonçalves et al., 2017; Moeller et al., 2018) and colourants (Mahdavi et al., 2016).

2.2.1 Gum Arabic and Maltodextrin as encapsulating material

One of the main factors that contribute to the efficiency of the microencapsulation process is the selection of encapsulating material. The selection of an appropriate encapsulating material is crucial because it has a strong influence on the feed properties before drying, retention of the core during the process and shelf life of the powder after drying (Jafari et al., 2008). Numerous encapsulating materials are available for food applications: (i) carbohydrate polymers (starch and its derivatives, cellulose and its derivatives, plant exudates), (ii) protein (gluten, isolates), and (iii) lipid (fatty acids/alcohols, glycerines, waxes, phospholipids) (Wandrey et al., 2010). Among the encapsulating materials, GA and MD are the most commonly used in spray drying (Maisuthisakul and Gordon, 2012; Tonon et al., 2009). A good encapsulating material should be highly soluble, have adequate film forming ability, produce a low viscous solution even at high concentrations and certified as “generally recognised as safe” (GRAS) materials (Shishir and Chen, 2017).

GA, also known as gum acacia, is a plant polysaccharide exudate of *Acacia senegal* and *Acacia seyal*. It has a complex structure (Figure 2.3) consisting a backbone of 1,3-linked β-D-galactose with extensive branching through 3- and 6-linked galactose and 3-linked arabinose. Constituent units include galactopyranose, arabinopyranose, arabinofuranose, rhamnopyranose, glucuropyranosyl uronic acid, and 4-O-methyl glucuropyranosyl uronic acid (Idris et al., 1998; Islam et al., 1997). GA consists of three major fractions: arabinogalactan (88%) with 3.8×10^5 g/mol, arabinogalactan-protein complex (10%) with 1.45×10^6 g/mol, and glycoprotein (1%) with 2.5×10^5 g/mol (Randall et al., 1989; Verbeken et al., 2003). The arabinogalactan fraction has film-

forming properties, while the existence of protein-containing portions, in particular the arabinogalactan-protein fraction, provides excellent emulsifying properties (Burnside, 2014; Randall et al., 1988). A wattle blossom model was proposed to describe the structure of the arabinogalactan-protein complex where carbohydrate blocks are covalently linked to a polypeptide chain through both serine and hydroxyproline residues (Connolly et al., 1988, 1987; Fincher and Stone, 1983; Mahendran et al., 2008). An alternative model was proposed by Qi et al. (1991), who described the arabinogalactan-protein complex as a twisted hairy rope of 150 nm length and 5 nm diameter. The polysaccharide is attached to the polypeptide backbone as small units of ~30 sugar residues through hydroxyproline linkages. The wattle blossom and twisted hairy rope model are shown in Figure 2.4.

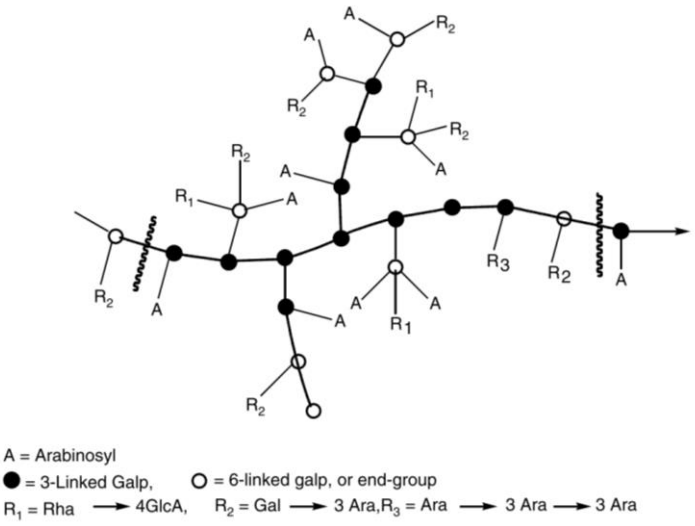

Figure 2.3 Chemical structure of gum Arabic (Izydorczyk et al., 2005).

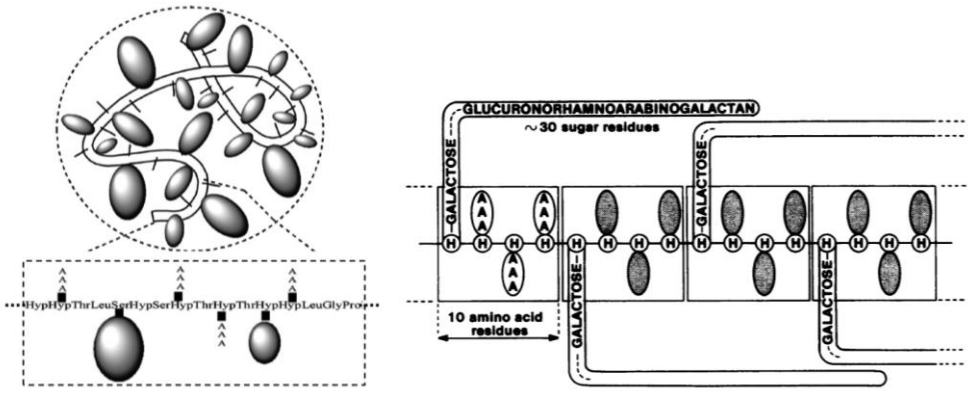

Figure 2.4 Model of the arabinogalactan-protein complex: wattle blossom (left) (Mahendran et al., 2008) and twisted hairy rope (right) (Qi et al., 1991).

GA is highly soluble in cold and hot water up to concentrations of about 50% (Wandrey et al., 2010). Unlike most polysaccharides used as a thickening or gelling agent, GA solution has low viscosity even at quite high concentrations and will not gel (Sanchez et al., 2018). At low shear, a GA solution at 30% solids has a lower viscosity than 1% xanthan gum and sodium carboxymethyl cellulose (Williams and Phillips, 2009). Thus, GA is favourable encapsulating solution than those made with other more viscous materials which may prevent clogging of the spray atomiser. Due to emulsifying ability, GA has been usually used to encapsulate lipids (Fernandes et al., 2014; Frascareli et al., 2012; Tonon et al., 2011b).

MD is produced from acid and/or enzymatic hydrolysis of starch and is composed of multiple D-glucose units linked by α-(1,4) glycosidic bond (Figure 2.5). MD is classified by dextrose equivalent (DE) which ranges from 3 to 20. The DE value measures the amount of reducing sugar relative to dextrose, thus indicates the level of hydrolysis of starch (Aidoo et al., 2013; Castro et al., 2016; Pycia et al., 2016). A higher DE value means a higher level of hydrolysis, thus

a lower molecular mass (Nurhadi et al., 2016). The molecular mass of MD can range from ~930 to 2498 g/mol (Takeiti et al., 2010).

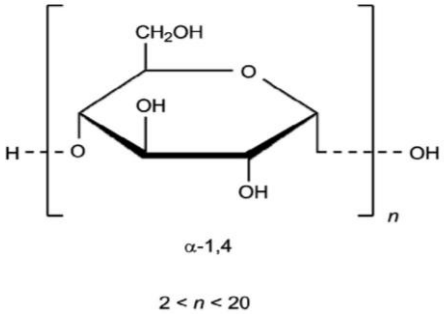

Figure 2.5 Chemical structure of maltodextrin and *n* is the number of glucose units (Aidoo et al., 2013).

MD is creamy white hygroscopic polysaccharide powder almost tasteless or only moderately sweet and easily digestible (Wandrey et al., 2010). Additional properties of MD include colourlessness in solutions, very high solubility (up to 97%) and fast dissolve in water (Raja et al., 1989; Wang and Wang, 2000). In fact, MD has been added to the formulation to improve the wettability of spray dried powder. Botrel et al. (2014) reported that partial substitution of whey protein isolate by MD improved the wettability properties of the spray dried fish oil. Caliskan and Dirim (2016) found that increasing the amount of MD caused a significant increase in the wettability of sumac extract powders.

GA has been recognised as an excellent encapsulating material. However, several problems including high cost and insufficient supply have limited its usage in microencapsulation. Alternatively, partial substitution of GA by other materials, such as MD can provide a good approach without compromise to the final quality of the encapsulated powder. Tatar et al. (2014) has used MD as a cheaper filler material to GA and hemicellulose to encapsulate fish oil. A

combination of GA and MD was found to be the best encapsulating material for spray dried drumstick oil as the obtained powder exhibited higher encapsulation efficiency and better oxidative stability (Premi and Sharma, 2017).

Table 2.1 lists a few examples of studies that used a mixture of GA and MD to encapsulate various food ingredients by spray drying. A two-fluid atomiser of laboratory Buchi spray dryer was commonly used by the researchers. The encapsulating materials with 9 to 50% solids concentration are preferred to avoid obstruction during atomisation. Moreover, a high solid concentration is recommended to reduce costs and increase drying efficiency. The feed solutions were commonly dried at an inlet temperature between 100 and 200 °C. The setting for operational conditions, especially the feed rate depends on the type of atomiser used. Generally, the feed rate in the range of 108 to1200 ml/h was applied during the process. For the two-fluid atomiser, the feed solutions were sprayed at the feed rate of 120 to 900 ml/h. The compositions of the GA:MD and operating conditions used in the studies may provide as a guideline for the production of encapsulated air microparticles.

Table 2.1 Application of a mixture of GA and MD as encapsulating material for spray drying.

Core material	Encapsulating material	CM:EM	Properties of encapsulated material	Type of spray dryer	Temperature	Operational conditions	Authors
Rosemary aroma	GA/MD$_{DE\ 10}$	1:6	Component ratio: 1:3 w/w Concentration: 30%	Rotary atomiser	Inlet: 200 °C Outlet: 95 °C	Spray disc speed: 39000 rpm (g value 53905) Raw material flux: 1.33 ×10^{-6} m^3s^{-1}	Janiszewska and Witrowa-Rajchert (2009)
-	GA/MD$_{DE\ 11}$	-	Component ratio: 1:2 w/w Concentration: 20-50%	Centrifugal Atomiser	Inlet: 120, 180°C Outlet: 113-142 °C	Feed rate: 1200 ml/h Air flow rate: 90,110, 130 kg/h	Paramita et al. (2010)
Flaxseed oil	GA/MD$_{DE\ 10}$	2:1	Component ratio: 1:1 w/w Concentration: 10%	Laboratory scale spray dryer	Inlet: 180 °C Outlet: 110 °C	Feed rate: 720 ml/h Air flow rate: 73 m^3/h Compressed air pressure: 0.06 MPa	Carneiro et al. (2013)
Rosemary essential oil	GA/MD$_{DE\ 10}$	1:4	Component ratio: 1:1 w/v Concentration: 20%	Two-fluid nozzle	Inlet: 170 °C	Feed rate: 900 ml/h	Fernandes et al. (2014)
Fish oil	GA/MD$_{DE\ 19}$	1:4	Component ratio: 1:3 w/w Concentration: 24%	Mini Spray Dryer Buchi B-290	Inlet: 164 °C Outlet: 102 °C	Feed rate: 480 ml/h Air flow rate: 0.6 m^3/h Aspirator rate: 35 m^3/h	Tatar et al. (2014)
Phytosterols	GA/MD$_{DE\ 16\text{-}19}$	3:10	Component ratio: 3:1 w/v Concentration: 20%	Mini Spray Dryer Buchi B-290 with two-fluid nozzle	Inlet: 160 °C	Feed rate: 120 ml/h Air flow rate: 35-38 m^3/h	Di Battista et al. (2015)
-	GA/MD$_{DE\ 20}$	-	Component ratio: 1:1 w/w Concentration: 20%	Pneumatic nozzle	Inlet: 150, 175, 200, 250 °C Outlet: 70 °C	-	Porras-Saavedra et al. (2015)
Phenolic extract	GA/MD$_{DE\ 4\text{-}7,\ DE\ 17\text{-}20}$	1:1, 1:2	Component ratio: 10:0, 8:2, 6:4 v/v Concentration: 9% solid	Mini Spray Dryer Buchi B-290	Inlet: 120, 140, 160, 180 °C	Feed rate: 720 ml/h Air flow rate: 35 m^3/h	Tolun et al. (2016)

CM: core material; WM: encapsulating material

Table 2.1 (continued)

Core material	Encapsulating material	CM:EM	Properties of encapsulated material	Type of spray dryer	Temperature	Operational conditions	Authors
Saffron extract	GA/$MD_{DE\ 16\text{-}19}$	1:20	Component ratio: 3:27 w/w Concentration: 30%	Mini Spray Dryer Buchi B-191	Inlet: 180 °C Outlet: 90 °C	Feed rate: 300 ml/h Air flow rate: 0.6 m^3/h Atomisation pressure: 20 psi	Rajabi et al. (2015)
Bitter melon aqueous extract	GA/$MD_{DE\ 18}$	1.5:1	Component ratio: 1:1 w/w Concentration: 4.4%	Mini Spray Dryer Buchi B-290	Inlet/outlet: 125.6 °C/72.9 °C, 130 °C /75°C, 140 °C /80°C, 150°C /85 °C, 154.1 °C /87.1 °C	Air flow rate: 35-38 m^3/h Compress air flow: 0.47 ml/h Aspirator: 100%	Tan et al. (2015)
Barberry extract	GA/$MD_{DE\ 18\text{-}20}$	12:100, 25:100, 35:100, 50:100	Component ratio: 1:3 w/v Concentration: 20%	Pilot spray dryer	Inlet: 150 °C Outlet: 100 °C	Feed rate: 800 ml/h	Mahdavi et al. (2016)
Phenolic compounds (spent coffee grounds)	GA/$MD_{DE\ 2}$	5:1	Component ratio: 1:1 w/w Concentration: 20%	Mini Spray Dryer Buchi B-191	Inlet: 100 °C	Feed rate: 108 ml/h Atomisation air flow rate: 0.6 m^3/h Aspirator: 75%	Ballesteros et al. (2017)

CM: core material; WM: encapsulating material

2.2.2 Factors influence powder properties

The factors that influence the characteristics of the spray dried product and that can be adjusted are: (i) properties of the liquid feed, and (ii) process parameters. However, liquid feed properties and process parameters and are not independent steps in the development of spray dried products as both determine the final product performance at the particle and bulk level. Figure 2.6 illustrates the feed properties and process parameters are inter-correlated with fundamental variables that rule the particle formation process and powder performance. The understanding of those relationships allows for the development of a more robust and well understood process (Vicente et al., 2013).

The type and concentration of encapsulating material and process parameters such as inlet air temperature and feed flow rate are among major factors that influence the final quality of the powder. The impact of those factors on the powder properties, e.g. powder yield, moisture content, water activity, hygroscopicity, wettability, solubility, particle size, bulk density and particle morphology are presented in the next section.

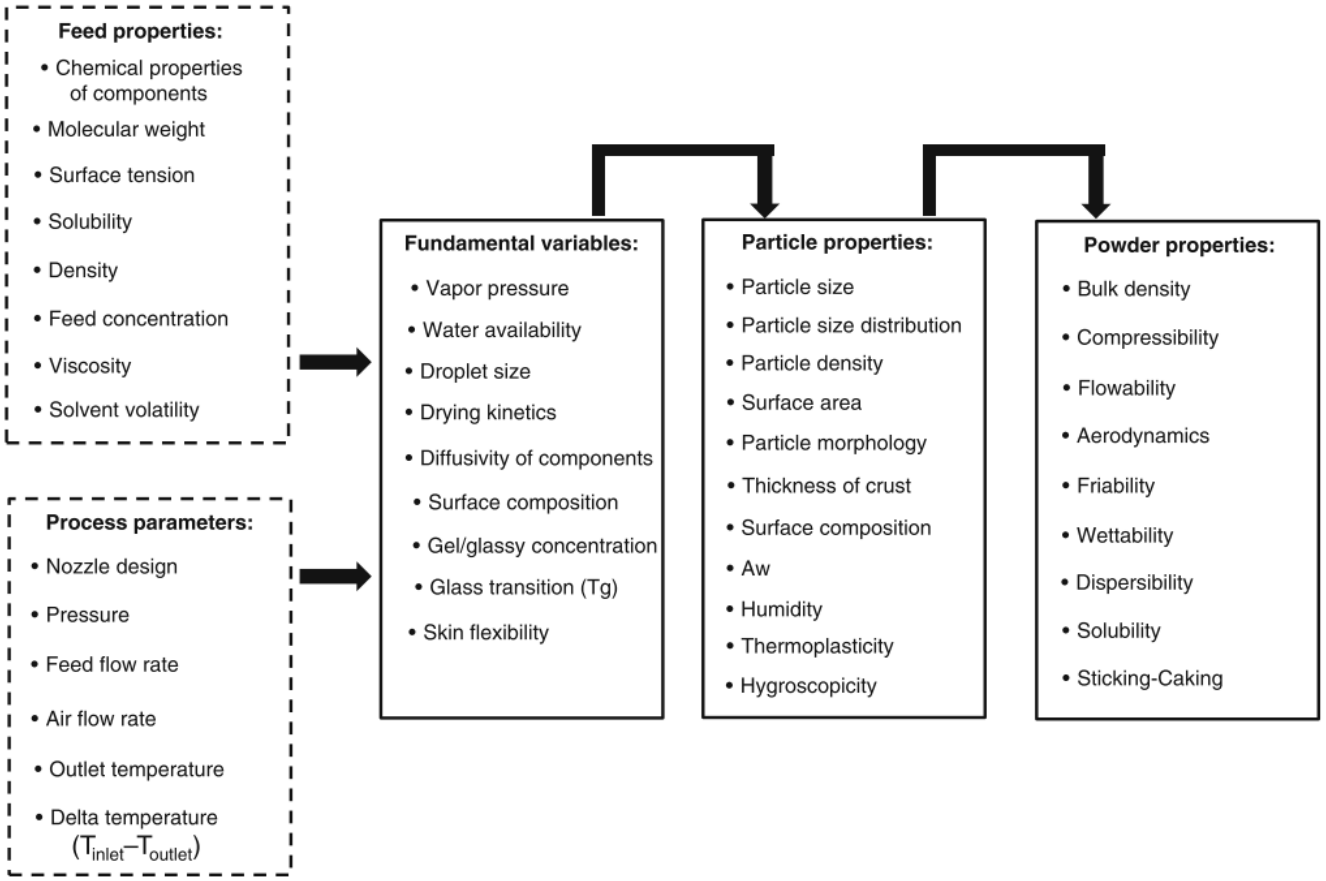

Figure 2.6 Diagram of relationships between feed properties, process parameters, fundamental variables, particle and powder properties in spray drying (Sadek et al., 2015b).

2.2.2.1 Powder yield

Powder yield is defined as the ratio between the mass powder collected after drying and the weight of total solids provided in the feed. The spray drying process is considered successful when a powder yield higher than 50% is achieved (Karaca et al., 2016). The main problem associated with a low powder yield is the stickiness and subsequent deposition of materials on the dryer surface. Powder stickiness occurs due to the low glass transition temperature of the materials. A high drying temperature during spray drying, which is usually higher than the glass transition temperature, results in the transformation of amorphous structures into a viscoelastic rubbery state where the polymer molecules become softer and more flexible because of greater molecular mobility (Bhandari et al., 1997; Keshani et al., 2015). Encapsulating materials which have higher glass transition temperature are commonly added to the feed solutions to prevent powder stickiness.

The use of different encapsulating materials can result in different powder yields. For example, Sanchez-Reinoso et al. (2017) obtained higher powder yield when spray dried cocoa aroma compounds with modified starch (59%) compared to MD (33%). Karaca et al. (2016) reported the yield for sour cherry powders produced with GA (68%) was lower than that produced with MD (77%). Spray dried concentrated yerba mate with MD DE 10 exhibited the highest powder yield than MD DE 15 and MD DE 20 as MD DE 10 had the highest glass transition temperature therefore decreasing the product stickiness (Negrão-Murakami et al., 2017). Similar results were also reported for spray dried black glutinous rice bran anthocyanins (Laokuldilok and Kanha, 2015) and spray dried grape polyphenols (Tolun et al., 2016) with different DE of MD. Spray dried black

mulberry powders produced with GA had lower glass transition temperature than MD DE6 and DE9, thus having lower powder yield (Fazaeli et al., 2012).

In general, a higher concentration of encapsulating material increases the powder yield as the solids content in the liquid feed increases. Increasing powder yield with increasing encapsulating material concentration was reported for *Satureja montana* extract (Vidović et al., 2014), saffron extract (Rajabi et al., 2015) and hydroxypropylated pea starch (Gouaou et al., 2018). On the other hand, Ribeiro et al. (2018) showed that the process yield of acerola and seriguela juice mix powder reduced with the increase of MD concentration from 14 to 16%. In the processing of acerola and seriguela juice, the lower powder yield was explained by a higher feed viscosity causing more solids to paste in the drying chamber.

There are contrasting results on the effect of the inlet air temperature on the powder yield. Some authors found that powder yield increased with an increase in the inlet temperature, while some authors reported the opposite. The positive relationship between the inlet temperature and powder yield was reported for black mulberry juice (Fazaeli et al., 2012), brucea javanica oil (Hu et al., 2016) and hydroxypropylated pea starch (Gouaou et al., 2018) due to more efficient heat and mass transfer processes occur at higher temperatures. On the other hand, lower powder yield with increasing temperature was reported for sugarcane juice powder (Ávila et al., 2015) and bitter melon aqueous extract powder (Tan et al., 2015) due to the fusion of the material to the wall of the drying chamber.

A higher feed flow rate, due to higher pump speed, creates larger feed droplets since fixed energy is applied to atomise more fluid in a given time. Therefore, slower drying occurs in the large droplets because of less effective heat transfer. As a result, increasing the feed flow rate negatively affects the powder yield (Karaca et al., 2016; Ribeiro et al., 2018; Tonon et al., 2008).

2.2.2.2 Moisture content and water activity

Moisture content represents the water composition in a food system, whereas water activity measures the availability of free water in a food system that is responsible for any biochemical reactions (Quek et al., 2007). The water activity can be defined as the ratio of water vapour pressure in the system (food) and the pure water vapour pressure at a constant value of pressure and temperature. Another possible definition is the equilibrium relative humidity of the air surrounding the food at the same temperature (Andrade et al., 2011). In general, the moisture content of the spray dried powder should lower than 5% and water activity values between 0.15 and 0.2 to assure biochemically and microbiologically stable and can be stored for long term usage (Bhandari, 2008; Tontul and Topuz, 2017).

The moisture content and water activity of the spray dried powders vary according to the encapsulating materials. Partial or total replacement of GA with MD, modified starch and inulin significantly affect the moisture content of rosemary essential oil powder. The samples prepared with inulin had higher moisture content than those prepared with pure GA and modified starch (Fernandes et al., 2014). Fazaeli et al. (2012) reported that black mulberry powder produced with higher DE values of MD had significantly higher moisture

content due to lower molecular weight MD contained shorter chains and more hydrophilic groups. However, Tolun et al. (2016) found that the utilisation of MD with different DE values to encapsulate grape polyphenols did not show a significant effect on the moisture content. The differences between obtained results could be related to the differences in drying temperature. In a study comparing different types of encapsulating material (GA, partially hydrolysed guar gum and polydextrose) on moisture content and water activity of spray dried Bordo grape skin extract, the moisture content did not differ significantly, but the water activity was significantly influenced by the encapsulating materials with the highest water activity found in the sample containing partially hydrolysed guar gum. However, in another study on spray drying of fish oil with different encapsulating materials (GA, GA-hemicellulose and hemicellulose), the moisture content and water activity of the final products were found to be similar (Tatar et al., 2014).

There are differing results on the effect of concentration of encapsulating materials on the moisture content and water activity of the final product. The moisture content and water activity of powders increased with increasing MD concentration due to an increase in viscosity that caused a reduction in heat transfer, thus making the outflow of water difficult (Ribeiro et al., 2018). Similar findings also reported for moisture content of watermelon juice powder produced with different amounts of MD (Oberoi and Sogi, 2015). However, Bhusari et al. (2014) reported an opposite trend of moisture content for tamarind pulp powder prepared with whey protein concentrate because of the greater water holding capacity of the protein in the amorphous state. Subtil et al. (2014)

reported no significant difference in moisture content and water activity of hydrolysed casein powders produced with different concentrations of GA.

The moisture content and water activity of the spray dried cocoa aroma compounds decreased with increasing inlet air temperature (Sanchez-Reinoso et al., 2017). Similar results were reported for pink guava juice (Shishir et al., 2014), grape polyphenols (Tolun et al., 2016), hydroxypropylated pea starch (Gouaou et al., 2018), acerola and seriguela juice mix (Ribeiro et al., 2018), groundnut milk (Saha et al., 2019).

As a general rule, increasing the feed flow rate results in higher moisture content and water activity of the powder (Hu et al., 2016; Movahhed and Mohebbi, 2016; Ribeiro et al., 2018; Shishir et al., 2016). The higher flow rates imply in shorter contact time between the droplet and drying air, thus making less effective heat transfer and cause the lower water evaporation (Ghollasi et al., 2018).

2.2.2.3 Hygroscopicity

Hygroscopicity is the ability of a material to absorb environmental moisture. It is generally calculated from the weight gain after placing the food powder in a high humid desiccator (relative humidity more than 60%) for a period until equilibrium is reached (generally one week) (Tontul and Topuz, 2017). A low hygroscopicity powder is desired to prevent aggregation of the powder as it affects the nutritional and flow properties of the powder (Mahdi et al., 2020). Powder with hygroscopicity more than 20% regarded as very hygroscopic (Nurhadi et al., 2012). According to Tonon et al. (2008), powder hygroscopicity decreases with powder moisture content. Powders with lower moisture content had a greater

capacity to absorb ambient moisture, higher hygroscopicity, as a result of the higher water concentration gradient between the powder and the surrounding air. Similar results were also reported by other researchers (Ferrari et al., 2012; Movahhed and Mohebbi, 2016).

Bhusari et al. (2014) reported a significant difference in hygroscopicity of tamarind pulp powders produced with three different encapsulating materials (MD, GA and whey protein concentrate). According to this report, the highest hygroscopicity was detected in the powders produced with MD. In fact, partial substitution of MD with GA resulted in less hygroscopic powder (Mahdavi et al., 2016). The DE value of MD showed a positive effect to the powders hygroscopicity due to difference in the chemical structure of MD and higher DE values indicate the greater the number of ramifications with hydrophilic groups to absorb water from the ambient air (Negrão-Murakami et al., 2017; Ribeiro et al., 2018).

In spray dried carrot-celery juice, MD concentration exhibited a contradictory effect on the hygroscopicity of the powder (Movahhed and Mohebbi, 2016). An increase in the addition of encapsulating material results in a decrease in the number of available binding sites, and thus decreasing the hygroscopicity of the powder (Horuz et al., 2012). Bhusari et al. (2014) explained that increasing the amount of encapsulating material may increase the glass transition temperature of the powder, thereby reducing the hygroscopicity. Similar results were also reported by several other researchers (Mishra et al., 2014; Ribeiro et al., 2018; Vidović et al., 2014).

Tolun et al. (2016) reported that increasing inlet air temperature led to a less hygroscopic powder of grape polyphenols. The positive relation between air temperature and hygroscopicity of powder was also observed for amla juice (Mishra et al., 2014), carrot-celery juice (Movahhed and Mohebbi, 2016) and cocoa aroma compounds (Sanchez-Reinoso et al., 2017). Castro-Muñoz et al. (2015) described the moisture content of the powders reduced at high temperatures and conversely increased the capture of water molecules by the powders. On the other hand, some authors reported lower hygroscopicity at higher drying temperatures (Bakar et al., 2013; Igual et al., 2014).

According to Movahhed and Mohebbi (2016) and Muzaffar et al. (2016), the powder produced at the higher feed rate had lower hygroscopicity. It could be associated with the higher moisture content of the powders (Tontul and Topuz, 2017).

2.2.2.4 Wettability and solubility

Wettability and solubility are important physical properties related to rehydrating or reconstituting the powders. Wettability refers to the ability of the bulk powder to absorb liquid under the influence of capillary forces (Tatar et al., 2014), whereas solubility can be defined as the ability of powders to form solution or suspension in water (Bicudo et al., 2015). The wettability is often determined by recording the time for the powder to become completely wetted (when all the powder particles penetrate the surface of the water) (Jinapong et al., 2008). The solubility of the powders can be expressed either as the average solubility time (time required to completely dissolve in water) (Caliskan and Dirim, 2016) or the solubility index (ratio between the mass of the powder in the supernatant after

centrifugation and the mass of the powder in the solution) (Mahdi et al., 2020). Typically, it is desirable to have powders with good wettability and high solubility especially when the powder is used as an additive in the production of other products, which can prevent processing difficulties and led to economic losses (Sharma et al., 2012; Tontul and Topuz, 2017). On the contrary, for encapsulated air microparticles the design is to delay particle wettability.

The wettability and solubility of the powders are directly related to the properties of the encapsulating material. Nurhadi et al. (2012) reported that honey powder produced with GA was more difficult to be wetted than MD due to GA containing more hydrophobic sites than MD. In a study that compared different types and combinations of encapsulating materials (GA, modified starch, modified starch:MD, modified starch:inulin, GA:MD and GA:inulin) to encapsulate rosemary essential oil, powders prepared with inulin exhibited the shortest wettability time, but the encapsulating materials had no effect on the solubility (Fernandes et al., 2014). Similarly, Botrel et al. (2014) reported that partial substitution of whey protein isolate by inulin improved the wettability properties of the fish oil powder and had similar solubility to those produced with whey protein isolate. These authors explained that inulin has a higher number of hydrophilic groups that highly interact with water and it is very soluble in water at 20-25 °C. Mahdavi et al. (2016) also observed no difference in the solubility of spray dried barberry extract with GA:MD, MD:gelatine and MD. However, in another study on spray dried fingered citron extract with different combinations of encapsulating material (GA, MD, modified starch and whey protein), the wettability and solubility of the powders were significantly influenced by the encapsulating materials. Powder prepared with a combination of GA and

modified starch exhibited the highest wettability but was poorly soluble in water (Mahdi et al., 2020).

The concentration of the encapsulating material has a significant effect on the wettability and solubility of powders. According to Caliskan and Dirim (2016), increasing the amount of MD caused a significant increase in the wettability times, but decreased the solubility time of the sumac extract powders. The increase in solubility with an increase in MD concentrations was reported for red pitaya peel powder (Bakar et al., 2013), satureja montana powder (Vidović et al., 2014) and sour cherry juice (Moghaddam et al., 2017). This was explained by the superior solubility of the MD (Goula and Adamopoulos, 2008). Similar findings were reported for soy protein isolate (Muzaffar and Kumar, 2015) and inulin (Daza et al., 2016).

There are contrasting results on the effect of the inlet temperature on wettability and solubility of the spray dried powders. A-Sun et al. (2016) reported that the wettability of coconut sugar powder increased with increasing inlet air temperature, but the solubility decreased. The authors explained that the low residual moisture content and formation of porous particles at high temperature had contributed to the increase in the powder wettability. At very high inlet temperature, a hard surface layer might be formed over the powder particle which could prevent water molecules from diffusing through to the inside of the particle (Chegini and Ghobadian, 2005). Some similar findings of solubility decreasing at high drying temperatures were reported for pomegranate juice (Horuz et al., 2012) and bitter melon (Tan et al., 2015). In another study, Ghollasi et al. (2018) found that inlet temperature had no significant effect on

the wettability of barberry juice powder, but the temperature increased the solubility. Similar results of solubility increasing with high temperature processing were also reported for black mulberry powders (Fazaeli et al., 2012), anthocyanin (Laokuldilok and Kanha, 2015), pomegranate juice (Muzaffar et al., 2016) and sour cherry (Moghaddam et al., 2017) which was attributed to the effect of inlet temperature on the moisture content of the powder. The lower the moisture content, the more soluble the powder (Fernandes et al., 2013; Goula and Adamopoulos, 2005). The higher temperature also results in less lump formation that is difficult to dissolve (Laokuldilok and Kanha, 2015). Mishra et al. (2014) and (Jafari et al., 2017) however reported no relationship between solubility and inlet temperature.

In general, the higher feed flow rate results in lower wettability and solubility of spray dried powders as a higher feed flow rate has positively increased the moisture content (Ghollasi et al., 2018; Muzaffar et al., 2016; Muzaffar and Kumar, 2015).

2.2.2.5 Particle size

Particle size is one of the most important physical parameters of powders as it is directly related to other physical properties of the product, such as appearance, bulk density, reconstitution property and flowability (Sharma et al., 2012). Particle size also plays an important role in powder handling, processing, transportation and storage properties (Tontul and Topuz, 2017). According to Fernandes et al. (2014), encapsulating material with higher viscosity would result in larger droplet formation during atomisation. The authors found particles produced with starch and GA had larger particle size and the addition of MD or

inulin to both formulations caused a reduction in the particle size as MD and inulin have lower viscosity. Additionally, the powder produced with GA resulted in larger particles compared to MD (Sarabandi et al., 2019). However, some studies reported that a combination of MD with other encapsulating materials such as inulin, oligofructose, GA, whey protein isolate or modified starch had no impact on the particle size, as observed in probiotic jussara juice powder (Paim et al., 2016) and flaxseed oil (Carneiro et al., 2013).

Particle size increased with an increase in the concentration of encapsulating materials (Rajabi et al., 2015; Shishir et al., 2016). This can be explained by the viscosity of the feed that increased with solids concentration, hence lead to larger droplets during atomisation.

Higher inlet air temperatures result in larger particles, which is related to a faster drying rate that promotes an early crust formation and prevents particle shrinkage during drying (Tonon et al., 2011a, 2011b). These results were reported for bitter melon (Tan et al., 2015), pink guava (Shishir et al., 2016), cocoa aroma (Sanchez-Reinoso et al., 2017) and barberry (Ghollasi et al., 2018).

The higher feed flow rate increases the size of the formed droplets, hence results in larger particles (Shishir et al., 2016; Tonon et al., 2011a). However, Ghollasi et al. (2018) found no significant effect of feed flow rate on the particle size of barberry juice powder. This is possibly because of a small difference of the feed flow rates used in the study (34, 36 and 38 ml/min).

2.2.2.6 Bulk density

Bulk density is defined as the mass of a given volume of powder and is expressed as kg m^{-3}. High bulk density powder is desirable to reduce shipping and packaging costs. Moreover, the bulk density influences other powder functionality, such as flowability and rehydration (Bicudo et al., 2015; Himmetagaoglu and Erbay, 2019). According to Tze et al. (2012), bulk density of powders is correlated with the particle size. Powder with a smaller particle size has a higher density due to the arrangement of the particles in close form, and thus occupies less space. As there are fewer empty spaces between the particles, a high bulk density powder can help to prevent oxidation and increase the stability of the powder (Goula and Adamopoulos, 2008).

Several published studies compared the effect of different encapsulating materials on the bulk density of powders. The bulk density of eggplant peel extract powders produced with MD was found to be greater than that of GA (Sarabandi et al., 2019). This finding was also confirmed by Bhusari et al. (2014) and Bicudo et al. (2015). The higher DE of MD led to an increase in bulk density which attributed by the lower glass transition temperature, hence higher stickiness (Fazaeli et al., 2012). However, the powder produced with a combination of MD and GA resulted in the densest particles as compared to other combinations of MD with whey protein concentrate or modified starch (Carneiro et al., 2013). Additionally, powder with GA had the higher bulk density than that of modified starch (Fernandes et al., 2014).

The bulk density of spray dried powder increased with the increasing concentration of encapsulating material (A-Sun et al., 2016; Vidović et al.,

2014). This increasing effect is attributed to the increase in the total solid content of the feed solution (Nadeem et al., 2011). Another possible reason could be due to agglomerate formation (Vidović et al., 2014). On the contrary, lower bulk density with increasing concentration of encapsulating material was reported for black mulberry juice (Fazaeli et al., 2012), pomegranate juice (Jafari et al., 2017) and sour cherry juice (Moghaddam et al., 2017). The reason for this reduction was explained by the decrease in moisture content or the higher air trapped in the particles.

The bulk density is generally decreasing at higher drying temperatures. The reason for this reduction is explained by the acceleration of the evaporation rate that creating more porous, hollow or fragmented particles. This phenomenon was observed in spray dried coconut sugar (A-Sun et al., 2016), beetroot juice concentrate (Bazaria and Kumar, 2016), pomegranate juice (Jafari et al., 2017), barberry juice (Ghollasi et al., 2018), cream (Himmetagaoglu and Erbay, 2019), groundnut milk (Saha et al., 2019) and eggplant peel extract (Sarabandi et al., 2019).

According to Ghollasi et al. (2018), the feed flow rate was positively affected by the bulk density of barberry juice powder. The higher flow rate shortens the contact time between droplets and drying air, thus leading to less efficient heat transfer. Indeed, Mahdavi et al. (2016) claimed a positive correlation between moisture content and bulk density of the powder. On the contrary, Bazaria and Kumar (2016) found that the feed flow rate did not significantly change the bulk density of the powder.

2.2.2.7 Particle morphology

The preferred morphology for spray dried particles is a uniform, spherical and smooth surface with no apparent cracks or fissures. Any damage in the particle surface reduces the protection and retention of the core material (Fernandes et al., 2014; Tan et al., 2015; Tatar et al., 2014). In the case of encapsulated air microparticles, it is also desired to produce particles with no breakage to make sure the air inside the particles are well protected by the shell walls. The rough surfaced particles are more sensitive to oxidation reactions compared to those of smooth surfaces because of their larger surface areas (Tolun et al., 2016). Moreover, the presence of dents has an adverse effect on the powder flowability properties (Rosenberg et al., 1985).

The type of encapsulating material has a significant impact on the morphology of spray dried particles. Particles produced with modified starch alone or with modified starch:MD possessed a higher proportion of spherical particles than that of GA, GA:MD, GA:inulin and modified starch:inulin (Figure 2.7) due to the matrices providing elasticity during the drying process (Fernandes et al., 2014). Tatar et al. (2014) observed the GA based particles had many dents and remarkably shrunk when compared to hemicellulose based particles. In another study, Rajabi et al. (2015) compared different compositions of MD:GA:gelatin to encapsulate saffron bioactive components by spray drying. The authors found that the number of dented particles was minimum when the powder produced without GA.

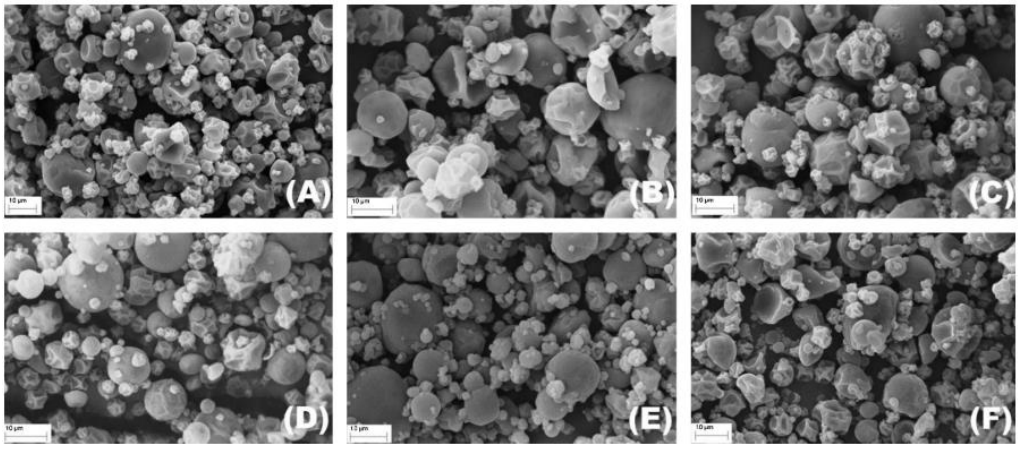

Figure 2.7 SEM images of the particles containing rosemary essential oil using the following encapsulating materials: (A) GA; (B) GA:MD; (C) GA:inulin; (D) modified starch; (E) modified starch:MD; and (F) modified starch:inulin (Fernandes et al., 2014).

On the contrary, Porras-Saavedra et al. (2015) reported the particle surface of spray dried GA was smooth, while MD and soy protein isolate were rough with dents. According to Ré (1998), the dented surfaced particles are formed due to slow film formation during drying of the droplets. Meanwhile, the formation of hollow particles is attributed to the vacuole formation that occurs after the hardening of the outer surface followed by the expansion of the air bubbles trapped inside the droplet. Porras-Saavedra et al. (2015) obtained the highest percentage of hollow particles (26%) in the formulations of MD:soy protein isolate and MD:GA, while GA:soy protein isolate had the highest percentage of compact particles. When the DE-value of MD decreased, the particles tended to become more spherical due to different in the molecular structure (Figure 2.8) (Fazaeli et al., 2012; Tolun et al., 2016).

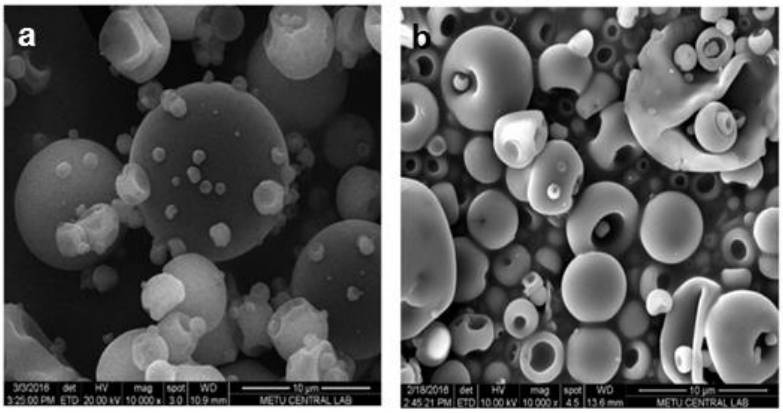

Figure 2.8 SEM images of particles produce with different DE of MD: (a) DE 4-7 and (b) DE 17-20 (Tolun et al., 2016).

Rajabi et al. (2015) reported that an increase in the MD concentration led to smoother surface particles, while dented particles tended to form at higher GA concentration. Many researchers have reported that particles produced from MD have smooth surface and the use of GA tends to form spherical dented particles (Kanakdande et al., 2007; Manickavasagan et al., 2015; Pang et al., 2014; Sarabandi et al., 2019; Tolun et al., 2016). Paramita et al. (2010) investigated the morphology of spray dried GA:MD produced at different solid content (20, 30, 40 and 50%) (Figure 2.9). A deeper surface groove was observed at a lower solid content, whereas smoother particles with vacuole at a higher solid content. The highest percentage of hollow particles (81%) was recorded at 40% solid concentration. The authors explained that increasing solid concentration enhanced the formation of a solid film crust on the surface of the particle and an inflated particle structure, thus increasing the particle size and percentage of the hollow particles. However, in a different study Fernandes et al. (2008) observed particles produced from different solid contents (30, 40, 50 and 60%) and at different MD:GA proportions (4:1, 3:2, 2:3 and 0:1) had no significant differences in their morphology.

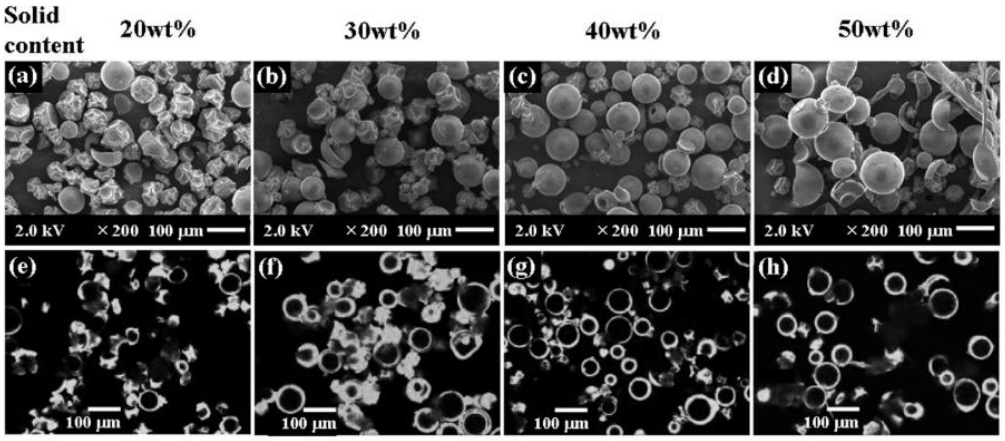

Figure 2.9 Effect of solid content on the morphology of spray dried GA:MD (mass ratio of 1:2) by SEM (a-d) and confocal laser scanning microscopy (e-h) (Paramita et al., 2010).

Generally, the higher inlet temperature results in smoother surfaces and more spherical particles, while wrinkled surfaces are produced at a lower temperature. These results were reported for MD to encapsulate pomegranate juice (Jafari et al., 2017), MD or modified starch to encapsulate cocoa aroma compounds (Sanchez-Reinoso et al., 2017), MD and sodium caseinate to encapsulate cream (Himmetagaoglu and Erbay, 2019). This was explained by the difference in the drying rate, in which the deformations appeared when the drying temperature was low that resulted in slower water diffusion and a long time of drying. In contrast, high drying temperatures produce faster evaporation and leading to the formation of a smooth and hard crust (Tonon et al., 2008). However, the surface of the particles tended to crack at high temperature because of the excessive evaporation rate (Tan et al., 2015).

There are differing reports on the effect of feed flow rate on the morphology of particles. Wang et al. (2015) reported powder particles dried under a reduced feed flow rate had smoother surface due to an increase in drying rate. On the other hand, Himmetagaoglu and Erbay (2019) observed an increase in the

number of irregularly shaped particles with shrinkages, collapses, cracks and fractures at high feed flow rate. Additionally, agglomeration of particles was initiated at high feed flow rate because of the high level of surface fat that causes inter particle liquid bridges.

2.3 Encapsulated Air Microparticles

The production of particles with targeted properties is difficult to achieve using empirical knowledge alone, therefore researchers have shifted to scientific based approaches to gain a better insight into particle formation in the spray drying process (Vehring, 2008; Vicente et al., 2013). The purpose of the research presented in this thesis was to produce hollow spray dried particles with controlled wettability, also referred to as encapsulated air microparticles. Understanding the fundamental principles of particle formation and segregation of components during the spray drying is required in order to successfully develop encapsulated air microparticles. As previously discussed, the hollow particles seem to be obtained at higher drying temperatures and lower feed flow rates. A mixture of GA and MD was selected as the encapsulating material based on the findings by Paramita et al. (2010) and Porras-Saavedra et al. (2015) who observed the hollow morphology of spray dried particles from this formulation. Moreover, the addition of GA would possibly control the wettability of particles due to the surface active character which would adsorb at the surface of the particles during the drying.

2.3.1 Particle formation

Control of particle morphology in the spray drying process has been receiving great research attention for decades (Nandiyanto and Okuyama, 2011). A wide range of particle morphologies can be produced by changing the drying conditions (Charlesworth and Marshall, 1960; Walton, 2000; Walton and Mumford, 1999a), and some of these possibilities are illustrated in Figure 2.10. The particles may be present as a solid, a hollow, a shrivelled or a blistered shape depending on drying history. For example, Alamilla-Beltrán et al. (2005) obtained three distinguished morphologies i.e. wrinkled, inflated and broken shells, when spray drying the same MD solution at different drying conditions (Figure 2.11).

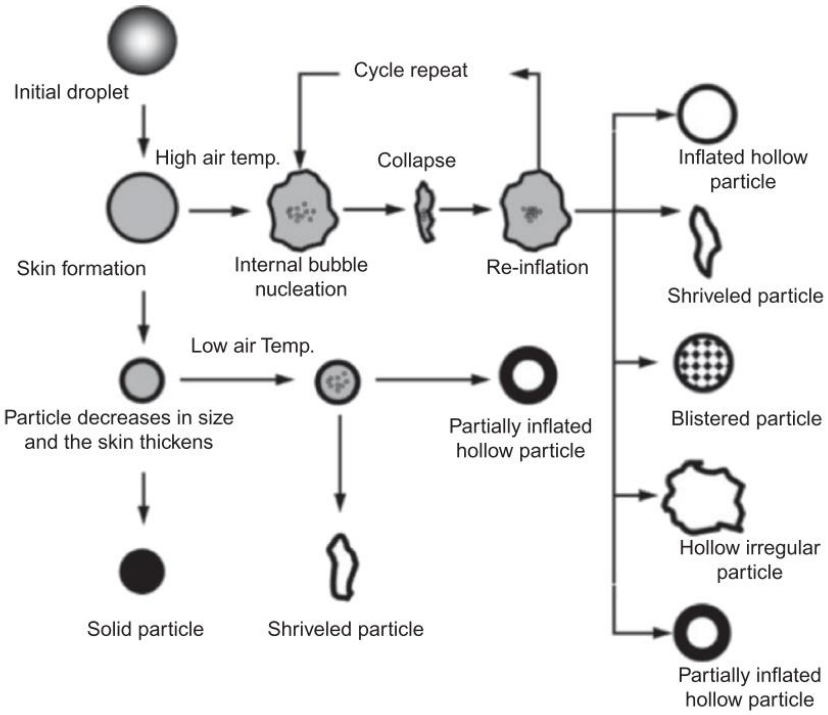

Figure 2.10 Schematic showing different particle morphologies obtained from the drying of a droplet (Walzel and Furuta, 2011).

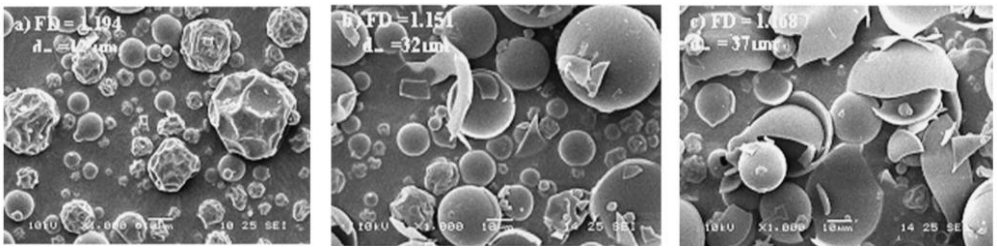

Figure 2.11 SEM images of MD particles at several drying conditions: (a) 110/74°C, (b) 170/145 °C and (c) 200/173 °C (Alamilla-Beltrán et al., 2005).

Over the few last decades, experimental studies at the spray drier scale and at the droplet scale, as well as modelling studies have been extensively developed for a greater understanding of the process of particle formation from a drying liquid droplet (Lima et al., 2019; Mezhericher et al., 2010a; Walton and Mumford, 1999b). The first scientific effort to study spray dried particle morphologies was carried out by Charlesworth and Marshall (1960). According to Anandharamakrishnan and Ishwarya (2015), drying kinetics is principal to the understanding of particle morphology. The drying kinetics of droplets containing dissolved or suspended solids has commonly been divided into two stages (Kim et al., 2009a; Mezhericher et al., 2010a), as illustrated in Figure 2.12.

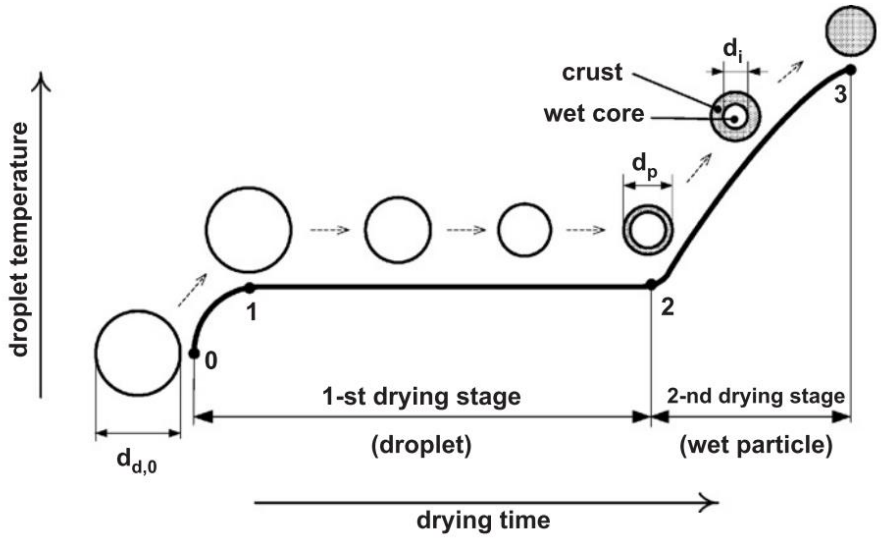

Figure 2.12 Typical drying history and morphological changes during the drying of a single droplet containing solids (Mezhericher et al., 2008).

The interval between points 0 and 1 (Figure 2.12) corresponds to the droplet's initial heating. Then, the free water evaporates from the droplet surface at a constant rate in the first drying stage (point 1-2). Moisture evaporation results in shrinkage of droplet diameter and enrichment of solutes at the surface of the droplet. When the concentration at the surface reaches the so-called critical concentration, a solid crust is formed (point 2). From this point, the second drying stage begins (point 2-3). Once the crust is formed, the drying rate decreases and the particle starts to heat up.

The rigidity of the crust determines the mechanism of moisture transport (Figure 2.13). If a rigid porous solid crust is formed, the evaporation occurs at the interface between the crust and the wet core. The vapour diffuses through the porous solid crust and the thickness of the crust increases as solid is deposited on the internal crust core interface to form a solid particle. If the crust is flexible and pliable, the crust is wetted by a continuous phase and the evaporation occurs from the crust outer surface (Mezhericher et al., 2008, 2010a). An increase in temperature of the particle causes vaporisation of the solvent within the wet core that can result in bubble formation. Depending on the mechanical properties of the crust, it may explode, crack, collapsed or inflate (Lima et al., 2019; Vehring et al., 2007). The second drying stage continues until the temperature of the drying air and particle equalise.

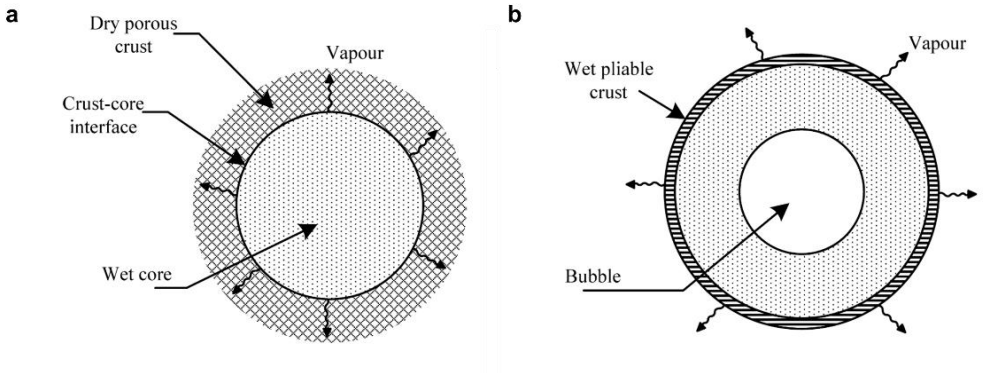

Figure 2.13 Mechanisms of droplet drying models: (a) droplet with a dry solid crust; (b) droplet with a pliable crust and a bubble (Ali et al., 2014).

2.3.2 Segregation of components

The functionality of a powder, such as wettability, dissolution, flowability and encapsulation efficiency is expected to be closely linked to the surface composition of the particles. In a multi component particle, the surface composition is influenced by the segregation of components during the drying process. The segregation of components has been extensively studied in spray dried milk (Foerster et al., 2016; Gaiani et al., 2006, 2007; Kim et al., 2002, 2009a; Murrieta-Pazos et al., 2011; Nijdam and Langrish, 2006; Nuzzo et al., 2017) and spray dried emulsions (Fäldt and Bergenståhl, 1995; Munoz-Ibanez et al., 2016) in order to produce good quality powders.

Many researchers have demonstrated that XPS is a powerful tool for investigating the chemical surface composition of spray dried powders (Gaiani et al., 2006; Nuzzo et al., 2017; Wang and Langrish, 2010). XPS is also known as electron spectroscopy for chemical analysis (ESCA). XPS probes the elemental composition on the surface (up to 10 nm depth) of a particle (Lee et al., 2014). The technique is based on energy-spectrum measurements of photoelectrons emitted from a material surface under irradiation with a

monochromatic soft X-ray radiation (Faldt et al., 1993; Murrieta-Pazos et al., 2012). Another approach is using time of flight secondary ion mass spectrometry (ToF-SIMS) to study the surface composition of spray dried powder (Momin et al., 2018; Wang et al., 2016). The ToF-SIMS uses a pulsed primary ion beam to desorb and ionize species from a sample surface (approximately 1 nm depth). The resulting secondary ions are accelerated into a mass spectrometer and are then mass analysed by measuring their time of flight from the sample surface to the detector (Murrieta-pazos et al., 2012). TOF-SIMS can provide mass spectral information, image information in the XY dimension across a sample and depth profile information on the Z dimension into a sample.

Confocal laser scanning microscopy (CLSM) and confocal Raman microscopy (CRM) are also relevant techniques to map the internal component distribution at the wall of particles (Both et al., 2018a, 2018b; Foerster et al., 2016; Munoz-Ibanez et al., 2016; Nuzzo et al., 2015b). CLSM requires fluorescent labelling of the components to be visualised, whereas CRM can visualise the internal structure of a dried particle without staining of the sample as the full Raman spectrum in each pixel of the image is used to construct an image of the localisation of the different molecular components (Munoz-Ibanez et al., 2016; Schutyser et al., 2019). Thus, the use of CLSM is limited to components with sufficiently different properties, such as oil, carbohydrate and protein, but cannot distinguish between components of similar dyeing properties, for example different polysaccharides (Munoz-Ibanez et al., 2016). A more recently developed technique is the combination of scanning electron microscopy coupled with energy dispersive X-ray spectroscopy (EDX) to characterise the

atomic composition of a sample or to map out the lateral distribution of elements from the imaged area (Murrieta-Pazos et al., 2011; Porras-Saavedra et al., 2015; Wang et al., 2015). The principle is based on the unique atomic structure of each element (Moran et al., 2014). To stimulate the emission of characteristic X-rays from a specimen, a high-energy beam of charged particles is focused into the sample that creates an EDX spectrum. The higher a peak in a spectrum, the more concentrated the element is in the sample (Murrieta-Pazos et al., 2012).

Controlling the mechanisms of component distribution during the drying process and the inclusion of specific components in the liquid feed are key to successful particle engineering (Porowska et al., 2015; Vehring, 2008). Factors that impact the component segregation are: difference in diffusivity of components, difference in component solubility, surface activity, hydrophobicity or hydrophilicity of components, and interaction between the solid components in a suspension (Porowska et al., 2015), as illustrated in Figure 2.14.

During drying, the solvent diffuses towards the surface of the droplet, while the solute diffuses to the centre. The solutes with the lowest diffusion coefficient are expected to dominate the particle surface (Meerdink and van't Riet, 1995; Nuzzo et al., 2015a). Solutes with low diffusivity often have low solubility as the diffusivity decreases with increasing molecular weight (Wang and Langrish, 2009). In spray dried milk, free fat tends to accumulate on the outermost layer of the particles, underneath this surface layer is fat globules that are covered by proteins, followed by lactose and salts. The segregation of materials that occurs during drying of milk droplets is because of the difference in the diffusivity of the

components, thus suggests that fat has the lowest diffusivity (Kim et al., 2002, 2003, 2009a; Nijdam and Langrish, 2006). The surface coverage of hydrophobic components, such as fat, gives poor wetting properties compared to the surface coverage of hygroscopic components (e.g. lactose) (Gaiani et al., 2007; Kim et al., 2002). The hydrophobic solutes, e.g. rifampicin (Wang et al., 2016) and oil droplets (Munoz-Ibanez et al., 2016), were preferentially deposited at the surface of spray dried particles.

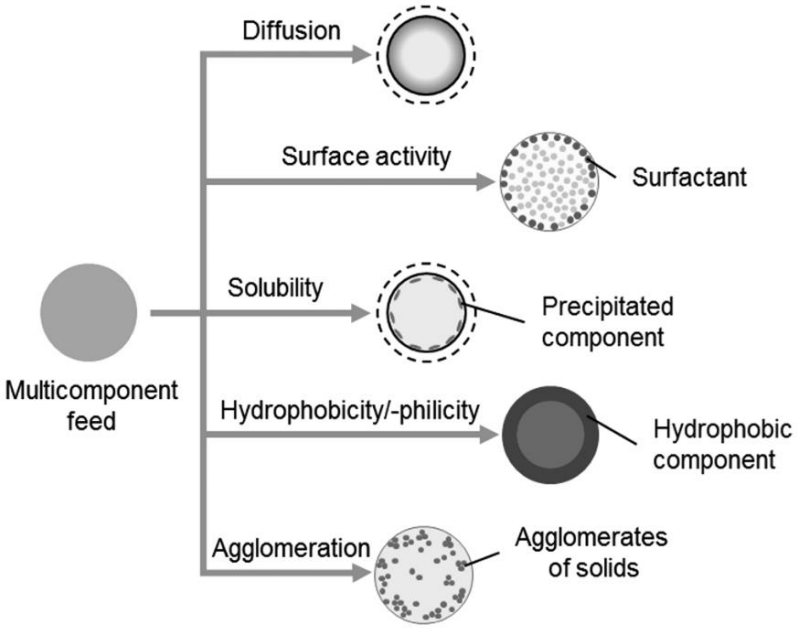

Figure 2.14 Possible interactions between the components of a multi component droplet that can impact on the surface composition of the dried particle (Porowska et al., 2015).

Surface active components tend to precipitate instantly at the liquid-air interface and thus appear on the outermost layer of the particle after the drying is completed (Fäldt and Bergenståhl, 1994). Nuzzo et al. (2015a) found enrichment of surface active polymers (bovine serum albumin, hydroxypropyl methyl cellulose and tri-block co-polymer Poloxamer) at the surface of spray dried and individually dried particles as indicated by XPS. However, a higher

level of surface active materials was observed at the surface of the single dried particles when compared to spray dried particles. In another study, Nuzzo et al. (2015b) used confocal Raman microscopy to investigate the phase segregation in the particles. The authors found that those surface active materials were enriched at the surface and segregated from the amorphous lactose matrix in the internal part of the particles. Munoz-Ibanez et al. (2016) observed that GA and MD tended to segregate during droplet drying. GA was overrepresented at the outer surface of the particles due to the surface active character of GA (Figure 2.15).

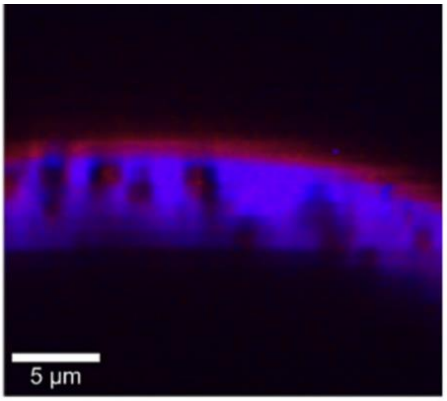

Figure 2.15 Internal mapping by confocal Raman microscopy of a spray dried particle. Red: GA and blue: MD (Munoz-Ibanez et al., 2016).

2.4 Drying Kinetics

As introduced above (Figure 2.12), the drying of a solution droplet comprises two main stages: droplet evaporation (first stage of drying) and formation of wet particle and drying of wet particle to fully dry particle (second stage of drying). In the following the mathematical relationships relating to either drying stage are introduced.

2.4.1 First drying stage

The evaporation of solvent from a solution droplet in a spray dryer is a coupled heat and mass transfer problem. The process is driven by the difference between the solvent's vapour pressure and its partial pressure in the gas phase. The hot gas temperature triggers a heat exchange from it to the droplets, while the vapor pressure difference causes a moisture transfer in the opposite direction (Santos et al., 2018). The rate of evaporation is determined by the balance of energy required to vaporise the solvent and the energy transported to the surface of the droplet.

The coefficients of heat and mass transfer can be estimated by the corresponding Nusselt (Equation 2.1) and Sherwood numbers (Equation 2.2) (Wisniewski, 2015). The Nusselt Number, Nu, is defined as the ratio of convective to conductive heat transfer across a boundary. The Sherwood Number, Sh, is a dimensionless number that represents the ratio of the convective mass transfer to the rate of diffusive mass transfer. It is the mass transfer equivalent of the Nu.

$$Nu = h * D_d/k \quad (2.1)$$

where h is the heat transfer coefficient by convection, k the thermal conductivity of gas layer around droplet and D_d the droplet diameter.

$$Sh = k_g * D_d/D \quad (2.2)$$

where k_g is the mass transfer coefficient, D the diffusion coefficient and D_d the droplet diameter.

Frequently used equations for Nusselt and Sherwood Numbers involve Reynolds, Prandtl and Schmidt Numbers (Masters, 1991; Ranz and Marshall, 1952).

Reynolds Number $Re = D_d * u/v$; Prandtl Number $Pr = v/\alpha$; Schmidt Number $Sc = v/D$

Heat transfer $Nu = a_1 + b_1 * Re^m * Pr^n$ (2.3)

Mass transfer $Sh = a_2 + b_2 * Re^m * Sc^n$ (2.4)

where D_d is the droplet diameter, D the mass diffusivity, α the thermal diffusivity, v the kinematic viscosity and u the velocity.

Typically, a_1 and a_2 are taken as 2 for evaporative processes. b_1 and b_2 are often taken as 0.6 according to the well-known work by Ranz and Marshall (1952). Depending on the experimental systems used and solvents chosen, a number of studies have yielded similar or different coefficients (Downing, 1966; Lin and Chen, 2002). However, in spray drying simulations, the Ranz and Marshall (1952) correlation has been the most widely used. The heat transfer and mass transfer correlations must be adequately matched in order to accurately predict the weight loss of a droplet over time and the temperature-time history of the particle (Chen, 2004).

During the first drying stage, the drying process proceeds at a constant evaporation rate as the moisture is removed constantly from the surface of the droplet. Hence, this stage is named the constant rate drying stage. The droplet

surface remains saturated with moisture, keeping it sufficiently cool and its temperature is constant at the wet bulb temperature (point 1-2 in Figure 2.12) (Che et al., 2012). The wet bulb temperature is the temperature of the drying gas when it becomes saturated with vapour from the liquid (Seydel et al., 2006). This is the lowest temperature that the drying gas can reach as a result of the evaporative cooling phenomenon, in which the gas is cooled as it spends latent heat of vaporisation (Santos et al., 2018).

An intense moisture evaporation at this stage is marked by droplet shrinkage. The evaporation rate constant, κ, is described to follow the radius squared law (Law and Law, 1982). This is based on the fact that during the constant rate period, the evaporation of a liquid droplet of diameter d is proportional to its surface area (Equation 2.5).

$$d^2(t) = {d_0}^2 - \kappa t \tag{2.5}$$

where d is the droplet diameter, d_0 the droplet initial diameter, t the time and κ the drying rate constant.

2.4.2 Second drying stage

The second stage of drying is defined by the solutes present in the droplet. As solvent evaporation takes place from the surface of the droplet, the solute concentration at the surface increases, causing a diffusional flux of solutes from the droplet surface towards the centre of the droplet. The diffusion coefficient of solutes are estimated using the Stokes–Einstein's equation and depend on the

internal liquid criteria such as solution viscosity, solute radii and temperature (Sadek et al., 2015b):

$$D = \frac{k_B T}{6\pi\eta R_h} \tag{2.6}$$

where k_B is the Boltzmann's constant, T the absolute temperature, η the viscosity of the solution and R_h the hydrodynamic radius of the solute.

The Peclet, Pe, number that reflects the extent of convection in relation to diffusion and is commonly expressed by:

$$Pe = \frac{h_0 J}{D} \tag{2.7}$$

where h_0 is the initial height of the droplet, J the evaporation flux estimated from the loss of volume, V, per area unit, A, at the beginning of the drying process $J = -(1/A)dV/dt$ and D is the solute diffusivity (Equation 2.6) according to solute size and the viscosity of water.

When the solute reaches a concentration beyond its saturation concentration, a thin shell (also known as crust) is formed at the droplet surface. The evaporation occurs now in the droplet on the boundary that separates the dry crust and wet core regions, as shown in Figure 2.16. Consequently, the drying rate slows down due to the decline of heat and mass transfer rates in the growing crust layer as the vapour generated at the evaporation surface diffuses through (the pores of) the crust to the outer droplet surface and the heat supplied by the drying gas is transferred to the evaporation surface by conduction (Golman and Julklang, 2013; Mezhericher et al., 2010a). Hence, this second stage is named

the falling rate stage of drying. The governing equations for heat and mass transfer during the falling rate period have been developed by many researchers (Dalmaz et al., 2007; Golman, 2012; Golman and Julklang, 2013; Mezhericher et al., 2010b, 2008, 2007).

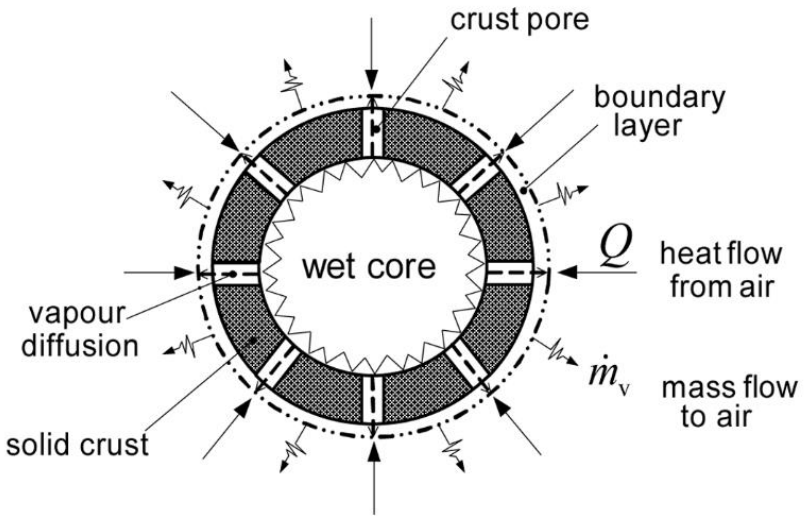

Figure 2.16 Model of drying a droplet containing insoluble or dissolved solids (Mezhericher et al., 2007).

During this period, the droplet temperature will increase until it becomes equal to that of the surrounding gas (so-called dry bulb temperature), and a non-evaporating solid sphere is developed. This indicates the presence of a particle with the least possible amount of residual solvent, which can either be an equilibrium amount or residual solvent that cannot be removed by the drying process. The particles are never heated above the outlet temperature of the dryer and the temperature of the final dried powder will be around 20 °C lower than the air outlet temperature (Gohel et al., 2009).

2.5 Single Droplet Drying

Particle formation and segregation of components during the spray drying process are still not well understood and represent an extensive research field. Understanding the development of particle morphology during drying creates prospects for controlling particle morphology, and thus particle functionality in spray drying processes. Many scientific studies have employed SDD experimental approaches to mimic the spray drying process by monitoring the drying behaviour of a single droplet under controlled air conditions. Ranz & Marshall (1952) were the first to investigate the drying kinetics of pure solvent droplets and droplets containing dissolved solids. Later, SDD approach was subsequently extended to monitor the morphological changes during the droplet-particle transition, as well as to study other key issues in the spray drying process such as control of both morphology and functionality of particles. Many studies have demonstrated the usefulness of SDD to investigate drying kinetics and particle formation (Both et al., 2018a; Bouman et al., 2016; Griesing et al., 2016; Perdana et al., 2013; Sadek et al., 2016; Tran et al., 2016), despite the larger droplet sizes used for single droplet drying compared to droplets created by the nozzles of spray dryers and therefore, slower drying kinetics.

The SDD apparatus should meet three criteria to achieve an accurate measurement (Fu et al., 2012): 1) the single droplet needs to be generated with controllable and reproducible size, 2) the air stream used for drying should have controlled temperature, velocity and humidity, 3) the monitoring methods of changes in droplet kinetics parameters such as mass, temperature and diameter must be accurate and robust to generate quantitative data for analysis and calculation. Several types of SDD experimental set-ups with regard to

droplet “fixation” in the controlled atmosphere have been described in the literature. These include droplet suspension from a filament (Tran et al., 2016), acoustic levitation or aerodynamic field (Griesing et al., 2016; Nuzzo et al., 2017; Pajander et al., 2015), a free-falling droplet (Vehring et al., 2007) and a sessile droplet on a hydrophobic substrate (Perdana et al., 2013, 2011; Tran et al., 2017), as illustrated in Figure 2.17. Table 2.2 compares the main features of those SDD techniques.

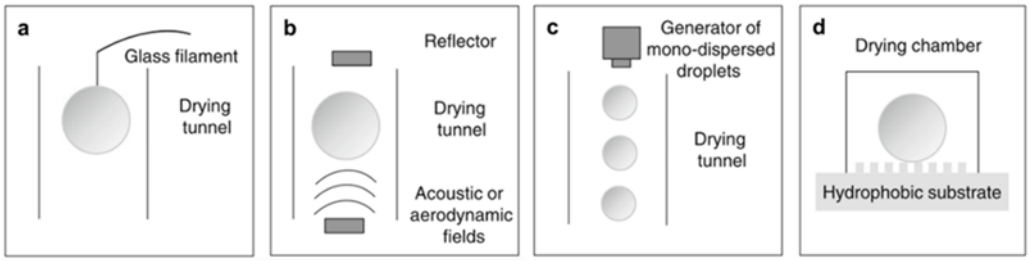

Figure 2.17 Single droplet drying techniques: (a) droplet suspension from a filament; (b) droplet levitated by acoustic or aerodynamic field; (c) free-falling droplet in a tall tower; (d) sessile droplet on a hydrophobic surface (Sadek et al., 2015b).

Table 2.2 Comparison between the different SDD techniques (Fu et al., 2012; Lima et al., 2019; Nuzzo et al., 2015a).

	Glass filament	Acoustic levitation	Free fall	Hydrophobic surface
Means of support	A fine glass filament	Acoustic or aerodynamic field	No support	A hydrophobic surface
Intrusive into droplet	Yes	No	No	Yes
Droplet size	0.5-9 mm	0.3-3 mm	0.2-0.4 mm	0.15-2 mm
Drying rate measurement	Direct method by connecting the glass filament to a microbalance that allows for continuous measurement during drying	Indirect method by converting the droplet diameter changes or droplet positions changes into mass changes	Indirect method by measuring the distance that the droplet travelled inside the tower, or collecting droplets at different heights of the tower	Indirect method by converting the droplet diameter changes
Similarity to actual spray drying process	Drying kinetics affected by the intrusive glass filament	Drying kinetics affected by the acoustic or aerodynamic field	Very similar to actual spray dryer	Drying kinetics affected by the intrusive hydrophobic surface
Advantages	Measurements on the drying kinetics and visualization of the droplet during drying are relatively less complex	Measurements on the drying kinetics and visualization of the droplet during drying are relatively less complex	Drying condition induced closely follows that of a spray dryer	Measurements on the drying kinetics and visualization of the droplet during drying are relatively less complex
Disadvantages	Intrusion of filament into the droplet	Possible effect of the acoustic waves affecting the mass transfer process	Measurements on the drying kinetic and visualization of the droplet during drying is complex and difficult	Intrusion of hydrophobic surface into the droplet

For this research, a sessile SDD deposited on a flat hydrophobic membrane was chosen as it allows direct observation of droplet-particle conversion. Perdana et al. (2011) were the first to investigate the drying of a single droplet on a hydrophobic membrane using the experimental set-up in Figure 2.18. The hydrophobic membrane is used to minimize the contact between the droplet and the surface and to maintain the spherical shape of the droplet. The hydrophobic surface can be achieved by specific treatment of the surface or by specific surface topography (Vakarelski et al., 2014; Xu and Choi, 2012; Yu et al., 2012). This technique has been successfully used by many researchers to investigate various events during particle formation, such as shell buckling (Sadek et al., 2016), hole formation (Bouman et al., 2016) and vacuole formation (Both et al., 2018a; Sadek et al., 2013).

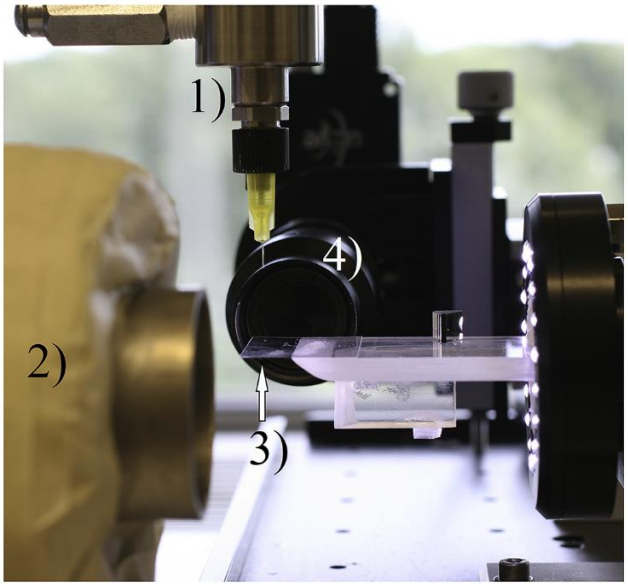

Figure 2.18 Sessile SDD platform with (1) micro dispenser with a needle tip, (2) insulated air tunnel, (3) sample holder with hydrophobic membrane, (4) camera (Both et al., 2018a).

The SDD has been frequently used to investigate the drying phenomena of milk and its derivatives. More recently, this approach has been extended to study other encapsulating materials such as MD (Siemons et al., 2020), GA (Zhang et al., 2019) and starch (Gouaou et al., 2018). Droplet composition and drying parameters can be varied to understand particle morphology development. During the SDD, different stages of particle morphology development can be distinguished (Schutyser et al., 2019): 1) the constant drying period, where phase separation of components may take place, 2) the locking point that is the first visual of skin formation, and 3) the final particle morphology development.

A few relevant SDD studies related to the effect of droplet compositions and drying parameters on the particle morphology are listed in Table 2.3. Each component in the droplets behaves differently during the drying process and the consistency of the developed skin will determine its final particle morphology; a rigid skin cannot easily deform, whereas a weak can continuously deform creating a wrinkled particle. In general, droplets with higher solids content, or higher drying temperature, or lower air humidity are more likely to form smooth surface particles with a large vacuole, while the opposite will lead to wrinkled particles.

Table 2.3 Summary of SDD studies on particle morphology development.

Droplet component	SDD technique	Influencing factor	Parameter range	Effect on morphology	Authors
Skim milk	Free flying droplet	Initial solids content	33-54%% w/w	• Low solids content, wrinkled • High solids content, hollow particles with thin crusts	Wu et al. (2014)
Whey protein isolate and native phosphocaseinate	Sessile pendant droplet and free flying droplet	Composition and SDD technique	Different compositional ratios and SDD techniques	• Whey protein – semi spherical, hollow • Casein micelles – wrinkled, dense • Protein mixtures – hybrid particles • Similar particle morphologies for both drying techniques	Sadek et al. (2014)
Milk protein	Sessile pendant droplet	Types of milk protein	Whey protein isolates or native phosphocaseinates	• Whey protein – smooth, spherical, broken particle • Native phosphocaseinates – twisted, wrinkled whole particle	Sadek et al. (2015a)
Whey protein isolate	Sessile droplet	Air temperature and initial solids content	Temperature 20-80 °C Initial solid 5-30% w/w	• Not affected by air temperature (formation of hole and vacuole) • Low solids content, wrinkled	Bouman et al. (2016)
Mannitol	Acoustic levitation	Air humidity	1 - 15% RH	• Porosity of particle decreases with increasing relative humidity	Griesing et al. (2016)
Casein micelle	Sessile pendant droplet	Air humidity	2 and 40% RH	• No effect on morphology	Sadek et al. (2016)
Lactose	Suspended droplet	Air temperature	Temperature 20-80 °C	• Low temperature, shrivelled with small cavities • High temperature, thinner crust with one single big cavity	Tran et al. (2016)

Table 2.3 (continued)

Droplet component	SDD technique	Influencing factor	Parameter range	Effect on morphology	Authors
Colloidal silica	Acoustic levitation	Size of particle and initial solids content	Micro- and nanosized particles Initial solids 1 and 30 w/w	• Microsuspensions – half apricot-like morphology • Nanosuspension at low solids – agglomerated spherical grain • Nanosuspension at high solids – fractured	Osman et al. (2017)
Lactose, whey protein and skim milk	Suspended droplet	Type of solute and air temperature	Different types of solute Temperature 60-180 °C	• Greater inflation/deflation for lactose and lactose:whey mixture than skim milk and whey protein • Low temperature (<100 °C), no inflation/deflation	Tran et al. (2017)
MD DE 12 and whey protein isolate	Sessile droplet	Composition and air temperature	Different compositional ratios Temperature 40-90 °C	• More whey protein, smooth and hollow • More MD, wrinkled with multiple vacuoles • Low temperature, smooth and hollow • High temperature, wrinkled	Both et al. (2018a)
Carbohydrates (lactose or MD DE 12) and proteins (micellar casein or whey protein)	Sessile droplet and acoustic levitation	Composition	Different ratios of protein and carbohydrate	• Lactose:whey protein – smooth • Lactose:casein, MD:casein and MD:whey protein – wrinkled • Particles with lactose smaller than with MD	Both et al. (2018b)

Table 2.3 (continued)

Droplet component	SDD technique	Influencing factor	Parameter range	Effect on morphology	Authors
Hydroxypropylated pea starch	Suspended droplet	Air temperature and initial solids content	Temperature 80-160 °C Initial solids 15-30% w/w	• High temperature and high solids content, hollow particles with smoother surface	Gouaou et al. (2018)
Whey protein isolate and MD DE 12	Sessile droplet	Composition and initial solids content	Different compositional Initial solid 30-40% (w/w)	• More whey protein, smooth-surface hollow • Higher solids content, wrinkled	Both et al. (2019a)
MD and GA	Glass filament	Type of wall materials and initial solids content	Different wall materials: MD DE 10, MD DE 17 and GA Initial solids 21 and 28 w/w	• MD DE 10 with high solids content – network-like bulges on the surface • MD DE 17 – smooth surface with no dents or bulges • GA – irregular wrinkles	Zhang et al. (2019)
MD	Sessile droplet	Dextrose equivalent of MD and air temperature	Different DE values (5 to 38)	• Low DE, smooth with large cavities • High DE, wrinkled	Siemons et al. (2020)

CHAPTER 3

Spray Drying of Mixed Gum Arabic and Maltodextrin Solutions

3.1 Introduction

This chapter explores the use of GA and MD mixtures as encapsulating materials to produce encapsulated air microparticles. To the best of the author's knowledge, there is no research paper on the effect of different proportions of GA and MD as encapsulating materials solely, without the addition of core material. Most of the published research has focused on the effectiveness of using these mixtures to encapsulate a core material such as anthocyanins (Mahdavi et al., 2016), phytosterols (Battista et al., 2015), essential oil (Fernandes et al., 2014), bioactive components (Rajabi et al., 2015) and polyphenol (Tolun et al., 2016).

The surface composition of particles is expected to play an important role in the particle morphology development during drying, as well as in the bulk physicochemical properties of powders. It is hypothesised that GA could appear at the surface of particles due to its amphiphilic character and would affect the microstructure of particles and the physicochemical properties of powders especially the wetting and dissolution. In order to clarify the effect of the ratio of GA:MD on the microstructure and surface composition of particles, microscopic (optical, SEM and FIB-SEM) and spectroscopic (XPS) techniques were employed in this research. Microscopy and image analysis equipment have

been widely utilised to characterise the surface and internal structure of spray dried particles. More detailed information regarding various microscopy techniques can be found elsewhere (Lamprecht et al., 2000; Moran et al., 2014; Rosenberg et al., 1985). A combination of different microscopy techniques is often used to provide a more comprehensive insight in the particle microstructure to aid in understanding the relationship between feed properties and process variables on particle attributes (Elversson and Millqvist-Fureby, 2005; Munoz-Ibanez et al., 2016; Porras-Saavedra et al., 2015). Surface composition analysis by XPS has been successfully applied to investigate the chemical surface composition of spray dried powders. Few works have used XPS to characterise the powder surface in relation to functional properties such as wetting (Gaiani et al., 2007, 2006; Kim et al., 2002; Wang et al., 2016) and flowability (Kim et al., 2005).

Bulk physicochemical properties are important to consider in the design of a high quality spray dried powder. Moisture content, water activity and hygroscopicity greatly influence powder stability and storage, as they could cause caking and reduce flowability (Tonon et al., 2009). Solubility, wetting and dissolution are characteristics that are associated with powder functionality. Size and morphology of particles can be crucial for a spray dried powder in terms of its final application, handling and shelf life, and also may impact the final product taste and texture (O'Hagan et al., 2005; Walton, 2000; Walton and Mumford, 1999a). As the functionality of a spray dried powder is attributed to its morphology and surface composition, understanding the complex mechanisms of microstructural development and distribution of components during particle

formation, and the ability to control its formation is therefore necessary in developing encapsulated air microparticles.

The main objective of this research chapter was to investigate the effect of the ratio of GA:MD on the morphology development of spray dried particles, the physicochemical properties of the bulk powder, as well as to determine the distribution of the components at the surface of the particles.

3.2 Materials and Methods

3.2.1 Materials

Maltodextrin DE 12-15 C*Dry MD 01910 (MD12) was kindly donated by Cargill (Haubourdin, France). Gum Arabic (GA) and silicone oil, used as a particle dispersion medium for optical microscopy, were purchased from Acros Organics (Geel, Belgium). Analytical reagent grade sodium chloride was purchased from Sigma-Aldrich (MO, USA). Distilled water was used in this research except for the spray drying where reverse osmosis water was used.

3.2.2 Preparation of feed solutions

The feed solutions were prepared by dissolving appropriate amounts of GA and MD12 in 500 ml of water (room temperature of 20 °C) using a high shear mixer (Silverson L4RT fitted with emulsor screen, Silverson Machines Ltd, Chesham, United Kingdom) at 8500 rpm for 6-8 min. The compositional ratio of GA:MD12 was varied as 0:100, 25:75, 50:50 and 75:25 at a total solids content of 30% w/v in all solutions.

3.2.3 Physicochemical property analyses of feed solutions

3.2.3.1 Viscosity

The steady shear viscosity of the solutions was measured on a rotational rheometer (MCR301, Anton Paar, Graz, Austria) fitted with a double-gap concentric cylinder measuring system (DG26.7/T200/SS, Anton Paar, Graz, Austria). Measurement temperature was 25 °C and shear rate varied logarithmically between 1 to 100 s^{-1} acquiring 10 equilibrium data points per decade. All measurements were performed in triplicate and the results are presented as mean ± standard deviation.

3.2.3.2 Hydrodynamic radius

The hydrodynamic radius (R_h) of GA and MD solution was determined by dynamic light scattering (DLS) using a Zetasizer Nano-ZS apparatus (Malvern Instruments, Malvern, UK) at 25 °C. The solutions were filtered using a 0.45 µm pore size filter to remove extraneous materials. Measurements were performed in triplicate for each sample.

DLS measures Brownian motion and relates this to the size of the particles. Brownian motion is the random movement of particles due to the random collision with the solvent molecules that surround them. Small particles move quickly and have a larger Brownian motion effect than larger particles (Malvern Instruments, 2018). The translational diffusion coefficient (D) was calculated according to the Stokes-Einstein (Equation 2.6).

3.2.4 Spray drying of powder

The feed solutions were spray dried in a co-current spray dryer (FT80 Tall Form Spray Dryer, Armfield, Bournemouth, UK) (Figure 3.1) equipped with a two-fluid nozzle atomiser with an orifice diameter of 1 mm. The operational conditions were: inlet temperature 180 °C; outlet temperature 70 ± 3 °C; air pressure 0.5 bar; feed rate 500 ml/h.

Figure 3.1 Laboratory scale spray dryer.

The drying temperature of 180 °C was selected based on a study carried out by Paramita et al. (2010). The feed solutions were kept constant at 30% w/v total solids to avoid obstruction of the nozzle when using a higher concentration of

GA. The powders were collected, vacuum-packed in polyethylene bags and stored at room temperature (20 ± 3 °C) until further analysis.

3.2.5 Microstructure property analyses of powders

3.2.5.1 Optical microscopy

To identify whether particles were hollow or solid, powders were dispersed in silicone oil prior to observation under a bright field optical microscope (Leitz Diaplan, Ernst Leitz Wetzlar Gmbh, Germany), as described by Munoz-Ibanez et al. (2016).

3.2.5.2 Scanning electron microscopy

To evaluate the surface morphology of the particles, powders were attached to double-sided adhesive carbon tape mounted on stubs, sputter coated with platinum under vacuum and examined with a scanning electron microscope (SEM) (Quanta 600 MLA, FEI Company, USA). The SEM was operated at an accelerating voltage of 15 kV. The shape factor of the particles was calculated from approximately 100 particles using the image processing software ImageJ (National Institutes of Health, USA). The percentage of smooth surface particles was calculated by manually counting smooth particles in the three different SEM images with approximately 1000 particles for each powder.

3.2.5.3 Focused ion beam-scanning electron microscopy

The samples prepared for SEM imaging were then further analysed by the focused ion beam of a double-beamed scanning electron microscope (FEI

Quanta 200 3D Dual Beam FIB/SEM, FEI Company, USA) to evaluate the internal morphology of the particles. An accelerating voltage of 10 kV and a beam current of 0.12 nA was used to rough dressing the shell of particles.

3.2.6 Bulk property analyses of powders

3.2.6.1 Water activity

The water activity of the powders was measured using a water activity meter (Aqualab Dew Point Water Activity Meter 4TE, USA) at 25 °C.

3.2.6.2 Moisture content

The moisture content of the powders was determined gravimetrically by oven drying at 105 °C to constant weight, following the official AOAC method (AOAC, 2000), and calculated by Equation 3.2.

$$\text{Moisture content}\ (\%) = \frac{\text{Mass of water loss}}{\text{Mass of powder sample}} \tag{3.2}$$

3.2.6.3 Hygroscopicity

Powder hygroscopicity was determined according to a method proposed by Cai and Corke (2000) with some modifications. Powders (approximately 0.5 g) were placed in a glass desiccator containing a saturated sodium chloride solution (75.3% RH) at 20 °C. After one week, powders were weighed and hygroscopicity (g/100 g) was expressed as the mass of water absorbed per 100 g of the sample.

3.2.6.4 Particle size distribution

The particle size distribution of spray dried powders was determined using a laser diffraction particle size analyser equipped with a dry powder system (LS 13 320, Beckman Coulter, USA). Data were analysed based on the Fraunhofer model with the equipment's software. Results are expressed as d_{50}, which is the median diameter, where fifty percent of the distribution has a smaller particle size and fifty percent has a larger particle size, and span as defined by Equation 3.3, both based on the volume-based particle size distribution.

$$\text{Span} = \frac{d_{90} - d_{10}}{d_{50}} \tag{3.3}$$

where d_{10} and d_{90} are the diameter at which ten and ninety percent of the distribution has a smaller particle size, respectively.

3.2.6.5 Water solubility

The water solubility was determined using the method suggested by Eastman and Moore (1984) with some modifications. Water (50 ml) first and then powder (0.5 g) were transferred into a 50 ml centrifuge tube and vortexed for 4 min followed by centrifugation at 1351 x g for 5 min at 25 °C. A 25 ml aliquot of the supernatant was transferred to a pre-weighed petri dish followed by oven drying at 105 °C overnight. The water solubility (%) was then calculated by Equation 3.4.

$$\text{Water solubility (\%)} = \frac{\text{Mass of solids in supernatant} \times 2}{\text{Mass of sample}} \tag{3.4}$$

3.2.6.6 Wetting time

The wetting time of powder was determined using a method described by Fuchs et al. (2006) with some modification. 1 g of powder was sprinkled on the surface of 100 ml of distilled water in a 100 ml glass beaker at 20 °C without agitation. The time taken for the powder to submerge into the water was recorded as wetting time and used for a relative comparison of the extent of wettability between the samples.

3.2.6.7 Dissolution time

The dissolution time was determined following a method described by El-Tinay and Ismail (1985) with modifications. 2 g of powder was added to 50 ml of water contained in a 100 ml glass beaker. The mixture was agitated with a magnetic stirrer (1103 Jenway, Staffordshire, UK) at 900 rpm using a stirring bar of 4.5 mm × 12 mm. The time for the powder to completely dissolve was recorded.

3.2.6.8 Bulk, tapped and true density

The bulk density of the powders was measured by weighing 2 g of the sample and gently loading it into a 10 ml graduated cylinder. The bulk density was calculated by dividing the mass of the powder by the final volume occupied by the powder in the cylinder (Equation 3.5). The tapped density was then measured after tapping the cylinder vigorously by hand on a bench until no further change in volume was observed (Equation 3.6).

$$\text{Bulk density} = \frac{\text{Mass of powder}}{\text{Bulk powder volume}} \tag{3.5}$$

$$\text{Tapped density} = \frac{\text{Mass of powder}}{\text{Tapped powder volume}} \tag{3.6}$$

For the determination of the true density, powders were dried in an oven at 40 °C for at least 12 h prior to analysis. The true density was then determined with a helium pycnometer (AccuPyc 1330, Micromeritics Instrument, Norcross, USA) at 27 ± 1 °C using an equilibrium rate of 0.005 psig/min, 10 purge cycles and 10 runs. Calibration of the pycnometer was performed using a standard stainless steel ball of known mass and volume.

3.2.6.9 Flowability

The flowability of the powders was evaluated in terms of the Carr index (CI) and the Hausner ratio (HR) as described by Lebrun et al. (2012), see Table 3.1. Both CI and HR were calculated from the bulk and tapped densities of the powders by Equation 3.7 and Equation 3.8, respectively.

$$\text{CI} = \frac{\text{Tapped density} - \text{Bulk density}}{\text{Tapped density}} \tag{3.7}$$

$$\text{HR} = \frac{\text{Tapped density}}{\text{Bulk density}} \tag{3.8}$$

Table 3.1 Specification of flowability of powders based on Carr Index and Hausner Ratio (Lebrun et al., 2012).

Flowability	Carr Index (%)	Hausner Ratio
Excellent	0-10	1.00-1.11
Good	11-15	1.12-1.18
Fair	16-20	1.19-1.25
Passable	21-25	1.26-1.34
Poor	26-31	1.35-1.45
Very poor	32-37	1.46-1.59
Very, very poor	>38	>1.60

3.2.7 Surface composition of particles

The surface composition of the spray dried particles and individual components that made up the feed solutions (GA and MD12) was characterised by XPS (Kratos Axis Ultra DLD, Kratos Analytical, UK) with a mono-chromated Al kα X-ray source (1486.6eV) operated at 10 mA emission current and 12 kV anode potential (120 W). The surface elemental composition of the pure component can be assumed to be the same as its bulk elemental composition (Faldt et al., 1993; Kim et al., 2009b). The powder samples were attached to the sample holder using double-sided conductive tape and then kept overnight in an ultra-high vacuum chamber. Three measurements were taken on each sample. The spectra obtained were analysed using the CasaXPS software (version 2.3.18). As nitrogen (N atom) was only presented in GA sample, the surface coverage of GA was calculated by assuming it is scale linearly with the N determination, with the maximum value corresponding to that measured for the pure GA.

3.2.8 Statistical analysis

All powders were prepared in two batches. Results were statistically analysed by one-way analysis of variance (ANOVA) using SPSS Statistics software (version 26, IBM SPSS Inc., USA). Duncan's multiple range test was used for post hoc comparison at $p < 0.05$.

3.3 Results and Discussion

3.3.1 Particle microstructure

To evaluate the influence of the encapsulating materials on the microstructure properties of the particles, particle morphology was observed by optical microscopy and SEM. Prior to the acquisition of the optical micrographs shown in Figure 3.2, the particles were suspended in silicone oil to enhance the contrast between the hollow and the solid particles (Munoz-Ibanez et al., 2016). The hollow interior of the particles could clearly be identified as a dark circular area on the images. Comparing Figure 3.2a-d, it becomes apparent that spherical particles were hollow, whereas dented particles were either hollow or solid. A mixture of hollow and solid particles has typically been produced by spray drying of mixed GA and MD (Paramita et al., 2010; Porras-Saavedra et al., 2015). The formation of a hollow particle can be explained by the formation of a vacuole (a vapour bubble) inside the particle soon after the skin development, which then inflates when the particle temperature exceeds the local ambient boiling point and the vapour pressure within the vacuole rises above the local ambient pressure (Nijdam and Langrish, 2006). A solid particle is formed as a result of homogenous evaporation and gradual precipitation of solute at the droplet surface (Vehring et al., 2007).

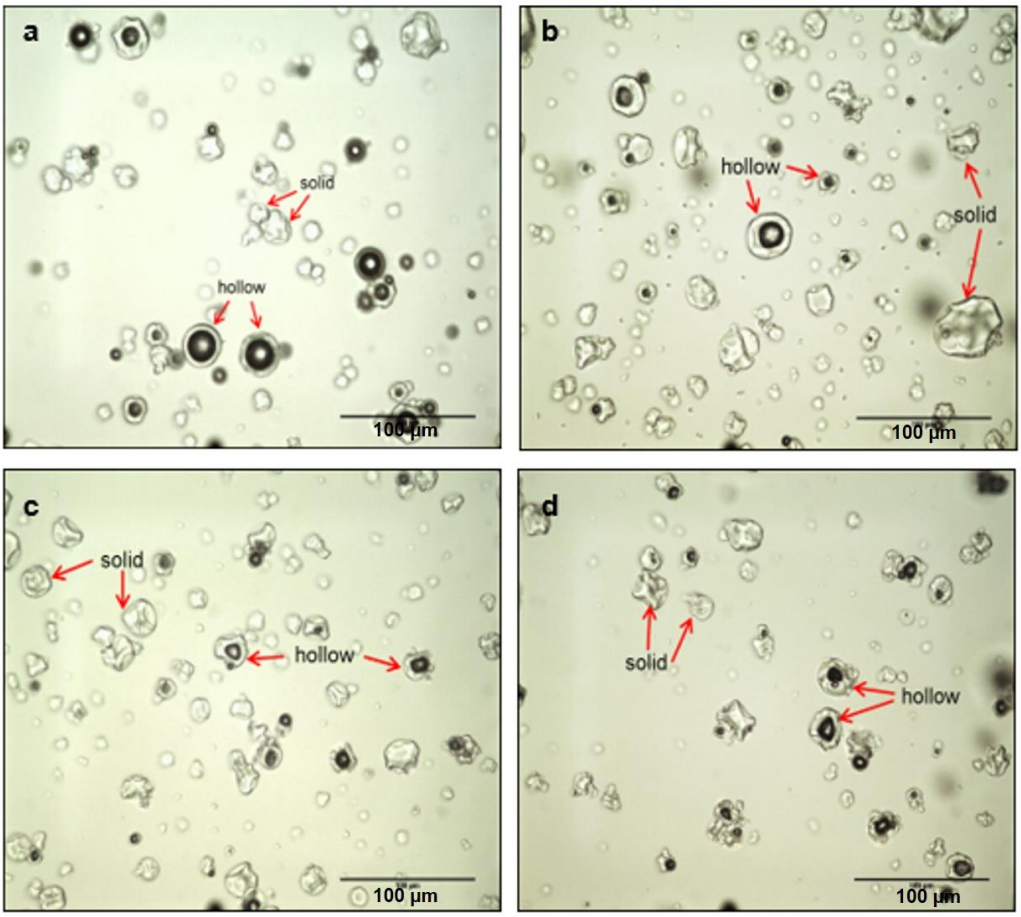

Figure 3.2 Optical micrographs of spray dried particles to illustrate internal morphology: a) 0:100, b) 25:75, c) 50:50, and d) 75:25 (GA:MD12). Dark circles indicate hollow particles while solid particles appeared transparent. Length of scale bar: 100 µm.

To obtain a clearer insight into the morphology of the particles, SEM images were acquired; Figure 3.3 shows one image for each ratio of GA:MD12 used as feed solution. In general, all powders displayed a combination of smooth and dented surface particles. The powders had spherical particles with a shape factor of 0.84 to 0.88; factors approaching 1 indicate a perfect sphere. There were no apparent cracks in any of the powders, which is an important observation in relation to the potential application of these particles. The presence of cracks would allow the liquid to easily enter into the particles while air would escape, defeating the purpose of the shell to protect the air inside the

particle. In principle, the particles should keep their microstructure upon addition into a food matrix before allowing for the shell to disintegrate and air inside the particle to be kinetically trapped by the food matrix. The absence of cracks also indicates that the particles had a strong shell that could withstand the pressure difference at the high spray drying temperature of 180 °C. MD particles have previously been found to crack when spray dried at an inlet temperature of 200 °C (Alamilla-Beltrán et al., 2005).

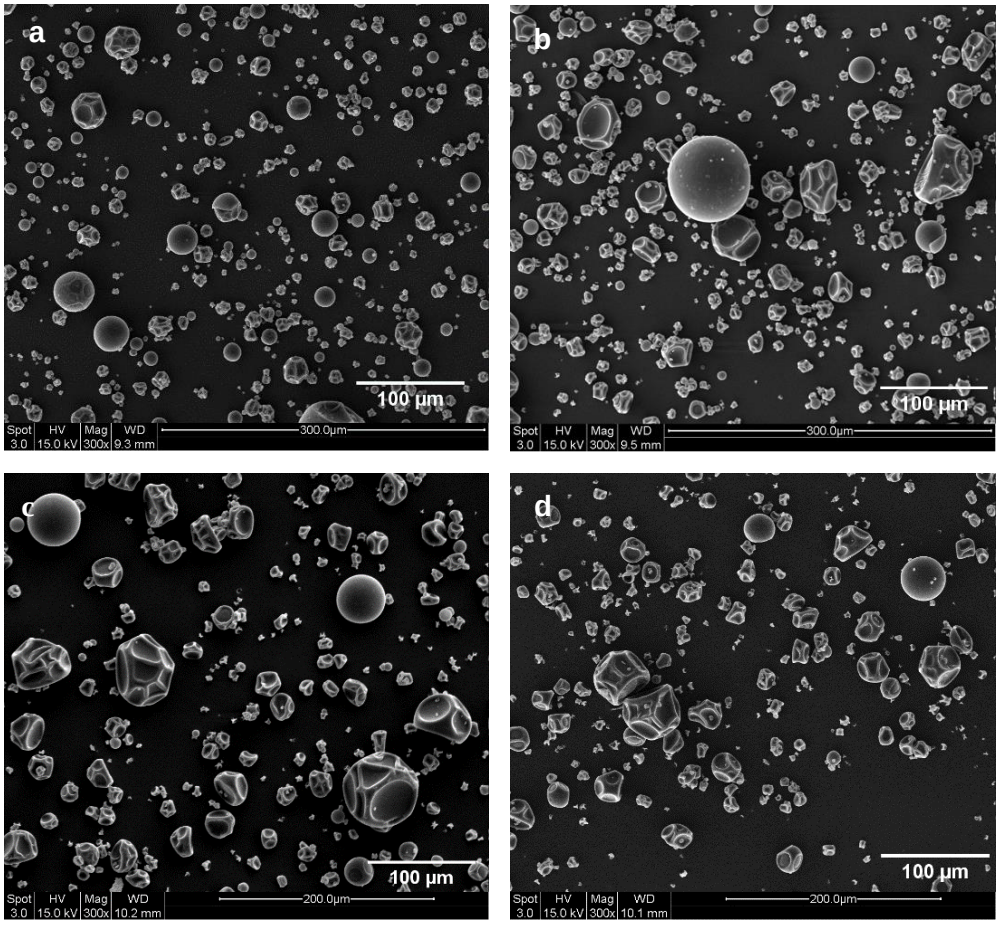

Figure 3.3 Images acquired by SEM of the surface morphology of spray dried particles: a) 0:100, b) 25:75, c) 50:50, and d) 75:25 (GA:MD12). Length of scale bar: 100 µm.

The dimensionless Peclet number (Pe), which is defined as the ratio between drying rate and solute diffusivity, controls particle formation (Osman et al., 2017; Vehring et al., 2007). At high Peclet number (Pe >> 1), hollow particles are likely to form because evaporation dominates and the surface becomes rapidly enriched in solutes that precipitate. On the other hand, solid particles are expected for low Peclet number (Pe < 1) as the diffusional motion of the solutes is fast reducing concentration gradients at the interfaces. In these experiments, the Peclet number was estimated using Equation 3.9 as defined by Tsapis et al. (2002):

$$Pe = \frac{R^2}{Dt_{dry}} \tag{3.9}$$

where R is the radius of the droplet, t_{dry} the drying time, and D the diffusion coefficient of the feed solution. We assume the R is half the size of the dried particles, based on findings by Alamilla-Beltrán et al. (2005) for spray dried MD at 170 °C using two-fluid nozzle; and $t_{dry} \sim$ 9 s (as referred to the manual of Armfield FT80 Tall Form Spray Dryer).

For GA solution: T = 25 °C, R_h = 17.5 nm, and η = 0.066 Pa.s (at 25 °C), D = 1.9 × 10^{-13} m^2/s, and MD12 solution: T = 25 °C, R_h = 10.6 nm, and η = 0.006 Pa.s (at 25 °C), D = 3.2 × 10^{-12} m^2/s. Peclet number was approximately 0.4 for the spray dried MD12 and 16.2 for the spray dried 75GA:25MD12 (assuming this mixture behaves as GA in regards to its surface active character). The value obtained for MD was close to the estimated Peclet number (Huang, 2011) for spray dried MD at 110 °C (Pe = 0.7) (Alamilla-Beltrán et al., 2005), with a similar

morphology of creased and smooth surface particles (Figure 3.3a). The large Peclet number for 75GA:25MD12 indicates the drying is inhomogeneous, favouring the formation of a skin and leading to a hollow particle. But in this case, both smooth and wrinkled particles were obtained (Figure 3.3d). For the hollow particles, the strength of the skin determines the degree of bending; weak skin will bend and buckle under pressure to form a wrinkled particle, while rigid skin cannot bend under pressure but will form a smooth surface particle (Sadek et al., 2014; Vehring, 2008). It is hypothesised that the addition of GA led to the formation of an elastic skin and therefore a higher drying rate would be required for the particle to inflate and form a spherical hollow particle.

The FIB-SEM was applied to gather further evidence of having hollow particles based on their smooth surface appearance. For each of the spray dried powders, particles differing in size and surface morphology (smooth and dented) were selected and milled using FIB to reveal the internal morphology, see Figure 3.4. FIB-SEM confirmed that regardless of size, a smooth surface particle was hollow with one large vacuole. However, it is hard to predict the internal structure of dented particles, which might be solid (Figure 3.4a-ii, b-ii) or hollow (Figure 3.4c-ii, d-ii). The smooth surface hollow particles had a thinner shell and larger vacuole compared to dented surface hollow particles of the same diameter. Regardless of the formulation, the shell thickness of the smooth surface particles was approximately one-tenth of its diameter (based on the observation of particle size between 7 and 38 µm). Therefore, the volume of air in the vacuole was estimated around 1.3×10^{-10} cm^3 for particle with a diameter of 7 µm and 2.1×10^{-8} cm^3 at particle diameter of 38 µm.

Based on the microscopic evidence presented in Figure 3.2 to Figure 3.4, it can be stated that the smooth surface appearance of particles was a reliable indicator of having a hollow particle. Smooth surface hollow particles are preferred in this research as particles with this morphology contain more air compared to dented hollow particles of the same size. The highest percentage of spherical smooth hollow particles (12%) was found for powder produced from only MD12 and an increase of the proportion of GA in the mixture resulted in a lower fraction of spherical smooth hollow particles (7% for 25GA:75MD12; 5% for 50GA:50MD12; 4% for 75GA:25MD12). This observation was expected owing to the difference in droplet size formed during atomisation. Feed solution containing only MD12 (6.44 mPa.s) had the lowest viscosity than solutions with GA (18 Pa.s for 25GA:75MD12; 28.85 mPa.s for 50GA:50MD12; 43.71 Pa.s for 75GA:25MD12), and thus droplets would break up into smaller droplets when the same air pressure was applied during atomisation process (Masters, 1991). Smaller droplets would result in a higher drying rate (Ranz and Marshall, 1952), which causes an instant solid crust formation to form hollow spherical particles.

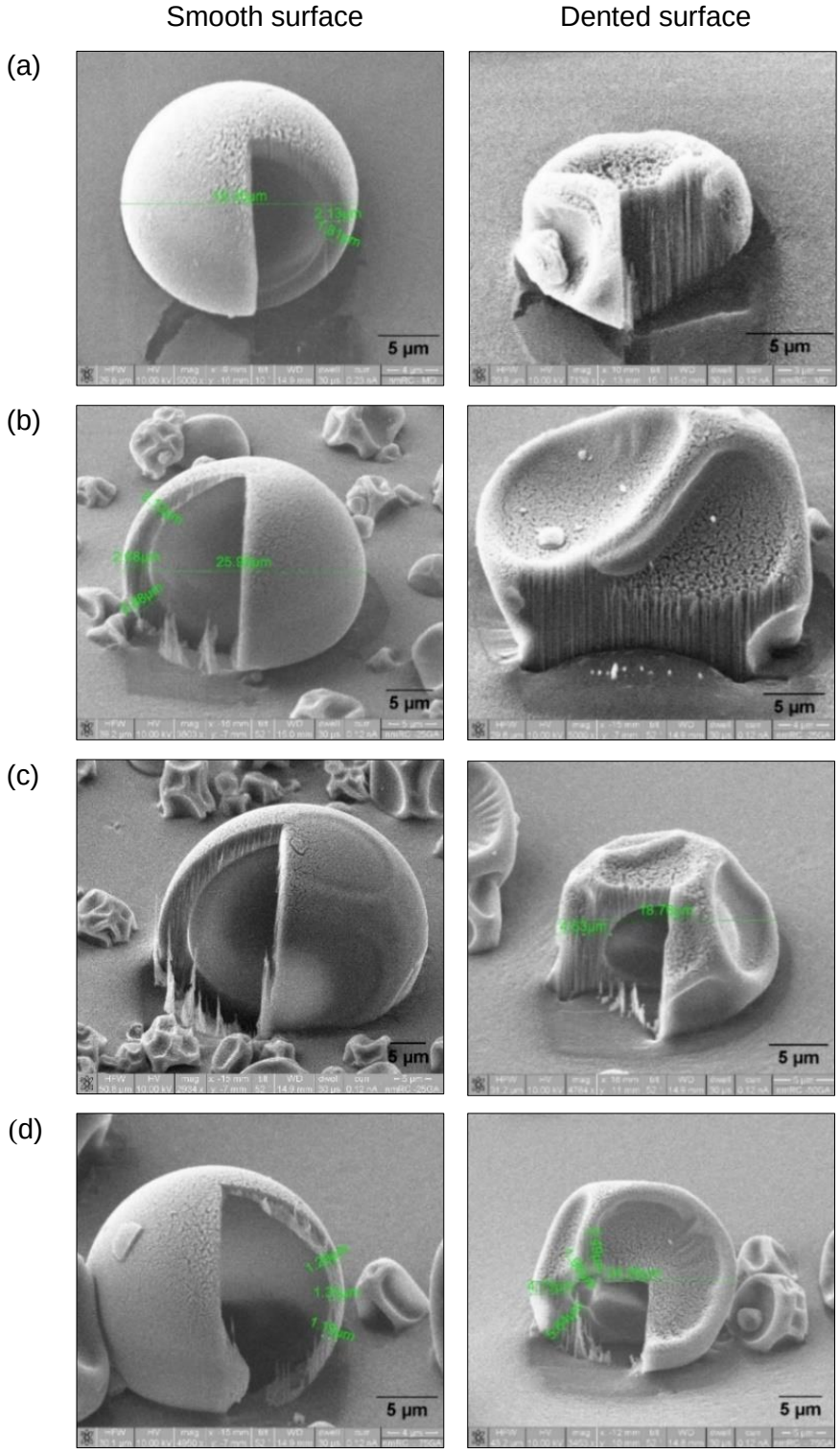

Figure 3.4 Images acquired by FIB-SEM showing the internal morphology (hollow or solid) of particles with different surface morphologies: a) 0:100, b) 25:75, c) 50:50 and d) 75:25 (GA:MD12). Length of scale bar: 5 µm.

3.3.2 Bulk physicochemical properties

The bulk physicochemical properties of the spray dried mixed GA and MD12 powders are reported in Table 3.2. Water activity and moisture content are important powder properties that greatly affect the shelf life of the powder produced. The water activity of the powders ranged between 0.14 and 0.17 and there were no statistically significant differences between the powders of different formulations. The moisture content was between 3.9 and 5.7%. The powder formed using 75GA:25MD12 exhibited a significantly higher moisture content than using 0GA:100MD12. However, the values of water activity and moisture content were within the expected range for spray dried powders, between 0.15-0.2 and <6% respectively to warrant chemical and microbiological stability (Bhandari, 2008; Fellows, 2009). Changing the compositional ratio of GA:MD in favour of GA has previously been reported to result in a significant increase in the moisture content of the finished powder as GA has a higher number of hydrophilic groups (Mahdavi et al., 2016). Materials with a high amount of hydrophilic groups can more easily bind water molecules from the ambient air during powder handling after spray drying and are thus more hygroscopic (Mohd Nawi et al., 2015). Indeed, the powder produced with the highest amount of GA was the most hygroscopic (8.4 ± 0.0 g/100 g sample). These results are in agreement with previous studies (Fernandes et al., 2014; Khazaei et al., 2014; Porras-Saavedra et al., 2015).

Information about particle size is useful as it may impact powder flowability, dissolution and wetting. The particle median diameter (d_{50}) for the spray dried powders was between 12.4 and 18.4 µm. Porras-Saavedra et al. (2015) reported smaller particles (2-7 µm) when using a pneumatic nozzle to spray dry

a mixture of soy protein isolate, GA and MD at different compositions (20% total solids). Paramita et al. (2010) obtained much larger particles (65-80 µm) when spray drying mixtures of GA and MD at a ratio of 2:1 (20-50% total solids) using a centrifugal atomiser. The mean particle size found in this research, spraying with a two-fluid nozzle, was between those particle size ranges, emphasising the need to carefully select the type of atomiser in future work depending on the destination of this novel food ingredient. With regard to the impact of composition on particle size characteristics, the presence of GA led to slightly larger particles and a broadening of the distribution as seen by the increase in the span. This quantitative data confirm the visual observations by SEM (Figure 3.2). The higher the feed solution viscosity, the larger the droplets formed during atomisation and, hence, the powders have larger particles. Similar observations were made by Outuki et al. (2016) for spray-dried *Eschweilera nana* Miers leaves extract with mixtures of Arabic and xanthan gums, and Tonon et al. (2011) for spray-dried flaxseed oil with GA.

The bulk density of the powders varied from 0.31 to 0.34 g/cm^3. These values are similar to those reported for encapsulated rosemary essential oil (0.31 g/cm^3) (Fernandes et al., 2014), but slightly lower than those for encapsulated flaxseed oil (0.40 g/cm^3) (Carneiro et al., 2013) powders, prepared with a mixture of GA and MD. The tapped density of the powders varied between 0.47 and 0.53 g/cm^3 and was reduced with an increasing amount of GA due to the characteristics of the particle size distribution. The increased particle size distribution span with increasing amount of GA facilitated a denser packing of the particles, as smaller particles can reduce the void space between particles (Sanchez-Reinoso et al., 2017). The true density of the powders ranged from

1.21 to 1.31 g/cm^3 and so was similar to that obtained for hollow polymer-stabilised spray dried dispersion particles (Gamble et al., 2016). For powder flowability, the ranges for both the Carr index (between 31.4% and 35.6%) and the Hausner ratio (between 1.46 and 1.55) indicate all samples had very poor flow characteristics (see Table 3.1). The hollow internal morphology of a fraction of the particles appeared to have impacted the flowability of the powders. A more free-flowing powder should have a higher bulk and tapped density.

All of the powders produced were highly soluble in water (> 92%) at 25 °C, although increasing the amount of GA slightly decreased water solubility. Both wetting and dissolution time exhibited the same trend, whereby powders with a higher amount of GA had longer wetting (increased from 9.6 to 71.0 min) and dissolution (increased from 20.6 to 41.8 min) times. The reason for this can be attributed to the amphiphilic structure of GA. A higher number of hydrophobic groups in the particles decreasing the interaction between particle surface with water, thus making it less wettable.

Table 3.2 Physical properties of powders prepared with different compositions of GA and MD12 at total solids of 30% w/v. Spray drying conditions were inlet temperature 180 °C; outlet temperature 70 °C; air pressure 0.5 bar; feed rate 500 ml/hr. Different superscript letters in the same row indicate significant difference between samples ($p < 0.05$).

Powder properties	Composition of GA:MD12			
	0:100	25:75	50:50	75:25
Water activity	0.14 ± 0.02^{a}	0.13 ± 0.00^{a}	0.17 ± 0.01^{b}	0.16 ± 0.01^{b}
Moisture content (%)	3.9 ± 0.5^{a}	4.2 ± 0.6^{a}	5.0 ± 0.5^{b}	5.7 ± 0.2^{c}
Hygroscopicity (g/100g)	6.3 ± 0.3^{a}	6.5 ± 0.3^{a}	6.7 ± 0.4^{a}	8.4 ± 0.0^{b}
Particle size, d_{10} (µm)	4.2 ± 0.1^{a}	6.0 ± 0.3^{c}	5.9 ± 0.3^{c}	5.3 ± 0.4^{b}
Particle size, d_{50} (µm)	12.4 ± 1.0^{a}	18.0 ± 1.3^{b}	18.1 ± 1.1^{b}	18.4 ± 0.2^{b}
Particle size, d_{90} (µm)	32.1 ± 1.9^{a}	50.2 ± 4.5^{b}	50.5 ± 2.6^{b}	53.5 ± 2.7^{b}
Span	2.0 ± 0.1^{a}	2.1 ± 0.1^{b}	2.2 ± 0.1^{b}	2.3 ± 0.1^{c}
Bulk density (g/cm^3)	0.34 ± 0.02^{b}	0.33 ± 0.01^{b}	0.34 ± 0.00^{b}	0.31 ± 0.00^{a}
Tapped density (g/cm^3)	0.53 ± 0.03^{b}	0.49 ± 0.02^{a}	0.49 ± 0.05^{a}	0.47 ± 0.01^{a}
True density (g/cm^3)	1.31 ± 0.01^{c}	1.22 ± 0.05^{a}	1.26 ± 0.03^{b}	1.21 ± 0.03^{a}
Carr index (%)	35.4 ± 0.05^{b}	32.8 ± 0.8^{ab}	31.4 ± 2.0^{a}	35.6 ± 1.1^{b}
Hausner ratio	1.55 ± 0.00^{bc}	1.49 ± 0.02^{ab}	1.46 ± 0.04^{a}	1.55 ± 0.03^{c}
Water solubility (%)	96 ± 2^{b}	93 ± 2^{ab}	93 ± 2^{ab}	92 ± 3^{a}
Wetting time (min)	10 ± 1^{a}	42 ± 8^{b}	55 ± 8^{c}	71 ± 10^{d}
Dissolution time (min)	21 ± 1^{a}	32 ± 4^{b}	35 ± 2^{c}	42 ± 3^{d}

3.3.3 Particle surface composition

Particle surface composition has a major influence on some functional properties of powders, especially wetting and dissolution. Therefore, the relative elemental surface composition of the particles was evaluated by XPS, acquiring reference data on the two individual components, as used to prepare the feed solutions, in the first instance. The results are summarized in Table 3.3. Not surprisingly, the C and O atom were the two predominant features in both individual components. The N atom was only detected in GA, rendering it a useful marker atom for the presence of GA on the surface of the spray dried samples. Similar results have been reported by Porras-Saavedra et al. (2015) and Munoz-Ibanez et al. (2016) for MD and GA samples.

The surface coverage by GA increased with an increasing amount of GA in the formulations, and thus confirms protein (N atom) as the surface active compound in GA adsorbing at the surface during drying. Approximately 68% (expressed as a mass fraction) of the surface of the particles was covered by GA when 25% of GA was added into the feed. It is interesting to note that the GA coverage at the surface of the particles remained the same when the proportion of GA was increased from 50% to 75%. This result suggests that rapid diffusion of GA toward the surface and become saturated very quickly so that further addition of GA had no impact on the N content (Shrestha et al., 2007). Similar findings have been reported by others studying the spray drying of mixtures of carbohydrates and proteins (Adhikari et al., 2009b, 2009a; Porras-Saavedra et al., 2015).

Table 3.3 Relative elemental composition of individual components and spray dried GA:MD12 measured by XPS. Different superscript letters in the same column indicate significant difference between samples ($p < 0.05$).

Sample	Relative atomic concentration (%)			GA on surface (%)
	C	O	N	
GA	56.4 ± 0.3^{a}	40.3 ± 0.3^{c}	3.3 ± 0.0^{b}	-
MD12	61.8 ± 1.3^{b}	38.2 ± 1.3b^{c}	*	-
Spray dried 0:100	64.3 ± 1.6^{b}	35.6 ± 1.6^{ab}	*	-
Spray dried 25:75	64.0 ± 3.0^{b}	33.8 ± 3.0^{a}	2.2 ± 0.2^{a}	68.2 ± 5.6^{a}
Spray dried 50:50	62.6 ± 0.6^{b}	34.3 ± 0.6^{a}	3.1 ± 0.4^{b}	95.2 ± 11.9^{b}
Spray dried 75:25	64.7 ± 0.3^{b}	32.0 ± 0.2^{a}	3.2 ± 0.2^{b}	98.9 ± 6.3^{b}

* not detected.

The longer wetting and dissolution times can be associated with a greater proportion of the hydrophobic protein on the particle surface. These data validate the earlier hypothesis that the particle wettability is controllable using GA. The thickness of the GA layer at the surface of a particle would possibly allow for wettability control. However, XPS only measures the composition of the outermost surface layer (2-10 nm) and does not account for the thickness of the layer. Munoz-Ibanez et al. (2016) studied the component distribution in spray dried powders composed of sunflower oil, MD and GA using confocal Raman microscopy. The authors reported that the surface layer of GA increased in thickness as the powder particle size increased; this fact is due to larger particles having a slower drying rate thus taking a longer time to dry and giving sufficient time for the GA to adsorb to the droplet surface.

3.4 Conclusions

This research has provided fundamental data towards the future development of encapsulated air microparticles by spray drying using a mixture of GA and

MD. The combined use of optical microscopy, SEM, FIB-SEM and XPS techniques provided complementary information to investigate the structure of the particles, as well as to improve understanding on functional properties of the powder. The microscopic images revealed that particles with a smooth surface were hollow with one large vacuole, while particles with a dented surface could be either hollow or solid. The percentage of spherical smooth hollow particles decreased as the proportion of GA in the mixture increased. However, the addition of GA increased the wetting and dissolution times, which is an important attribute for the encapsulated air microparticles. This would prevent the air inside the particles from instantly escape into the matrix when added as an ingredient in making ice cream. Surface composition analysis by XPS showed GA enriched at the surface of the particle, thus explaining the increment in wetting and dissolution time of the powder. These results suggest that GA can be added to control the wettability of spray dried particles. For the next experiments, a single droplet drying technique will be employed to gain a better understanding of the development of encapsulated air microparticles at the particle level.

CHAPTER 4

Sessile Single Droplet Drying of Mixed Gum Arabic and Maltodextrin Solutions

4.1 Introduction

Chapter 3 highlighted the potential of using mixed solutions of GA and MD in producing hollow particles by spray drying. In this chapter, a re-designed set-up of sessile SDD on a hydrophobic surface that was introduced by Perdana et al. (2011) (as shown in Figure 2.18) was used to gain insights into particle morphology development during spray drying. Several controlling parameters, including the ratio of GA:MD, drying temperature, droplet size, solids concentration and DE-value of MD were examined.

Thus far there does not appear to be a report on SDD of mixed GA and MD solutions. There are two reports regarding SDD of GA and MD. Zhang et al. (2019) studied the structure formation of noni juice microencapsulated with MD or GA using a glass-filament SDD set-up. The second study is by Siemons et al. (2020) who used sessile SDD on a hydrophobic membrane to investigate the impact of the DE of MD on the particle morphology. More commonly, SDD experiments have been applied to study the drying kinetics and morphological changes of droplets of milk (or its derivatives), as already summarised in Table 2.3.

Following the drying of a single droplet, its wetting and dissolution properties were examined by observing the behaviour of a water droplet deposited onto the particle surfaces. This in-situ approach follows suggestion in literature (Fu et al., 2011; Lum et al., 2018). Its advantage is that wetting and dissolution behaviour of a particle can be directly linked to its drying history (Fu et al., 2012; Lum et al., 2018; Zhang et al., 2019), as the exact duplication of SDD conditions are rather challenging in this type of experiment. To complete the results of the in-situ testing, harvested particles were also examined in bulk. The water sorption behaviour of the dried particles was quantified using dynamic vapour sorption (DVS) equipment.

In order to better understand the observed drying characteristics and the properties of the dried particles, the physicochemical properties of the two biopolymers utilised in this research were also analysed. These included molecular characteristics, solution viscosity and examination of mixture homogeneity (that is absence of phase separation). It is well known that the molecular characteristics of polymers have a great influence on solution viscosity, solubility, viscoelasticity and mixing behaviour (Bower, 2002; Loret et al., 2005; Pycia et al., 2016), and thus might affect the particle morphology development during drying. The occurrence of buckling during droplet drying is related to the formation of elastic skin, which depends on the physicochemical properties of the dissolved polymers (Pauchard and Allain, 2003a; Tsapis et al., 2005). Each polymer in the droplets would behave differently upon concentration and thus determines the strength of the skin (Both et al., 2019a).

As the overall aim of this research was to produce encapsulated air microparticles that have a hollow internal structure and controlled surface wettability, the objectives of the research reported in this chapter were:

1) to evaluate the effect of droplet compositions (compositional ratio of GA:MD, solids concentration and DE-value of MD) and processing parameters (drying temperature and droplet size) on the drying kinetics and final morphology of mixed GA and MD droplets using SDD technique; and
2) to examine the wettability, dissolution and water sorption behaviour of the dried particles.

4.2 Materials and Methods

4.2.1 Materials

Maltodextrin DE 7.5-9.9 C*Dry MD 01958 (MD7) and DE 12-15 C*Dry MD 01910 (MD12), both corn starch, were kindly provided as a gift from Cargill Ltd. (Haubourdin, France). Light microscopy images of GA, MD7 and MD12 as received are shown in Appendix A Figure A.1.

Two different dextrose equivalents of MD, MD7 and MD12, were utilised in this research. The MD12 was previously selected for the spray drying in work reported in Chapter 3. This choice was based on a report by Paramita et al. (2010) who obtained a larger fraction of hollow particles (up to 81%) when spray drying mixed solutions of GA and MD DE 11. In another study, Siemons et al. (2020) found that drying low DE MD (DE 5) had the tendency to lead to smooth-

surface hollow particles compared to high DE MDs (DE 21 to 38). Therefore, it was decided to include a low DE MD in this research reported in this chapter.

Reverse osmosis water was used for the preparation of the droplet solutions and Milli-Q grade water was used in the wetting and dissolution experiments.

4.2.2 Molecular characteristics of GA and MD

The weight average molecular weight (M_w), number average molecular weight (M_n), hydrodynamic radius (R_h) and intrinsic viscosity ([η]) of GA, MD7 and MD12 were measured by size-exclusion chromatography coupled with a multi angle laser-light scattering (SEC-MALS) system. The SEC-MALS system was equipped with a degassing unit (Postnova Analysis PN7505), a pump (Shimadzu LC-10 AD HPLC), an auto sampler (Spark-Holland Marathon Basic), a guard column (ShodexTM LB-G 6B) and a column (ShodexTM LB-805) connected in series. Light scattering intensities were simultaneously measured at 18 angles as a function of elution volume using a light scattering photometer (DAWN HELEOS II), connected in series to an on-line differential viscometer (ViscoStar II) and a refractive index detector (Optilab rEX). GA solution (at 0.5 mg/ml) and MD solutions (at 5 mg/ml) were filtered through cellulose–acetate membrane filters (0.45 mm pore size), and then were injected onto the columns. Milli-Q water was used as eluent with a flow rate of 0.5 ml/min. The measurements were carried out at room temperature (20 °C) with linearly polarised light at a wavelength of 632.8 nm (He-Ne laser). Data were collected and analysed by ASTRA software version 6 (Wyatt Technology Co., California, USA).

4.2.3 Preparation of droplet solutions and assessing mixtures for miscibility

Solutions were prepared by dispersing the appropriate amounts of GA powder and MD powder in 20 ml of water at room temperature (20 °C). The ratio of GA:MD in the solutions was varied at 0:100, 25:75, 50:50, 75:25 and 100:0 (on a dry basis) at the same time as the solids concentration of the feed solution was varied at 20, 30 and 40% w/v of total solids. The solutions were stirred using a spatula for approximately 10-15 min until the powder appeared visually dissolved and then left for at least 1 h at room temperature to fully hydrate. Prior to use, on the same day of preparation, the solutions were gently stirred to ensure they were homogenous, carefully avoiding the incorporation of air.

Mixing of biopolymers in solution may lead to a phase separated system instead of a homogenous mixture (Butler and Heppenstall-Butler, 2001; Lorén and Hermansson, 2000; Mao et al., 2013), and aqueous solutions of GA and MD have previously been shown to phase separate (Annable et al., 1994). Therefore, a subset of the mixtures as used as droplet solutions for the SDD experiments was assessed for phase behaviour. Only MD7 based mixtures were assessed due to the higher molecular weight of MD7 compared to MD12 (Avaltroni et al., 2004; Dokic et al., 1998), experimentally confirmed in this research, see Section 4.3.1. Higher molecular weight components are more likely to phase separate from each other (Loret et al., 2005), and in the case of confirming miscibility of GA with MD7 for mixture concentrations applied in this research it was deemed valid to assume that GA:MD12 mixtures were also single phase. Miscibility was assessed as follows:

Solutions (10 ml) containing all ratios of GA and MD7 at 20% and 40% w/v total solids were placed in centrifuge tubes and left quiescently on the centrifuge rack for 24 h at room temperature before centrifugation at 3118 x g (Rotina 380 R, Hettich GmbH & Co., Tuttlingen, Germany) for 3 h at 25 °C. The centrifuge tubes were visually inspected for bulk separation after the initial 24 h storage period and after centrifugation. For further investigation, the solutions were examined in a fluorescent microscope (EVOS Fl Imaging System, Advanced Microscopy Group, Washington, USA) following the addition of a drop of rhodamine B (0.1 g/l in water) to fluorescently label the protein component of GA (Jin et al., 2016).

4.2.4 Physicochemical property analyses of droplet solutions

The viscosity of droplet solutions and the hydrodynamic radius of GA and MDs in solution at 20 and 40% w/v total solids was determined according to the method in Section 3.2.3.1 and 3.2.3.2, respectively.

4.2.5 Sessile single droplet drying

For sessile SDD experiments, a hydrophobic surface was produced by coating a glass slide with of a commercially available water repellent agent (Glaco Mirror Coat Zero, Japan), an alcohol based suspension of silica nanoparticles functionalised by an organic hydrophobising agent (Vakarelski et al., 2014), and drying in an oven at 100 °C for 5 min. A hydrophobic surface was used to minimise the contact between the droplet and the surface for conductive heat transfer during drying, as well as to maintain the spherical shape of the droplet (Both et al., 2018a; Perdana et al., 2013).

Droplets of 1, 2 and 3 µl of 0GA:100MD, 50GA:50MD and 100GA:0MD (MD12, 30% total solids) were formed with a micropipette (Pipetman Classic P10, Gilson, France) and deposited onto the hydrophobic surface to evaluate the effect of droplet volume and compositional ratio on the contact angle between the droplet and the hydrophobic surface. The contact angle measurements were performed at room temperature using a contact angle analyser (DSA 10 Mk2, Krüss GmbH, Germany) equipped with an image analysis software (Drop Shape Analysis, Krüss GmbH, Germany) (Figure 4.1). The radius (R) and the height (H) of each droplet were measured (Figure 4.2) and the ratio R/H calculated to describe the roundness of a droplet. The contact angle (θ) was also computed. Four replicates were made per formulation.

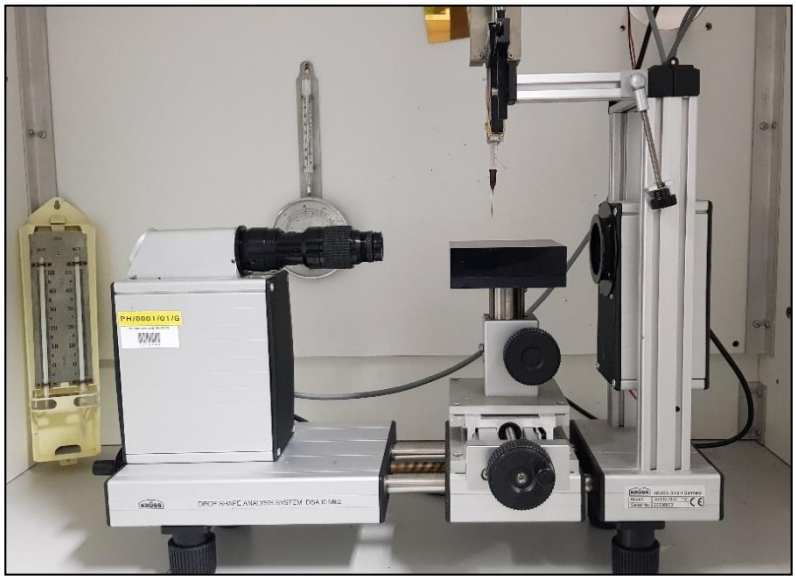

Figure 4.1 Krüss DSA 10 Mk2 goniometer.

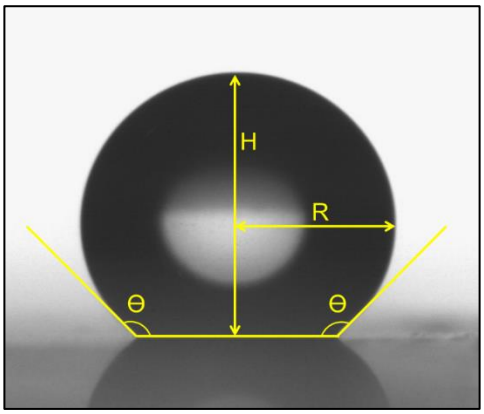

Figure 4.2 Image of a droplet acquired with the set-up shown in Figure 4.1 and parameters assessed via image analysis: droplet radius R, droplet height H and contact angle θ.

Figure 4.3 shows the exterior and interior of the environmental chamber (Thermotron 3200, Michigan, USA) set-up for the sessile SDD experiments. The chamber allowed for temperature and humidity control. A thermocouple placed at the top of the chamber was used to monitor the air temperature. Air inlet could be manually controlled via a throttle which was set to its lowest possible setting (0.4%) for these experiments. Silica gel was placed at the bottom of the chamber to keep a constant relative humidity upon opening and closing the chamber. Before a drying experiment, the chamber was pre-conditioned at the desired drying temperature and 1% relative humidity (RH) for at least 40 min. A droplet of the desired volume was then deposited onto the hydrophobic surface using a micropipette and drying followed for 13 min. The chamber took approximately a minute to restabilise to its pre-set settings after the door was closed.

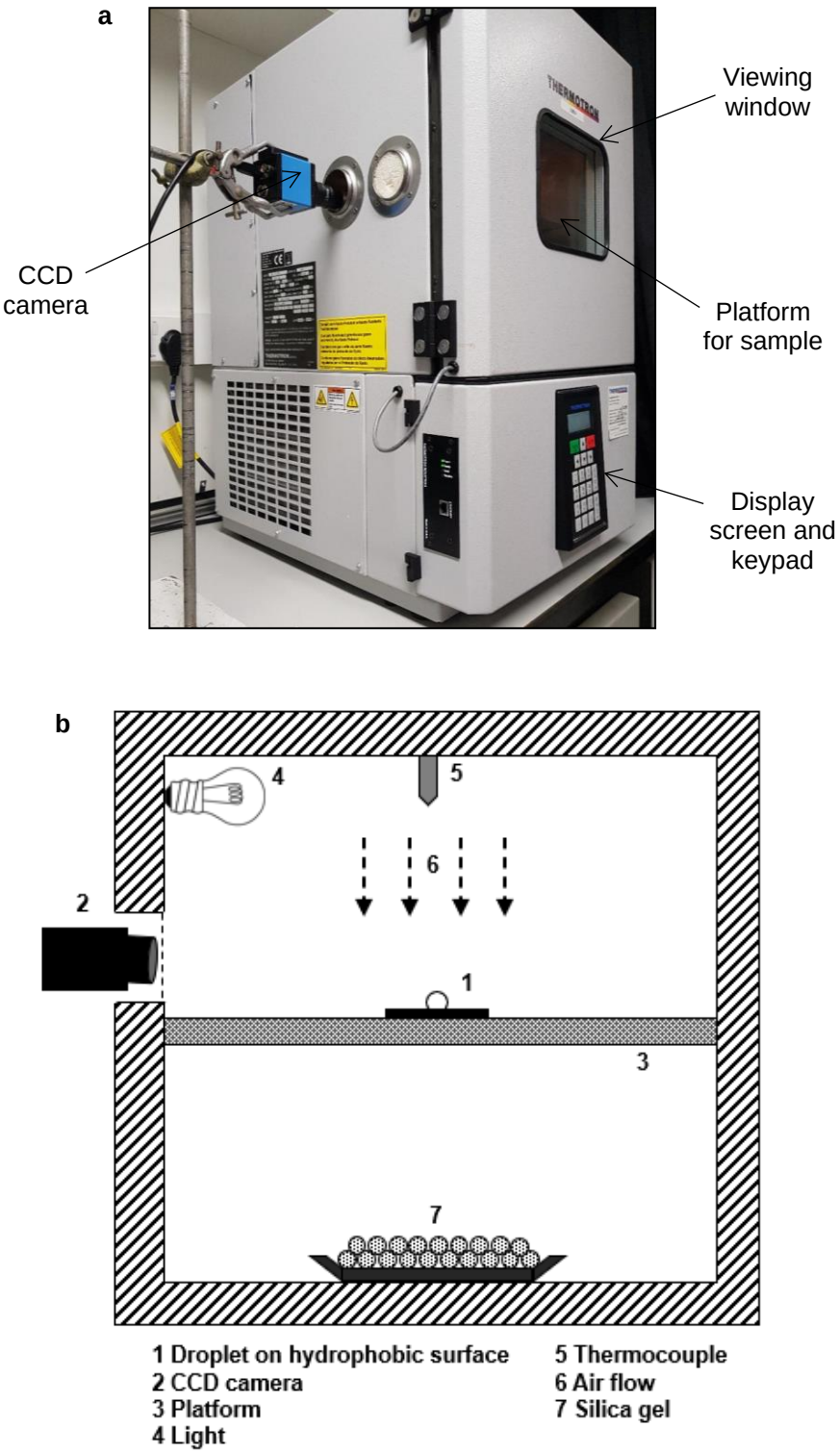

Figure 4.3 Experimental set-up of the sessile SDD: a) photograph of the exterior of environmental chamber, and b) schematic view of the interior of environmental chamber.

The following SDD drying experiments were carried out to study the effect of the compositional ratio of GA:MD, drying temperature, initial droplet volume, initial solids concentration and DE-value of MD on the drying kinetics and particle morphology development:

1. Firstly, the combined effect of compositional ratio and drying temperature was evaluated by drying 2 µl droplets of various compositional ratios of GA:MD (MD12, 30% total solids) at 80, 100 and 120 °C.
2. To determine the influence of droplet size, 1 and 3 µl droplets of 0GA:100MD and 50GA:50MD (MD12, 30% total solids) were dried at 100 °C.
3. To investigate the combined effect of the compositional ratio of GA:MD, initial solids concentration and DE-value of MD, droplets (2 µl) of varied ratios of GA:MD were prepared with MD7 and MD12 at a concentration of 20 and 40% total solids and dried at 120 °C.

The evolution of the droplet shape during drying was captured with the CCD camera, equipped with a macro lens (Linos, Qioptiq Photonics GmbH & Co., Goettingen, Germany), and IC Capture software at a frame rate of one per second. At least 4 droplets were dried at each of the experimental conditions outlined above. The dried particles were collected and stored at room temperature (20 °C) in a desiccator containing dried silica gel to prevent moisture absorption until further analysis.

The captured images were analysed using ImageJ software (National Institute of Health, Maryland, USA) as follows:

1. A sequence of images was opened in a folder as a stack. The time lag between each image was 10 s. This allowed for multiple images to be processed at the same time and helped to visualise changes in the droplet size over time. Figure 4.4a shows an example of an individual image.
2. A scale was set using a microscope stage calibration slide that was captured at the same setting of the actual experiment.
3. The images were cropped.
4. The images were inverted to change the background colour, see Figure 4.4b.
5. The images were enhanced to obtain better contrast between the droplet and the background, see Figure 4.4c. Automatic boundary detection was unsuccessful due to a poor automatic threshold detection between the droplet and the background. Therefore, a circle was manually fitted to the boundary between the droplet and air, see Figure 4.4d, and its radius recorded by the image processing software.
6. The droplet shrinkage from beginning until skin formation (locking point) and the initial drying rates were then calculated according to the radius squared law (Bouman et al., 2016) (Equation 4.1).

$$\frac{R^2(t)}{R_0^2} = 1 - \frac{\kappa}{R_0^2}t \tag{4.1}$$

Here R is the droplet radius (mm), R_0 is the initial droplet radius (mm), t is the time (s) and κ is the drying rate constant (mm^2/s).

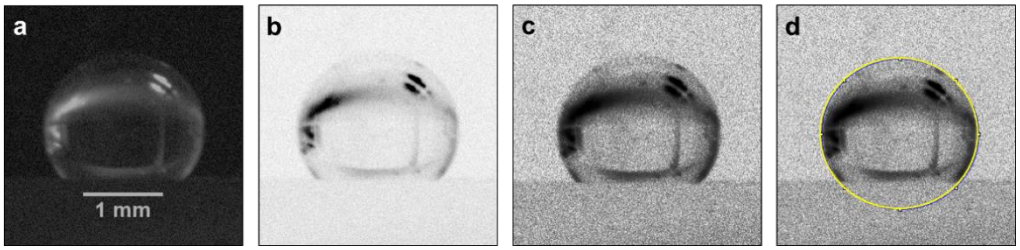

Original image | Inverted image | Enhanced image | A manually inserted circle (in yellow)

Figure 4.4 Steps of image processing using ImageJ.

It should be noted that the experiments for the evaluation of drying temperature and droplet size were carried out at different camera settings to the experiments of initial solids concentration and DE-value of MD. This means that the experimental conditions applied in both sets of experiments led to slightly different values of drying rate constant.

4.2.6 Microstructure analyses

The 3D microstructure of individual dried particles was assessed utilising X-ray micro-computed tomography (micro-CT) (Phoenix Nanotom S scanner, GE Sensing & Inspection Technologies, Germany or SkyScan 1172, Bruker, Belgium). SEM was then used to visualise external and internal particle morphologies. An intact particle and a second fractured particle, selected from the same set of experimental conditions and deliberately fractured using a sharp stainless steel tweezer, were mounted on aluminium stubs with double-sided sticky carbon tape and sputter coated under vacuum with platinum. The SEM (JSM 6490LV, JEOL, Japan) was operated at an accelerating voltage of 5 kV and magnification of 100. Micrographs from both methods were manually analysed for particle diameter and shell thickness, utilised the image processing software ImageJ. The measurements for shell thickness were taken at the

thinnest and the thickest part of the shell, not selected from the flat bottom part of the particles that was attached to the hydrophobic surface, and then averaged to report the result.

4.2.7 Wettability and dissolution properties of dried particles

The method of directly assessing the wettability and dissolution of dried particles through observation was developed based on literature (Fu et al., 2011; Lum et al., 2018) and utilising the contact angle analyser (DSA 10 Mk2, Krüss GmbH, Germany) introduced in Section 4.2.5. Initially, a dried particle was placed on a thin layer of an adhesive putty (Blu Tack) attached to a glass slide to ensure the particle was kept in position. This glass slide was then placed into the contact angle analyser and a droplet of either 0.5 µl or 1.5 µl of Milli-Q water, formed with a micropipette, deposited onto the surface the particle. Camera recording of the dissolution process was started immediately. The dissolution was defined as the time required for the particle to dissolve. The recorded images were used to identify the time of the last visible changes during the dissolution process which was then taken as the dissolution time.

Particle wettability, also referred to as surface hydrophilicity, was quantified by measuring the initial apparent projected contact angle (APCA) (Lum et al., 2018) as follows, and illustrated in Figure 4.5. The APCA has been introduced as the two-dimensional projected contact angle of a water droplet at the point of the three phase contact line between the solid-liquid interface (particle-water) and the tangent to liquid-vapour (water-air) interface. The measurement location of the APCA on the images was identified by first overlaying an image of the particle before wetting with the water droplet, with the particle interface to its

surroundings outlined by the image processing software (Image J) (Figure 4.5a), with the image of the same particle after first contact with the water droplet (Figure 4.5b), as a procedure within ImageJ. An overlay image was used to avoid error in APCA measurement due to light refraction between the solid-liquid interface causing difficulty in identifying the tangent of solid interface (Figure 4.5c). For each particle, the right hand side and the left hand side APCA were determined and the data averaged for reporting.

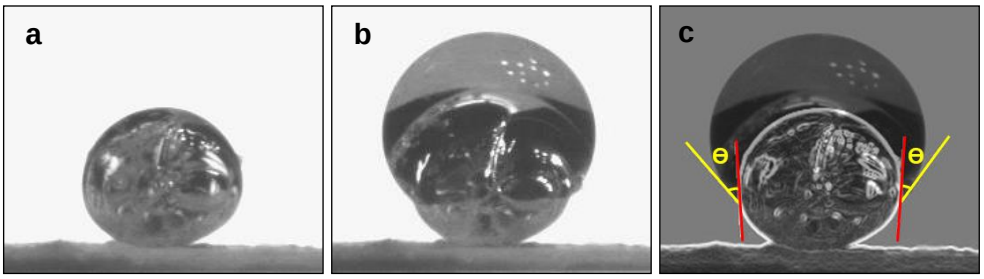

Figure 4.5 a) Particle before wetting with water droplet, b) Particle when first attached to water droplet, and c) APCA measurement of an overlay image using ImageJ software.

4.2.8 Water sorption property of dried particles

Finally, water sorption property was acquired with commercial dynamic vapour sorption (DVS) equipment (DVS Resolution, Surface Measurement Systems Ltd., UK) to further assess the interaction of the dried particles with water or, more precisely, a moist atmosphere. The equipment was fitted with a digital microscope (AM7115MZT Dino-Lite, AnMo Electronics Corporation, The Netherlands) to monitor changes in the state and the dimensions of the particles during the test. The DVS equipment operates as a controlled atmosphere microbalance monitoring the variation of the sample mass to an accuracy of a million parts of a gram with time over a range of relative humidity. Between 5 to 10 mg of dried particles, typically 6-9 individual particles, were placed onto a flat

quartz sample pan which was then positioned inside the equipment. Humidity inside the sample chamber was then incrementally increased by 10% RH from 0 to 90% RH. Each humidity level was held for 240 min, the temperature inside the chamber was kept constant at 25 °C and the sample weight was recorded every minute. The results are presented as water sorption and rate of water sorption over RH.

4.2.9 Statistical analysis

Data were analysed for differences through two-way ANOVA with a Tukey's post hoc test ($p < 0.05$) to evaluate the combined effect of compositional ratio (GA:MD) and other factors (drying temperature, droplet volume, solids concentration and DE-value of MD). Results are reported based on their mean and standard deviation. Calculations were performed using SPSS Statistics software (version 26, IBM SPSS Inc., USA).

4.3 Results and Discussion

4.3.1 Molecular characteristics of GA and MD

It is important to determine molecular characteristics of a polymer as it has a profound influence on the physical properties, such as viscosity, solubility, tensile strength and chemical resistance (Fan et al., 2014). The results of the molecular characteristics analysis of the batches of GA, MD7 and MD12, respectively, utilised in this research are reported in Table 4.1, alongside literature data. The M_w, M_n and R_h obtained for GA are within the range of values reported in literature (Gashua et al., 2016; Idris et al., 1998). The characteristics of GA may vary significantly, depending on the geographical origin, species,

age of the trees, climatic conditions, soil environment and even the place of exudation on the tree (Masuelli, 2013). The molecular weight and hydrodynamic radius of GA is much larger than MD due to its highly branched and complex structure (Sanchez et al., 2017), therefore having the highest value of intrinsic viscosity. According to Dokic et al. (2004) intrinsic viscosity is closely correlated with the average molecular weight of the polymer and at the low concentration range it is independent on the solution concentration.

The results for all four molecular characteristics of both MD samples considered in this research are also in within the range of values reported in literature (Dokic et al., 2004, 1998; Takeiti et al., 2010). As expected, the molecular weight and hydrodynamic radius of the MD samples decreased with increasing degree of starch hydrolysis (expressed by the DE value) resulting in a lower value of intrinsic viscosity (Dokic et al., 2004; Pycia et al., 2016). Other than the DE value, the molecular characteristics of MD might also be influenced by the type of the hydrolysis process (i.e. enzyme or acid), botanical source (i.e. maize, potato, rice), type of chemical modification of starch and manufacturer (Dokic et al., 2004, 1998; Pycia et al., 2016; Takeiti et al., 2010; Wang and Wang, 2000).

Table 4.1 Molecular characteristics of GA, MD7 and MD12 (highlighted) and comparison with literature.

Sample	Molecular characteristic				Reference
	$M_w \times 10^3$ (g/mol)	$M_n \times 10^3$ (g/mol)	R_h (nm)	[η] (ml/g)	
GA	473.8	283.5	10.7	17.2	
A. senegal trees of varying age and location	200 – 790	160 – 450	10 – 21	10.4 – 19.8	Idris et al. (1998)
A. senegal, A. seyal, A. mellifera, A. tortilis	-	2010 - 2950	-	-	Daoub et al. (2016)
A. senegal, A. seyal	485 – 1140	277 – 684	13.0 – 17.3	-	Gashua et al. (2016)
MD7	3.8	3.6	1.5	6.4	
MD12	2.9	2.3	1.2	4.6	
MD of different DE and hydrolysis process	0.8 – 1.8	-	-	2.9 – 6.0	Dokic et al. (1998)
MD DE 2 to 19	9.0 – 155.0	1.3 – 7.5	-	-	Avaltroni et al. (2004)
MD of different DE and botanical sources	0.7 – 9.9	-	-	2.5 – 15.5	Dokic et al. (2004)
MD of different DE from various manufacturers	1.8 – 17.4	0.6 – 2.5	-	-	Takeiti et al. (2010)
MD DE 6, 11 and 16 produced from various chemically modified starches	-	-	-	0.5 – 8.4	Pycia et al. (2016)

Mw = molecular weight, *Mn* = number average molecular weight, R_h = hydrodynamic radius, [η] = intrinsic viscosity

4.3.2 Miscibility of droplet component solutions

A phase separated system is usually characterised by the appearance of turbidity in solution, either immediately or after standing, and the system separates into two layers following centrifugation (Hu et al., 2018). As can be seen in Figure 4.6, the mixtures, regardless of formulation, exhibited no signs of separation after standing quiescently for 24 h and after centrifugation, thus indicating that the solutions were compatible at all mixing ratios.

Here, a sedimentation layer was observed in the centrifuged solutions due to undissolved GA. The proportion of this layer increased with increasing GA concentration and did not occur in MD solutions. However, it is said that GA is highly soluble in cold and hot water up to concentrations of about 50% w/v (Islam et al., 1997; Sanchez et al., 2017). Figure A.2 (in Appendix A) shows the light microscopy images of the initial solutions. From the fluorescence microscopy images (Figure A.3 and Figure A.4 in Appendix A), it is clear to see the amount of undissolved GA in the supernatant reduced when compared to the initial solution before centrifugation.

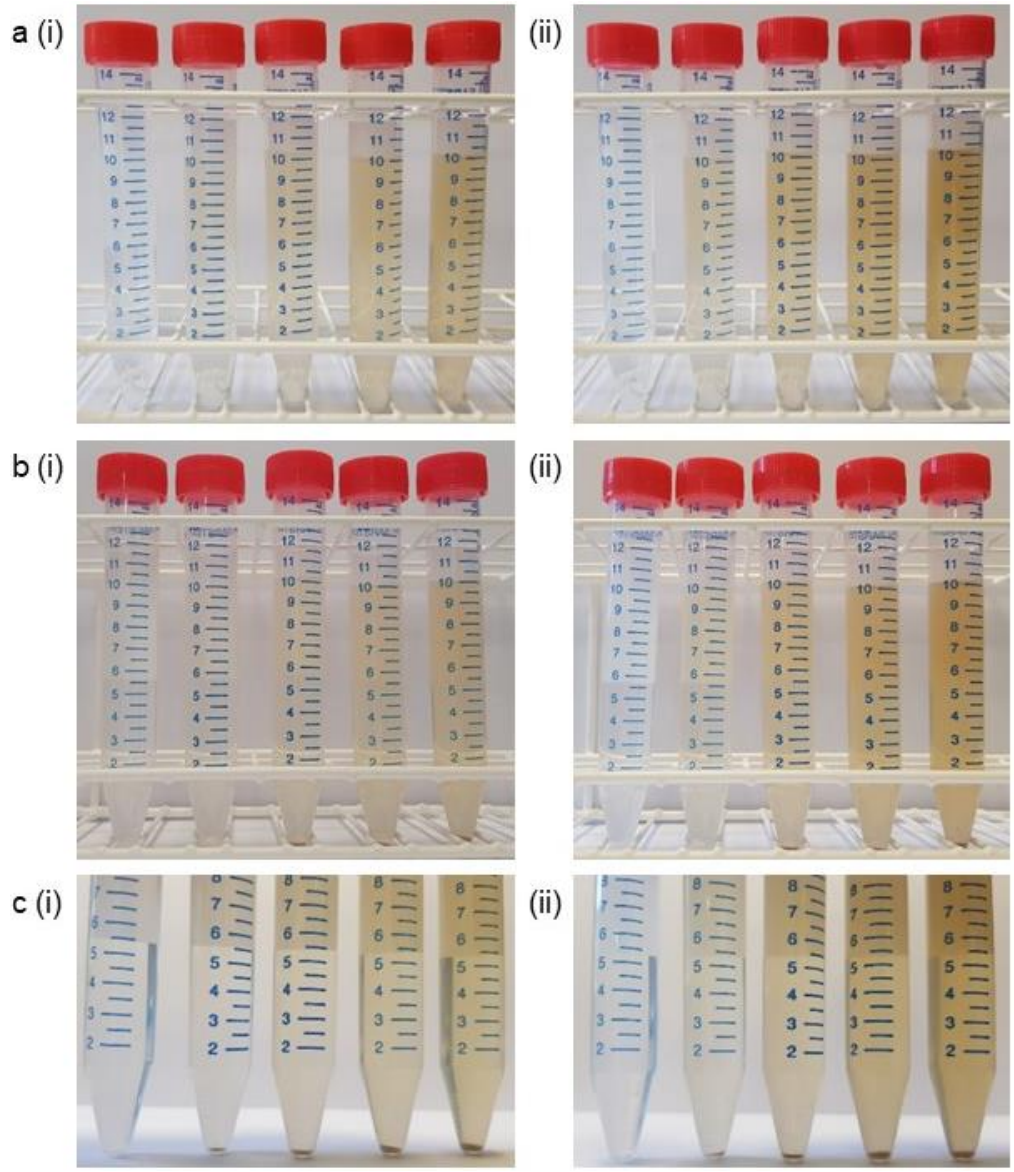

Figure 4.6 Miscible GA:MD7 solutions at a) initial, b) after 24 h and c) after centrifugation, containing (i) 20% and (ii) 40% w/v total solids with various compositions (from left to right: 0:100, 25:75, 50:50, 75:25 and 100:0).

Figure 4.7 compares the data for phase separation, or absence thereof, as obtained in this research (at 25 °C) to data of Annable et al. (1994) who studied the phase separation of GA:potato MD at 45 °C. These authors reported co-solubility and compatibility of the two biopolymers at low polymer concentrations, but two liquid layers were formed at higher concentrations (Annable et al., 1994). It was also reported that the threshold concentration, defined as minimum total polymer concentration necessary for phase separation to occur, was 47% (approximately 40% GA and 5% potato MD). As all samples of GA:MD7 were below the threshold concentration, therefore homogenous solutions would be expected.

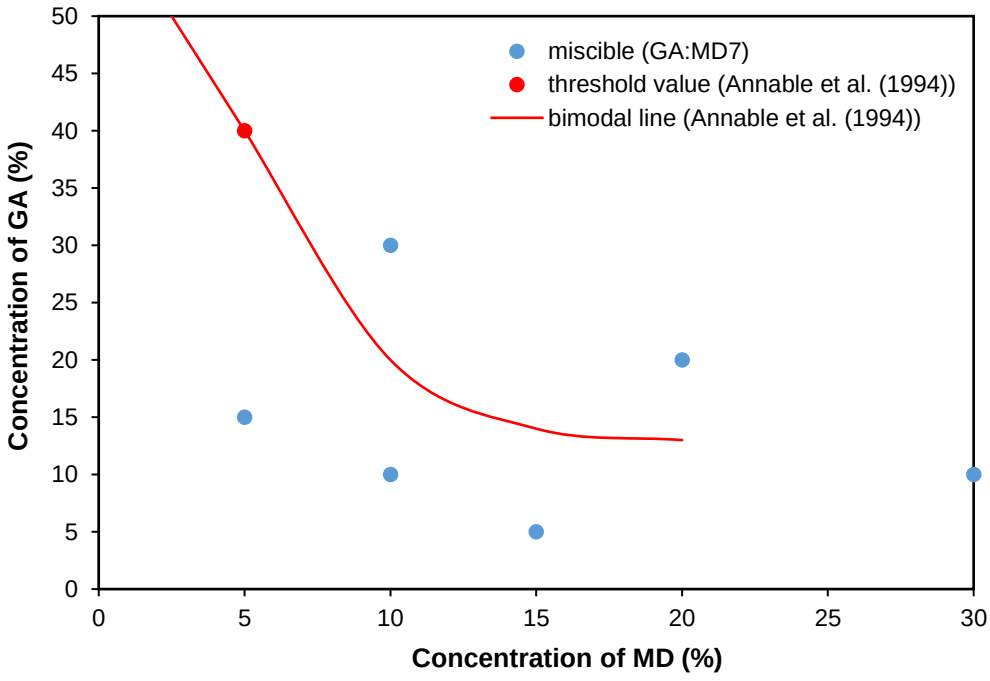

Figure 4.7 Phase diagram of GA and MD mixtures, where blue dot represents miscible solutions of GA:MD7 (corn), and red dot is the threshold value and red line is a bimodal line that separates between miscible and immiscible regions of GA:potato MD solutions as observed by Annable et al. (1994).

4.3.3 Physicochemical properties of droplet solutions

4.3.3.1 Viscosity

The viscosity of the solutions was measured to ensure good atomisation in later spray drying experiments (Chapter 5) for the validation of the SDD data. The maximum admissible viscosity for Buchi mini spray dryer B-290 was used as a guideline (Buchi, 2019). All solutions had considerably lower viscosity (Table 4.2) than the suggested value (300 mPa.s).

Table 4.2 Viscosity of droplet solutions at 25 °C. The standard deviation was less than 62%. Different superscript letters in the same column indicate significant difference between samples ($p < 0.05$).

Solution (GA:MD)	DE of MD	Total solids (%)	Viscosity (mPa.s)
0:100	7	20	5^{b}
25:75	7	20	11^{d}
50:50	7	20	15^{f}
75:25	7	20	19^{g}
100:0	7	20	25^{i}
0:100	7	40	23^{h}
25:75	7	40	54^{k}
50:50	7	40	75^{m}
75:25	7	40	107^{o}
100:0	7	40	166^{p}
0:100	12	20	3^{a}
25:75	12	20	9^{c}
50:50	12	20	13^{e}
75:25	12	20	18^{g}
0:100	12	40	11^{d}
25:75	12	40	35^{j}
50:50	12	40	59^{l}
75:25	12	40	99^{n}

All solutions showed Newtonian behaviour (Figure 4.8) as previously reported in literature (Dickinson, 2016; Li et al., 2011; Pycia et al., 2016; Verbeken et al., 2003). GA solutions were reported to behave as a Newtonian fluid across a wide range of concentrations and at high shear rates (50-100 s^{-1}), but to display more pronounced shear thinning flow behaviour in dilute/semi-dilute regime and low shear rate ranges (1-10 s^{-1}) due to the presence of micro-aggregates in the solutions (Li et al., 2009; Mothé and Rao, 1999; Sanchez et al., 2002). At the same solids concentration, the viscosity of GA solution was much higher than MD solution. Therefore, the viscosity of solutions increased with the increase in the GA proportion and total solids. Solutions prepared with MD7 had a greater viscosity than those with MD12 due to the higher percentage of long oligosaccharide chains (Kasapis et al., 1993). These results are consistent with previous observations that the viscosity of MD depends on the DE-value and solute concentration (Dokic et al., 1998).

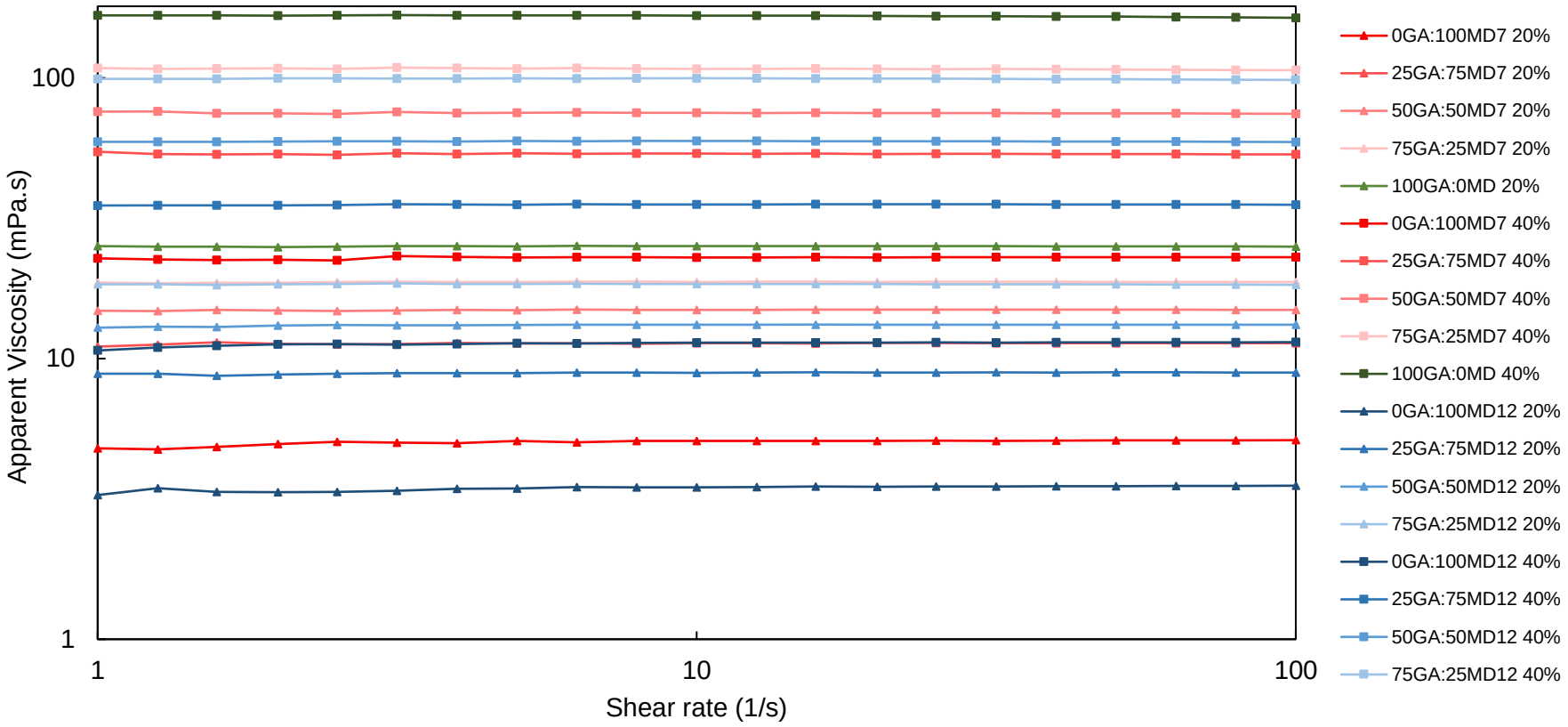

Figure 4.8 Viscosity of droplet solutions.

4.3.3.2 Hydrodynamic radius and diffusion coefficient

The value of the hydrodynamic radius and the diffusion coefficient of GA and MD at different solids concentrations obtained in this research are reported in Table 4.3. The hydrodynamic radius of GA increased with solids concentration, possibly related to the molecular association of GA molecules. This result is consistent with the findings of Li et al. (2009). The structure of GA is highly branched and its granule-shaped molecules form particulate aggregates when solvated in water. The extend of the molecular aggregation depends on the concentration regime. The isolated aggregates observed in the dilute regime organise into large network structures in the semi-concentrated regime (Figure 4.9) (Li et al., 2009). Therefore, in the concentration regime investigated in this research (20 to 40% solids), aggregated network structure was expected. Indeed, the viscosity of the 40% GA solution was too high to be amenable to DLS analysis to measure the hydrodynamic radius. In the case of the MD solutions, hydrodynamic radius data were independent of solids concentration and DE value. MD molecules have an on average an ovoid-like shape in solution (Avaltroni et al., 2004).

According to the Stokes-Einstein equation (Equation 2.6), the diffusion coefficient is inversely proportional to the solution viscosity and hydrodynamic radius. Hence, MD12 at 20% concentration exhibited the highest diffusion coefficient as a result of having the lowest viscosity and smallest hydrodynamic radius. It can be expected that GA at 40% concentration had the lowest diffusion coefficient.

Table 4.3 Hydrodynamic radius and diffusion coefficient of GA and MD at different concentrations, as determined by DLS. Different superscript letters in the same column indicate significant difference between samples ($p < 0.05$).

Sample		Hydrodynamic radius (nm)	Diffusion coefficient $\times 10^{-12}$ (m^2/s)
MD7	20% solids	9.7 ± 0.1^a	44.8
	40% solids	9.2 ± 0.7^a	10.6
MD12	20% solids	10.1 ± 0.3^a	62.3
	30% solids	10.6 ± 0.2^a	32.1
	40% solids	10.1 ± 1.0^a	5.0
GA	20% solids	9.4 ± 1.1^a	9.2
	30% solids	17.5 ± 1.8^b	1.9

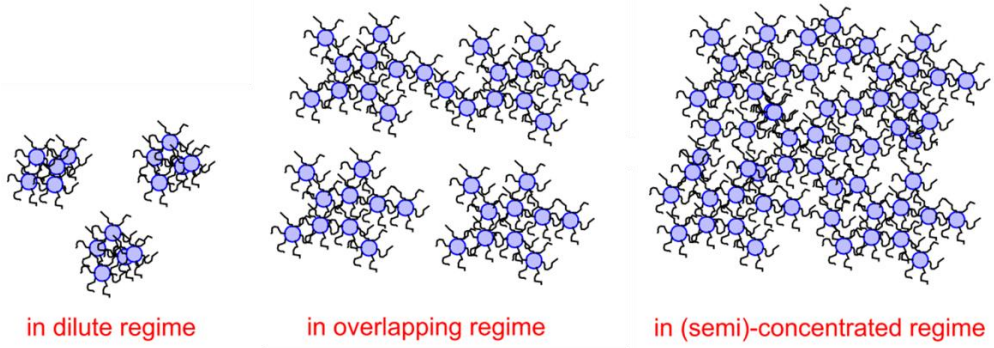

Figure 4.9 Particulate aggregates of GA in solutions at different concentration regime as proposed by Li et al. (2009).

4.3.4 Properties of droplets on hydrophobic surface

Table 4.4 shows the diameter, contact angle and roundness of droplets prepared with different compositional ratios of GA:MD12 at various volumes that were deposited on the hydrophobic surface. Figure 4.10 shows representative images of droplets for one of the set of data. The diameter was calculated as 2R with R measures as outlined in Figure 4.2. Both, a smaller deposited droplet volume and an increased proportion of GA in the droplet solution resulted in a smaller diameter value. However, all droplets had a similar contact angle and

sphericity. The contact angle values found here were larger than those reported by Perdana et al. (2011) and Sadek et al. (2013). These authors used polypropylene and substrate patterned with cylindrical pillars as the hydrophobic surfaces in their SDD experiments. These were more hydrophobic than the glass slide treated with water repellent used here. The values of the radius/height ratio (~0.6) found here were similar to those reported by Both et al. (2018b) for droplets containing mixed component formulations and milk deposited onto a hydrophobic membrane.

Table 4.4 Diameter, contact angle and radius/height ratio of droplets at different volumes and compositional ratios (MD12, 30% total solids). Different superscript letters in the same column indicate significant difference between samples ($p < 0.05$).

Sample		Diameter (mm)	Contact angle (°)	R/H
0GA:100MD	1 µl	1.95 ± 0.05^{cd}	150 ± 8^{a}	0.60 ± 0.02^{a}
	2 µl	2.06 ± 0.03^{de}	154 ± 6^{a}	0.60 ± 0.02^{a}
	3 µl	2.26 ± 0.01^{f}	149 ± 4^{a}	0.61 ± 0.01^{a}
50GA:50MD	1 µl	1.83 ± 0.04^{ab}	147 ± 7^{a}	0.60 ± 0.02^{a}
	2 µl	2.04 ± 0.05^{de}	150 ± 6^{a}	0.61 ± 0.01^{a}
	3 µl	2.12 ± 0.05^{e}	155 ± 5^{a}	0.60 ± 0.01^{a}
100GA:0MD	1 µl	1.75 ± 0.03^{a}	149 ± 5^{a}	0.60 ± 0.01^{a}
	2 µl	1.88 ± 0.09^{bc}	155 ± 4^{a}	0.60 ± 0.00^{a}
	3 µl	2.05 ± 0.04^{de}	154 ± 7^{a}	0.61 ± 0.02^{a}

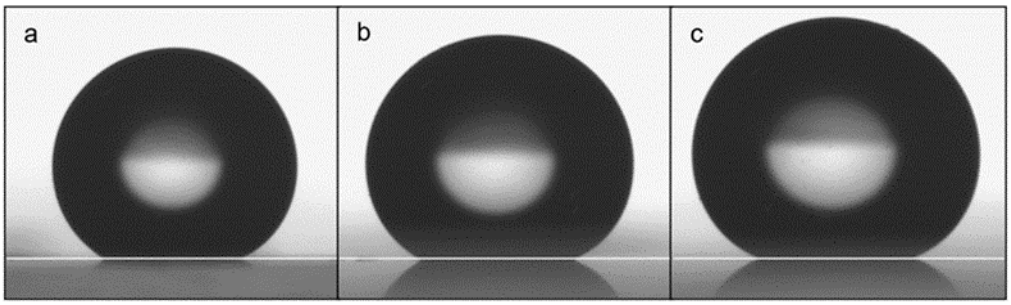

Figure 4.10 50GA:50MD droplets (MD12, 30% total solids) at volume of a) 1 µl, b) 2 µl and c) 3 µl on a hydrophobic surface.

4.3.5 Particle development during drying

The morphological development during drying could be divided into two stages: (i) the constant rate period and (ii) the falling rate period. The impact of the compositional ratio, drying temperature, droplet size, initial solids concentration of the solution and DE of MD on the drying kinetics at each stage are discussed in more detail in the following:

4.3.5.1 Constant rate period

At the beginning of the drying process, each droplet shrank progressively while retaining its shape with a constant base radius. Figure 4.11 to Figure 4.13 show photographs of the drying process of droplets of different GA:MD12 at 30% total solids, which were dried at 80, 100 and 120 °C, respectively.

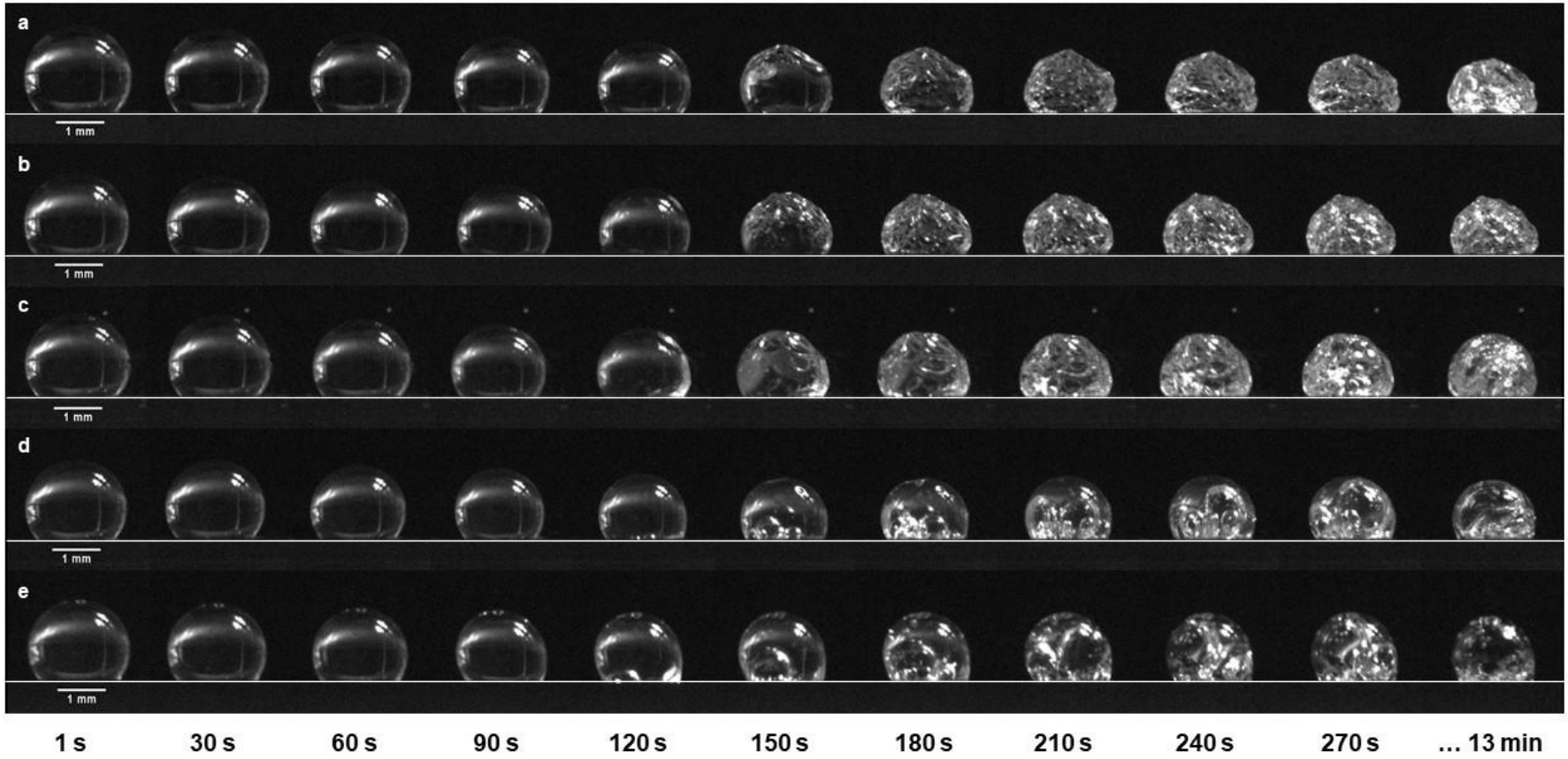

Figure 4.11 Time series of droplets with different compositions of GA:MD12 dried at 80 °C: (a) 0:100, (b) 25:75, (c) 50:50, (d) 75:25, and (e) 100:0. Droplets had an initial total solids content of 30% w/v and initial droplet volume of 2 µl.

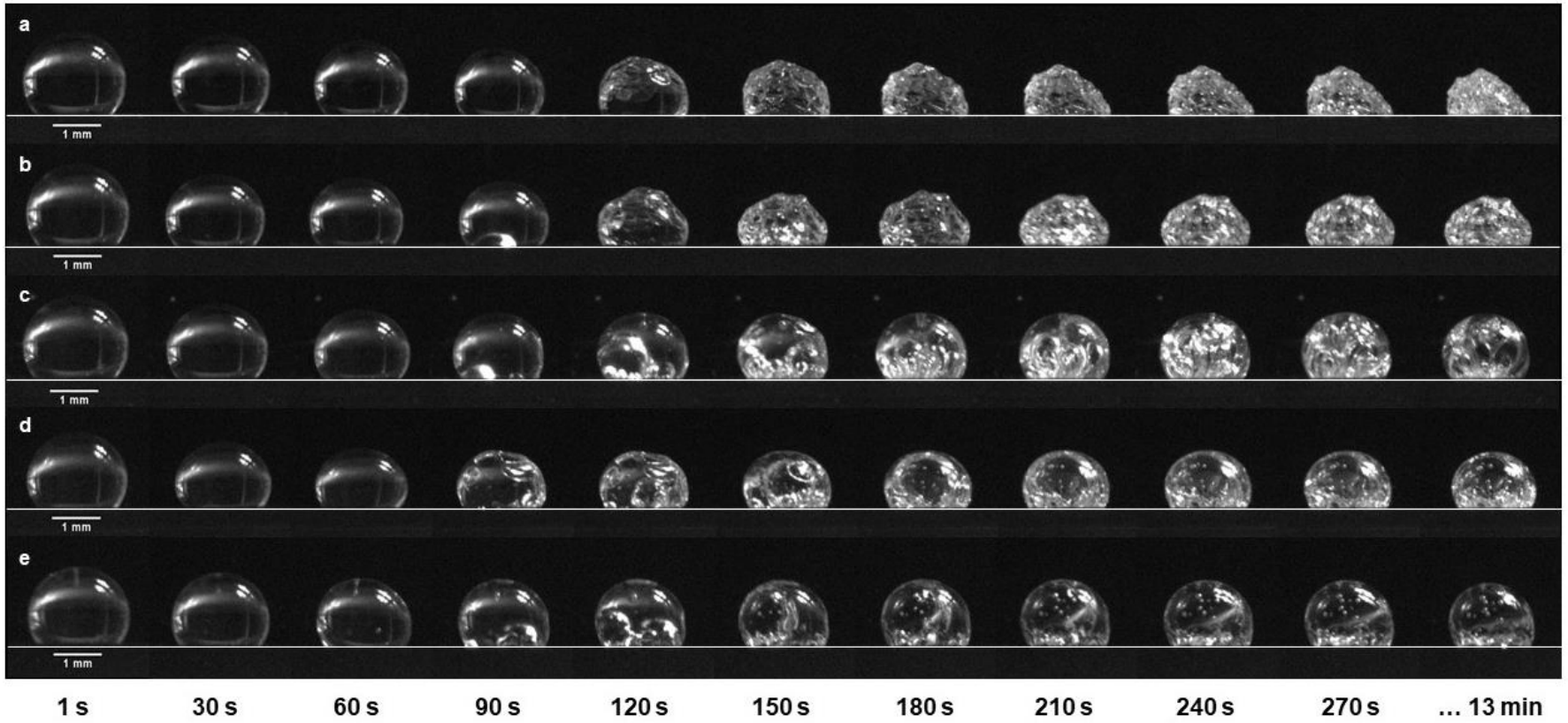

Figure 4.12 Time series of droplets with different compositions of GA:MD12 dried at 100 °C: (a) 0:100, (b) 25:75, (c) 50:50, (d) 75:25, and (e) 100:0. Droplets had an initial total solids content of 30% w/v and initial droplet volume of 2 µl.

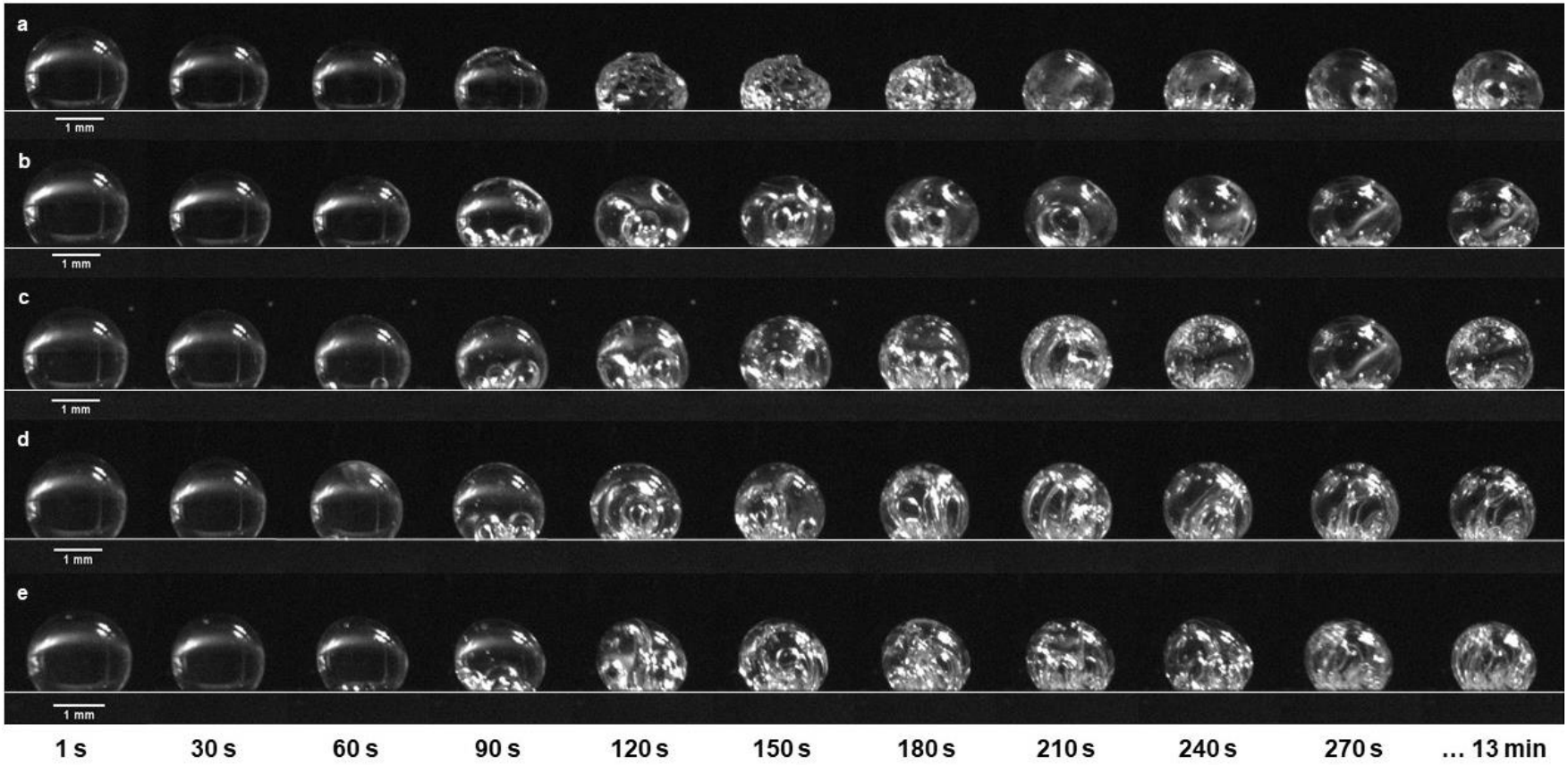

Figure 4.13 Time series of droplets with different compositions of GA:MD12 dried at 120 °C: (a) 0:100, (b) 25:75, (c) 50:50, (d) 75:25, and (e) 100:0. Droplets had an initial total solid of 30% w/v and initial droplet volume of 2 µl.

A graph of the square of the normalised radius was plotted against time for each sample and each drying temperature, in Figure 4.14 for droplets 50GA:50MD12. The data decrease linearly with the time which describes the process of constant rate drying (Jakubczyk et al., 2012). The graphs for the other samples, all showing this linear relationship, can be found in Figure A.5 to Figure A.7 in Appendix A.

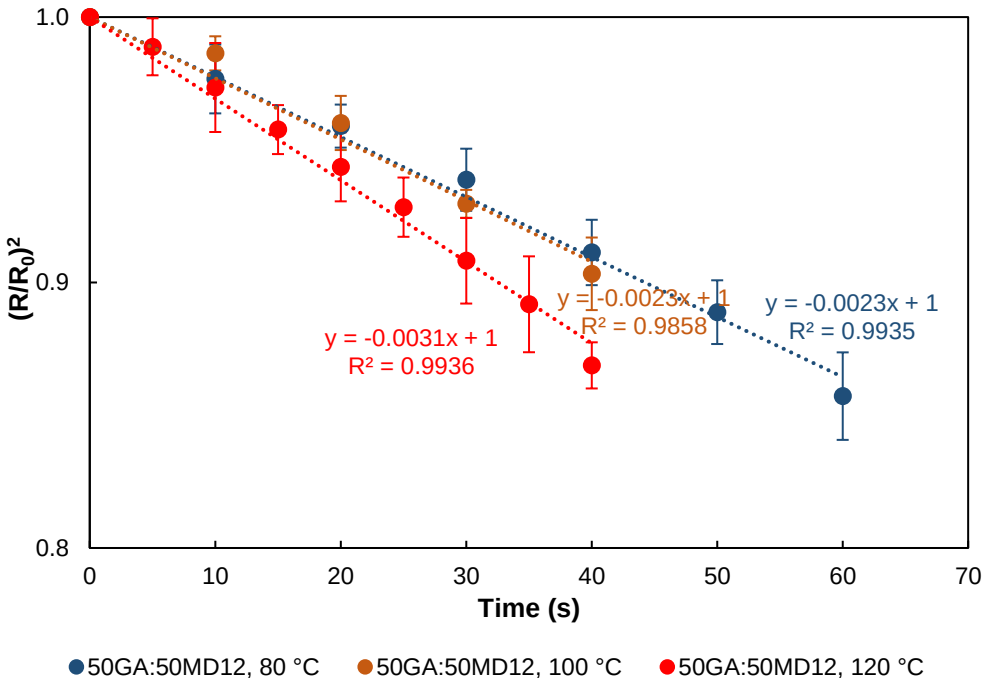

Figure 4.14 Normalised radius squared of 50GA:50MD12 droplets against time and dried at different temperatures. Blue: 80 °C, orange: 100 °C and red: 120 °C. Droplets had an initial total solids content of 30% w/v and an initial droplet volume of 2 µl. Lines were fitted to the experimental data.

The drying rate contants (κ) were calculated from the slope of the straight lines of the radius squared curves (Equation 4.1). The results for each compositional ratio of GA:MD12, which were dried at different drying temperatures and initial droplet volumes are shown in Figure 4.15. While having different ratios of GA:MD12, the drying rate constant was comparable to each other at the same

drying temperature. As expected, droplets dried at 120 °C had the highest drying rate constant, as a result of greater saturation vapour pressure on the droplet surface at higher drying temperature (Tran et al., 2016). However, the drying rate constant was the same when droplets were exposed to 80 °C and 100 °C, possibly because these temperatures were below the boiling temperature of the solvent.

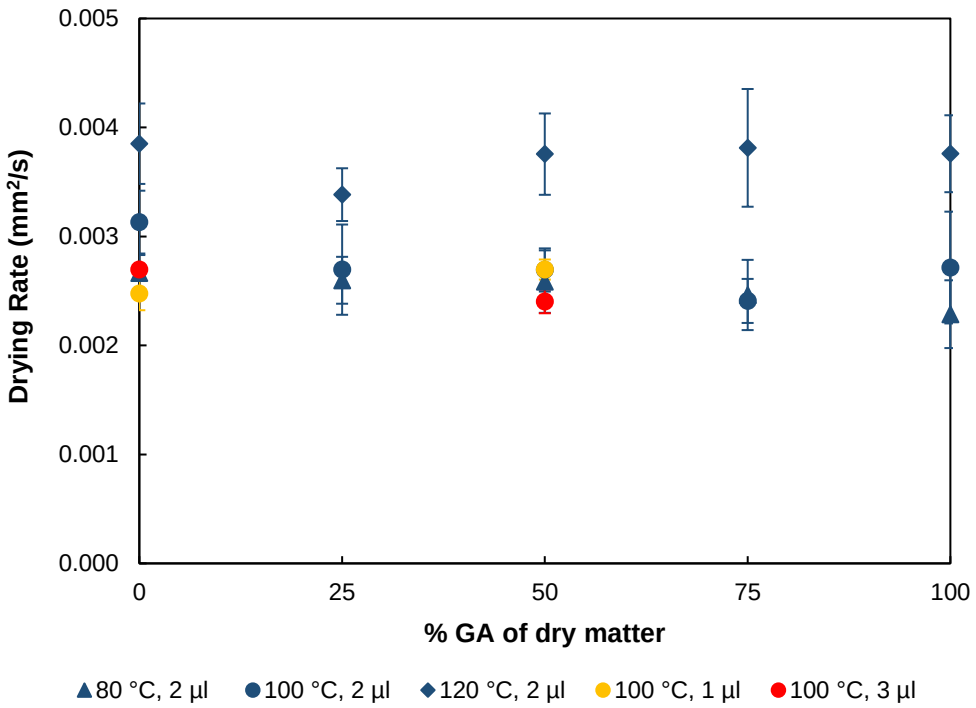

Figure 4.15 Drying rate constant of droplets with different compositions of GA:MD12, drying temperatures and droplet volumes. Drying temperature: 80 °C (triangles), 100 °C (circles) and 120 °C (diamonds); droplet volume: 1 µl (yellow), 2 µl (blue) and 3 µl (red). Droplets had an initial total solids content of 30% w/v.

To assess the impact of initial droplet volume on drying rate constant, 0GA:100MD12 and 50GA:50MD12 droplets dried at 100 °C were selected as two different final particle morphologies developed. Wrinkled particles formed from 0GA:100MD12, whereas smooth surface particles were observed for 50GA:50MD12 (Figure 4.12a and c respectively). This is discussed in more

detail later on (Section 4.3.5.2 and 4.3.5.3). At the same droplet composition, the initial droplet volume (diameter of 1.8 mm at 1 µl, 2.0 mm at 2 µl and 2.1 mm at 3 µl) appeared not to impact on the drying rate constant. Bouman et al. (2016) reported a similar observation studying the SDD of whey protein solutions at droplet diameters of 1.0, 2.0 and 3.0 mm.

Droplets dried at higher temperature showed a tendency to produce smooth-surface hollow particles (as shown in Figure 4.11 to Figure 4.13) and therefore the drying temperature of 120 °C was chosen to further evaluate the impact of initial solids concentration and DE-value of MD on the drying kinetics of droplets and the final particle morphology. Ignoring the data for pure GA droplets, Figure 4.16 shows faster drying at lower initial solids concentration. This observation is consistent with previous reports (Nešić and Vodnik, 1991; Tran et al., 2016) and can be explained by the higher amount of water and thus, free water at the droplet surface to readily evaporate from the droplet surface during the constant rate drying period.

GA droplets dried at the same rate for both solids concentrations, possibly due to having a similar diffusion coefficient as a result of aggregated network formation at high concentration of GA (Section 4.3.3.2). On the other hand, MD droplets at 20% solids concentration had much higher diffusion coefficient than at 40%, meaning that MD molecules in the droplet with lower concentration can easily diffuse to the centre of the droplet to prevent saturation at the surface, and thus enhanced the water evaporation from the surface of the droplet. At the same solids concentration, the drying rate constants of all droplets (excluding GA at 40% solids) were somewhat similar to each other. Therefore, the drying

rate during the constant rate period is not governed by internal diffusion but the water activity at the droplet surface. As refer to isotherms presented later in the thesis (Figure 4.40), in that both 20% and 40% solids samples would be expected to show very high water activity of about the same values (more than 90%) and thus have very similar drying rates. The DE-value of MD had no influence on the drying rate constant (Figure 4.16), except for 50GA:50MD12 droplets at 20% solids that had slightly higher drying rate constant than 50GA:50MD7 droplets which is most likely due to experimental errors.

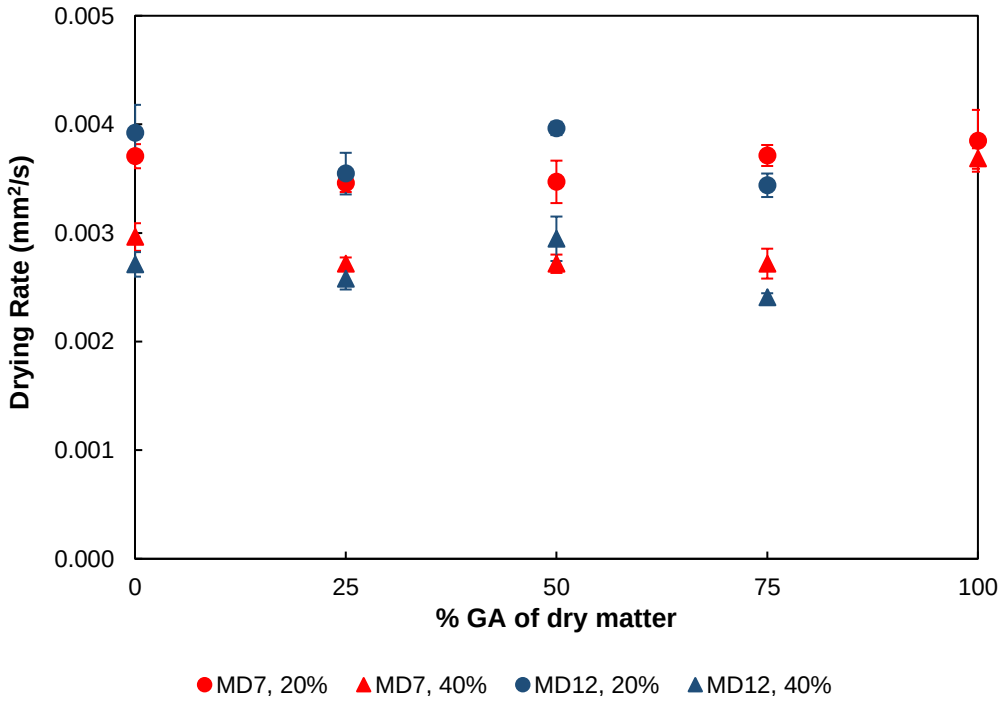

Figure 4.16 Drying rate constant of droplets with different compositions of GA:MD, solids concentrations and DE-values of MD. Solids concentration: 20% w/v (circles) and 40% w/v (triangles); DE-value of MD: MD7 (red) and MD12 (blue). Droplets had an initial volume of 2 µl and were dried at 120 °C.

Overall, the drying rate constants obtained in this research were higher than those reported by Bouman et al. (2016) and Both et al. (2018a) for their SDD studies utilising a hydrophobic membrane. Their results were in the range of

0.0004 to 0.0016 mm^2/s, whereas the data found here were between 0.0023 to 0.0044 mm^2/s. This discrepancy is most likely due to the different drying chamber design. The lower drying rate constants were obtained in an open chamber design (as shown in Figure 2.18), whereas here a closed drying chamber was utilised. This allowed for better control of the temperature and environmental conditions, and thus more efficient drying.

4.3.5.2 Falling rate period

As drying progressed, the formation of a skin was observed. This is the result of an increase in solids concentration at the surface of the droplet due to continued evaporation of water. Ultimately, the saturation concentration is reached and a skin starts to form. Droplet shrinking comes to an arrest due to the strength of the developed skin (Both et al., 2018a). The corresponding point in time is referred to as the locking point, which is the moment of first visual skin formation (Schutyser et al., 2019). It marks the transition from the constant drying rate period to the falling drying rate period. The drying of a liquid droplet changes to the drying of a particle with a wet core. Heat transferred from the air to the particle by convection is consumed for water evaporation, as well as for the increase in the temperature of the wet core (Tran et al., 2017). This research has identified three important events that occurred during the falling rate period and had a major impact on the final particle morphology: the locking point, buckling and bubble formation.

According to Tran et al. (2016), the locking point can be identified by one of three methods, that is when the droplet diameter becomes constant, or the evaporation flux starts to decrease, or visually from camera images. In this

research, the locking point was defined as the point at which the droplet became asymmetric and this was determined visually from camera images, as described by Both et al. (2018a). The locking point and the normalised droplet radius at the locking point for droplets dried at different drying temperatures and droplet volumes are shown in Figure 4.17.

Droplets richer in GA and dried at higher temperature reached the locking point earlier in the drying process and at a larger radius, compared to those that were higher in MD and dried at lower temperature. GA had a larger molecular weight and a higher hydrodynamic radius than MD (Table 4.1) meaning a lower diffusion coefficient (Table 4.3), and thus the GA enriched in the liquid layer close to the droplet surface leading to the skin forming at a bigger droplet size. Moreover, GA is surface active and therefore will accumulate at the air-water interface (Munoz-Ibanez et al., 2016). On the contrary, droplets with only MD had a later locking point and hence a smaller droplet radius at the locking point. At higher drying temperature, earlier locking points were obtained as in agreement with Both et al. (2018a) and Siemons et al. (2020), which explained by faster drying.

At the same droplet composition and drying temperature, a larger droplet volume appeared to attain locking point later (Figure 4.17a), but having the same normalised radius (R/R_0) as the smaller droplets (Figure 4.17b). Droplets of different initial volumes experienced a similar drying rate during the constant rate period (Figure 4.15), therefore a larger droplet required more time to reach the critical skin concentration. This observation is consistent with studies of Both et al. (2019a) for mixed whey protein isolate and MD droplets.

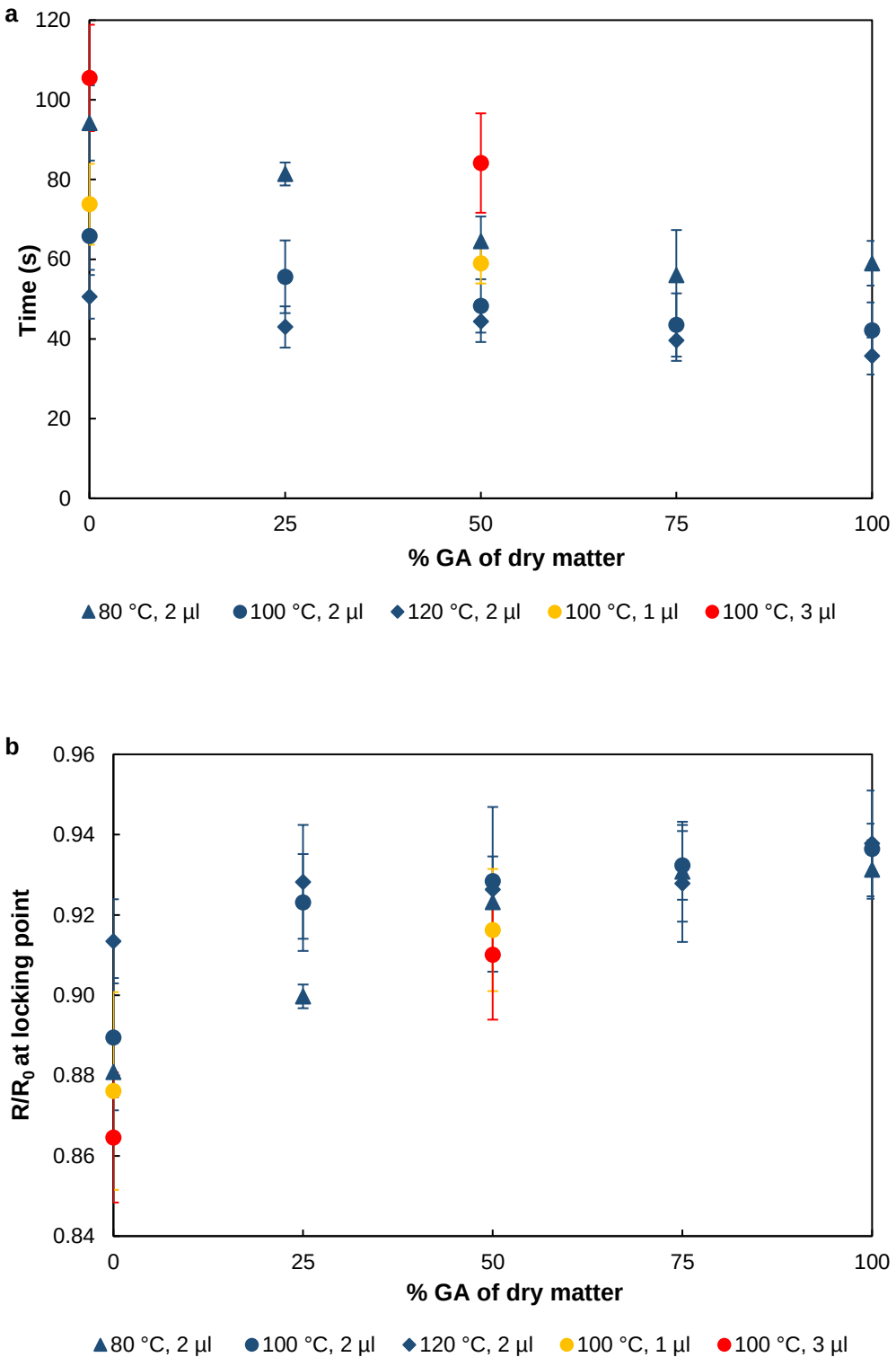

Figure 4.17 a) Locking point time and b) normalised radius (R/R_0) at the locking point for droplets of different compositions of GA:MD12, drying temperatures and droplet volumes. Drying temperature: 80 °C (triangles), 100 °C (circles) and 120 °C (diamonds); droplet volume: 1 µl (yellow), 2 µl (blue) and 3 µl (red). Droplets had an initial total solid of 30% w/v.

The combined effects of GA:MD composition, solids concentration and DE-value of MD on the locking point and the droplet radius at the locking point are shown in Figure 4.18, for constant initial droplet volume (2 µl) and drying temperature (120 °C). Droplets containing a higher solids concentration had an earlier locking point and reached the locking point with a larger radius, even though the drying rate constant was slower (Figure 4.16). This result is in agreement with other research which found that more solute in the initial droplet led to a larger final particle (Tran et al., 2016). Both et al. (2019a) reported an increase in the amount of dry matter content from 30 to 40 % (w/w) reduced the locking point time by about half. Here, the time taken to reach the locking point was shortened by approximately 40% when the initial solids increased from 20 to 40%.

DE-value of MD showed no influence on the locking point time and the size at the locking point (Figure 4.18). The exception was 75GA:25MD7 droplets at 40% solids that had faster locking point and at larger droplet radius than 75GA:25MD12 droplets, possibly related to slightly higher drying rate during constant rate period (Figure 4.16). Siemons et al. (2020), who studied SDD of MD in a wider range of DE-value (DE 5 to 38), found that MD DE 5 developed a skin earlier and at a larger normalised radius than droplets with higher DE, as having the highest viscosity upon concentration.

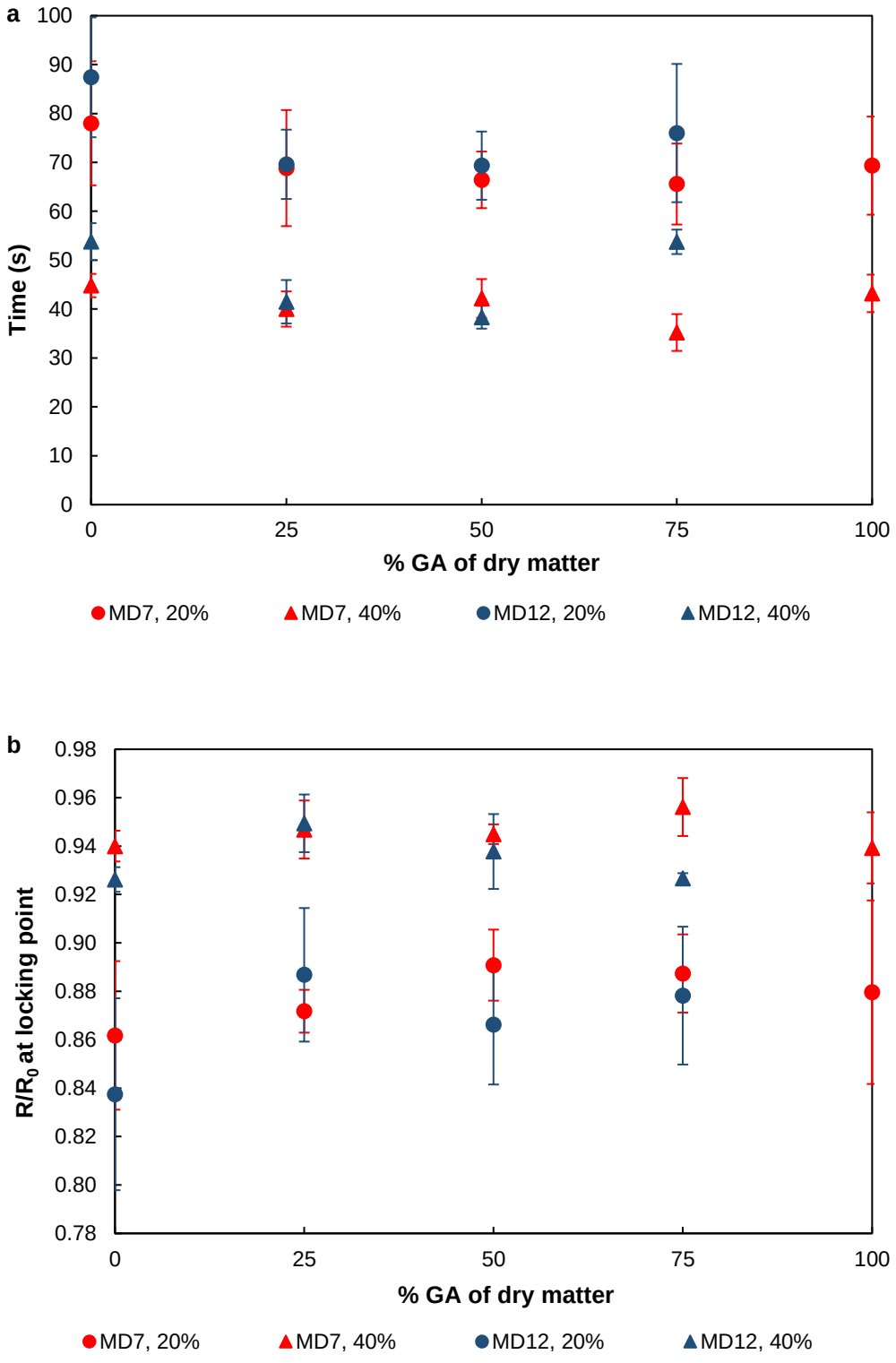

Figure 4.18 a) Locking point time and b) normalised radius (R/R_0) at the locking point for droplets of different compositions of GA:MD, solids concentrations and DE-values of MD. Solids concentration: 20% w/v (circles) and 40% w/v (triangles); DE-value of MD: MD7 (red) and MD12 (blue). Droplets had an initial volume of 2 µl and were dried at 120 °C.

At both concentrations and DE-values, MD droplets behaved similarly to the previous observation (Figure 4.17); the late locking point with the smallest radius. However, the impact of the compositional ratio at the locking point seemed to be suppressed at high drying temperature as no clear trend was observed (Figure 4.18). At low temperature, an increase in the ratio of GA resulted in a decrease in the locking point time and thus at a larger droplet size (Figure 4.17).

The dimensionless Peclet number, which governs whether drying is uniform or not, can also be used to predict the distribution of components during the particle formation process (Vehring et al., 2007). The Peclet number of a single drying droplet can be calculated according to Equation 4.2 (Vehring, 2008):

$$Pe = \frac{\kappa}{8D} \tag{4.2}$$

where κ is the drying rate constant ($m^2.s^{-1}$) (from Figure 4.15 and Figure 4.16) and D the diffusion coefficient of the solute in the liquid phase ($m^2.s^{-1}$) (Table 4.3). When Pe >> 1, the evaporation dominates over diffusional transport, and drying is non-uniform as the solute cannot follow the shrinkage of the droplets, leading to skin formation (Bouman et al., 2016; Kawakami et al., 2010). Calculated Peclet numbers are reported in Table 4.5. All droplets displayed large Peclet numbers, therefore the drying was inhomogenous, favouring the formation of a skin at some stage during the drying process. This process is expected to lead to the formation of hollow particles (Vehring et al., 2007), as long as the thickness and mechanical properties of the skin are also favourable (Sadek et al., 2015a).

GA exhibited the highest Peclet number and MD12 had the lowest Peclet number, in accordance with the lowest and the highest diffusion coefficient respectively (Table 4.3). In a system with two solutes, the solute with a higher Peclet number would enrich at the surface relative to a solute with a lower Peclet number (Nuzzo et al., 2015a). Therefore, GA would expect to dominate at the surface of a droplet containing a mixture of GA and MD. Indeed, XPS had confirmed the tendency of preferential accumulation of GA at the surface of the spray dried GA:MD particles (Chapter 3). The Peclet number increased markedly with increased solids concentration and drying temperature. This can be explained by the concomitantly decreasing diffusion coefficient and the higher drying rate at higher drying temperature.

Table 4.5 Peclet number estimation for GA and MD droplets at different drying temperatures and solids concentrations (at initial droplet volume of 2 µl).

Sample	Drying Temperature (°C)	Peclet number
MD7, 20% solids	120	114
MD7, 40% solids	120	413
MD12, 20% solids	120	78
MD12, 30% solids	80	105
	100	121
	120	152
MD12, 40% solids	120	682
GA, 20% solids	120	514
GA, 30% solids	80	1520
	100	1784
	120	2510

From the time series in Figure 4.11 to Figure 4.13, it can be observed that buckling appeared at some point after skin formation. Buckling has previously been described in literature and its onset related to the formation of a thin elastic shell (Pauchard and Allain, 2003a, 2003b; Tsapis et al., 2005). In this model, it is envisaged that the accumulation of solutes at the droplet surface induces the formation of a viscoelastic layer. With progressive water evaporation, this layer becomes rigid but behaves like an elastic shell. Depending on the materials in the droplet, the rigid skin can be either a gelled or glassy skin. This skin does not impede evaporation, thus evaporation still continues by water vapour diffusion through the skin. The shell is forced to bend inward as the volume included inside the shell decreases, while its surface remains constant. The buckling only happens when a rigid skin forms before the interior of the droplet has completely dried or gelled (Pauchard and Allain, 2003b). In this research, buckling of GA:MD droplets appeared at the top of droplets due to this area experienced a greater drying as the heated air was flowing from the top of the chamber.

Another interesting phenomenon that occurs during the falling rate period is bubble formation. Skin formation is a necessary condition for bubble formation, but skin formation does not necessarily lead to bubble formation (Arai and Doi, 2012). When a droplet is dried at a temperature close to, or above, the boiling point of the solvent, vapour formation can cause bubble nucleation inside the droplet (Both et al., 2018a). However, bubble nucleation may also happen at a temperature below the atmospheric boiling temperature due to a pressure decrease in the solution covered by a skin layer (Arai and Doi, 2012). Here, bubbles were found to appear inside droplets that were dried at 80 °C, around

65 to 210 s into the drying process depending on GA:MD (Figure 4.11). As can be seen in Figure 4.11 to Figure 4.13, the bubbles expanded from the inside to out as the internal pressure within the wet particle started to increase, pushing the solution towards the internal surface to allow for the water vapour to be released through the skin. Eventually, a large vacuole formed. The growth rate of the bubble (which consists of a mixture of vapour and dissolved air) is driven by air diffusion. When bubbles nucleate, air diffuses from the solution to the bubble because the partial air pressure in the bubble is lower than the atmospheric pressure (Arai and Doi, 2012).

The occurrence of buckling indicates the apparent onset of rigid skin (Pauchard and Allain, 2003b). Graphs of the onset of buckling and bubble formation are shown in Figure 4.19 for different drying temperatures and droplet volume, and in Figure 4.20 for the two solids concentrations of 20% and 40% and both DE-values of MD considered in this research. GA droplet is assumed to form a gelled skin during buckling, while the rigid skin for MD is a glassy skin. The buckling of GA droplets took place earlier than MD droplets due to early skin formation, and thus resulted in faster bubble nucleation. For droplets containing a mixture of GA and MD (at 80 and 100 °C), they buckled practically at the same time, but bubble formed earlier at higher ratios of GA (Figure 4.19). Droplets that higher in GA reached the boiling temperature faster due to the early skin formation, thus formed thicker skin.

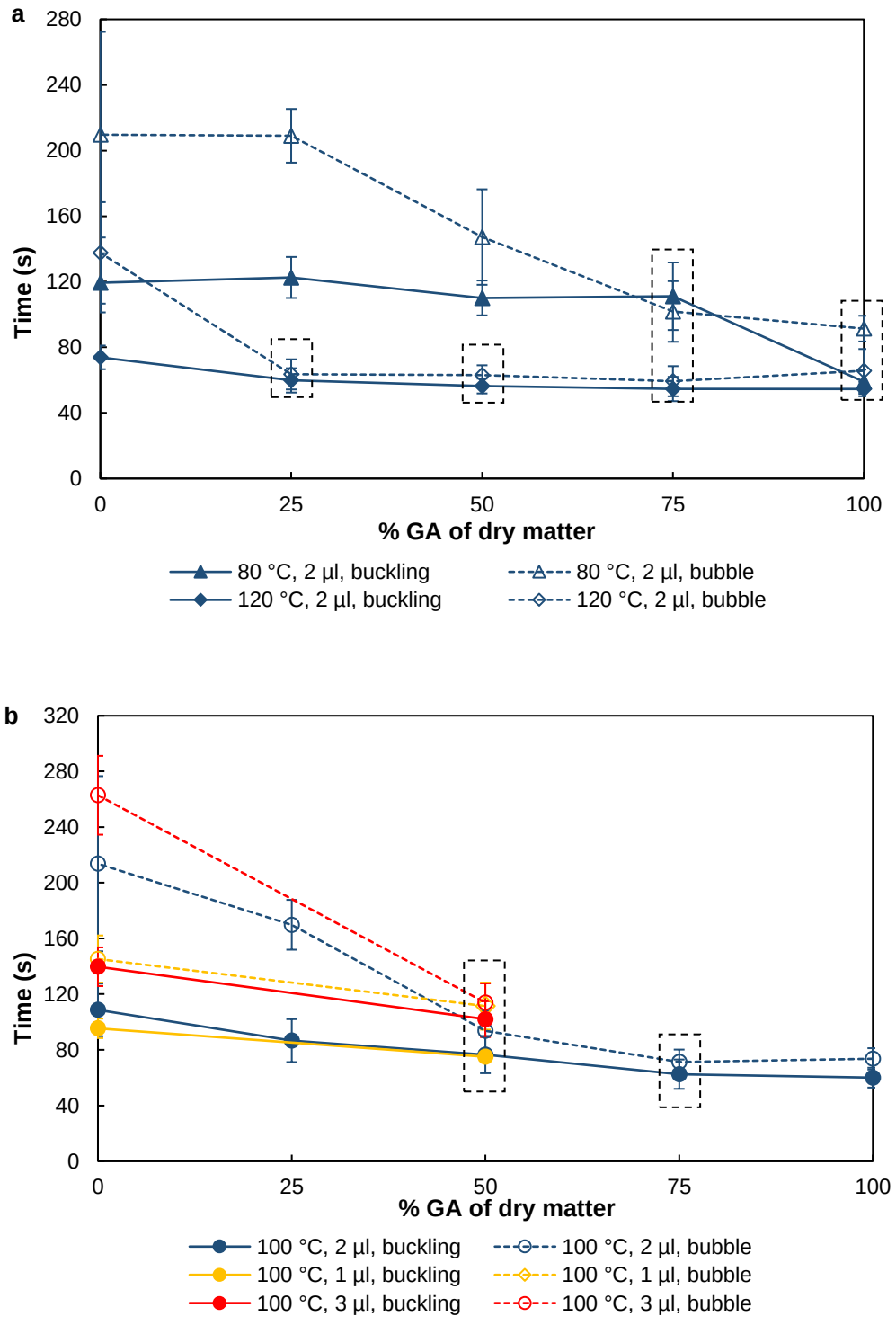

Figure 4.19 The onset of buckling and bubble formation during drying of droplets of different compositions of GA:MD12: a) at varied drying temperature, and b) at varied initial droplet volume. Drying temperature: 80 °C (triangles), 100 °C (circles) and 120 °C (diamonds); droplet volume: 1 µl (yellow), 2 µl (blue) and 3 µl (red). Droplets had an initial total solids content of 30% w/v. The dotted box shows when both wrinkling and bubble appear at the same time and smooth-surface hollow particle is obtained.

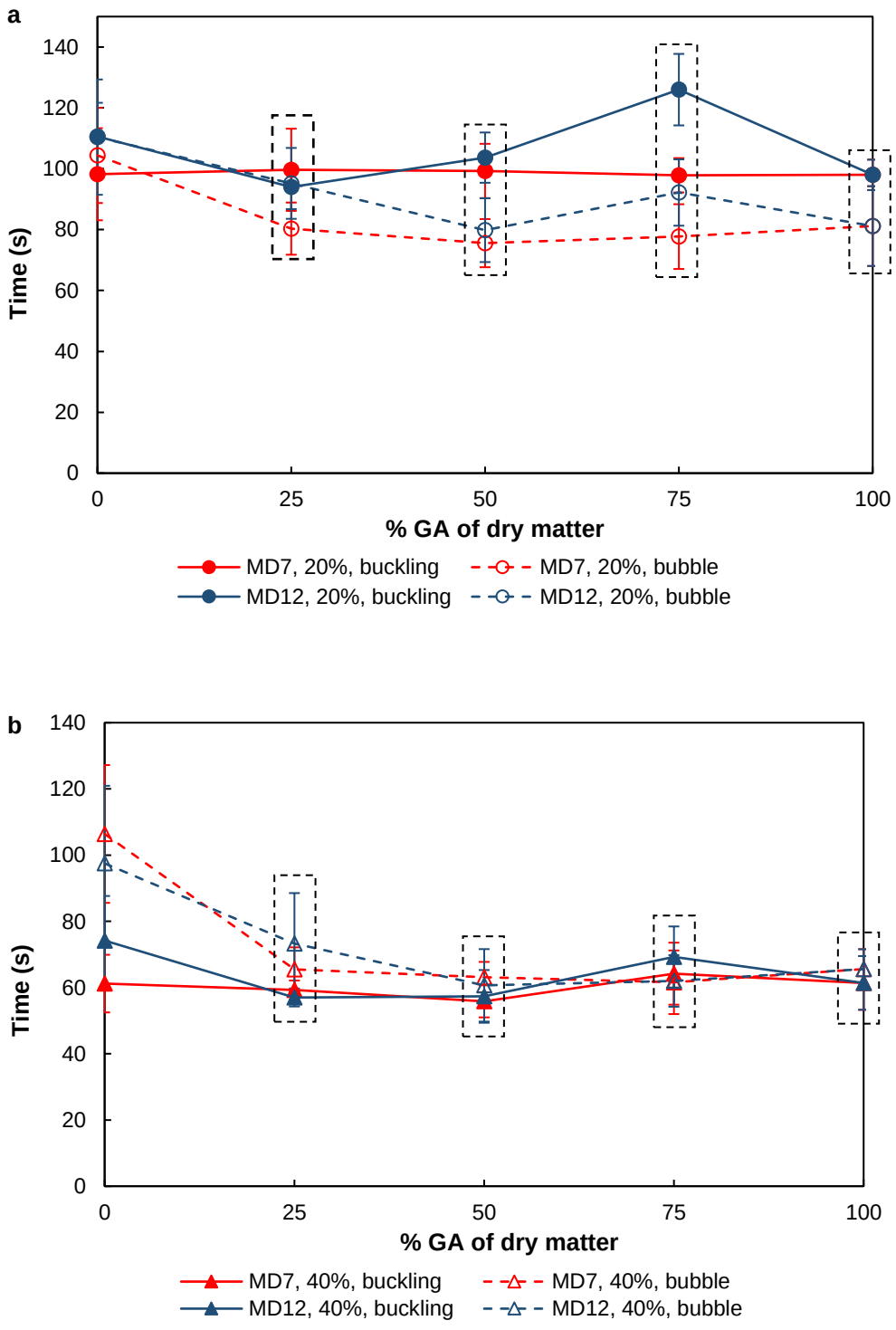

Figure 4.20 The onset of bucking and bubble formation during drying of droplets of different compositions of GA:MD and DE-value of MD: a) 20% w/v solids concentration, and b) 40% w/v solids concentration. Solids concentration: 20% w/v (circles) and 40% w/v (triangles); DE-value of MD: MD7 (red) and MD12 (blue). Droplets had an initial volume of 2 µl and were dried at 120 °C. The dotted box shows when both wrinkling and bubble appear at the same time and smooth-surface hollow particle is obtained.

Buckling and bubble formation occurred earlier at either higher drying temperature (Figure 4.19a), or smaller droplet volume (Figure 4.19b). This can be explained by the higher drying rate constant at high temperature and the effect of early onset of skin formation. At 20% solids, the skin tended to deform after bubble formation (Figure 4.20a), while the skin buckled prior to the bubble nucleation at 40% solids (Figure 4.20b). The skin layer appeared sooner at 40% solids leading to a rapid formation of rigid skin that eventually buckled. On the contrary, droplets containing 20% solids underwent a long shrinkage stage before the skin formation, thus the droplets' size was greatly reduced, and the droplets were heated up to the boiling temperature before the skin became rigid. Droplets prepared with MD7 showed a similar trend to those with MD12 at both solids concentrations (Figure 4.20). It was therefore concluded that the DE of MD had no impact on the occurrence of buckling and bubble formation, at least not in the range considered in this research.

Regardless of solids concentration, buckling and bubble formation seemed to occur concurrently when droplets dried at a higher temperature and/or contained a high amount of GA (showed in the dotted square in Figure 4.19 and Figure 4.20). Assessing their final morphology (Section 4.3.5.3), it was found that these droplets yielded smooth surface particles with one large vacuole. The immediate bubble nucleation would push the buckled skin back to its spherical shape, and as a consequence, a smooth-surface hollow particle was formed. In contrast, a later bubble formation would result in a greater deformation which eventually dried as a wrinkled surface hollow particle. For example, droplets containing 0GA:100MD12 dried at 80 and 100 ˚C, 25GA:75MD12 dried at 80 and 100 ˚C, and 50GA:50MD12 dried at 80 ˚C.

Inflation/deflation took place in several cycles during the drying process. This phenomenon involves vapour production and pressure increase in the wet core of the particle, dilative skin deformation with increased diameter (inflation) and skin disruption with vapour escape accompanied by reorganisation of the skin to a smaller diameter (deflation) (Tran et al., 2017). The inflation/deflation cycles are completed when the skin is thick enough to maintain the shape of the particle, which is referred to as the final crust formation. After this point, the wet core continued to dry to form fully dried particles.

The onset of final crust formation for droplets that were dried at 120 ˚C is shown in Figure 4.21. It is difficult to determine the final crust formation for the wrinkled particles, therefore it is not included in this research. Droplets with a higher ratio of GA and the higher of the two solids concentrations considered here had an earlier final crust formation, as having an early locking point resulted in faster skin hardening. When compared to the size at the locking point, particles with 20% solids experienced a greater shrinkage (~13%) than 40% solids (~8%). Particles containing only MD but of different DE reached the final crust at different times, although they had similar locking points. This could be explained by a greater buckling of MD12 than MD7, as will be discussed later. The comparatively large surface area resulted in faster drying of the skin.

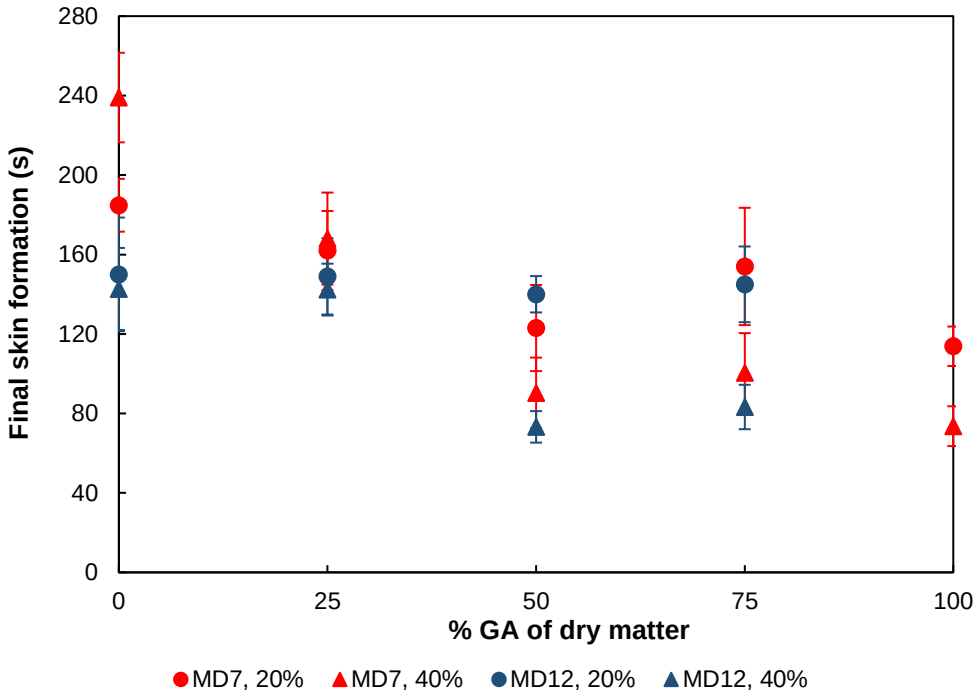

Figure 4.21 The onset of final crust formation for droplets containing different solids concentrations and DE-values of MD. Solids concentration: 20% w/v (circles) and 40% w/v (triangles); DE-value of MD: MD7 (red) and MD12 (blue). Droplets had an initial volume of 2 µl and were dried at 120 °C.

Skin formation is the key factor in the morphology development of a drying droplet (Both et al., 2018a). The rigidity of the skin determines the final particle morphology (Both et al., 2019a). The degree of buckling could give an indication of the strength of the developed skin. In the following, the effect of each individual parameter on the drying behaviour and the morphological development of drying droplets will be highlighted:

Droplets dried at 80 °C were selected for investigating the impact of GA:MD on the morphology development during drying. In Figure 4.11 five time series of drying droplets at different compositions of GA:MD (30% total solids) are shown. At first, an ideal shrinkage (retaining spherical droplet shape) with no influence of the compositional ratio was observed. This was followed by the skin

formation. Droplets higher in GA had an earlier locking point (94 s for 0:100, 81 s for 25:75, 65 s for 50:50, 56 s for 75:25 and 59 s for 0:100 GA:MD12) at a larger droplet radius as a result of the lower diffusion coefficient of GA molecules (and hence higher Peclet number) compared to MD12 molecules (Table 4.3). Once the skin was formed, the droplets evolved in different ways depending on the properties of the skin. Droplets buckled nearly at the same time, except for GA droplet that buckled earlier. An increase in the GA resulted a faster bubble formation (120 s for 0GA:100MD12 and 91 s for 100GA:0MD12). The shape of the skin after the locking point varied with GA:MD. Droplets with more MD appeared crumpled (Figure 4.11a-b), which was indicative of a thin and weak skin (Sugiyama et al., 2006; Tsapis et al., 2005), leading to wrinkled particles at the end of the drying process. On the other hand, the surface of droplets that contained more GA than MD only buckled at a few points as a result of an apparently much more elastic and thicker skin (Figure 4.11d-e), leading to the formation of smooth surface, thus hollow particles. The viscosity of a GA solution is much higher than that of a MD solution (Table 4.2), therefore it is likely GA droplet reached the critical skin rigidity sooner in the drying process, resulting in a more stable skin that can resist against surface stresses. In contrast, viscosity at the surface of MD droplet increased slowly during drying and developed a skin that more susceptible to surface deformation. Indeed, MD12 solution has been shown to still behave liquid-like when concentrated to 70% (w/w) (Both et al., 2019a).

The influence of the drying temperature was investigated for droplets composed of 25GA:75MD12 (30% total solids) applying drying temperature of 80 °C (Figure 4.11b), 100 °C (Figure 4.12b) and 120 °C (Figure 4.13b). The duration

of the constant rate period became shorter as the drying temperature increased: the locking point was 81 s at 80 °C, 56 s at 100 °C and 43 s at 120 °C. However, the droplets attained the locking point at a similar radius, around 93% of their initial radius. At 80 °C, the skin started to crumple at 123 s and a bubble formed at 209 s. Meanwhile, droplets dried at 120 °C had an early onset of buckling (at 60 s) with immediate bubble formation at 64 s, as having a greater drying rate constant. At the end of the drying, a wrinkled particle was formed at 80 °C, whereas a smooth surface particle was produced at 120 °C due to the faster expansion of the bubbles that push the surface outward and assume a spherical shape. It can therefore be concluded that the production of smooth surface hollow particles requires a high drying temperature.

Figure 4.25 shows images of 0GA:100MD12 and 50GA:50MD12 droplets with initial droplet volumes of 1 and 3 µl, dried at 100 °C (30% total solids). Both droplets had a comparable drying rate constant, irrespective of their composition and initial volume. Therefore, the larger droplets had a later locking point than the smaller droplets: 106 s (0GA:100MD12) and 84 s (50GA:50MD12) at 3 µl droplets; 66 s (0GA:100MD12) and 50 s (50GA:50MD12) at 1 µl droplets. A prolonged constant rate period permitted for the further evaporation to take place, hence the larger droplets (of the same composition) were locked at a very similar relative remaining radius as the small ones (~87% of the initial radius for 0GA:100MD12 droplets and ~91% of the initial radius for 50GA:50MD12 droplets). Both buckling and bubble appeared faster in the droplets that had smaller initial volume. At the end of drying, similar surface morphologies were obtained from two different initial droplet volumes of the same droplet composition; wrinkled particles for 0GA:100MD12 and smooth

surface particles for 50GA:50MD12. However, larger particles were produced at the larger initial volume.

Figure 4.23 to Figure 4.26 exhibit the drying of droplets of a mixture of GA and MD7 or MD12 at solids concentration of 20 and 40%. An example of 50GA:50MD7 droplets containing 20 and 40% solids (Figure 4.23c and Figure 4.24c, respectively) was chosen to at first demonstrate the effect of solids concentration on the morphology development. Initially, the droplets were constantly shrinking until locking. Droplet with the higher solids content reached the locking point earlier (42 s) and at larger droplet radius (95% of the initial radius) compared to the droplet that was lower in solids (locked at 66 s with 89% of the initial radius). Unlike droplets containing 30% and 40% solids, the skin of the droplet with 20% solids deformed (at 104 s) after the bubble nucleation (at 76 s). This implied that the wet core temperature was higher at lower solids concentration. Eventually, smooth surface particles were obtained at both solids concentrations, but droplet that initially contained more solids content formed a larger particle as a result of the earlier onset of skin formation and thus at larger relative droplet radius.

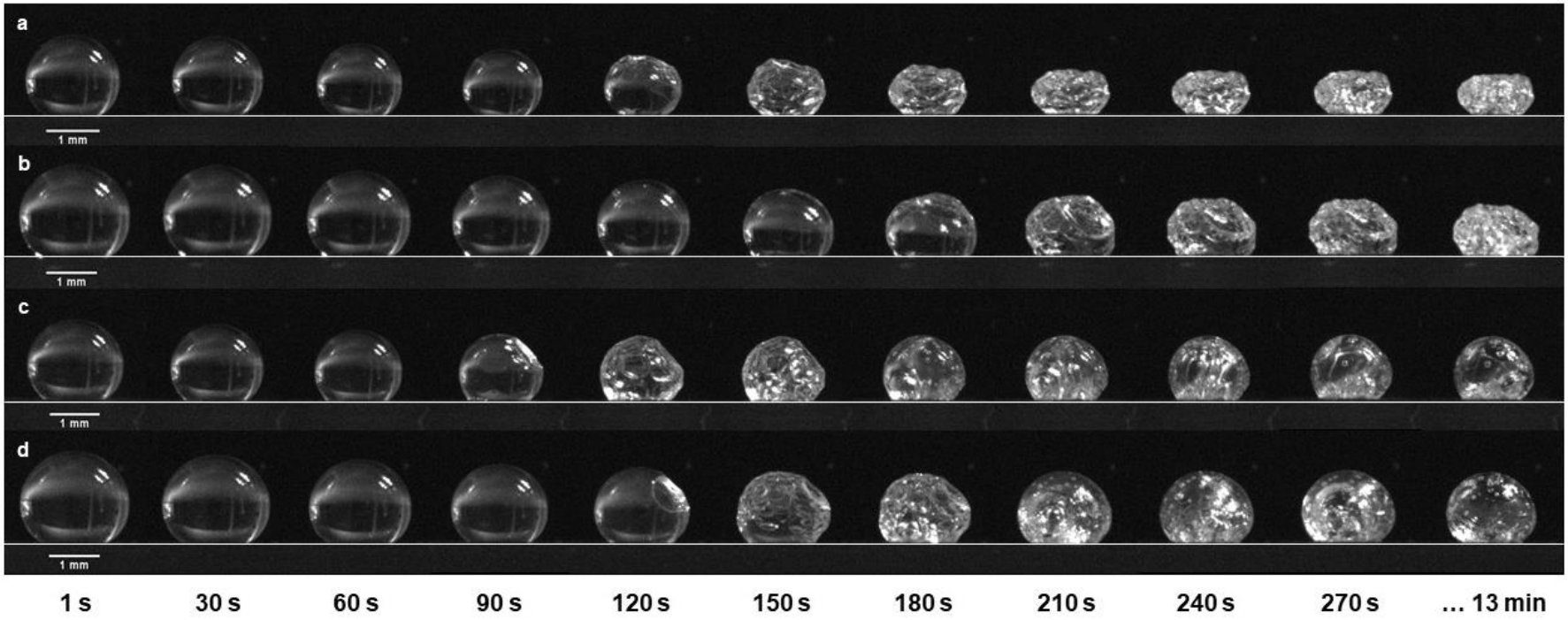

Figure 4.22 Time series of droplets with different initial volumes and compositions of GA:MD12: (a) 1 µl, 0:100; (b) 3 µl, 0:100; (c) 1 µl, 50:500; (d) 3 µl, 50:50. Droplets had an initial total solids content of 30% w/v and were dried at 100 °C.

To demonstrate the influence of the DE-value of MD on morphology changes during drying, the drying of a droplet containing only MD7 (Figure 4.23a) and MD12 (Figure 4.25a) respectively at 20% solids concentration are contrasted in the following. Initially, droplets remained liquid and shrank in a homogeneous way. Both droplets attained the locking point at the same time (at around 83 s) and at similar droplet radius (approximately 85% of their initial radius). Then, followed by a simultaneous skin buckling and bubble nucleation (at 105 s). During the drying, the surface of the MD12 droplet crumpled, while the surface of the MD7 droplet buckled. Hence, the DE of MD appeared to affect the material properties of the skin with MD7 leading to a stronger skin than MD12. This observation was supported by Siemons et al. (2020), who observed steeper increase in viscosity upon concentration of MD DE 5 solution compared to MD DE 12, thereby the droplet acquired elasticity sooner in the drying process. Consequently, a smooth surface was obtained from MD7 and a wrinkled particle was produced by MD12 at the end of drying. Similar results were obtained for MD7 (Figure 4.24a) and MD12 (Figure 4.26a) at 40% solids.

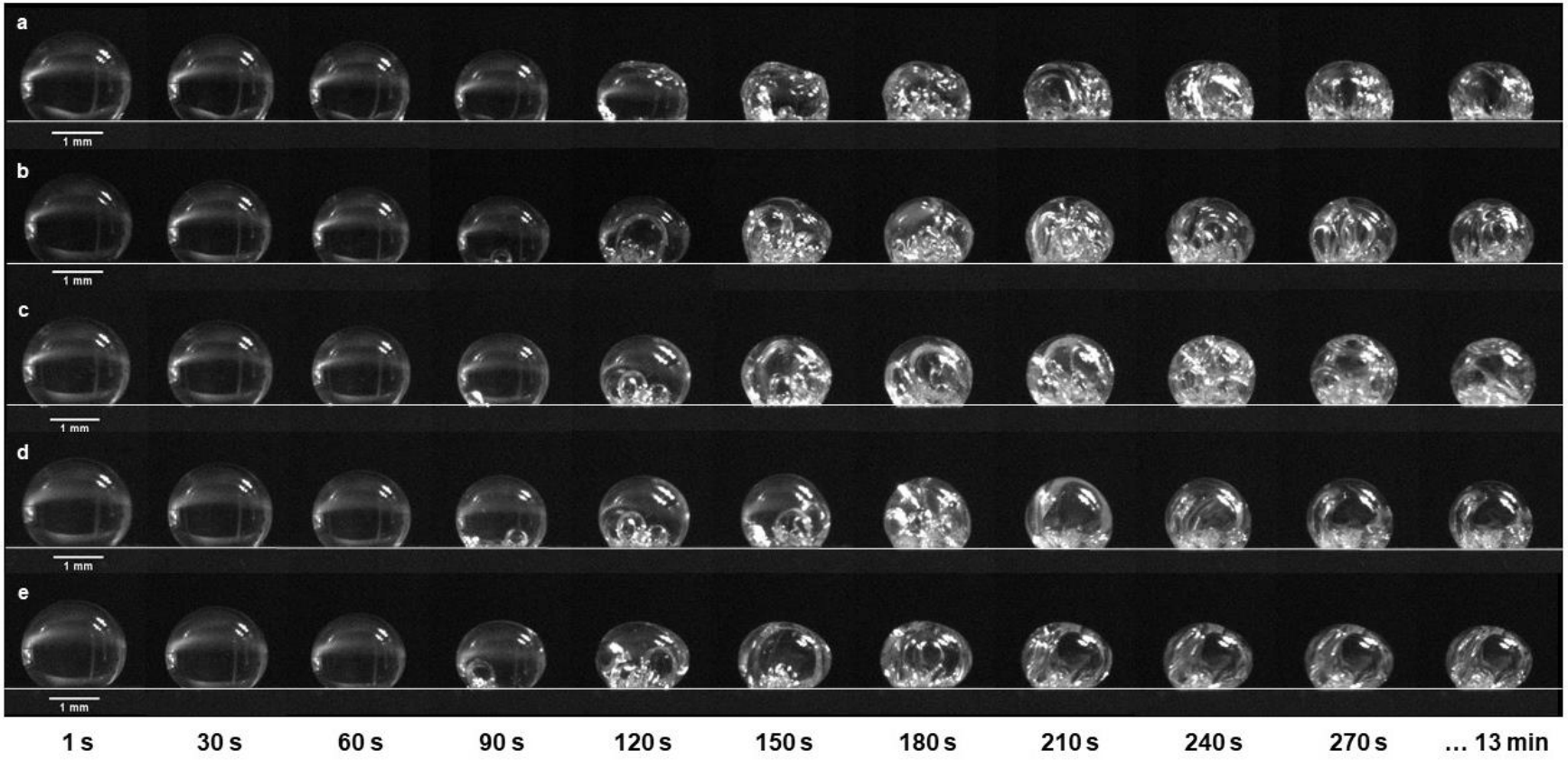

Figure 4.23 Time series of droplets with different compositions of GA:MD7 at 20% solids concentration: (a) 0:100, (b) 25:75, (c) 50:50, (d) 75:25, and (e) 100:0. Droplets had an initial volume of 2 µl and were dried at 120 °C.

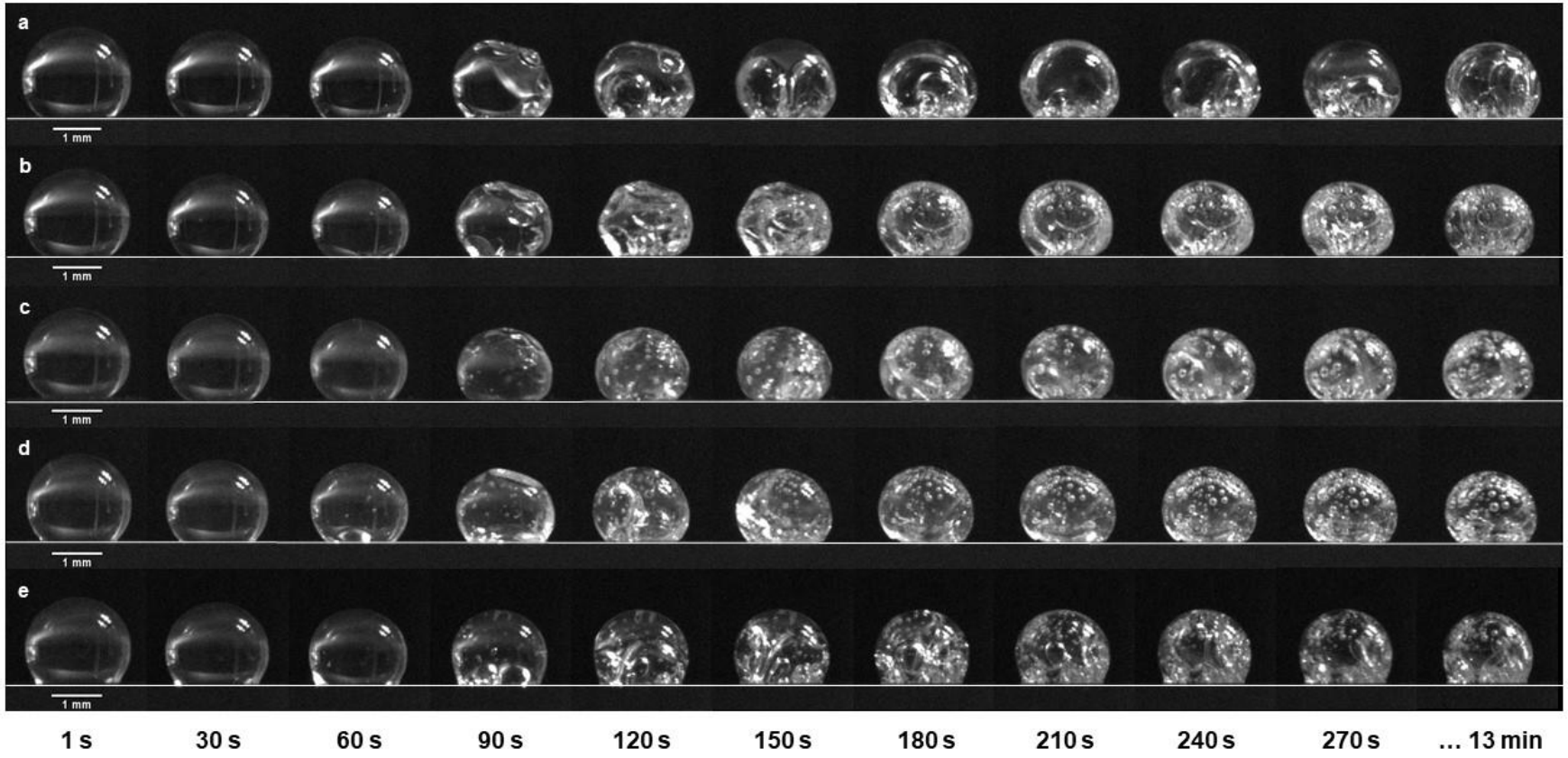

Figure 4.24 Time series of droplets with different compositions of GA:MD7 at 40% solids concentration: (a) 0:100, (b) 25:75, (c) 50:50, (d) 75:25, and (e) 100:0. Droplets had an initial volume of 2 µl and were dried at 120 °C.

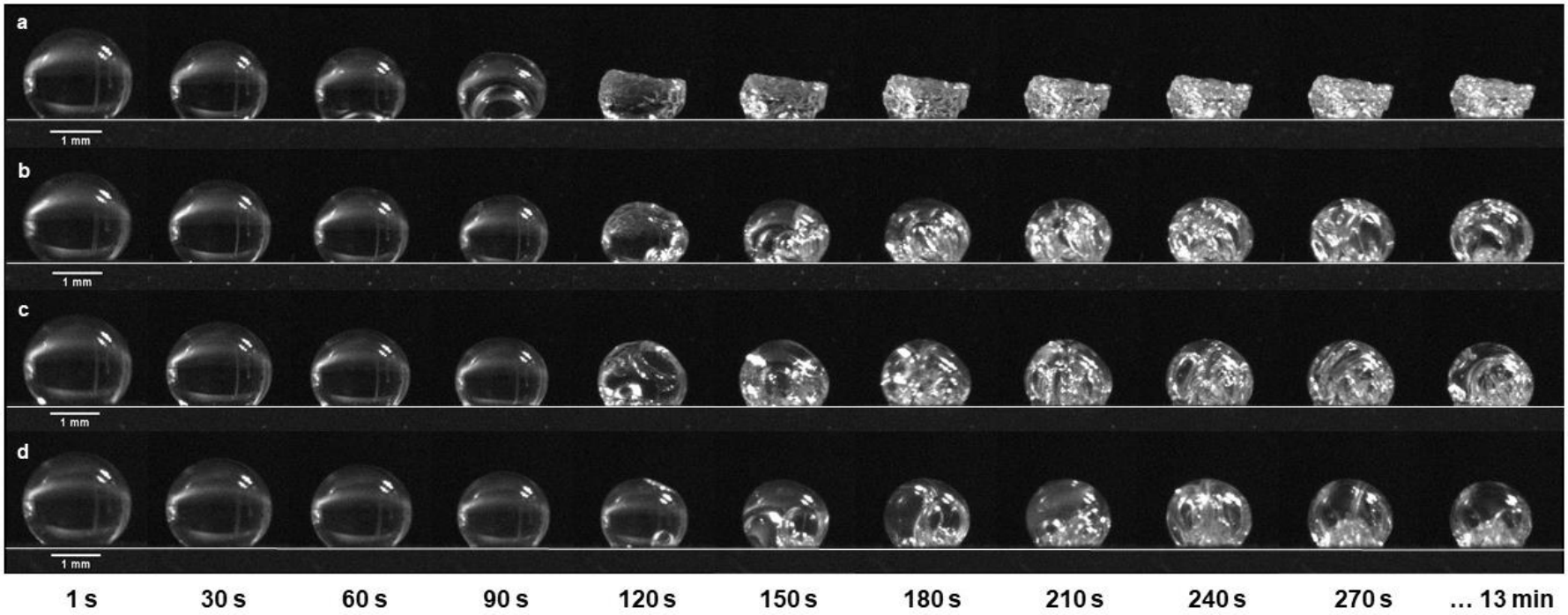

Figure 4.25 Time series of droplets with different compositions of GA:MD12 at 20% solids concentration: (a) 0:100, (b) 25:75, (c) 50:50, and (d) 75:25. Droplets had an initial volume of 2 µl and were dried at 120 °C.

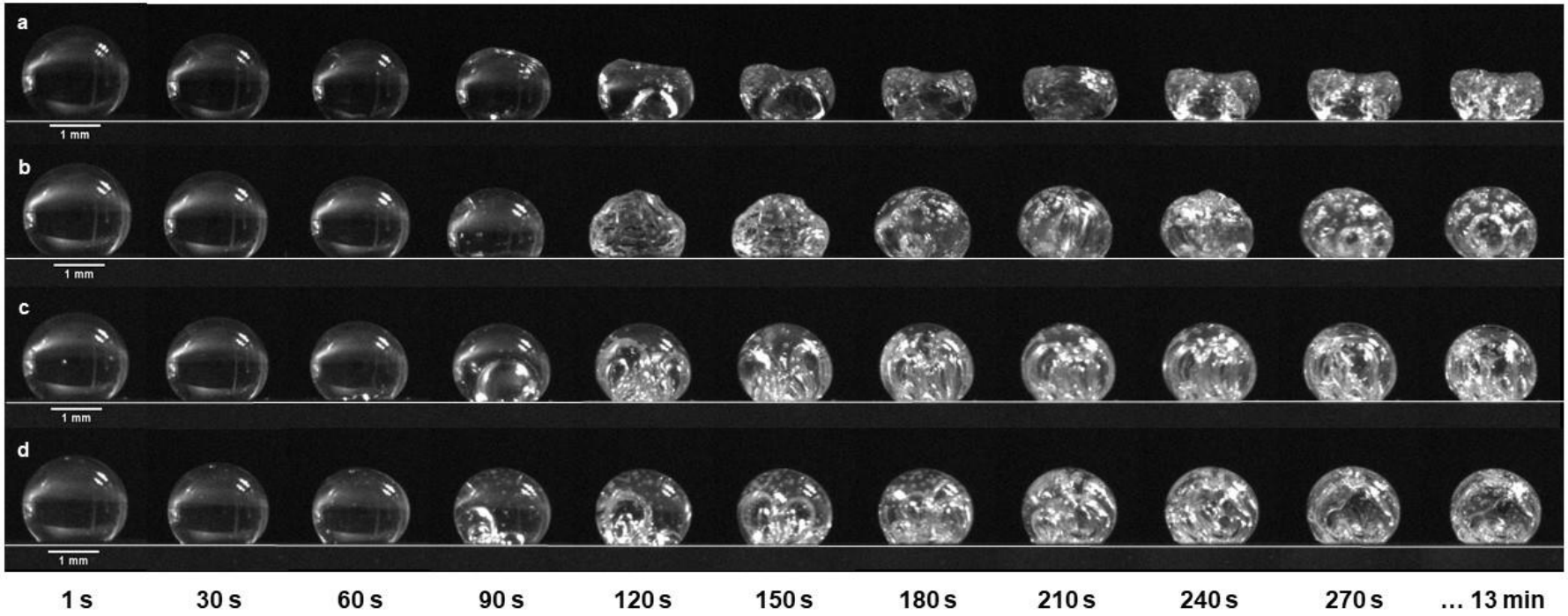

Figure 4.26 Time series of droplets with different compositions of GA:MD12 at 40% solids concentration: (a) 0:100, (b) 25:75, (c) 50:50, and (d) 75:25. Droplets had an initial volume of 2 µl and were dried at 120 °C.

4.3.5.3 Final particle morphology

Final particle morphologies were visualised by micro-CT (Figure 4.27 to Figure 4.31) and SEM (Figure 4.32 and Figure 4.33) to examine their surface and internal structure, respectively. Four types of particle morphologies were obtained from the drying: smooth surface particles with one large vacuole, wrinkled surface particles with one large vacuole, wrinkled surface particles with multiple small vacuoles and wrinkled surface solid particles. Similar to the previous observation of morphology of spray dried particles in Chapter 3, smooth surface particle morphology is indicative of the presence of one large vacuole.

The micro-CT images in Figure 4.27 and Figure 4.28 illustrate the influence of droplet composition and drying temperature on particle morphology. The final morphologies obtained here exhibited a transition from a wrinkle to a smoother surface with an increase in the GA ratio. GA provided the skin with rigidity and eventually led to the formation of hollow particles with a smooth surface. Nonetheless, Zhang et al. (2019) obtained a wrinkled with several vacuoles from SDD of GA. In comparison with the particle obtained in this research, the different internal structure indicates that the droplet underwent a slower drying process even though it had comparable droplet volume (2 µl) and drying temperature (90 °C). The addition of MD polymers seemed to weaken the gel network formed by GA, thus developed a skin with inadequate elasticity to withstand stresses exerted on the droplet surface, and subsequently formed wrinkled particles. Such behaviour of MD was previously observed during SDD of mixed MD with whey protein (Both et al., 2018a, 2018b).

The impact of drying temperature can be observed clearly for 25GA:75MD12 and 50GA:50MD12 particles. As the drying temperature increased, the droplets showed a transition from a wrinkled to a smoother surface with one large vacuole. This observation was found to be similar to other researchers (Gouaou et al., 2018; Tran et al., 2016). As previously described, a higher drying rate constant at high temperature caused faster bubble nucleation and led to the formation of smoother particles. However, a contradictory result was reported by Both et al. (2018a) for particles containing 50% MD and 50% whey protein. A lower drying temperature had allowed for extensive phase separation, which resulted in more whey protein enrichment at the droplet surface, thereby providing the skin strength and leading to the formation of smooth hollow particles. When spray drying oil-in-water emulsions with GA and MD, Munoz-Ibanez et al. (2016) observed a thicker surface layer of GA with an increase in particle size as a result of a slower drying rate.

For MD droplets, it was wrinkled and had multiple smaller vacuoles when dried at 80 °C, but formed a smooth surface with one large vacuole at 120 °C. This is in good agreement with earlier observations in laboratory spray drying experiments (Alamilla-Beltrán et al., 2005). In SDD, Siemons et al. (2020) obtained a similar dented particle after drying MD DE 12 at 60 °C. The internal morphology obtained at low temperature is well in line with the work by Both et al. (2018a) who observed 6 vacuoles in SDD of 99% MD12 and 1% whey protein at 90 °C. A later and slower bubble formation at low temperature, combined with an increase in the viscosity of the bulk solution, prevented extensive bubble coalescence from occurring.

In some cases, two different morphologies were observed for different individual particles dried at the same conditions. A smooth and wrinkled surface particle was obtained after drying 0GA:100MD12 at 120 °C (Figure 4.27c-i) and 75GA:25MD12 at 80 °C (Figure 4.27a-iv). It happened due to these conditions were close to the transition. A small variation in, for example, initial size, contact angle with the hydrophobic surface and drying conditions, can give rise to sufficiently different skin properties during drying, hence different particle morphology (Both et al., 2018a). It is therefore expected that 0GA:100MD12 will form a smooth surface with one large vacuole when drying the droplet above 120 °C, while a wrinkled surface will be produced by 75GA:25MD12 at a drying temperature below 80 °C.

The final particle morphologies at different initial droplet volumes are demonstrated in Figure 4.29. Again, GA has proved to play a key role in the development of a smooth-surface hollow particle. For 50GA:50MD12, the initial volume of the droplets had no influence on the particle morphology, which produced smooth surface particles with one large vacuole. On the other hand, 0GA:100MD12 droplets formed a similarly wrinkled surface but with different internal structure depending on the initial volume. A large vacuole was created at 1 µl droplet volume, while a solid particle formed at 3 µl droplet volume. During the constant rate period, both droplets had comparable drying rates, but the drying rate of the smaller droplet seemed higher during the falling rate period as a consequence of early skin formation. This difference then led to the formation of a vacuole in one case and a solid particle in the other case.

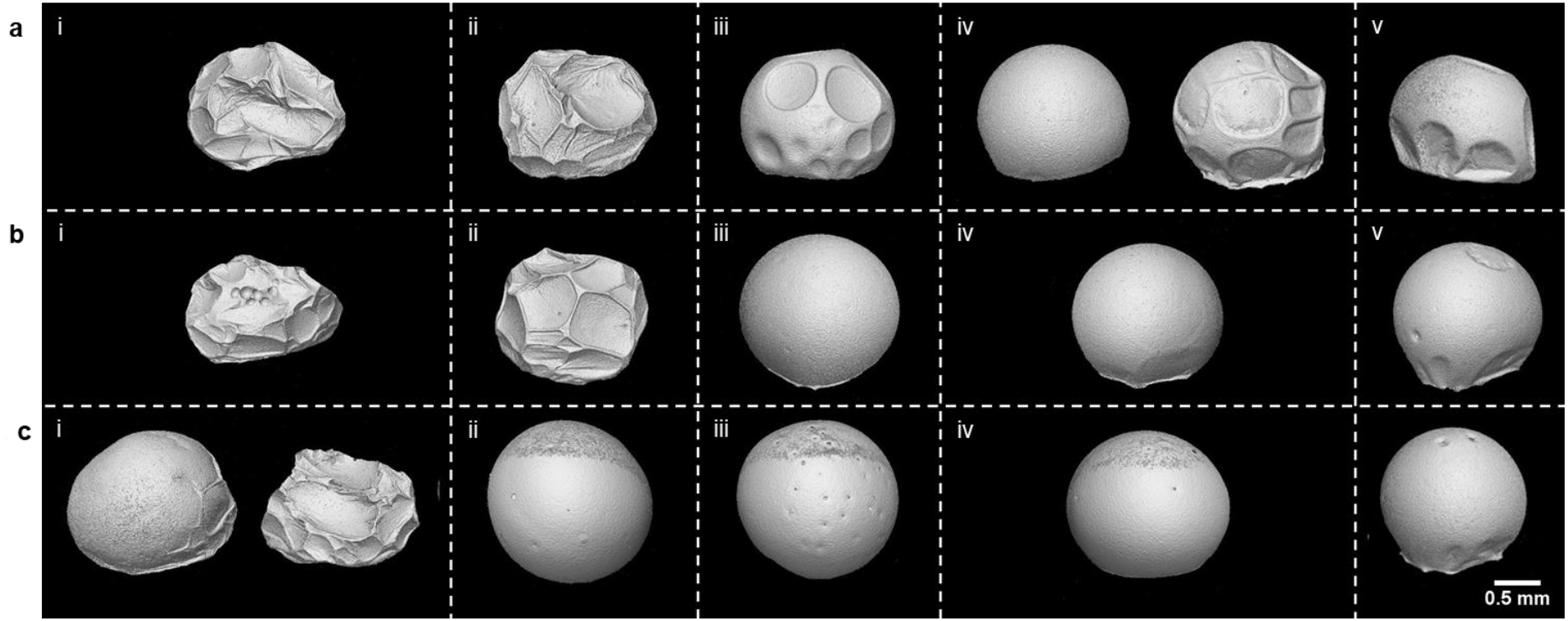

Figure 4.27 Front view images of micro-CT of final particles with varied drying temperature: (a) 80 °C, (b) 100 °C, (c) 120 °C, and composition of GA:MD12: (i) 0:100, (ii) 25:75, (iii) 50:50, (iv) 75:25, (v) 100:0. Droplets had an initial total solids content of 30% w/v and initial droplet volume of 2 µl.

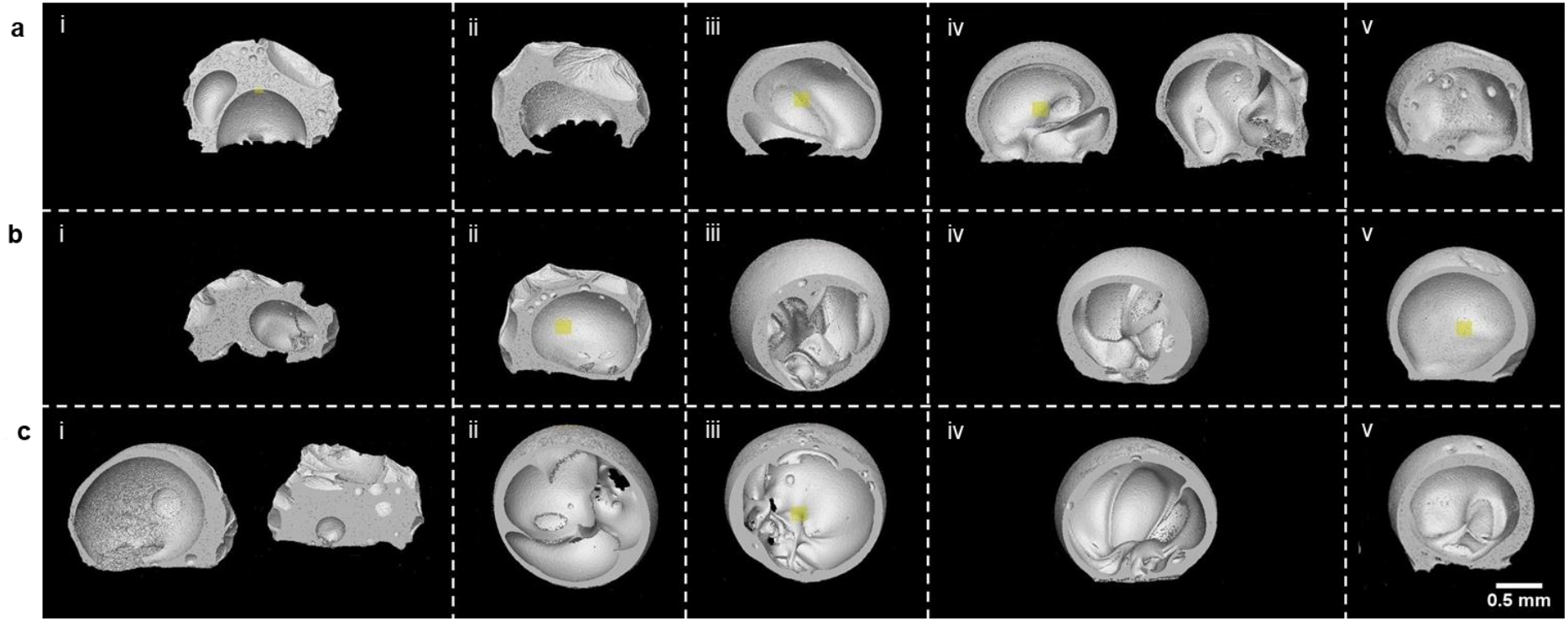

Figure 4.28 Cross-section images of micro-CT of final particles with varied drying temperature: (a) 80 °C, (b) 100 °C, (c) 120 °C, and composition of GA:MD12: (i) 0:100, (ii) 25:75, (iii) 50:50, (iv) 75:25, (v) 100:0. Droplets had an initial total solids content of 30% w/v and initial droplet volume of 2 µl.

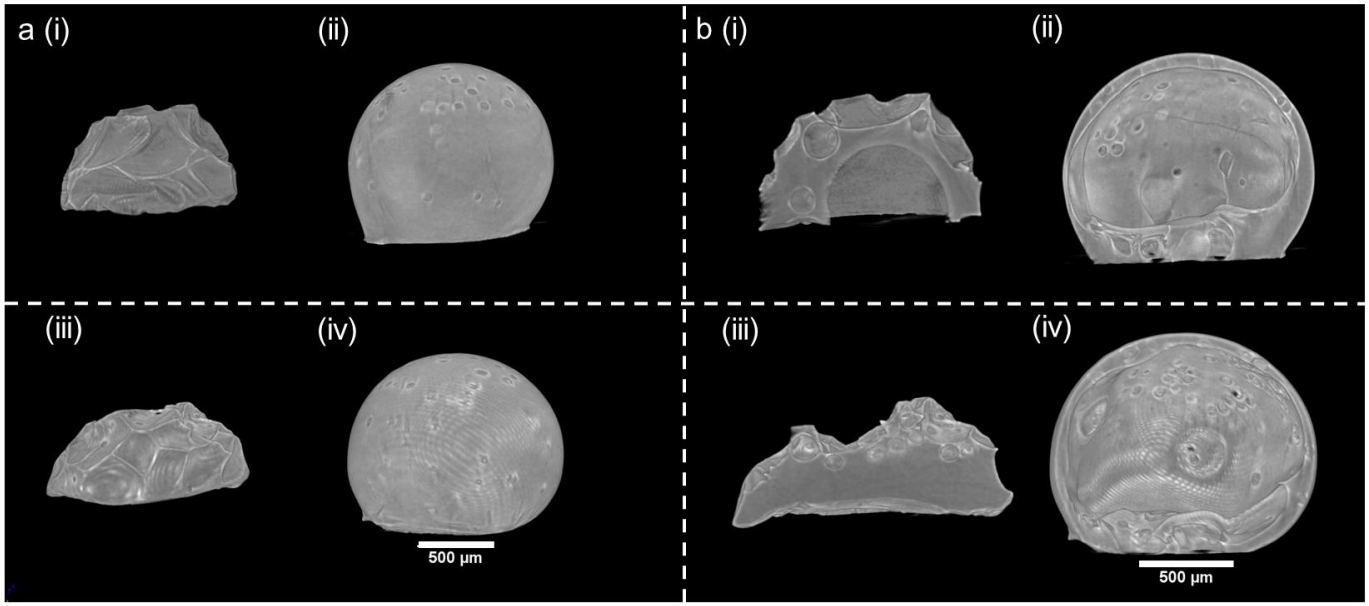

Figure 4.29 Micro-CT images of final particles with (a) front view and (b) cross-section, with varied droplet volume and composition of GA:MD12: (i) 1 µl, 0:100; (ii) 1 µl, 50:50; (iii) 3 µl, 0:100; (iv) 3 µl, 50:50. Droplets had an initial total solids content of 30% w/v and were dried at 100 °C.

The influence of the solids concentration and DE-value of MD on the final particle morphology can be seen in micro-CT (Figure 4.30 and Figure 4.31) and SEM (Figure 4.32 and Figure 4.33) images. Apparently, a high drying temperature diminished any impact of solids concentration and DE of MD. All formulations produced smooth spherical particles with one large vacuole. The exception were the previously discussed particles containing only MD12 that had either a wrinkled or smooth surface with a single vacuole. The observation that a different DE of MD led to different particle morphologies is in accordance with results obtained by Siemons et al. (2020), in which MD DE 5 formed a smooth particle with large cavity, while MD DE 12 produced a dented particle after drying at 90 °C. The authors speculated that the skin of MD DE 12 behaved like a rubbery material for a longer time during drying compared to MD DE 5, thus resulting in more surface instabilities. They also observed dented morphologies for MD DE 21, DE 29 and DE 38. A SDD study by Zhang et al. (2019) reported that particle MD DE 10-13 displayed irregular wrinkles with small vacuoles, whereas a relatively smooth surface dense particle was produced by MD DE 17-20.

When dried at 120 °C, solids concentration had no obvious impact on the surface and the internal morphology of the particles. However, particles containing more solids had larger diameters and thicker shells than those with less solids (Table 4.6). The skin of droplets with 40% solids appeared sooner in the drying process (Figure 4.18), meaning the fixation of a larger surface area of the droplet. The shell became thicker as solutes continued to precipitate at the internal surface of the droplet. Lin and Gentry (2003) found that increasing the initial solute concentration of sodium chloride and ammonium chloride in

their droplet solutions led to larger SDD particles. A thicker shell with increasing initial concentration was reported for single dried whey protein (Sadek et al., 2013) and hydroxypropylated pea starch (Gouaou et al., 2018).

Table 4.6 Diameter of dried particles and thickness of shells as measured from micro-CT and SEM images. The values reported based on single measurements.

Sample (GA:MD)		Diameter (µm)		Shell thickness (µm)	
		Micro-CT	SEM	Micro-CT	SEM
MD7, 20% solids	0:100	1284	1714	152	51
	25:75	1292	1829	57	47
	50:50	1365	1708	79	71
	75:25	1336	1678	109	72
	100:0	1241	1670	77	73
MD7, 40% solids	0:100	1490	2094	141	135
	25:75	1511	1927	95	140
	50:50	1403	1969	114	125
	75:25	1353	1923	171	146
	100:0	1093	1871	143	132
MD12, 20% solids	0:100	1233	1912	83	39
	25:75	1288	1897	90	73
	50:50	1313	1840	98	70
	75:25	1305	2026	82	56
MD12, 40% solids	0:100	1398	1965	307	96
	25:75	1537	2053	157	97
	50:50	1438	1859	89	52
	75:25	1327	1674	122	121

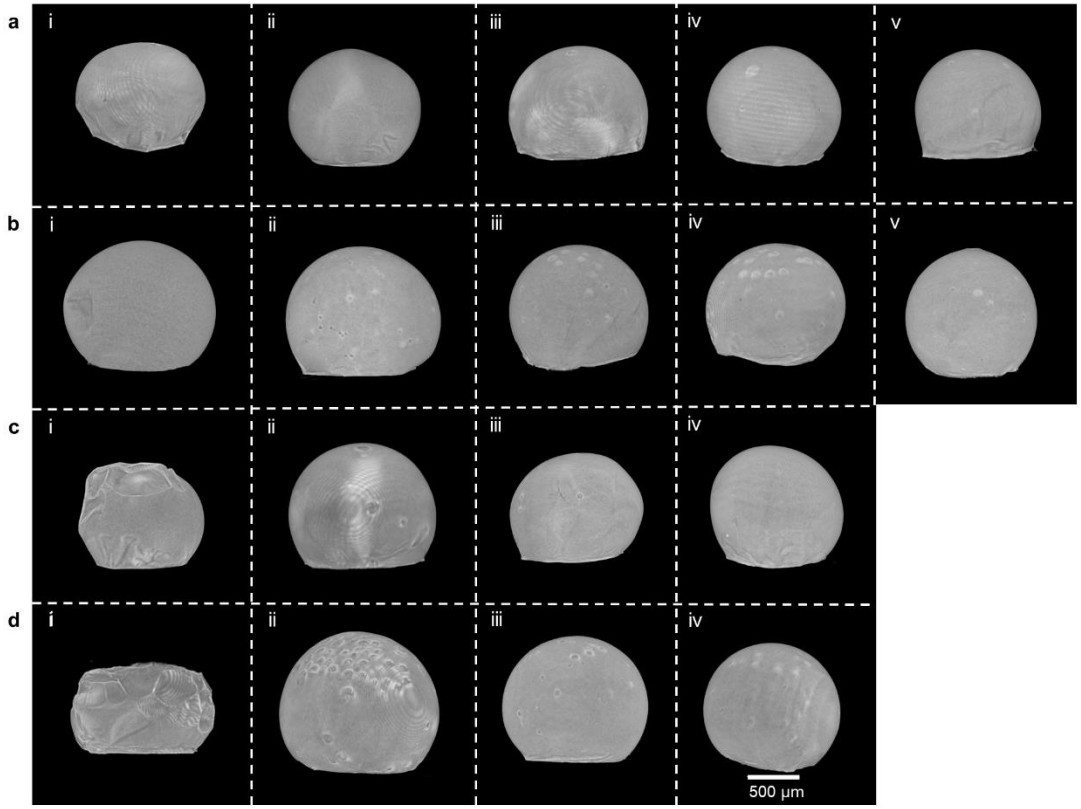

Figure 4.30 Front view images of micro-CT of final particles with varied DE-value of MD and solids concentration: (a) MD7 & 20%, (b) MD7 & 40%, (c) MD12 & 20%, and (d) MD12 & 40%, at different compositions of GA:MD: (i) 0:100, (ii) 25:75, (iii) 50:50, (iv) 75:25, and (v) 100:0. Droplets had an initial volume of 2 µl and were dried at 120 °C.

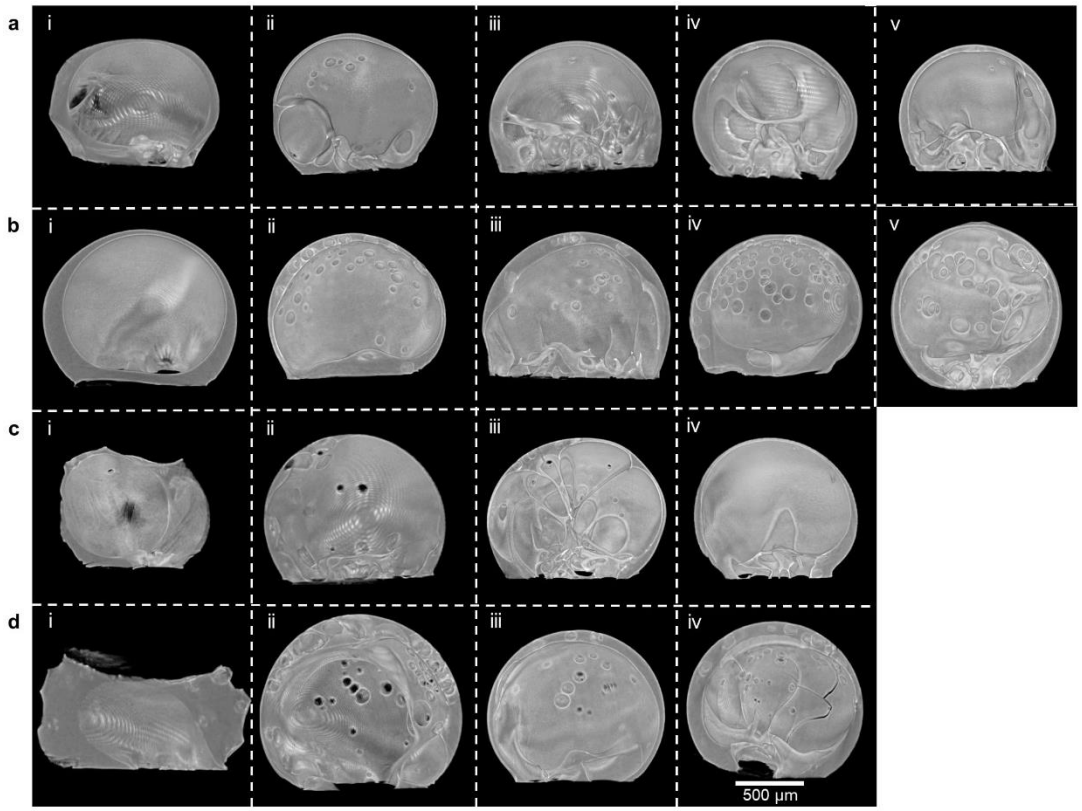

Figure 4.31 Cross-section images of micro-CT of final particles with varied DE-value of MD and solids concentration: (a) MD7 & 20%, (b) MD7 & 40%, (c) MD12 & 20%, and (d) MD12 & 40%, at different compositions of GA:MD: (i) 0:100, (ii) 25:75, (iii) 50:50, (iv) 75:25, and (v) 100:0. Droplets had an initial volume of 2 µl and were dried at 120 °C.

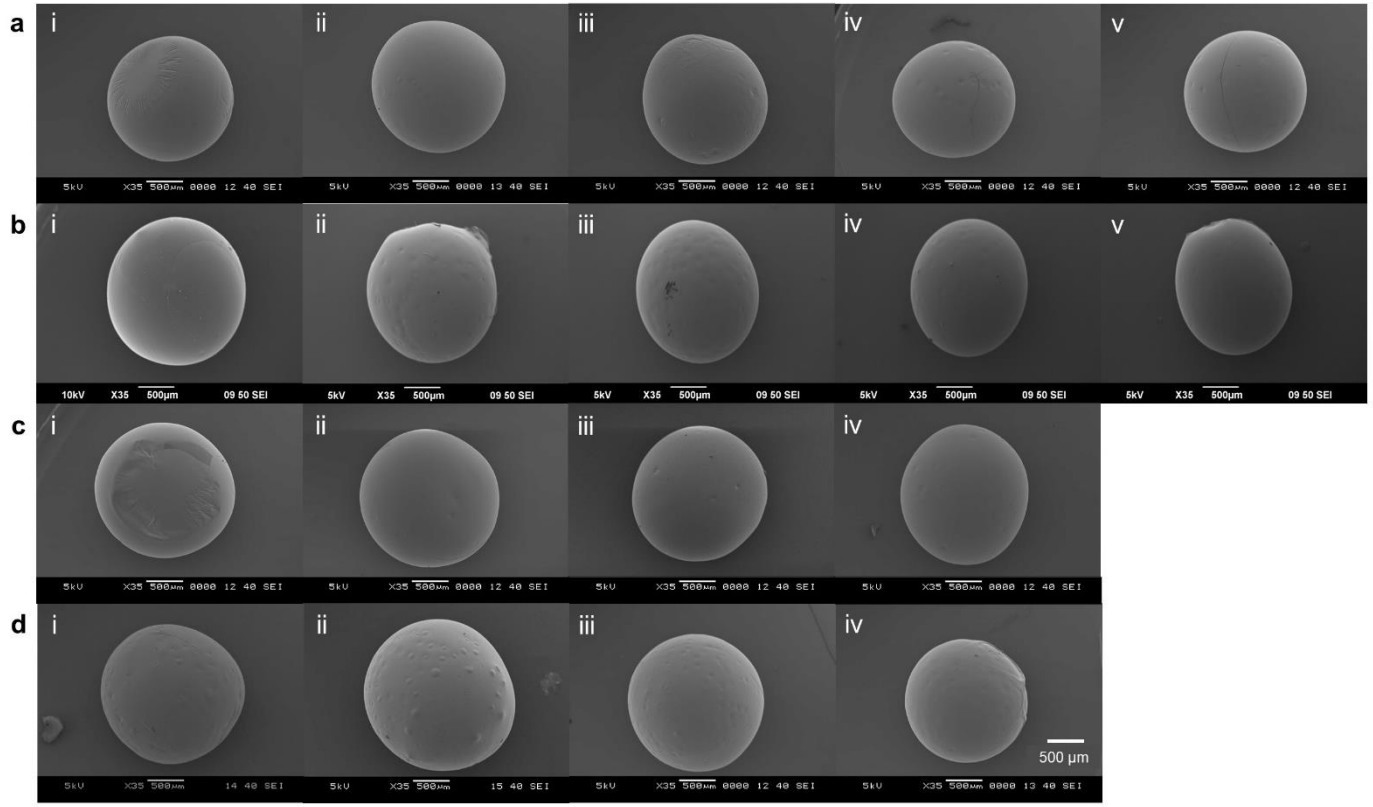

Figure 4.32 SEM images of whole particles with varied DE-value of MD and solids concentration: (a) MD7 & 20%, (b) MD7 & 40%, (c) MD12 & 20%, and (d) MD12 & 40%, at different compositions of GA:MD: (i) 0:100, (ii) 25:75, (iii) 50:50, (iv) 75:25, and (v) 100:0. Droplets had an initial volume of 2 µl and were dried at 120 °C.

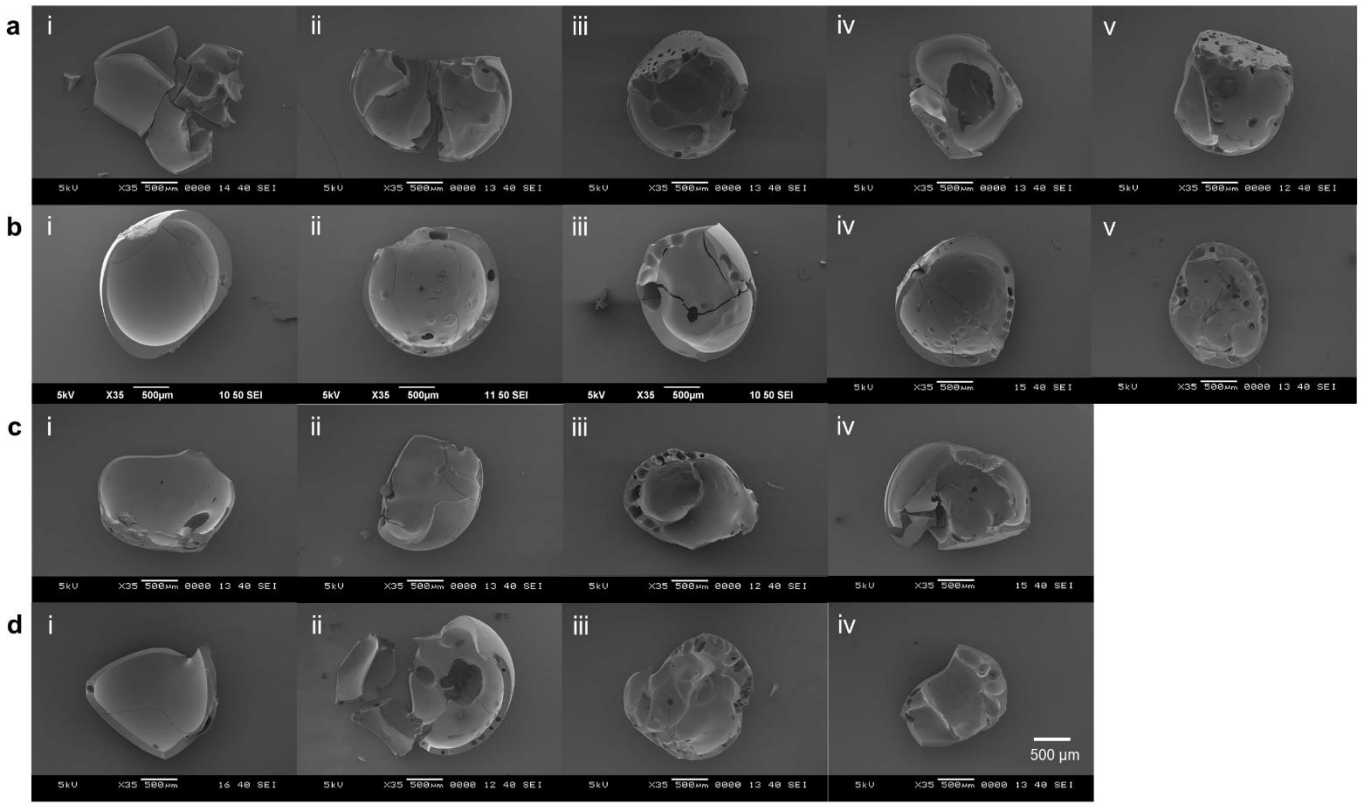

Figure 4.33 SEM images of fractured particles with varied DE-value of MD and solids concentration: (a) MD7 & 20%, (b) MD7 & 40%, (c) MD12 & 20%, and (d) MD12 & 40%, at different compositions of GA:MD: (i) 0:100, (ii) 25:75, (iii) 50:50, (iv) 75:25, and (v) 100:0. Droplets had an initial volume of 2 µl and were dried at 120 °C.

The morphology of particles obtained in the SDD experiments was compared with the morphology of the spray dried powders produced in the first stage of this PhD research (Section 3.3.1). Particles dried at the two different drying scales containing the same compositional ratio, solids concentration and DE of MD produced quite similar particle morphologies consisting of smooth surface particles with one vacuole and wrinkled surface particles with either one vacuole or solid. However, none of the spray dried powders displayed wrinkled particles with multiple small vacuoles as observed in SDD of MD12 at 80 °C. SDD particles tended to form vacuoles rather than solid as having higher drying rate (Peclet number between 105 and 152) compared to spray drying systems (Peclet number between 0.4 and 0.7).

Regarding the effect of the compositional ratio, an increase in the GA in the spray drying droplets had resulted in a lower fraction of smooth-surface hollow particles, which in contradiction to the SDD results. Three possible reasons could be offered to explain the differences in the particle morphologies produced in both drying systems. First, the different droplet sizes in spray drying and SDD may be a factor in the different effect of GA content on particle smoothness. Second, droplets contained higher ratios of GA were dried at a slower rate due to larger droplet formation during atomisation process and thus yielded wrinkled hollow or wrinkled solid particles, as discussed in Section 3.3.1. Another reason could be related to the early locking and formation of more elastic skin by the droplets richer in GA, which might cause denting when particles collided with one another. Results from SDD experiments suggest that the spray drying process should be performed at higher temperature and lower feed rate in order

to increase the drying rate and thus produce more smooth surface hollow particles.

Both droplet compositions (ratio of GA:MD, solid concentration and DE-value of MD) and processing conditions (drying temperature and droplet volume) played important roles in determining the drying rate as well as the shape and size of the dried particles. Overall, the morphology development during drying of GA:MD droplets was governed by the mechanical strength of the skin and the rate of the drying process, as summarised in Figure 4.34. A high ratio of GA, high solids and a low DE of MD provided strength to the skin that was then more stable against surface compression and thus developed a smooth shaped particle. Fast bubble nucleation at high drying temperature and smaller droplet volume led to the formation of a large vacuole in the particle. The opposite conditions would form a weak skin that could not resist the surface stresses developed during drying, leading to a wrinkled particle with a solid interior.

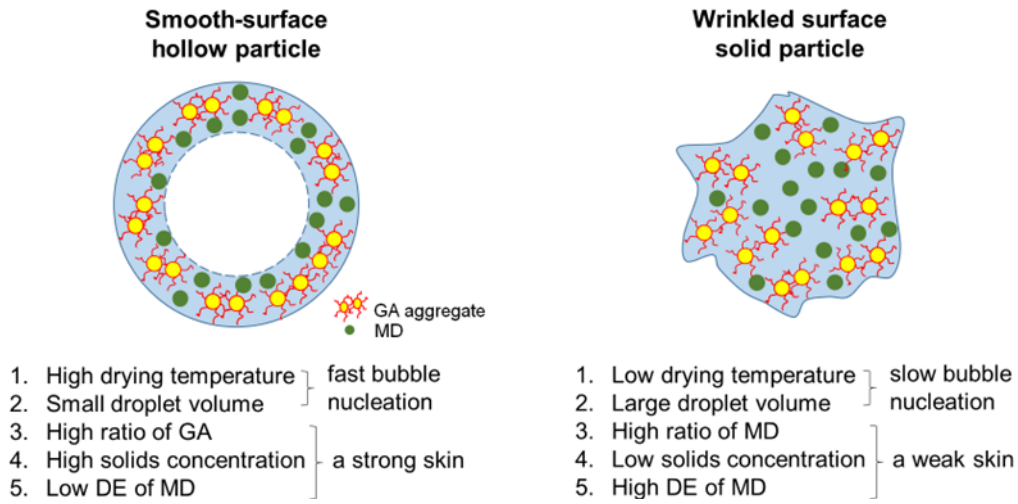

Figure 4.34 Influence of droplet compositions and processing parameters on final particle morphology.

4.3.6 Wettability and dissolution of dried particles

The wettability of the dried particles was analysed by attaching a water droplet to the surface of the particle. The degree of the apparent water droplet coverage on the dried particle was measured using the APCA measurements, see Figure 4.35 for the two examples of actual data taken. The APCA values, presented in Figure 4.36, were then used as an indicator of the degree of wettability.

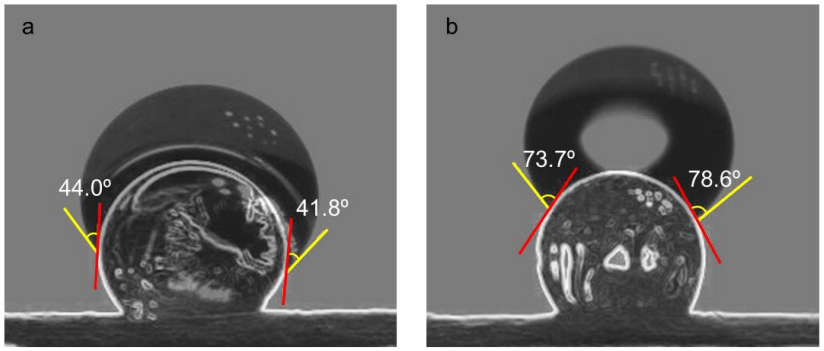

Figure 4.35 APCA measurement of particles: a) 0GA:100MD7 and b) 75GA:25MD7 (at 40% solids concentration).

The values ranged between 34.6 and 76.2°, but all were below 90° which would relate be the characteristic of a hydrophobic surface. Overall, the values steadily increased with an increase of GA in the droplet solution though, indicating that the surface became increasingly hydrophobic owing to the amphiphilic character of GA. The wettability measurement with the small water droplet (0.5 µl) displayed a similar trend to the large one (1.5 µl). Interestingly, particles that contained 75% GA exhibited similar contact angles to those with 100% GA. In Chapter 3 it was reported that the wetting time of spray dried powders increased with increasing GA due to the accumulation of GA at the particle surface, evidenced by XPS. Those data revealed that surface coverage at 75% and 100% GA was similar, meaning that a maximum surface coverage with GA

seemed to have been reached for 75% GA. This situation is reflected in the APCA data here.

Initial solids concentration and DE value of MD were found not to impact on the particle wettability, except for particles with only MD. At both solids concentration, particles prepared with only MD7 had a larger APCA compared to MD12. This behaviour could be associated with MD7 that being slightly hydrolysed, thus containing a larger fraction of high molecular weight polysaccharide than MD12 and became less dissolve in water. Takeiti et al. (2010) also observed a decrease in wetting time with the increase in the degree of hydrolysis of starch.

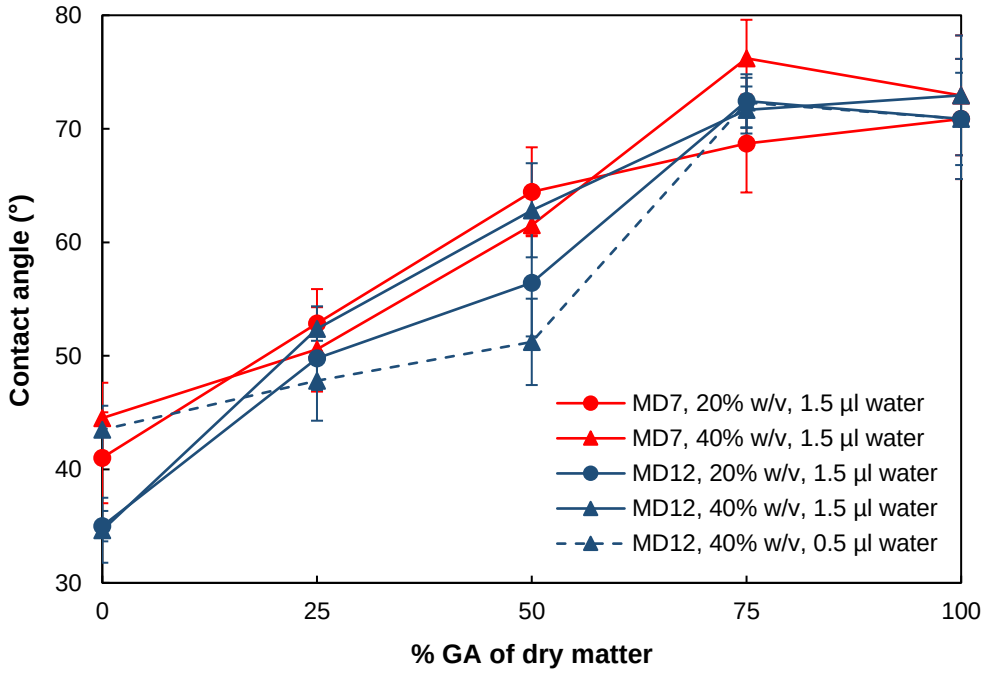

Figure 4.36 Contact angles between water droplets and dried particles of different compositions of GA:MD, solids concentrations and DE-values of MD. Water droplet volume: 0.5 µl (dotted line) and 1.5 µl (solid line); solids concentration: 20% w/v (circles) and 40% w/v (triangles); DE-value of MD: MD7 (red) and MD12 (blue).

The water droplet positioned onto each particle to determine the APCA was then observed over time until it was completely taken up by the particle. This time was defined as the dissolution time. Dissolution is an important property for encapsulated air microparticles. Highly dissolve encapsulated air microparticles would result in the air inside the particle easily escaping into the food matrix, and eventually lead to poor quality of the final product. Selection of the right formulation is therefore crucial for a specific application, for example in manufacturing ice cream. The dissolution time data recorded in this research are plotted in Figure 4.37. Image sequences for the dissolution behaviour of 20% and 40% initial solids concentration particles are provided in Figure 4.38 and Figure 4.39, respectively.

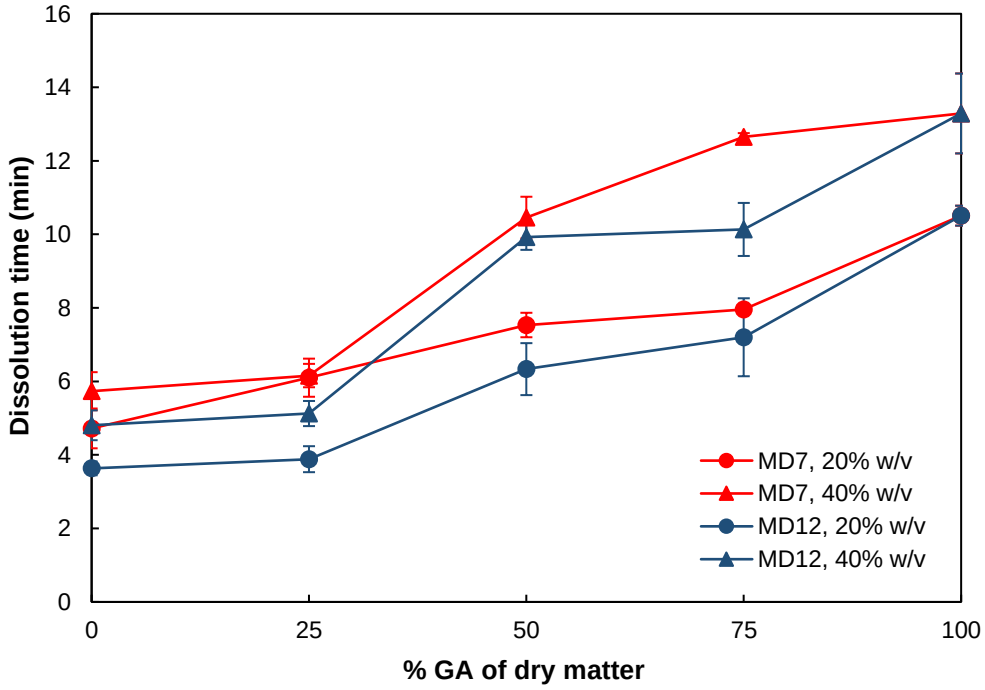

Figure 4.37 Dissolution time of dried particles at varied compositions of GA:MD, solids concentrations and DE-values of MD. Solids concentration: 20% w/v (circles) and 40% w/v (triangles); DE-value of MD: MD7 (red) and MD12 (blue).

Not surprisingly, the results of the dissolution times exhibited the same trend as the APCA data. Particles with a high amount of GA dissolved slower than those with a high amount of MD. This finding is also in line with the dissolution time of spray dried powders reported in Chapter 3, in which an increase in the hydrophobic groups of GA resulted in a longer dissolution time. Compared to the APCA data though, the dissolution time was significantly affected by the initial solids concentration of a droplet. Comparing particles with only MD and GA respectively at 20% solids, the particles of MD7 (4.7 ± 0.5 min) and MD12 (3.6 ± 0.2 min) dissolved quicker than GA (10.5 ± 0.3 min). When the solids concentration increased, MD7 and MD12 particles required more time to complete the dissolution process, which were 5.7 ± 0.5 min and 4.8 ± 0.4 min respectively, while GA particles were dissolved at 13.3 ± 1.1 min. Particles with higher solids content had thicker shells which became sufficiently strong in resisting the penetration of the water droplet, hence increased the particle's dissolution time. Longer dissolution times for thicker shelled particles have previously been reported in literature (Caliskan and Dirim, 2016; Movahhed and Mohebbi, 2016).

Particles prepared with MD7 took longer to dissolve than particles with MD12. This is in agreement with findings of Zhang et al. (2019) who reported that SDD of fermented noni juice with higher DE MD was rehydrated faster than lower DE because of more hydrophilic groups at the higher DE that could bind with water molecules more easily. Their results also revealed that particles containing GA had the lowest dissolution rate among the three wall materials studied.

Particle	Before dissolution	Dissolution progresses →					
		1 s	2 min	4 min	6 min	8 min	10 min
0GA:100MD7		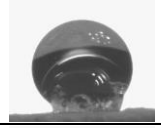		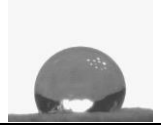			
0GA:100MD12		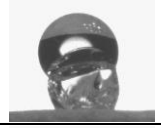	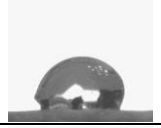				
25GA:75MD7	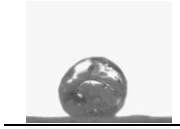	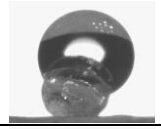	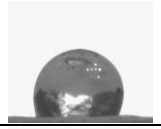				
25GA:75MD12		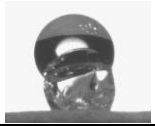	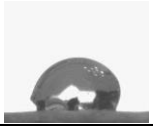	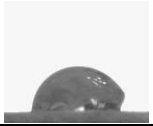			
50GA:50MD7	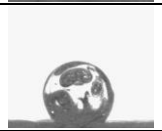	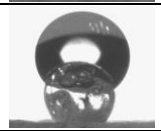	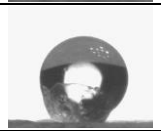	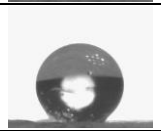			
50GA:50MD12	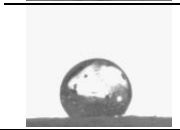	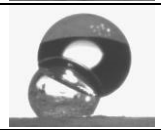	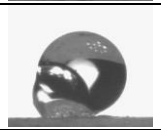	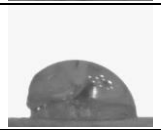			

Figure 4.38 Dissolution behaviours of dried particles at 20% solids concentration with 1.5 µl water droplet. Water droplet is added at t=1s.

Particle	Before dissolution	Dissolution progresses →					
		1 s	2 min	4 min	6 min	8 min	10 min
75GA:250MD7	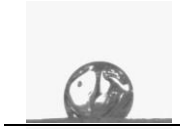	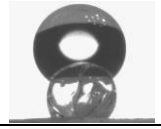		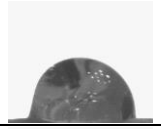	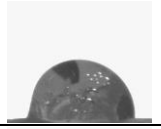	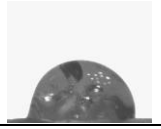	
75GA:25MD12	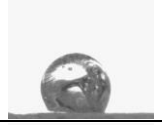	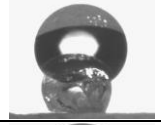	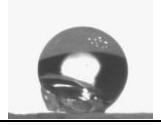	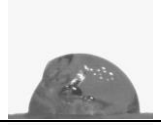	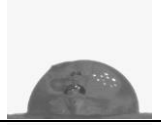		
100GA:0MD	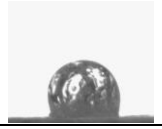	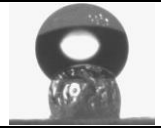	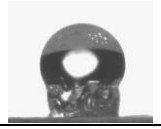	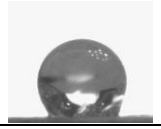	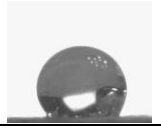	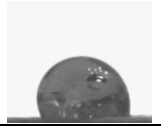	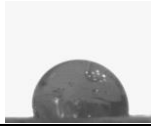

Figure 4.38 (continued)

Particle	Before dissolution	Dissolution progresses →						
		1 s	2 min	4 min	6 min	8 min	10 min	12 min
0GA:100MD7	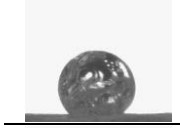	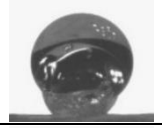	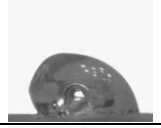	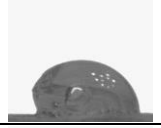				
0GA:100MD12		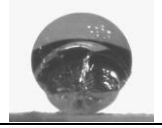	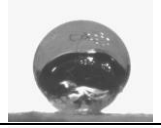	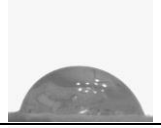				
25GA:75MD7	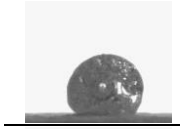	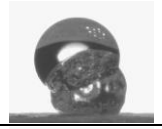	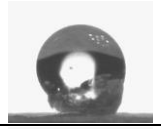	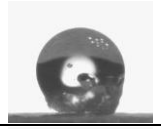	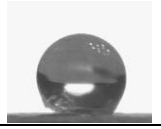			
25GA:75MD12		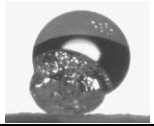	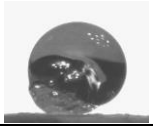					
50GA:50MD7	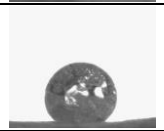	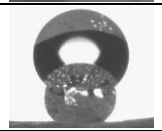	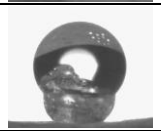	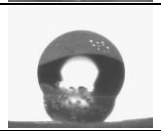	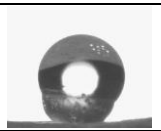	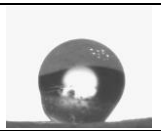	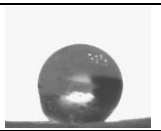	
50GA:50MD12		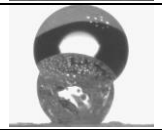	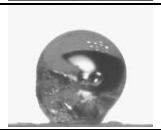	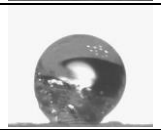		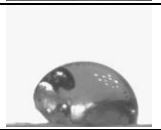		

Figure 4.39 Dissolution behaviours of dried particles at 40% solids concentration with 1.5 µl water droplet. Water droplet is added at t=1s.

Particle	Before dissolution	Dissolution progresses →						
		1 s	2 min	4 min	6 min	8 min	10 min	12 min
75GA:250MD7	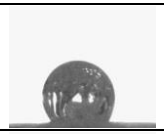	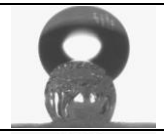	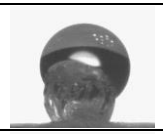	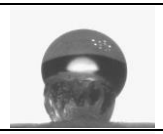	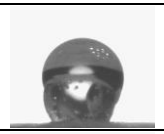	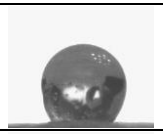	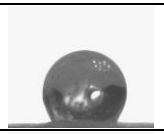	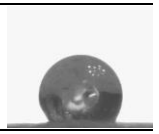
75GA:25MD12	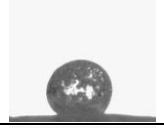	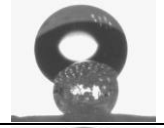		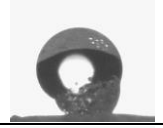		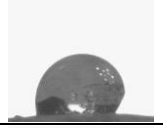		
100GA:0MD	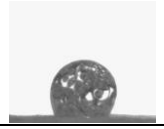	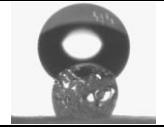	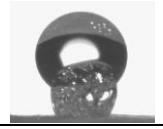	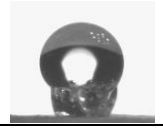	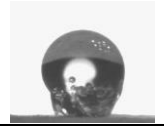	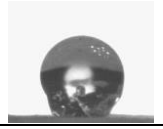	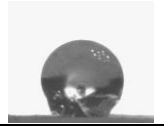	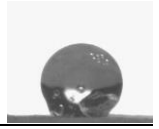

Figure 3.39 (continued)

4.3.7 Water sorption of dried particles

Water sorption and rate of water sorption data acquired at a range of relative humidities are given in Figure 4.40a and b, respectively. These data were taken to develop a better understanding of water penetration into the shell in addition to the APCA and dissolution time data. The water sorption behaviour of the dried particles displayed two distinct regions, namely 0-40% RH and >40% RH. In the first region, the rate of water sorption increased linearly with the increase in RH. Water sorption in the lower RH range was mostly due to surface adsorption as the rates of water sorption were very low and the particles did not swell (Figure 4.41).

During the first period (0-40% RH), all particles prepared with different ratios of GA:MD7 at 40% initial solids concentration had quite similar water sorption (and thus rate of water sorption), which were attributed to the presence of GA at the surface of particles. Clearly, particles containing only MD7 exhibited the lowest water uptake. Particles of 50GA:50MD7 produced with the lower solids (20% solids) had the highest water content as having a thinner shell and the water molecules would adsorb and penetrate the shell. As compared to particles containing MD12, particles with MD7 had higher rate of water sorption and water content due to the longer polymeric chain at lower DE of MD. When the polymer chains are longer, there is a high possibility that chains may tend to entangle with each other, resulting in a disordered system and thereby increasing the free-volume (Castro et al., 2016).

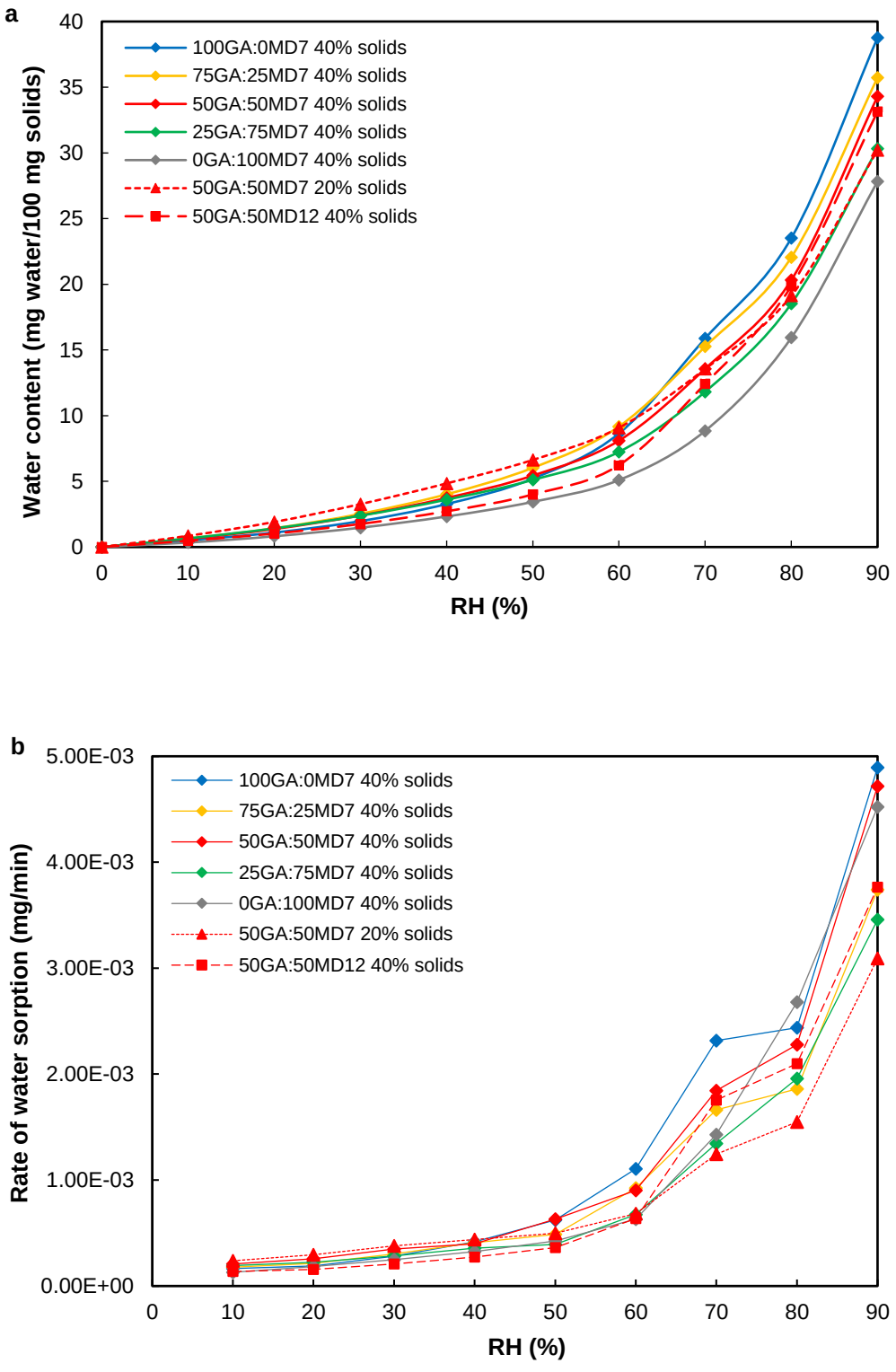

Figure 4.40 a) Water sorption and b) rate of water sorption as a function of RH for the dried particles produced with different ratios of GA and MD7. Also shown are one sample prepared from a different solids concentration (50GA:50MD7 20% solids) and one sample with a different DE-value of MD (50GA:50MD12 40% solids).

In the next region (40 to 90% RH), the sample mass increased dramatically due to the fast migration of water into the shell of particles and thus initiated swelling (Figure 4.41). Overall, the extent of hydration resulted in the highest water absorption by particles containing only GA. In contrast, particles with only MD7 had the lowest water content. Surprisingly, particles with only GA did not collapse at 90% RH (Figure 4.41e), whereas particles of only MD7 dissolved with viscous flow appearance (Figure 4.41a). At 80% RH, GA particles experienced a greater swelling, approximately 7.6 ± 0.8% of their initial size, compared to MD7 particles which swelled by 3.8 ± 0.6%. Swelling of particles would result in a slower rate of wetting and sinkability (Freudig et al., 1999), which is consistent with the wetting and dissolution data obtained in this research (Section 4.3.6 and Chapter 3). Relative humidity more than 60% may also reflect hygroscopicity of the particles (Tontul and Topuz, 2017). Herein, GA was more hygroscopic than MD. Similar findings were reported for the spray dried powders in Chapter 3, as well as in the literature (Gabas et al., 2007; Kurozawa et al., 2009; Pérez-Alonso et al., 2006; Tonon et al., 2011a).

At elevated relative humidity (80 to 90% RH), an increase in the GA ratio resulted in higher water retention. As can be seen in Figure 4.41, particle size increased as the humidity increased from 0 to 80% RH due to swelling and the structure of the particles at 90% RH was greatly influenced by their composition. At 90% RH, particles containing 25% GA formed bridges between particles (Figure 4.41b), which could be associated with the particle agglomeration. Meanwhile, particles produced with 50% GA and more (Figure 4.41c-g) were stable and able to maintain their shape, showing no tendency to collapse or dissolve. Therefore, it may be suggested that particles should contain at least

50% GA to prevent them from collapse for the application in a high moisture system.

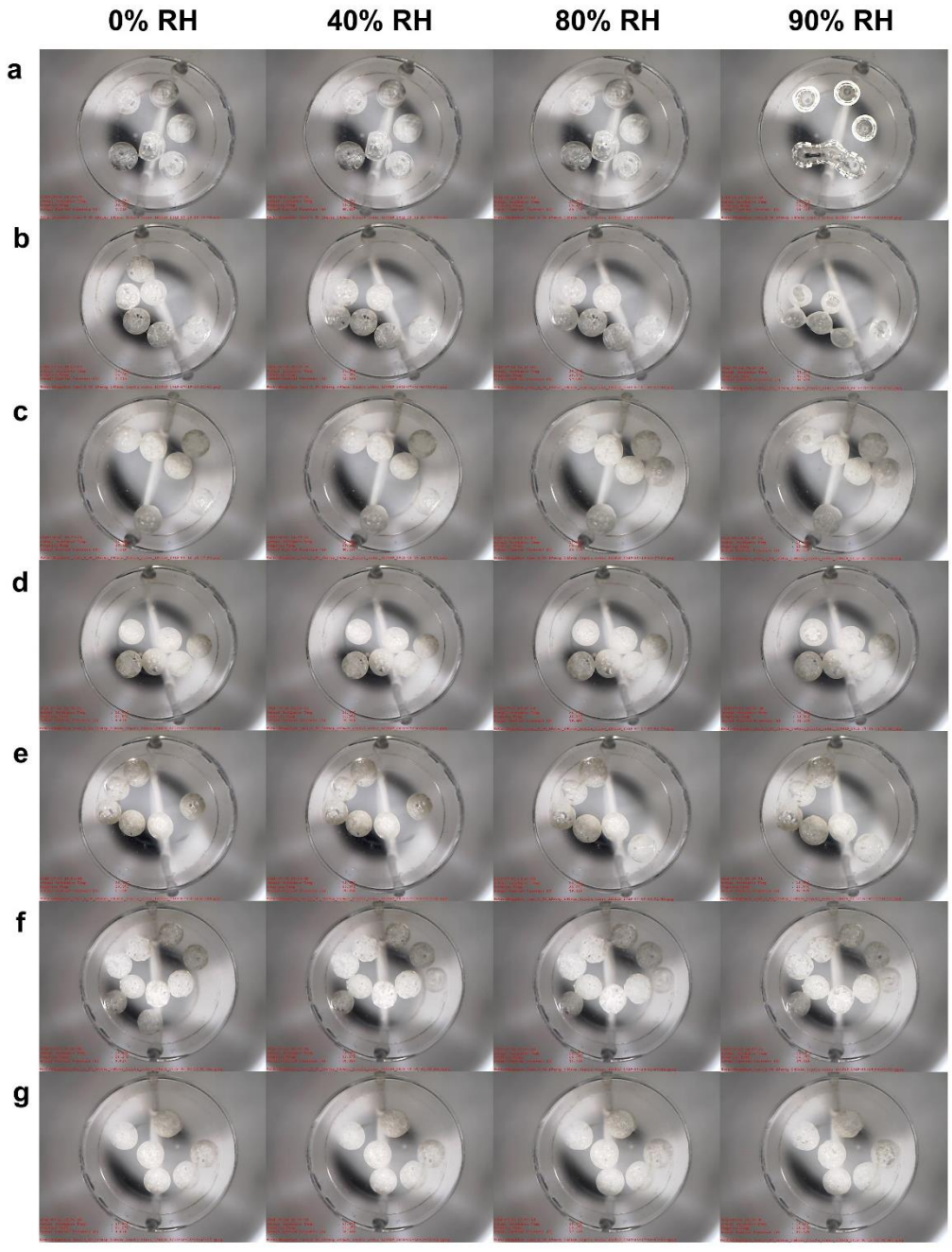

Figure 4.41 Images of particles during DVS analysis at different RH. Particles were produced with different compositions of GA:MD, DE-values of MD and solids concentrations: (a) 0GA:100MD7, 40% w/v; (b) 25GA:75MD7, 40% w/v; (c) 50GA:50MD7, 40% w/v; (d) 75GA:25MD7, 40% w/v; (e) 100GA:0MD7, 40% w/v; (f) 50GA:50MD7, 20% w/v; and (g) 50GA:50MD12, 40% w/v.

At 40 to 90% RH, particles with 40% solids absorbed water faster than those with 20% solids because the thicker shell was able to hold more water and thus had greater water retention. Comparing the effect of DE of MD, both particles (50GA:50MD7 and 50GA:50MD12) had a similar water content (at 80-90% RH). MD of lower DE (less hydrolysed) has less hydrophilic groups, and one would expect that it absorbs less water (Tonon et al., 2011a). However, DE of MD seemed not to impact on the water content of particles because of the greater impact of GA on the water absorption.

4.4 Conclusions

Understanding particle morphology development during drying would allow for better control of the final particle and thus particle functionality in spray drying processes. For this research, it seemed that the ratio of GA:MD, rather than processing parameters, had the most impact on the final particle morphology. A lower diffusion coefficient of GA than MD (thus a high Peclet number) caused an enrichment of GA at the droplet surface that gave the skin rigidity to resist surface compression. Droplets with a high ratio of GA quickly attained the locking point, resulting in rapid nucleation of bubble and eventually leading to the formation of smooth surface particles with one large vacuole.

The shell thickness and particle size could be altered by varying the solids content and the initial droplet size. It was then possible to control the surface wettability and dissolution of particles. The surface of the particle became less wettable with an increase in GA due to greater surface coverage by GA. Particles with a higher ratio of GA and higher solids had the ability to hold water, so it required more time to dissolve.

This research has demonstrated that particles with specified morphologies and wetting properties can be produced by appropriate selection of the droplet formulation and process parameters. An attempt to validate the idea that the SDD set-up can be utilised to design spray drying processes to deliver the desired particle morphology and properties was undertaken in the next step of this PhD research.

CHAPTER 5

Validating Sessile Single Droplet Drying as Design Tool for Obtaining Desired Particle Morphologies via Spray Drying

5.1 Introduction

Particle morphologies that were obtained in sessile SDD experiments (Chapter 4) included smooth and wrinkled surface particles with one vacuole, wrinkled surface with multiple vacuoles and wrinkled solid particles. Smooth-surface hollow particles were of most interest as the overall aim of this research was to create air microparticles as an ingredient for foam-based foods. The sessile SDD experiments were carried out to predict compositions (ratio of GA:MD, solids concentration and DE-value of MD) and drying conditions (temperature and droplet size) to obtain predominantly this morphology in the spray drying process. Indeed, a number of studies have demonstrated the effectiveness of the SDD technique as an investigative and predictive tool for spray drying. For example, Bouman et al. (2016) and Sadek et al. (2016) employed SDD technique to investigate hole formation and shell buckling during drying of whey protein and caseins droplets. Ullum et al. (2010) developed a new empirical drying model from a levitated single particle drying to use in computational fluid dynamics (CFD) simulations of the spray drying process. In other studies, Both et al. (2020, 2018) found that the particle morphology of mixed MD and whey protein obtained from SDD and pilot scale spray drying were almost identical.

In addition, Gouaou et al. (2018) used the SDD to optimise the production of hydroxypropylated pea starch powder at a pilot scale.

The findings reported in Chapter 4 suggested that the formation of smooth-surface hollow particles require process conditions leading to a high drying rate and a formulation favouring the formation of a strong skin. For the following reasons, the formulation based equal parts of GA and MD of the lower DE of the two MD assessed in Chapter 4 was selected:

(i) DVS analysis on single dried particles indicated that particles should contain at least 50% GA to maintain their shape when applied in a high relative humidity system (Chapter 4);

(ii) MD of DE 7 had the tendency to form smooth-surface hollow particles compared to MD of DE 12 due to the stronger skin (Chapter 4);

(iii) XPS data of spray dried particles reported in Chapter 3 revealed that the surface coverage of GA was similar for the 50% and the 75% GA formulation, however formulation with 50% GA was chosen because of GA is the more expensive ingredient.

The feed solutions (50GA:50MD7) were prepared at various solids concentrations of 20 and 40% (w/v) and spray dried at different drying temperatures of 180 and 220 °C and feed flow rates of 300 and 500 ml/h, to assess the spectrum of spray dried particle morphologies versus SDD morphologies, expecting hollow particles to dominate for high drying rates, that is at high drying temperature and low feed rate producing smaller droplets, and

high solid concentration that forming stronger skin. Therefore, the main objectives of the research reported in this chapter study were:

1) to compare the morphology of particles obtained from single droplet drying with spray drying; and
2) to analyse the bulk physicochemical properties of resultant powders.

5.2 Methods

5.2.1 Spray drying of powder

Feed solutions of 50GA:50MD7 were prepared at 20% and 40% w/v total solids by dispersing the appropriate amount of each dry powder of GA and MD7 in 500 ml of reverse osmosis water and leaving on a roller mixer at room temperature (20 ± 3 °C) overnight to ensure complete dissolution. Spray drying was performed at a co-current spray dryer (FT80 Tall Form Spray Dryer, Armfield, Bournemouth, UK) equipped with a two-fluid nozzle atomiser with an orifice diameter of 1 mm. The air pressure was set at 0.5 bar. Inlet temperature and feed flow rate conditions are detailed in Table 5.1. Each experiment was carried out in duplicate and spray dried powders were stored in vacuum-sealed plastic bags at room temperature (20 °C) until use.

Table 5.1 Formulation of the feed solutions and spray drying conditions used for producing encapsulated air microparticles.

Formulation (50GA:50MD7)	Spray drying conditions		
	Inlet temperature (°C)	Outlet temperature (°C)	Feed flow rate (ml/h)
20% w/v	180	76	500
	220	90	300
	220	86	500
40% w/v	180	76	500
	220	90	300
	220	86	500

5.2.2 Microstructure property analyses of spray dried powders

The microstructure of the powders was visualised utilising the optical microscopy and SEM method described in Section 3.2.5.1 and 3.2.5.2, respectively.

5.2.3 Bulk property analyses of powders

5.2.3.1 Water activity, moisture content, particle size distribution and dissolution time

The powders were analysed for water activity, moisture content, particle size distribution and dissolution time according to the method described in Section 3.2.6.1, 3.2.6.2, 3.2.6.4 and 3.2.6.7, respectively.

5.2.3.2 Wettability and dispersibility (Turbiscan methodology)

The dissolution ability of a powder in a liquid depends on many parameters, such as wettability, sinkability and dispersibility. Wettability is the speed of the powder layer to penetrate into the water under the effect of capillary force, sinkability corresponds to the ability of the powder to sink into water and dispersibility represents the ability of the powder to separate into individual particles when dispersed in water (Fang et al., 2008; Sadek et al., 2014). The terms wettability and sinkability are often interchangeable as the powder is usually considered to be wetted from the point that it starts to sink into the solution (Fang et al., 2008).

The wettability and dispersibility of the powders were analysed using a vertical scan analyser (Turbiscan LAB, Formulation, France), as proposed by the equipment manufacturer (Application note Turbiscan, 2016) with some modifications. The apparatus is comprised of a detection head equipped with a near-infrared light source (880 nm) and two synchronous detectors. The transmission detector receives the light (T), which goes through the sample (0°), while the backscattering detector receives the light backscattered (BS) by the sample (135°). The signal value of transmitting light is used to analyse clear liquids, while the backscattering light is used to analyse non-clear liquids or samples with high concentration (Qi et al., 2017). Here, only T was observed as there was little backscattering of the samples.

A glass cell was filled with 17 ml of distilled water and 0.5 g of powder was deposited on the water surface without stirring. The cell was then immediately placed into the apparatus and the light source scanned the sample from the

bottom to the top at 2 min intervals for 20 min in total. Temperature was set to 25 °C. An example of Turbiscan profile is shown in Figure B.1 in Appendix B. By measuring the peak thickness at different times, it is possible to evaluate the migration rate of particles. The powder wettability was evaluated by measuring the peak thickness at 32-34 mm of the height of the cell at different times using the Turbisoft Lab 2.2 software. The dispersibility of the powder was measured by the peak thickness as a function of time in the middle zone of the cell (5-30 mm) (see Appendix B Figure B.2).

5.2.4 Statistical analysis

Each measurement was conducted in triplicate and the difference between the mean values was determined using analysis of variance (ANOVA) with Duncan's multiple range test ($p < 0.05$) using the statistical software SPSS (version 24, IBM SPSS Inc., USA).

5.3 Results and Discussion

5.3.1 Particle microstructure

The microstructure of the spray dried particles, prepared at different solids concentrations and dried under different process conditions, is depicted in Figure 5.1 and Figure 5.2 by means of optical and SEM micrographs, respectively. Both sets of micrographs show that the particles varied in size but were predominantly spherical with no apparent crack or fissures. All powders presented a similar surface structure characterised by a mixture of wrinkled and smooth particles.

Based on the insights gained in Chapter 3, smooth surface particles in the SEM images were classified as hollow particles and their fraction in each sample evaluated. The results are included in Table 5.2. The powder prepared from the higher solids feed solution dried at the higher drying temperature and the lower feed rate had the highest percentage of hollow particles (15%). In contrast, the powder prepared from the lower solids feed solution dried at the lower drying temperature and the higher feed flow rate exhibited the lowest percentage of hollow particles (2%). These observations could be explained by the fact that the higher drying temperature resulted in higher drying rate combined with the higher solids concentration had contributed to the formation of a stronger skin and thus smooth-surface hollow particles.

Powders that were produced with a similar solids concentration and feed flow rate were compared to evaluate the impact of drying temperature on the final particle morphology. Clearly, an increase in the drying temperature resulted in a higher fraction of smooth surface particles; at 220 °C, approximately 5% (at 20% solids) and 11% (at 40% solids) of the particles were hollow as compared to the lower temperature (2% hollow particle at 20% solids and 5% hollow particle at 40% solids). This observation confirmed the previous assumption of obtaining more smooth surface hollow particles when spray dried at higher inlet temperature. The gelled skins that developed in the droplets containing a high amount of GA were dried faster at high drying temperature, thus prevent them from denting when collided with one another.

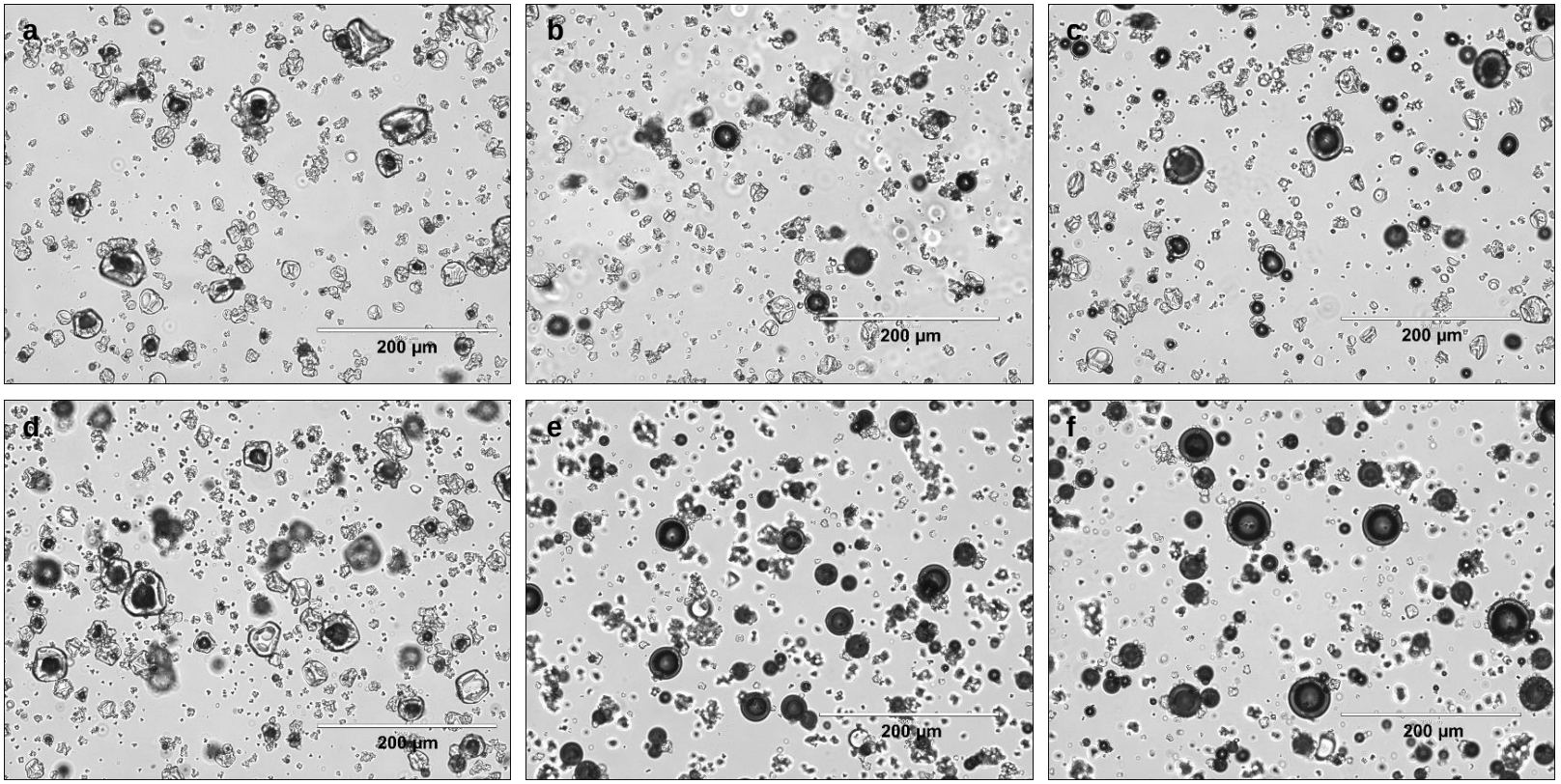

Figure 5.1 Optical micrographs of spray dried 50GA:50MD7 prepared with various initial solids content and dried at different drying rates and feed rates: a) 20% solids, 180 °C, 500ml/h, b) 20% solids, 220 °C, 300ml/h, c) 20% solids, 220 °C, 500ml/h, d) 40% solids, 180 °C, 500ml/h, e) 40% solids, 220 °C, 300ml/h, and f) 40% solids, 220 °C, 500ml/h.

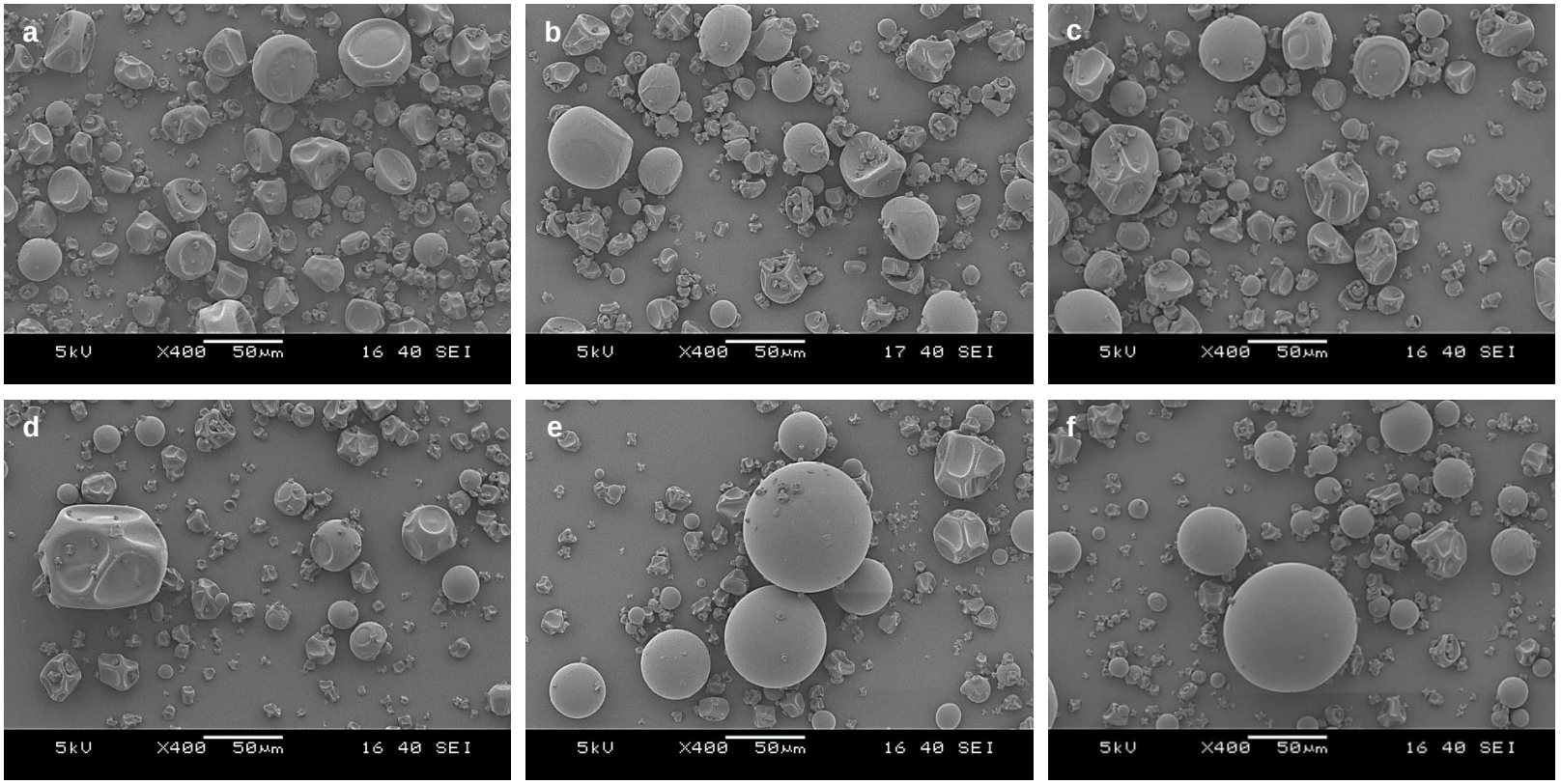

Figure 5.2 SEM images of spray dried 50GA:50MD7 prepared with various initial solids content and dried at different drying rates and feed rates: a) 20% solids, 180 °C, 500ml/h, b) 20% solids, 220 °C, 300ml/h, c) 20% solids, 220 °C, 500ml/h, d) 40% solids, 180 °C, 500ml/h, e) 40% solids, 220 °C, 300ml/h, and f) 40% solids, 220 °C, 500ml/h.

Table 5.2 Physical properties of 50GA:50MD7 powders prepared with various initial solids concentrations and dried at different drying temperatures and feed flow rates. Different superscript letters in the same row indicate significant difference between the samples ($p < 0.05$).

Powder properties	Initial solids concentration and spray drying conditions					
	20% solids, 180 °C, 500 ml/h	20% solids, 220 °C, 300 ml/h	20% solids, 220 °C, 500 ml/h	40% solids, 180 °C, 500 ml/h	40% solids, 220 °C, 300 ml/h	40% solids, 220 °C, 500 ml/h
Hollow particles (%)	2	5	5	5	15	11
Water activity	0.17 ± 0.01^{b}	0.28 ± 0.02^{c}	0.26 ± 0.01^{c}	0.17 ± 0.00^{b}	0.14 ± 0.01^{a}	0.26 ± 0.02^{c}
Moisture content (%)	5.4 ± 0.2^{b}	6.3 ± 0.3^{cd}	6.5 ± 0.2^{d}	5.1 ± 0.4^{b}	4.4 ± 0.3^{a}	6.0 ± 0.4^{c}
Particle size, d_{10} (µm)	4.1 ± 0.0^{a}	4.6 ± 0.2^{b}	5.1 ± 0.1^{c}	5.9 ± 0.4^{d}	5.6 ± 0.3^{d}	5.7 ± 0.3^{d}
Particle size, d_{50} (µm)	15.6 ± 0.4^{a}	16.0 ± 1.1^{a}	18.6 ± 0.3^{b}	24.4 ± 2.4^{c}	24.0 ± 1.0^{c}	23.6 ± 1.4^{c}
Particle size, d_{90} (µm)	38.6 ± 1.2^{ab}	35.0 ± 1.6^{a}	41.4 ± 1.4^{b}	61.7 ± 5.4^{e}	57.2 ± 2.9^{d}	52.4 ± 2.8^{c}
Span	2.2 ± 0.0^{bc}	1.9 ± 0.1^{a}	2.0 ± 0.1^{a}	2.3 ± 0.0^{c}	2.1 ± 0.1^{b}	2.0 ± 0.1^{a}
Dissolution time (min)	43 ± 2^{a}	54 ± 5^{b}	52 ± 5^{ab}	54 ± 4^{b}	59 ± 1^{b}	57 ± 6^{b}

Droplets of the same formulation and drying temperature but dried at different feed flow rates were compared to investigate the effect of droplet size on the morphology of particles. At both solids concentrations (20% and 40%), an increase in the feed rate had no substantial impact on the percentage of hollow particles. However, an increase in the solids concentration contributed to a greater fraction of smooth-surface hollow particles. Thus, confirming the findings reported in the SDD (Chapter 4) that particle morphology was predominantly influenced by the drying temperature and the droplet size had no significant effect (referred to particles 50GA:50MD12), while a strong skin formed at the high solids concentration was required to sustain the spherical shape of the particle during drying.

5.3.2 Bulk physicochemical properties

The bulk physicochemical properties of the spray dried 50GA:50MD7 powders are summarised in Table 5.2. All spray dried samples presented values of water activity lower than 0.3, while the percentage of moisture content ranged from 4.4 to 6.5%. The effects of initial solids concentration, drying temperature and feed flow rate on the water activity were similar to the moisture content, as discussed in more detail in the following. A similar relationship water activity and moisture content was also observed for black mulberry juice powder (Fazaeli et al., 2012).

The initial solids concentration appeared not to impact the powder's water activity and moisture content, which is in line with the findings reported by Şahin-Nadeem et al. (2013), as a result of efficient drying at both solids concentrations. Other authors though have reported a negative or a positive correlation between

the concentration of encapsulating material and the moisture content of the powders, with the water activity following the same trend. A reduction in moisture content (water activity) upon increasing the solids concentration of the feed solution has been found for watermelon powder (Quek et al., 2007) and sumac extract powder (Caliskan and Dirim, 2016) as increased content of the encapsulating material reduced the free water for evaporation (Tontul and Topuz, 2017). On the other hand, Oberoi and Sogi (2015) showed that the moisture content and water activity of watermelon juice powder increased with increasing solids concentration due to the higher viscosity of the feeds, which reduced the heat and mass transfer, and thus making the outflow of water difficult (De Souza et al., 2015).

The water activity and moisture content of the spray dried powders were significantly affected by the air inlet temperature. One might expect that the feed with higher inlet temperature would produce drier powder because of a greater temperature gradient between the atomised feed and the drying air, resulting in a greater driving force for water evaporation (Tonon et al., 2011a). However, the reverse appeared to be true in which higher moisture content and water activity were observed when dried at the higher temperature. Using a very high drying temperature may induce an instant formation of skin on the droplet surface, which contributed to difficulties in water diffusion (Tontul and Topuz, 2017). On the contrary, some studies reported a decrease in the moisture content (as well as water activity) of the final product with an increase in the drying temperature (Daza et al., 2016; Laokuldilok and Kanha, 2015; Sanchez-Reinoso et al., 2017).

It was expected that a drier powder would be obtained at the lower feed flow rate due to the smaller droplet size and thus increased evaporation rate in the drying chamber. While this was indeed observed for the feed solution of the higher solids content (40%), see Table 5.2, which in agreement with literature (Behboudi-Jobbehdar et al., 2013; Hu et al., 2016). However, the feed rate hardly impacted on the moisture content and water activity of the powder sprayed from the lower solids content (20%) feed solution. This observation can only be explained by the morphological differences between the two powders. At 20% solids, the feed rate had no impact on the proportion of hollow particles in the powder. Meanwhile, at 40% solids, powder dried at the lower feed rate (300 ml/h) had a greater proportion of hollow particles compared to the powder processed at the higher feed rate (500 ml/h). The results suggest that the hollow particles held less water than the solid particles.

The particle size distribution of all powders showed a bimodal distribution (Figure 5.3), i.e. there are two distinct peaks, each one representing a predominant size. This characteristic allows smaller particles to penetrate into the spaces between the larger ones, thus occupying less space, as can be seen in the SEM images presented in Figure 5.2. Increasing the solids concentration from 20% to 40% in the feed solution resulted in larger particles for a number of reasons including larger droplet size and earlier onset of skin formation. The latter was found in SDD experiments of this PhD research (Chapter 4). The former is a well-known consequence of the increased feed stock solution viscosity at higher solids (Fernandes et al., 2014; Jafari et al., 2017; Outuki et al., 2016).

With respect to the influence of inlet air temperature on particle size, no significant difference was observed in the median diameter (d_{50}) for powders with 40% solids, but for the powder containing 20% solids drying at a higher temperature produced a significantly larger particle size. The hotter drying air resulted in larger particles due to the rapid evaporation of moisture at the surface of the particle promoting the formation of a hard skin that prevented further shrinkage during drying. Such findings have been reported in the literature (Jafari et al., 2017; Nijdam and Langrish, 2006). It was found that particle size increased with the increasing feed flow rate for powder prepared at 20% solids but had no impact on powders with 40% solids. A higher feed rate would form bigger droplets and thus, bigger particles were obtained (Al-Asheh et al., 2003; Shishir et al., 2016). As both drying temperature and feed flow rate exhibited no influence on the particle size at 40% solids, it may suggest that the solids concentration of the feed is the main contributing factor to the particle size. The span value of the powders ranged between 1.9 and 2.3 which indicates a homogeneous distribution (Fernandes et al., 2014).

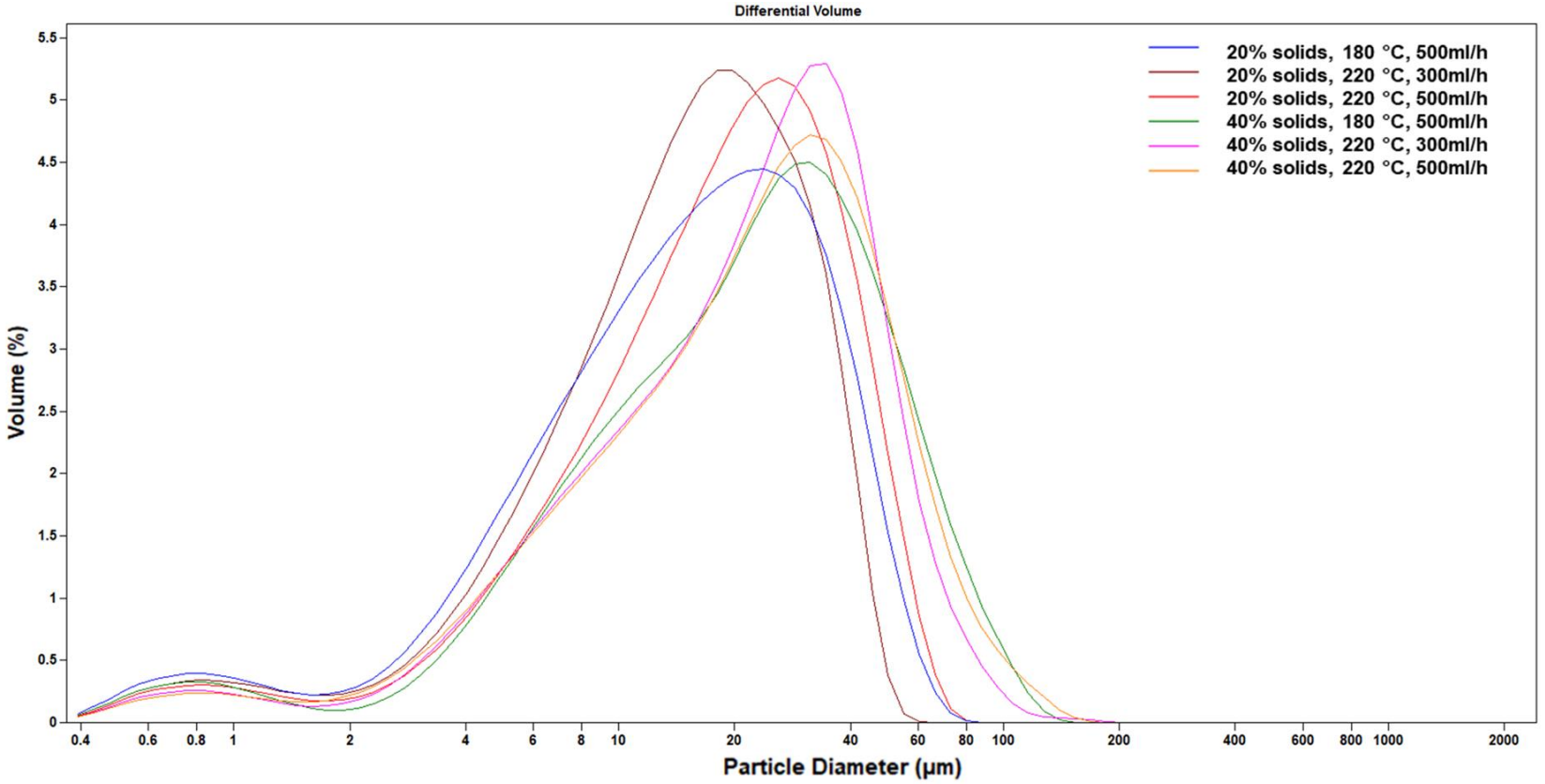

Figure 5.3 Particle size distribution of spray dried 50GA:50MD7 at different solids concentrations, drying temperatures and feed flow rates.

The dissolution time for all powders was similar, between 52 and 59 min, except for powder with 20% solids dried at 180 °C and feed rate of 500 ml/h which had the shortest dissolution time of 43 min, see Table 5.2. Powder with the smallest particles and least proportion of hollow particles tended to dissolve much easier in water, thus it may suggest that the size and morphology of particles can influence the dissolution behaviour of powder. These data were acquired with a relative simple dissolution test comprising the observation of powder to dissolve in water under agitation. Therefore, a set up applied the Turbiscan based dissolution test to investigate the dissolving powder instrumentally rather than relying on observation by eye. Figure 5.4 presents the evolution of peak thickness over time during wetting and dispersion of particles. As can be seen in Figure 5.4a, all powders reached maximum wetting at 6 min. The slope from t=0 min to the highest point (t=6 min) can give an indication of wettability rate; greater value meaning better wettability. After 8 min, the standard deviation became larger as the water surface was not fully covered by the powder and the remaining powder on the surface may vary between measurements. The slope from t=0 min to the linear zone (t=8 min) in Figure 5.4b provides dispersibility rate; a higher value indicates powder is easily dispersed.

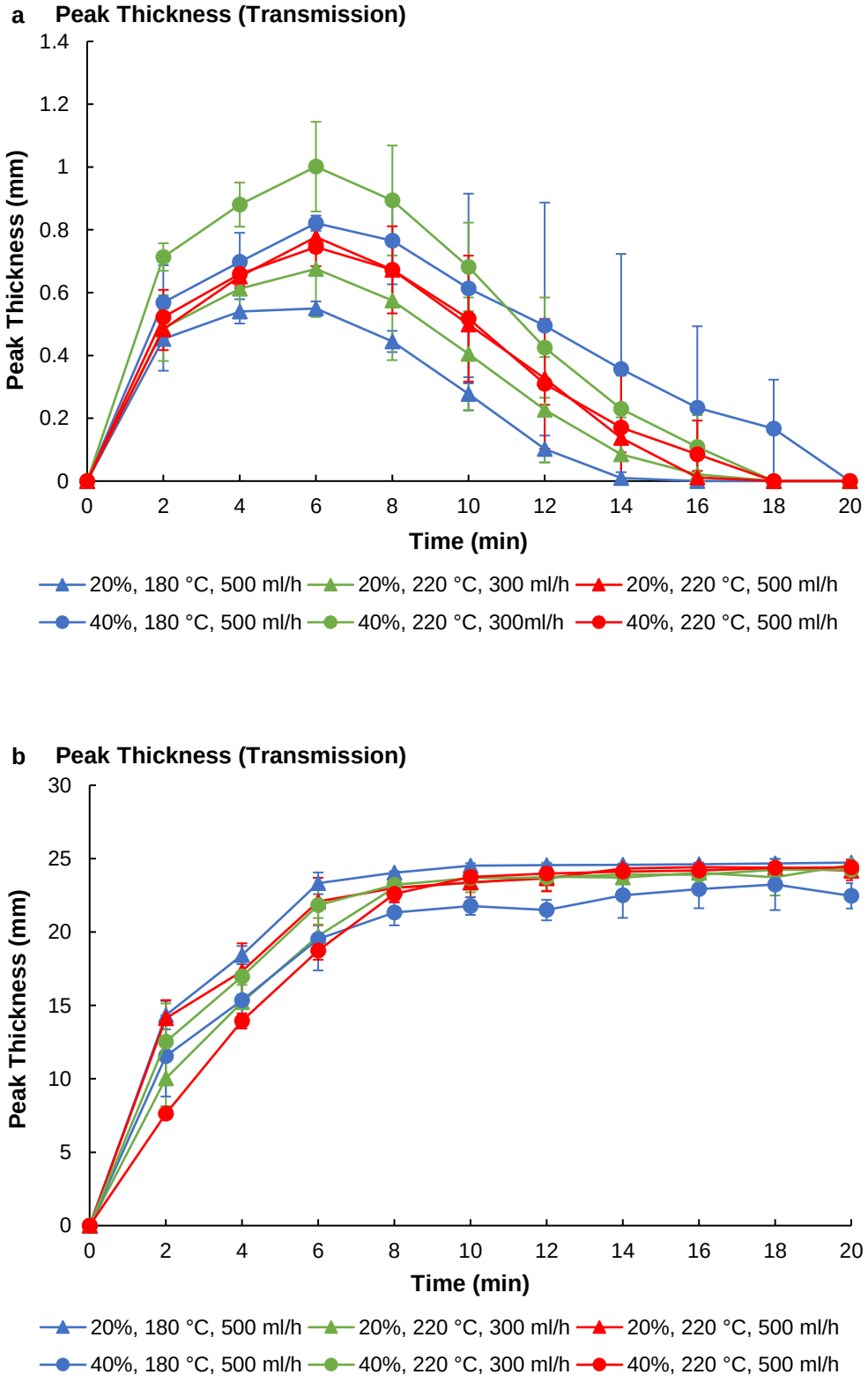

Figure 5.4 Peak thickness at different times for a) wettability and b) dispersibility of spray dried powders.

Both wettability and dispersibility rates of powders are listed in Table 5.3. Powder with 20% solids concentration and dried at 180 °C and feed rate of 500 ml/h exhibited the worst wettability, meanwhile powder prepared with 40% solids and dried at 220 °C and feed rate of 300 ml/h had the best wettability. This behaviour is possibly related to the particle size and morphology, in which the small and solid particles was less wettable than the large and hollow particles. Fang et al. (2008) reported that good wettability is favoured when the particles are large and have high porosity. The powder produced at 20% and 40% solids (both dried at 180 °C and feed rate of 500 ml/h) were, respectively, the fastest and the slowest to disperse in water. These results suggest that the small and solid particles had better dispersibility than the large and solid particles. In fact, a quite similar result to dispersibility was observed for the dissolution time even though stirring was applied during the dissolution time measurements, whereas no stirring for the dispersibility measurements.

Table 5.3 Wettability and dispersibility rates of spray dried powders in water at 25 °C. Different superscript letters in the same column indicate significant difference between samples ($p < 0.05$).

Powder	Slope of peak thickness (mm/min)	
	Wettability	Dispersibility
20% solids, 180 °C, 500ml/h	0.09 ± 0.00^{a}	$3.01 \pm 0.01b^{c}$
20% solids, 220 °C, 300ml/h	0.11 ± 0.03^{ab}	2.88 ± 0.09^{bc}
20% solids, 220 °C, 500ml/h	0.13 ± 0.01^{b}	2.88 ± 0.12^{bc}
40% solids, 180 °C, 500ml/h	0.14 ± 0.01^{b}	2.67 ± 0.11^{a}
40% solids, 220 °C, 300ml/h	0.17 ± 0.02^{c}	2.90 ± 0.02^{bc}
40% solids, 220 °C, 500ml/h	0.12 ± 0.01^{b}	2.83 ± 0.07^{b}

5.4 Conclusions

Particle morphology produced using spray drying agrees well with the single dried particles in Chapter 4, in which a feed solution containing a higher amount of solids and dried at higher drying temperature had a tendency to form smooth-surface hollow particles. The droplet size (i.e. feed flow rate) had no significant influence on the formation of smooth-surface hollow particles. Therefore, the re-designed SDD set-up developed in Chapter 4 can be used as a predictive tool for obtaining desired particle morphologies in spray drying processes.

All samples comply with the standard acceptable moisture and water activity levels for spray dried powders. The powder produced at higher inlet temperature and lower feed flow rate had a lower moisture content and water activity, while the solids concentration of the feed had no effect. However, the powder produced with higher solids content formed larger particles. For formulations with 20% solids, increasing the inlet air temperature and feed flow rate caused an increase in particle size, but seemed not to impact at 40% solids. Regarding the dissolution, powder with 20% solids concentration and dried at 180 °C and feed rate of 500 ml/h took the longest time to wet, but the easiest to disperse and dissolve in water as a result of having the least hollow particles and the smallest particles.

CHAPTER 6

Conclusions and Recommendations for Future Work

6.1 Conclusions

This PhD research has explored the potential of producing encapsulated air microparticles using mixed gum Arabic (GA) and maltodextrin (MD) solutions. The droplet compositions (ratio of GA:MD, solids concentration and DE-value of MD) and process conditions (drying temperature and droplet volume) significantly impact the final particle morphology and the wetting properties of the resultant particles. A sessile SDD on a hydrophobic surface was successfully utilised to gain detailed insight into the spray drying behaviour of GA:MD droplets. Overall, the morphology development of particles was controlled by the mechanical strength of the skin and the drying rate.

As illustrated in Figure 6.1, the drying of a droplet could be divided into two stages: the first stage (constant rate period) where the droplet shrank uniformly as evaporation took place at the droplet surface and the second stage (falling rate period) started when a skin formed until the droplet fully dried. During the constant rate period, a high drying rate was observed in the droplets that were dried at higher temperature and contained lower solids concentration. The ratio of GA:MD, initial droplet size and DE of MD had no impact on the drying rate during this period.

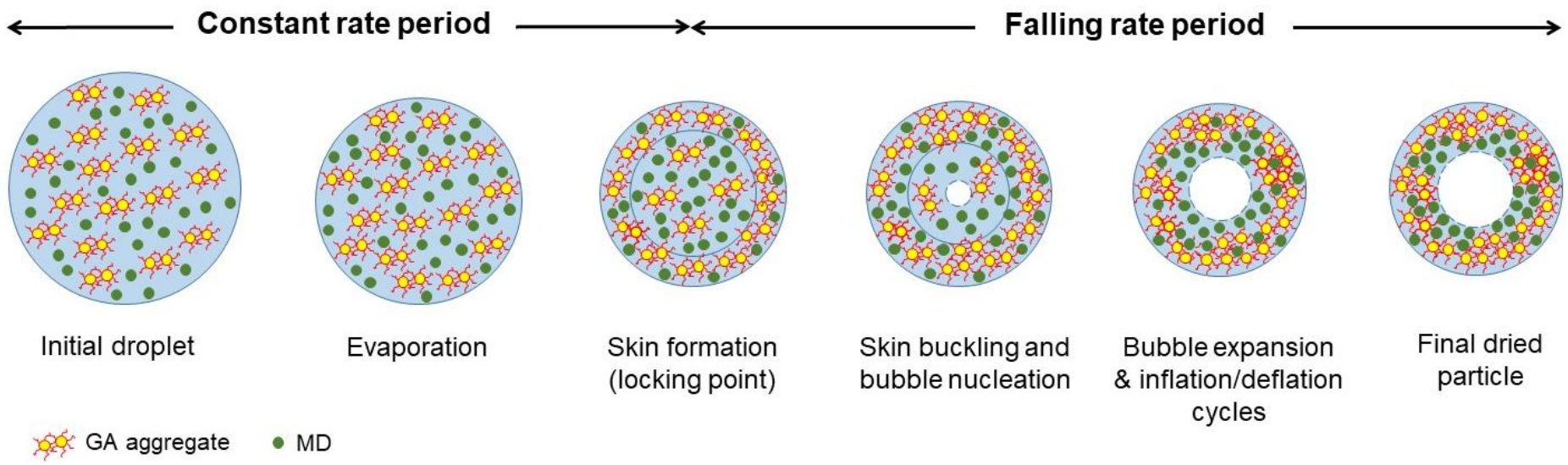

Figure 6.1 Schematic illustration of particle formation during drying of a droplet containing a mixture of GA and MD.

Three events that happen during the falling rate period, which were the skin formation (so-called locking point), buckling and bubble formation, had major influences on the final particle morphology. Droplets containing a higher amount of GA, a higher solids concentration and a lower DE of MD and were dried at a higher temperature and had a smaller initial droplet volume tended to attain the locking point earlier. The buckling was almost absent at these conditions as they favoured the formation of a rigid skin, thus creating a smooth surface particle. The strength of the skin was primarily contributed by the presence of GA. A high drying rate, mainly due to a high drying temperature, a smaller initial droplet volume and the early onset of skin formation, resulted in a faster nucleation of the bubbles, thus leading to the formation of a large vacuole.

Despite the differences in time and length scales, both spray drying and SDD systems produced quite similar particle morphologies. Spray drying the feed containing a high solids content at a high inlet temperature and a slow feed rate produced the highest fraction of spherical smooth hollow particles. Indeed, such conditions had led to the formation of smooth and hollow particles during SDD. However, when studying the individual effect of the compositional ratio, both drying processes developed different particle morphologies. In SDD experiments, droplets with more GA yielded smooth and hollow particles, whereas in spray drying this was the other way around. The spray drying process is more complex than SDD, other factors such as the formation of different droplet sizes during atomisation, fluctuation in relative humidity and drying temperature, as well as collisions between droplets in the drying chamber could affect the drying rate and morphology of spray dried particles.

Regarding the wetting, spray dried particles exhibited similar behaviour to the SDD particles. Particles produced with a higher amount of GA were less wettable and had a slower dissolution rate, both as a result of enrichment of GA at the surface of particles. Solids concentration had no effect on the surface wettability, but greatly influenced the dissolution of particles. Particles prepared from solutions containing higher solids had thicker shells, thus took longer time to dissolve. Particles with a higher DE of MD showed improved wetting and dissolved faster in water than those with lower DE, both observations are due to the presence of more hydrophilic groups. When exposed to a high moisture environment, particles containing a high amount of GA, a high solids concentration and a lower DE of MD were able to absorb more water and swelled without collapsing.

In conclusion, GA is a promising encapsulating material that can potentially be used for the development of encapsulated air microparticles as it had the tendency to form smooth surface-hollow particles and the ability to control the particle surface's wettability. The functionality and size of the particles can be tailored by applying different amounts of GA, solids contents and initial droplet volumes in order to meet the specific requirements for the application in the food systems, for example in ice cream production.

6.2 Recommendations for Future Work

The following interesting and challenging research areas could be further investigated.

1. Study of the segregation of GA and MD in the single dried particles. Segregation of the components through the particle is possibly influenced by the internal structure of the particles and thus may affect the wettability of the particles. Confocal Raman microscopy (CRM) and time of flight secondary ion mass spectroscopy (ToF-SIMS) are the possible techniques to investigate the segregation of components in the particles. In this research, there was an attempt to map the distribution of GA and MD in the particles using energy dispersive X-ray spectroscopy (EDX) coupled with SEM, CRM and ToF-SIMS. However, the main obstacle to these analyses was the sample preparation required to obtain a good cross-section of the particle. The particle was embedded in the epoxy and microtomed using a sharp glass knife to slice the particle. This sample preparation seemed not to be an appropriate technique as the particle might crack during drying of the epoxy, the particle peeled off during the microtoming process, as well as it was difficult to differentiate between the particle and epoxy as both are colourless. In the x-ray photoelectron spectroscopy (XPS) analysis, the presence of N atom in GA can be an indicator of the presence of protein. However, EDX failed to detect the presence of the N atom due to a very small amount and the equipment being less sensitive. On the other hand, ToF-SIMS is very sensitive equipment but required a flat surface for the mapping as a slight tilt on the surface might result in more beam being exposed to the area and led to a

wrong mapping. It is impossible to get a perfectly flat surface using the microtoming technique. Therefore, future experiments could include sample preparation that freezes the particle, then cut with a focused ion beam (FIB) and immediately analysed with ToF-SIMS.

2. This research has demonstrated that the presence of GA played a crucial role in obtaining hollow particles as it provided strength to the skin and thus prevented from collapsing during drying. Therefore, further study on how the rigidity of the skin contributes to the formation of hollow particles should be carried out, for examples using a thin film as a model system for spray drying (Both et al., 2019b; Sadek et al., 2015a) and measuring the rheological properties at high concentrations (Both et al., 2019a; Siemons et al., 2020). Thin film drying and rheology analysis can be used as a complementary technique to single droplet drying which allows investigation of the relationship between the dynamic rheological properties of the skin with the development of the morphology of drying droplets.

3. Functionality requirements of encapsulated air microparticles are determined by their target application. Therefore, it is necessary to perform an assessment on the performance of the particles as an ingredient in the targeted product to obtain some sort of feedback loop between the properties and functionality of the particles and the process.

4. To find a cheaper material than GA for producing encapsulated air microparticles. Protein, e.g. gelatin (Meng and Cloutier, 2014) and casein (Both et al., 2018b), or hydrocolloids containing proteinaceous

component, e.g. pectin (Leroux et al., 2003), gum karaya and gum tragacanth (Verbeken et al., 2003), are the possible materials to replace GA due to surface active of the protein that will adsorb at the air-water interface during droplet drying, and thus allow for wettability control of the particle.

References

A-Sun, K., Thumthanaruk, B., Lekhavat, S., Jumnongpon, R., 2016. Effect of spray drying conditions on physical characteristics of coconut sugar powder. Int. Food Res. J. 23(3), 1315–1319.

Adhikari, B., Howes, T., Bhandari, B.R., Langrish, T.A.G., 2009a. Effect of addition of proteins on the production of amorphous sucrose powder through spray drying. J. Food Eng. 94, 144–153.

Adhikari, B., Howes, T., Bhandari, B.R., Truong, V., 2000. Experimental studies and kinetics of single drop drying and their relevance in drying of sugar-rich foods: A review. Int. J. Food Prop. 3(3), 323–351.

Adhikari, B., Howes, T., Wood, B.J., Bhandari, B.R., 2009b. The effect of low molecular weight surfactants and proteins on surface stickiness of sucrose during powder formation through spray drying. J. Food Eng. 94, 135–143.

Aidoo, R.P., Depypere, F., Afoakwa, E.O., Dewettinck, K., 2013. Industrial manufacture of sugar-free chocolates - Applicability of alternative sweeteners and carbohydrate polymers as raw materials in product development. Trends Food Sci. Technol. 32, 84–96.

Al-Asheh, S., Jumah, R., Banat, F., Hammad, S., 2003. The use of experimental factorial design for analysing the effect of spray dryer operating variables on the production of tomato powder. Food Bioprod. Process. 81(Part C), 81–88.

Alamilla-Beltrán, L., Chanona-Pérez, J.J., Jiménez-Aparicio, A.R., Gutiérrez-López, G.F., 2005. Description of morphological changes of particles along spray drying. J. Food Eng. 67, 179–184.

Ali, M., Mahmud, T., Hegg, P.J., Ghadiri, M., Djurdjevic, D., Ahmadian, H., de Juan, L.M., Amdaor, C., Bayly, A., 2014. A one-dimensional plug-flow model of a counter-current spray drying tower. Chem. Eng. Res. Des. 92, 826–841.

Anandharamakrishnan, C., Ishwarya, S.P., 2015. Introduction to spray drying, in: Spray Drying Techniques for Food Ingredient Encapsulation. John Wiley & Sons Ltd, West Sussex, UK.

Andrade, R.D.P., Roberto, L.M., Pérez, C.E.C., 2011. Models of sorption isotherms for food: Uses and limitations. Vitae 18(3), 325–334.

Annable, P., Fitton, M.G., Harris, B., Phillips, G.O., Williams, P.A., 1994. Phase behaviour and rheology of mixed polymer systems containing starch. Top. Catal. 8(3-4), 351–359.

AOAC, 2000. Official methods of AOAC International, 15th ed. Association of Official Analytical Chemists, Maryland, USA.

Application note Turbiscan, 2016. Method to estimate reconstitution of food powder in liquid. Appl. note. URL https://www.formulaction.com/applications-and-library/library (accessed 11.4.19).

Arai, S., Doi, M., 2012. Skin formation and bubble growth during drying process of polymer solution. Eur. Phys. J. E 35(57), 1–9.

Avaltroni, F., Bouquerand, P.E., Normand, V., 2004. Maltodextrin molecular weight distribution influence on the glass transition temperature and viscosity in aqueous solutions. Carbohydr. Polym. 58, 323–334.

Ávila, E.L., Cortés Rodríguez, M., Ciro Velásquez, H.J., 2015. Influence of maltodextrin and spray drying process conditions on sugarcane juice powder quality. Rev. Fac. Nac. Agron. Medellín 68(1), 7509–7520.

Bakar, J., Ee, S.C., Muhammad, K., Hashim, D.M., Adzahan, N., 2013. Spray-drying optimization for red pitaya peel (*Hylocereus polyrhizus*). Food Bioprocess Technol. 6, 1332–1342.

Ballesteros, L.F., Ramirez, M.J., Orrego, C.E., Teixeira, J.A., Mussatto, S.I., 2017. Encapsulation of antioxidant phenolic compounds extracted from spent coffee grounds by freeze-drying and spray-drying using different coating materials. Food Chem. 237, 623–631.

Battista, C.A. Di, Constenla, D., Ramírez-Rigo, M.V., Piña, J., 2015. The use of arabic gum, maltodextrin and surfactants in the microencapsulation of phytosterols by spray drying. Powder Technol. 286, 193–201.

Bazaria, B., Kumar, P., 2016. Effect of whey protein concentrate as drying aid and drying parameters on physicochemical and functional properties of spray dried beetroot juice concentrate. Food Biosci. 14, 21–27.

Behboudi-Jobbehdar, S., Soukoulis, C., Yonekura, L., Fisk, I., 2013. Optimization of spray-drying process conditions for the production of maximally viable microencapsulated *L. acidophilus* NCIMB 701748. Dry. Technol. 31(11), 1274–1283.

Bhandari, B., 2008. Spray drying and powder properties, in: Hui, Y.H., Clary, C., Farid, M.M., Fasina, O.O., Noomhorn, A., Welti-Chanes, J. (Eds.), Food Drying Science and Technology Microbiology, Chemistry, Applications. DEStech Publications Inc, Pennsylvania, USA.

Bhandari, B.R., Datta, N., Howes, T., 1997. Problems associated with spray drying of sugar-rich foods. Dry. Technol. 15(2), 671–684.

Bhusari, S.N., Muzaffar, K., Kumar, P., 2014. Effect of carrier agents on physical and microstructural properties of spray dried tamarind pulp powder. Powder Technol. 266, 354–364.

Bicudo, M.O.P., Jó, J., Oliveira, G.A. de, Chaimsohn, F.P., Sierakowski, M.R., Freitas, R.A. de, Ribani, R.H., 2015. Microencapsulation of juçara (*Euterpe edulis* M.) pulp by spray drying using different carriers and drying temperatures. Dry. Technol. 33, 153–161.

Both, E.M., Boom, R.M., Schutyser, M.A.I., 2020. Particle morphology and powder properties during spray drying of maltodextrin and whey protein mixtures. Powder Technol. 363, 519–524.

Both, E.M., Karlina, A.M., Boom, R.M., Schutyser, M.A.I., 2018a. Morphology development during sessile single droplet drying of mixed maltodextrin and whey protein solutions. Food Hydrocoll. 75, 202–210.

Both, E.M., Nuzzo, M., Millqvist-Fureby, A., Boom, R.M., Schutyser, M.A.I., 2018b. Morphology development during single droplet drying of mixed component formulations and milk. Food Res. Int. 109, 448–454.

Both, E. M., Siemons, I., Boom, R.M., Schutyser, M.A.I., 2019a. The role of viscosity in morphology development during single droplet drying. Food Hydrocoll. 94, 510–518.

Both, E.M., Tersteeg, S.M.B., Boom, R.M., Schutyser, M.A.I., 2019b. Drying kinetics and viscoelastic properties of concentrated thin films as a model system for spray drying. Colloids Surfaces A Physicochem. Eng. Asp. 585, 124075.

Botrel, D.A., de Barros Fernandes, R.V., Borges, S.V., Yoshida, M.I., 2014. Influence of wall matrix systems on the properties of spray-dried microparticles containing fish oil. Food Res. Int. 62, 344–352.

Bouman, J., Venema, P., de Vries, R.J., van der Linden, E., Schutyser, M.A.I., 2016. Hole and vacuole formation during drying of sessile whey protein droplets. Food Res. Int. 84, 128–135.

Bower, D.I., 2002. An introduction to polymer physics. Cambridge University Press, Cambridge, England.

Buchi, 2019. Mini spray dryer B-290. URL https://www.buchi.com/gb-en/products/spray-drying-and-encapsulation/mini-spray-dryer-b-290 (accessed 5.31.19).

Burnside, E., 2014. Hydrocolloids and gums as encapsulating agents, in: Anilkumar, G., Vasisht, N., Khare, A., Sobel, R. (Eds.), Microencapsulation in the Food Industry. Academic Press, California, USA.

Butler, M.F., Heppenstall-Butler, M., 2001. Phase separation in gelatin/maltodextrin and gelatin/maltodextrin/gum Arabic mixtures studied using small-angle light scattering, turbidity, and microscopy. Biomacromolecules 2, 812–823.

Cai, Y.Z., Corke, H., 2000. Production and properties of spray-dried *Amaranthus betacyanin* pigments. J. Sens. Nutr. Qual. food 65(6), 1248–1252.

Caliskan, G., Dirim, S.N., 2016. The effect of different drying processes and the amounts of maltodextrin addition on the powder properties of sumac extract powders. Powder Technol. 287, 308–314.

Carneiro, H.C.F., Tonon, R. V., Grosso, C.R.F., Hubinger, M.D., 2013. Encapsulation efficiency and oxidative stability of flaxseed oil microencapsulated by spray drying using different combinations of wall materials. J. Food Eng. 115, 443–451.

Castro-Muñoz, R., Barragán-Huerta, B.E., Yáñez-Fernández, J., 2015. Use of gelatin-maltodextrin composite as an encapsulation support for clarified juice from purple cactus pear (*Opuntia stricta*). LWT - Food Sci. Technol. 62, 242–248.

Castro, N., Durrieu, V., Raynaud, C., Rouilly, A., 2016. Influence of DE-value on the physicochemical properties of maltodextrin for melt extrusion processes. Carbohydr. Polym. 144, 464–473.

Charlesworth, D.H., Marshall, W.R., 1960. Evaporation from drops containing dissolved solids. AIChE J. 6(1), 9–23.

Che, L., Li, D., Chen, X.D., 2012. Convective drying kinetics of single droplets of aqueous glucose. Dry. Technol. 30, 1029–1036.

Chegini, G.R., Ghobadian, B., 2005. Effect of spray-drying conditions on physical properties of orange juice powder. Dry. Technol. 23(3), 657–668.

Chen, X.D., 2004. Heat-mass transfer and structure formation during drying of single food droplets. Dry. Technol. 22(1-2), 179–190.

Connolly, S., Fenyo, J.C., Vandevelde, M.C., 1988. Effect of a proteinase on the macromolecular distribution of *Acacia senegal* gum. Carbohydr. Polym. 8, 23–32.

Connolly, S., Fenyo, J.C., Vandevelde, M.C., 1987. Heterogeneity and homogeneity of an arabinogalactan-protein: *Acacia senegal* gum. Top. Catal. 1(5-6), 477–480.

Dalmaz, N., Ozbelge, H.O., Eraslan, A.N., Uludag, Y., 2007. Heat and mass transfer mechanisms in drying of a suspension droplet: A new computational model. Dry. Technol. 25, 391–400.

Daoub, R.M.A., Elmubarak, A.H., Misran, M., Hassan, E.A., Osman, M.E., 2016. Characterization and functional properties of some natural Acacia gums. J. Saudi Soc. Agric. Sci. 17(3), 241–249.

Daza, L.D., Fujita, A., Fávaro-Trindade, C.S., Rodrigues-Ract, J.N., Granato, D., Genovese, M.I., 2016. Effect of spray drying conditions on the physical properties of Cagaita (*Eugenia dysenterica* DC.) fruit extracts. Food Bioprod. Process. 97, 20–29.

De Souza, V.B., Thomazini, M., Balieiro, J.C.D.C., Fávaro-Trindade, C.S., 2015. Effect of spray drying on the physicochemical properties and color stability of the powdered pigment obtained from vinification byproducts of the Bordo grape (*Vitis labrusca*). Food Bioprod. Process. 93, 39–50.

Desai, K.G.H., Park, H.J., 2005. Recent developments in microencapsulation of food ingredients. Dry. Technol. 23(7), 1361–1394.

Dickinson, E., 2016. Hydrocolloids acting as emulsifying agents - How do they do it? Food Hydrocoll. 78, 2–14.

Dokic, L., Jakovljevic, J., Dokic, P., 2004. Relation between viscous characteristics and dextrose equivalent of maltodextrins. Starch/Staerke 56, 520–525.

Dokic, P., Jakovljevic, J., Dokic-Baucal, L., 1998. Molecular characteristics of maltodextrins and rheological behaviour of diluted and concentrated solutions. Colloids Surfaces A Physicochem. Eng. Asp. 141, 435–440.

Downing, C.G., 1966. The evaporation of drops of pure liquids at elevated temperatures: Rates of evaporation and wet-bulb temperatures. AIChE J. 12(4), 760–766.

Eastman, J.E.D., Moore, C.O.R., 1984. Cold-water-soluble granular starch for gelled food compositions. US Pat. 4465702.

El-Tinay, A.H., Ismail, I.A., 1985. Effects of some additives and processes on the characteristics of agglomerated and granulated spray-dried roselle powder. Acta Aliment. Hungaricae 14(3), 283–295.

Elversson, J., Millqvist-Fureby, A., 2005. Particle size and density in spray drying-effects of carbohydrate properties. J. Pharm. Sci. 94, 2049–60.

Elversson, J., Millqvist-Fureby, A., Alderborn, G., Elofsson, U., 2003. Droplet and particle size relationship and shell thickness of inhalable lactose particles during spray drying. J. Pharm. Sci. 92(4), 900–910.

Encina, C., Vergara, C., Giménez, B., Oyarzún-Ampuero, F., Robert, P., 2016. Conventional spray-drying and future trends for the microencapsulation of fish oil. Trends Food Sci. Technol. 56, 46–60.

Esfanjani, A.F., Jafari, S.M., Assadpoor, E., Mohammadi, A., 2015. Nano-encapsulation of saffron extract through double-layered multiple emulsions of pectin and whey protein concentrate. J. Food Eng. 165, 149–155.

Estevinho, B.N., Rocha, F., Santos, L., Alves, A., 2013. Microencapsulation with chitosan by spray drying for industry applications – A review. Trends Food Sci. Technol. 31, 138–155.

Fäldt, P., Bergenståhl, B., 1995. Fat encapsulation in spray-dried food powders. J. Am. Oil Chem. Soc. 72, 171–176.

Fäldt, P., Bergenståhl, B., 1994. The surface composition of spray-dried protein-lactose powders. Colloids Surfaces A Physicochem. Eng. Asp. 90(2-3), 183–190.

Faldt, P., Bergenstahl, B., Carlsson, G., 1993. The surface coverage of fat on food powders analyzed by Esca (electron spectroscopy for chemical analysis). Food Struct. 12(2), 225–234.

Fan, W., Fan, X., Tian, W., Zhu, X., Zhang, W., 2014. Differential analysis on precise determination of molecular weight of triblock copolymer using SEC/MALS and MALDI-TOF MS. Polym. Test. 40, 116–123.

Fang, Y., Selomulya, C., Chen, X.D., 2008. On Measurement of food powder reconstitution properties. Dry. Technol. 26(1), 3–14.

Fang, Z., Bhandari, B., 2010. Encapsulation of polyphenols – A review. Trends Food Sci. Technol. 21, 510–523.

Fazaeli, M., Emam-Djomeh, Z., Kalbasi Ashtari, A., Omid, M., 2012. Effect of spray drying conditions and feed composition on the physical properties of black mulberry juice powder. Food Bioprod. Process. 90, 667–675.

Fellows, P.J., 2009. Properties of food processing, in: Fellows, P.J. (Ed.), Food Processing Technology: Principles and Practice. Woodhead Publishing, New York, USA.

Fernandes, L.P., Turatti, I.C., Lopes, N.P., Ferreira, J.C., Candido, R.C., Oliveira, W.P., 2008. Volatile retention and antifungal properties of spray-dried microparticles of *Lippia sidoides* essential oil. Dry. Technol. 26(12), 1534–1542.

Fernandes, R.V. de B., Borges, S.V., Botrel, D.A., 2014. Gum arabic/starch/maltodextrin/inulin as wall materials on the microencapsulation of rosemary essential oil. Carbohydr. Polym. 101, 524–532.

Fernandes, R.V. de B., Borges, S.V., Botrel, D.A., 2013. Influence of spray drying operating conditions on microencapsulated rosemary essential oil properties. Ciência e Tecnol. Aliment. 33(Supl. 1), 171–178.

Ferrari, C.C., Germer, S.P.M., de Aguirre, J.M., 2012. Effects of spray-drying conditions on the physicochemical properties of blackberry powder. Dry. Technol. 30, 154–163.

Fincher, G.B., Stone, B.A., 1983. Arabinogalactan-proteins: structure, biosynthesis and function. Annu. Rev. Plant Physiol. 34, 47–70.

Flores, F.P., Singh, R.K., Kerr, W.L., Pegg, R.B., Kong, F., 2014. Total phenolics content and antioxidant capacities of microencapsulated blueberry anthocyanins during in vitro digestion. Food Chem. 153, 272–278.

Foerster, M., Gengenbach, T., Woo, M.W., Selomulya, C., 2016. The influence of the chemical surface composition on the drying process of milk droplets. Adv. Powder Technol. 27, 2324–2334.

Frascareli, E.C., Silva, V.M., Tonon, R. V., Hubinger, M.D., 2012. Effect of process conditions on the microencapsulation of coffee oil by spray drying. Food Bioprod. Process. 90, 413–424.

Freudig, B., Hogekamp, S., Schubert, H., 1999. Dispersion of powders in liquids in a stirred vessel. Chem. Eng. Process. Process Intensif. 38, 525–532.

Fu, N., Woo, M.W., Chen, X.D., 2012. Single droplet drying technique to study drying kinetics measurement and particle functionality: A review. Dry. Technol. 30(15), 1771–1785.

Fu, N., Woo, M.W., Chen, X.D., 2011. Colloidal transport phenomena of milk components during convective droplet drying. Colloids Surfaces B Biointerfaces 87, 255–266.

Fuchs, M., Turchiuli, C., Bohin, M., Cuvelier, M.E., Ordonnaud, C., Peyrat-Maillard, M.N., Dumoulin, E., 2006. Encapsulation of oil in powder using spray drying and fluidised bed agglomeration. J. Food Eng. 75, 27–35.

Gabas, A.L., Telis, V.R.N., Sobral, P.J.A., Telis-Romero, J., 2007. Effect of maltodextrin and arabic gum in water vapor sorption thermodynamic properties of vacuum dried pineapple pulp powder. J. Food Eng. 82, 246–252.

Gaiani, C., Ehrhardt, J.J., Scher, J., Hardy, J., Desobry, S., Banon, S., 2006. Surface composition of dairy powders observed by X-ray photoelectron spectroscopy and effects on their rehydration properties. Colloids Surfaces B Biointerfaces 49, 71–78.

Gaiani, C., Scher, J., Ehrhardt, J.J., Linder, M., Schuck, P., Desobry, S., Banon, S., 2007. Relationships between dairy powder surface composition and wetting properties during storage: importance of residual lipids. J. Agric. Food Chem. 55, 6561–6567.

Gamble, J.F., Terada, M., Holzner, C., Lavery, L., Nicholson, S.J., Timmins, P., Tobyn, M., 2016. Application of X-ray microtomography for the characterisation of hollow polymer-stabilised spray dried amorphous dispersion particles. Int. J. Pharm. 510, 1–8.

Gashua, I.B., Williams, P.A., Baldwin, T.C., 2016. Molecular characteristics, association and interfacial properties of gum Arabic harvested from both *Acacia senegal* and *Acacia seyal*. Food Hydrocoll. 61, 514–522.

Gharsallaoui, A., Roudaut, G., Chambin, O., Voilley, A., Saurel, R., 2007. Applications of spray-drying in microencapsulation of food ingredients: An overview. Food Res. Int. 40, 1107–1121.

Ghollasi, A., Yazdi, F.T., Varidi, M., Mohebbi, M., 2018. Effect of spray drying conditions and feed composition on the physical properties of barberry (*Berberis vulgaris*) juice powder. J. Food Bioprocess Eng. 1(2), 17–32.

Gibbs, B.F., Kermasha, S., Alli, I., Mulligan, C.N., 1999. Encapsulation in the food industry: A review. Int. J. Food Sci. Nutr. 50(3), 213–224.

Gohel, M.C., Parikh, R.K., Nagori, S.A., Gandhi, A. V., Shroff, M.S., Patel, P.K., Gandhi, C.S., Patel, V.P., Bhagat, N.Y., Poptani, S.D., Kharadi, S.R., Pandya, R.B., Patel, T.C., 2009. Spray drying: A review. Pharm. Rev. 7(5).

Golman, B., 2012. Modeling of the drying kinetics of slurry droplet in spray drying. ASEAN J. Chem. Eng. 11(2), 1–7.

Golman, B., Julklang, W., 2013. Analysis of drying kinetics of a slurry droplet in the falling rate period of spray drying. Int. J. Chem. Sci. Eng. 7(9), 793–797.

Gonçalves, A., Estevinho, B.N., Rocha, F., 2017. Design and characterization of controlled-release vitamin A microparticles prepared by a spray-drying process. Powder Technol. 305, 411–417.

Gouaou, I., Shamaei, S., Koutchoukali, M.S., Bouhelassa, M., Tsotsas, E., Kharaghani, A., 2018. Impact of operating conditions on a single droplet and spray drying of hydroxypropylated pea starch: Process performance and final powder properties. Asia-Pacific J. Chem. Eng. 14, 1–18.

Goula, A.M., Adamopoulos, K.G., 2008. Effect of maltodextrin addition during spray drying of tomato pulp in dehumidified air: I. Drying kinetics and product recovery. Dry. Technol. 26(6), 714–725.

Goula, A.M., Adamopoulos, K.G., 2005. Spray drying of tomato pulp in dehumidified air: II. The effect on powder properties. J. Food Eng. 66, 35–42.

Griesing, M., Grosshans, H., Hellwig, T., Sedelmayer, R., Gopireddy, S.R., Pauer, W., Gutheil, E., Moritz, H.U., 2016. Influence of air humidity on the particle formation of single mannitol-water droplets during drying. Chemie-Ingenieur-Technik 88(7), 929–936.

Himmetagaoglu, A.B., Erbay, Z., 2019. Effects of spray drying process conditions on the quality properties of microencapsulated cream powder. Int. Dairy J. 88, 60–70.

Horuz, E., Altan, A., Maskan, M., 2012. Spray drying and process optimization of unclarified pomegranate (*Punica granatum*) juice. Dry. Technol. 30(7), 787–798.

Hu, B., Han, L., Gao, Z., Zhang, K., Al-Assaf, S., Nishinari, K., Phillips, G.O., Yang, J., Fang, Y., 2018. Effects of temperature and solvent condition on phase separation induced molecular fractionation of gum arabic/hyaluronan aqueous mixtures. Int. J. Biol. Macromol. 116, 683–690.

Hu, L., Zhang, J., Hu, Q., Gao, N., Wang, S., Sun, Y., Yang, X., 2016. Microencapsulation of brucea javanica oil: Characterization, stability and optimization of spray drying conditions. J. Drug Deliv. Sci. Technol. 36, 46–54.

Huang, D., 2011. Modeling of particle formation during spray drying. Eur. Dry. Conf. - EuroDrying'2011 26–28.

Idris, O.H.M., Williams, P.A., Phillips, G.O., 1998. Characterisation of gum from *Acacia senegal* trees of different age and location using multidetection gel permeation chromatography. Food Hydrocoll. 12(4), 379–388.

Igual, M., Ramires, S., Mosquera, L.H., Martínez-Navarrete, N., 2014. Optimization of spray drying conditions for lulo (*Solanum quitoense* L.) pulp. Powder Technol. 256, 233–238.

Islam, A.M., Phillips, G.O., Sljivo, A., Snowden, M.J., Williams, P.A., 1997. A review of recent developments on the regulatory, structural and functional aspects of gum arabic. Food Hydrocoll. 11(4), 493–505.

Izydorczyk, M., Cui, Steve W., Wang, Q., 2005. Polysaccharide gums: structures, functional properties, and applications, in: Cui, Steven W. (Ed.), Food Carbohydrates: Chemistry, Physical Properties, and Application. CRC Press, Florida, USA.

Jafari, S.M., Assadpoor, E., Bhandari, B., He, Y., 2008. Nano-particle encapsulation of fish oil by spray drying. Food Res. Int. 41, 172–183.

Jafari, S.M., Ghalegi Ghalenoei, M., Dehnad, D., 2017. Influence of spray drying on water solubility index, apparent density, and anthocyanin content of pomegranate juice powder. Powder Technol. 311, 59–65.

Jakubczyk, D., Kolwas, M., Derkachov, G., Kolwas, K., Zientara, M., 2012. Evaporation of micro-droplets: The "radius-square-law" revisited. Acta Phys. Pol. A 122(4), 709–716.

Janiszewska, E., Witrowa-Rajchert, D., 2009. The influence of powder morphology on the effect of rosemary aroma microencapsulation during spray drying. Int. J. Food Sci. Technol. 44, 2438–2444.

Jin, W., Ge, H., Wang, Y., Du, X., Li, B., 2016. Molecular migration of konjac glucomannan and gum Arabic phase separation and its application in oil-water interfaces. Food Hydrocoll. 61, 868–876.

Jinapong, N., Suphantharika, M., Jamnong, P., 2008. Production of instant soymilk powders by ultrafiltration, spray drying and fluidized bed agglomeration. J. Food Eng. 84, 194–205.

Kanakdande, D., Bhosale, R., Singhal, R.S., 2007. Stability of cumin oleoresin microencapsulated in different combination of gum arabic, maltodextrin and modified starch. Carbohydr. Polym. 67, 536–541.

Karaca, A.C., Guzel, O., Ak, M.M., 2016. Effects of processing conditions and formulation on spray drying of sour cherry juice concentrate. J. Sci. Food Agric. 96, 449–455.

Kasapis, S., Morris, E.R., Norton, I.T., Clark, A.H., 1993. Phase equilibria and gelation in gelatin/maltodextrin systems - Part I: Gelation of individual components. Carbohydr. Polym. 21, 243–248.

Kawakami, K., Sumitani, C., Yoshihashi, Y., Yonemochi, E., Terada, K., 2010. Investigation of the dynamic process during spray-drying to improve aerodynamic performance of inhalation particles. Int. J. Pharm. 390, 250–259.

Keshani, S., Daud, W.R.W., Nourouzi, M.M., Namvar, F., Ghasemi, M., 2015. Spray drying: An overview on wall deposition, process and modeling. J. Food Eng. 146, 152–162.

Khazaei, K.M., Jafari, S.M., Ghorbani, M., Hemmati Kakhki, A., 2014. Application of maltodextrin and gum Arabic in microencapsulation of saffron petal's anthocyanins and evaluating their storage stability and color. Carbohydr. Polym. 105, 57–62.

Kim, E.H.-J., Chen, X.D., Pearce, D., 2009a. Surface composition of industrial spray-dried milk powders. 2. Effects of spray drying conditions on the surface composition. J. Food Eng. 94, 169–181.

Kim, E.H.-J., Chen, X.D., Pearce, D., 2009b. Surface composition of industrial spray-dried milk powders. 3. Changes in the surface composition during long-term storage. J. Food Eng. 94, 182–191.

Kim, E.H.-J., Chen, X.D., Pearce, D., 2003. On the mechanisms of surface formation and the surface compositions of industrial milk powders. Dry. Technol. 21(2), 265–278.

Kim, E.H.-J., Chen, X.D., Pearce, D., 2002. Surface characterization of four industrial spray-dried dairy powders in relation to chemical composition, structure and wetting property. Colloids Surfaces B Biointerfaces 26, 197–212.

Kim, E.H.-J., Xiao, D.C., Pearce, D., 2005. Effect of surface composition on the flowability of industrial spray-dried dairy powders. Colloids Surfaces B Biointerfaces 46, 182–187.

Kurozawa, L.E., Park, K.J., Hubinger, M.D., 2009. Effect of maltodextrin and gum arabic on water sorption and glass transition temperature of spray dried chicken meat hydrolysate protein. J. Food Eng. 91, 287–296.

Lamprecht, A., Schäfer, U.F., Lehr, C.-M., 2000. Visualization and quantification of polymer distribution in microcapsules by confocal laser scanning microscopy (CLSM). Int. J. Pharm. 196, 223–226.

Laokuldilok, T., Kanha, N., 2015. Effects of processing conditions on powder properties of black glutinous rice (*Oryza sativa* L.) bran anthocyanins produced by spray drying and freeze drying. LWT - Food Sci. Technol. 64, 405–411.

Law, C.K., Law, H.K., 1982. A d^2-law for multicomponent droplet vaporization and combustion. AIAA J. 20(4), 522–527.

Lebrun, P., Krier, F., Mantanus, J., Grohganz, H., Yang, M., Rozet, E., Boulanger, B., Evrard, B., Rantanen, J., Hubert, P., 2012. Design space approach in the optimization of the spray-drying process. Eur. J. Pharm. Biopharm. 80, 226–234.

Lee, Y., Lee, S.-Y., Donovan, J.D., 2014. Stability characterization and sensory testing in food products containing microencapsulants, in: Anilkumar, G., Niraj, V., Atul, K., Robert, S. (Eds.), Microencapsulation in the Food Industry. Academic Press, San Diego, USA.

Leroux, J., Langendorff, V., Schick, G., Vaishnav, V., Mazoyer, J., 2003. Emulsion stabilizing properties of pectin. Food Hydrocoll. 17, 455–462.

Li, X., Fang, Y., Al-Assaf, S., Phillips, G.O., Nishinari, K., Zhang, H., 2009. Rheological study of gum arabic solutions: Interpretation based on molecular self-association. Food Hydrocoll. 23, 2394–2402.

Li, X., Zhang, H., Fang, Y., Al-Assaf, S., Phillips, G.O., Nishinari, K., 2011. Rheological properties of gum Arabic solution: The effect of arabinogalactan protein complex (AGP), in: Kennedy, J.F., Phillips, Glyn O, Williams, P.A. (Eds.), Gum Arabic. RSC Publishing, Cambridge, UK.

Lima, R. de S., Ré, M.-I., Arlabosse, P., 2019. Drying droplet as a template for solid formation: A review. Powder Technol. 359, 161–171.

Lin, J.C., Gentry, J.W., 2003. Spray drying drop morphology: Experimental study. Aerosol Sci. Technol. 37(1), 15–32.

Lin, S.X.Q., Chen, X.D., 2002. Improving the glass-filament method for accurate measurement of drying kinetics of liquid droplets. Chem. Eng. Res. Des. 80(Part A), 400–409.

Lorén, N., Hermansson, A.M., 2000. Phase separation and gel formation in kinetically trapped gelatin/maltodextrin gels. Int. J. Biol. Macromol. 27, 249–262.

Loret, C., Schumm, S., Pudney, P.D.A., Frith, W.J., Fryer, P.J., 2005. Phase separation and molecular weight fractionation behaviour of maltodextrin/agarose mixtures. Food Hydrocoll. 19, 557–565.

Lum, A., Mansouri, S., Hapgood, K., Woo, M.W., 2018. Single droplet drying of milk in air and superheated steam: Particle formation and wettability. Dry. Technol. 36(15), 1802–1813.

Madene, A., Jacquot, M., Scher, J., Desobry, S., 2006. Flavour encapsulation and controlled release - A review. Int. J. Food Sci. Technol. 41, 1–21.

Mahdavi, S.A., Jafari, S.M., Assadpoor, E., Dehnad, D., 2016. Microencapsulation optimization of natural anthocyanins with maltodextrin, gum Arabic and gelatin. Int. J. Biol. Macromol. 85, 379–385.

Mahdi, A.A., Mohammed, J.K., Al-Ansi, W., Ghaleb, A.D.S., Al-Maqtari, Q.A., Ma, M., Ahmed, M.I., Wang, H., 2020. Microencapsulation of fingered citron extract with gum arabic, modified starch, whey protein, and maltodextrin using spray drying. Int. J. Biol. Macromol. 152, 1125–1134.

Mahendran, T., Williams, P.A., Phillips, G.O., Al-Assaf, S., Baldwin, T.C., 2008. New insights into the structural characteristics of the arabinogalactan-protein (AGP) fraction of gum arabic. J. Agric. Food Chem. 56, 9269–9276.

Maisuthisakul, P., Gordon, M.H., 2012. Influence of polysaccharides and storage during processing on the properties of mango seed kernel extract (microencapsulation). Food Chem. 134, 1453–1460.

Malvern Instruments, 2018. Dynamic light scattering: An introduction in 30 minutes. Tec. note. URL https://www.malvernpanalytical.com/en/learn/knowledge-center/technical-notes/TN101104DynamicLightScatteringIntroduction (accessed 8.12.19).

Manickavasagan, A., Thangavel, K., Dev, S.R.S., Delfiya, D.S.A., Nambi, E., Orsat, V., Raghavan, G.S.V., 2015. Physicochemical characteristics of date powder produced in a pilot-scale spray dryer. Dry. Technol. 33(9), 1114–1123.

Mao, P., Zhao, M., Zhang, F., Fang, Y., Phillips, G.O., Nishinari, K., Jiang, F., 2013. Phase separation induced molecular fractionation of gum arabic-sugar beet pectin systems. Carbohydr. Polym. 98, 699–705.

Masters, K., 1991. Spray Drying Handbook, 5th ed. Longman Scientific & Technical, Essex, UK.

Masuelli, M. a., 2013. Hydrodynamic properties of whole Arabic gum. Am. J. Food Sci. Technol. 1(3), 60–66.

Meerdink, G., van't Riet, K., 1995. Modeling segregation of solute material during drying of liquid foods. AIChE J. 41(3), 732–736.

Meng, Y., Cloutier, S., 2014. Gelatin and other proteins for microencapsulation, in: Anilkumar, G., Niraj, V., Atul, K., Robert, S. (Eds.), Microencapsulation in the Food Industry. Academic Press, San Diego, USA.

Mezhericher, M., Levy, A., Borde, I., 2010a. Theoretical models of single droplet drying kinetics: A review. Dry. Technol. 28(2), 278–293.

Mezhericher, M., Levy, A., Borde, I., 2010b. Spray drying modelling based on advanced droplet drying kinetics. Chem. Eng. Process. Process Intensif. 49, 1205–1213.

Mezhericher, M., Levy, A., Borde, I., 2008. Heat and mass transfer of single droplet/wet particle drying. Chem. Eng. Sci. 63, 12–23.

Mezhericher, M., Levy, A., Borde, I., 2007. Theoretical drying model of single droplets containing insoluble or dissolved solids. Dry. Technol. 25(6), 1025–1032.

Mishra, P., Mishra, S., Mahanta, C.L., 2014. Effect of maltodextrin concentration and inlet temperature during spray drying on physicochemical and antioxidant properties of amla (*Emblica officinalis*) juice powder. Food Bioprod. Process. 92, 252–258.

Moeller, H., Martin, D., Schrader, K., Hoffmann, W., Lorenzen, P.C., 2018. Spray- or freeze-drying of casein micelles loaded with Vitamin D2: Studies on storage stability and in vitro digestibility. Lwt 97, 87–93.

Moghaddam, A.D., Pero, M., Askari, G.R., 2017. Optimizing spray drying conditions of sour cherry juice based on physicochemical properties, using response surface methodology (RSM). J. Food Sci. Technol. 54(1), 174–184.

Mohd Nawi, N., Muhamad, I.I., Mohd Marsin, A., 2015. The physicochemical properties of microwave-assisted encapsulated anthocyanins from *Ipomoea batatas* as affected by different wall materials. Food Sci. Nutr. 3(2), 91–99.

Moran, L.L., Yin, Y., Cadwallader, K.R., Padua, G.W., 2014. Testing tools and physical, chemical, and microbiological characterization of microencapsulated systems, in: Anilkumar, G., Niraj, V., Atul, K., Robert, S. (Eds.), Microencapsulation in the Food Industry. Academic Press, San Diego, USA.

Mothé, C.G., Rao, M.A., 1999. Rheological behavior of aqueous dispersions of cashew gum and gum arabic: Effect of concentration and blending. Food Hydrocoll. 13, 501–506.

Movahhed, M.K., Mohebbi, M., 2016. Spray drying and process optimization of carrot-celery juice. J. Food Process. Preserv. 40, 212–225.

Munoz-Ibanez, M., Nuzzo, M., Turchiuli, C., Bergenståhl, B., Dumoulin, E., Millqvist-Fureby, A., 2016. The microstructure and component distribution in spray-dried emulsion particles. Food Struct. 8, 16–24.

Murrieta-Pazos, I., Gaiani, C., Galet, L., Calvet, R., Cuq, B., Scher, J., 2012. Food powders: Surface and form characterization revisited. J. Food Eng. 112(1-2), 1–21.

Murrieta-Pazos, I., Gaiani, C., Galet, L., Cuq, B., Desobry, S., Scher, J., 2011. Comparative study of particle structure evolution during water sorption: Skim and whole milk powders. Colloids Surfaces B Biointerfaces 87, 1–10.

Muzaffar, K., Dinkarrao, B.V., Kumar, P., 2016. Optimization of spray drying conditions for production of quality pomegranate juice powder. Cogent Food Agric. 2(1127583), 1–9.

Muzaffar, K., Kumar, P., 2015. Parameter optimization for spray drying of tamarind pulp using response surface methodology. Powder Technol. 279, 179–184.

Nadeem, H.Ş., Torun, M., Özdemir, F., 2011. Spray drying of the mountain tea (*Sideritis stricta*) water extract by using different hydrocolloid carriers. LWT - Food Sci. Technol. 44, 1626–1635.

Nandiyanto, A.B.D., Okuyama, K., 2011. Progress in developing spray-drying methods for the production of controlled morphology particles: From the nanometer to submicrometer size ranges. Adv. Powder Technol. 22, 1–19.

Nedovic, V., Kalusevic, A., Manojlovic, V., Levic, S., Bugarski, B., 2011. An overview of encapsulation technologies for food applications. Procedia Food Sci. 1, 1806–1815.

Negrão-Murakami, A.N., Nunes, G.L., Pinto, S.S., Murakami, F.S., Amante, E.R., Petrus, J.C.C., Prudêncio, E.S., Amboni, R.D.M.C., 2017. Influence of DE-value of maltodextrin on the physicochemical properties, antioxidant activity, and storage stability of spray dried concentrated mate (*Ilex paraguariensis* A. St. Hil.). LWT - Food Sci. Technol. 79, 561–567.

Nešić, S., Vodnik, J., 1991. Kinetics of droplet evaporation. Chem. Eng. Sci. 46(2), 527–537.

Nijdam, J.J., Langrish, T.A.G., 2006. The effect of surface composition on the functional properties of milk powders. J. Food Eng. 77, 919–925.

Nurhadi, B., Andoyo, R., Mahani, Indiarto, R., 2012. Study the properties of honey powder produced from spray drying and vacuum drying method. Int. Food Res. J. 19(3), 907–912.

Nurhadi, B., Roos, Y.H., Maidannyk, V., 2016. Physical properties of maltodextrin DE 10: Water sorption, water plasticization and enthalpy relaxation. J. Food Eng. 174, 68–74.

Nuzzo, M., Millqvist-Fureby, A., Sloth, J., Bergenstahl, B., 2015a. Surface composition and morphology of particles dried individually and by spray drying. Dry. Technol. 33(6), 757–767.

Nuzzo, M., Overgaard, J.S., Bergenståhl, B., Millqvist-Fureby, A., 2017. The morphology and internal composition of dried particles from whole milk - From single droplet to full scale drying. Food Struct. 13, 35–44

Nuzzo, M., Sloth, J., Brandner, B., Bergenstahl, B., Millqvist-Fureby, A., 2015b. Confocal Raman microscopy for mapping phase segregation in individually dried particles composed of lactose and macromolecules. Colloids Surfaces A Physicochem. Eng. Asp. 481, 229–236.

O'Hagan, P., Hasapidis, K., Coder, A., Helsing, H., Pokraja, G., 2005. Particle size analysis of food powders, in: Onwulata, C. (Ed.), Encapsulated and Powdered Foods. Taylor & Francis, Boca Raton, USA.

Oberoi, D.P.S., Sogi, D.S., 2015. Effect of drying methods and maltodextrin concentration on pigment content of watermelon juice powder. J. Food Eng. 165, 172–178.

Osman, A., Goehring, L., Patti, A., Stitt, H., Shokri, N., 2017. Fundamental investigation of the drying of solid suspensions. Ind. Eng. Chem. Res. 56(37), 10506–10513.

Outuki, P.M., de Francisco, L.M.B., Hoscheid, J., Bonifácio, K.L., Barbosa, D.S., Cardoso, M.L.C., 2016. Development of arabic and xanthan gum microparticles loaded with an extract of *Eschweilera nana* Miers leaves with antioxidant capacity. Colloids Surfaces A Physicochem. Eng. Asp. 499, 103–112.

Paim, D.R.S.F., Costa, S.D.O., Walter, E.H.M., Tonon, R. V., 2016. Microencapsulation of probiotic jussara (*Euterpe edulis* M.) juice by spray drying. LWT - Food Sci. Technol. 74, 21–25.

Pajander, J.P., Matero, S., Sloth, J., Wan, F., Rantanen, J., Yang, M., 2015. Raman mapping of mannitol/lysozyme particles produced via spray drying and single droplet drying. Pharm. Res. 32, 1993–2002.

Pang, S.F., Yusoff, M.M., Gimbun, J., 2014. Assessment of phenolic compounds stability and retention during spray drying of *Orthosiphon stamineus* extracts. Food Hydrocoll. 37, 159–165.

Paramita, V., Iida, K., Yoshii, H., Furuta, T., 2010. Effect of additives on the morphology of spray-dried powder. Dry. Technol. 28(3), 323–329.

Pauchard, L., Allain, C., 2003a. Buckling instability induced by polymer solution drying. Europhys. Lett. 62(6), 897–903.

Pauchard, L., Allain, C., 2003b. Mechanical instability induced by complex liquid desiccation. Comptes Rendus Phys. 4, 231–239.

Perdana, J., Fox, M.B., Schutyser, M.A.I., Boom, R.M., 2013. Mimicking spray drying by drying of single droplets deposited on a flat surface. Food Bioprocess Technol. 6, 964–977.

Perdana, J., Fox, M.B., Schutyser, M.A.I., Boom, R.M., 2011. Single-droplet experimentation on spray drying: Evaporation of a sessile droplet. Chem. Eng. Technol. 34(7), 1151–1158.

Pérez-Alonso, C., Beristain, C.I., Lobato-Calleros, C., Rodríguez-Huezo, M.E., Vernon-Carter, E.J., 2006. Thermodynamic analysis of the sorption isotherms of pure and blended carbohydrate polymers. J. Food Eng. 77, 753–760.

Porowska, A., Dosta, M., Heinrich, S., Fries, L., Gianfrancesco, A., Palzer, S., 2015. Influence of feed composition and drying parameters on the surface composition of a spray-dried multicomponent particle. Dry. Technol. 33, 1911–1919.

Porras-Saavedra, J., Palacios-González, E., Lartundo-Rojas, L., Garibay-Febles, V., Yáñez-Fernández, J., Hernández-Sánchez, H., Gutiérrez-López, G., Alamilla-Beltrán, L., 2015. Microstructural properties and distribution of components in microparticles obtained by spray-drying. J. Food Eng. 152, 105–112.

Premi, M., Sharma, H.K., 2017. Effect of different combinations of maltodextrin, gum arabic and whey protein concentrate on the encapsulation behavior and oxidative stability of spray dried drumstick (*Moringa oleifera*) oil. Int. J. Biol. Macromol. 105, 1232–1240.

Pycia, K., Juszczak, L., Gałkowska, D., Witczak, M., Jaworska, G., 2016. Maltodextrins from chemically modified starches. Selected physicochemical properties. Carbohydr. Polym. 146, 301–309.

Qi, W., Fong, C., Lamport, D.T.A., 1991. Gum arabic glycoprotein is a twisted hairy rope: A new model based on o-galactosylhydroxyproline as the polysaccharide attachment site. Plant Physiol. 96, 848–855.

Qi, X., Dong, Y., Wang, H., Wang, C., Li, F., 2017. Application of Turbiscan in the homoaggregation and heteroaggregation of copper nanoparticles. Colloids Surfaces A Physicochem. Eng. Asp. 535, 96–104.

Quek, S.Y., Chok, N.K., Swedlund, P., 2007. The physicochemical properties of spray-dried watermelon powders. Chem. Eng. Process. Process Intensif. 46, 386–392.

Raja, K.C.M., Sankarikutty, B., Sreekumar, M., Jayalekshmy, A., Narayanan, C.S., 1989. Material characterization studies of maltodextrin samples for the use of wall material. Starch - Stärke 41(8), 298–303.

Rajabi, H., Ghorbani, M., Jafari, S.M., Sadeghi Mahoonak, A., Rajabzadeh, G., 2015. Retention of saffron bioactive components by spray drying encapsulation using maltodextrin, gum Arabic and gelatin as wall materials. Food Hydrocoll. 51, 327–337.

Randall, R.C., Phillips, G.O., Williams, P.A., 1989. Fractionation and characterization of gum from *Acacia senegal*. Top. Catal. 3(1), 65–75.

Randall, R.C., Phillips, G.O., Williams, P.A., 1988. The role of the proteinaceous component on the emulsifying properties of gum arabic. Top. Catal. 2(2), 131–140.

Ranz, W.E., Marshall, W.R., 1952. Evaporation from drops - Part 1. Chem. Eng. Prog. 48(3), 141–146.

Ray, S., Raychaudhuri, U., Chakraborty, R., 2016. An overview of encapsulation of active compounds used in food products by drying technology. Food Biosci. 13, 76–83.

Ré, M.I., 1998. Microencapsulation by spray drying. Dry. Technol. 16(6), 1195–1236.

Ribeiro, C.M.C.M., Magliano, L.C. dos S.A., Costa, M.M.A. de, Bezerra, T.K.A., Silva, F.L.H. da, Maciel, M.O.S., 2018. Optimization of the spray drying process conditions for acerola and seriguela juice mix. Food Sci. Technol. 2061, 1–8.

Rosenberg, M., Kopelman, I.J., Talmon, Y., 1985. A scanning electron microscopy study of microencapsulation. J. Food Sci. 50, 139–144.

Sadek, C., Li, H., Schuck, P., Fallourd, Y., Pradeau, N., Le Floch-Fouéré, C., Jeantet, R., 2014. To what extent do whey and casein micelle proteins influence the morphology and properties of the resulting powder? Dry. Technol. 32, 1540–1551.

Sadek, C., Pauchard, L., Schuck, P., Fallourd, Y., Pradeau, N., Le Floch-Fouéré, C., Jeantet, R., 2015a. Mechanical properties of milk protein skin layers after drying: Understanding the mechanisms of particle formation from whey protein isolate and native phosphocaseinate. Food Hydrocoll. 48, 8–16.

Sadek, C., Schuck, P., Fallourd, Y., Pradeau, N., Jeantet, R., Le Floch-Fouéré, C., 2016. Buckling and collapse during drying of a single aqueous dispersion of casein micelle droplet. Food Hydrocoll. 52, 161–166.

Sadek, C., Schuck, P., Fallourd, Y., Pradeau, N., Le Floch-Fouéré, C., Jeantet, R., 2015b. Drying of a single droplet to investigate process–structure–function relationships: A review. Dairy Sci. Technol. 95, 771–794.

Sadek, C., Tabuteau, H., Schuck, P., Fallourd, Y., Pradeau, N., Le Floch-Fouéré, C., Jeantet, R., 2013. Shape, shell, and vacuole formation during the drying of a single concentrated whey protein droplet. Langmuir 29, 15606–15613.

Saha, D., Nanda, S.K., Yadav, D.N., 2019. Optimization of spray drying process parameters for production of groundnut milk powder. Powder Technol. 355, 417–424.

Şahin-Nadeem, H., Dinçer, C., Torun, M., Topuz, A., Özdemir, F., 2013. Influence of inlet air temperature and carrier material on the production of instant soluble sage (*Salvia fruticosa* Miller) by spray drying. LWT - Food Sci. Technol. 52, 31–38.

Sanchez-Reinoso, Z., Osorio, C., Herrera, A., 2017. Effect of microencapsulation by spray drying on cocoa aroma compounds and physicochemical characterisation of microencapsulates. Powder Technol. 318, 110–119.

Sanchez, C., Nigen, M., Mejia Tamayo, V., Doco, T., Williams, P., Amine, C., Renard, D., 2018. Acacia gum: History of the future. Food Hydrocoll. 78, 140–160.

Sanchez, C., Renard, D., Robert, P., Schmitt, C., Lefebvre, J., 2002. Structure and rheological properties of acacia gum dispersions. Food Hydrocoll. 16, 257–267.

Sansone, F., Mencherini, T., Picerno, P., D'Amore, M., Aquino, R.P., Lauro, M.R., 2011. Maltodextrin/pectin microparticles by spray drying as carrier for nutraceutical extracts. J. Food Eng. 105, 468–476.

Santos, D., Maurício, A.C., Sencadas, V., Santos, J.D., Fernandes, M.H., Gomes, P.S., 2018. Spray drying: An overview, in: Limited, I. (Ed.), Biomaterials: Physics and Chemistry. London, UK.

Sarabandi, K., Jafari, S.M., Mahoonak, A.S., Mohammadi, A., 2019. Application of gum Arabic and maltodextrin for encapsulation of eggplant peel extract as a natural antioxidant and color source. Int. J. Biol. Macromol. 140, 59–68.

Schrooyen, P.M.M., Meer, R. van der, Kruif, C.G. De, 2001. Microencapsulation: Its application in nutrition. Proc. Nutr. Soc. 60, 475–479.

Schutyser, M.A.I., Both, E.M., Siemons, I., Vaessen, E.M.J., Zhang, L., 2019. Gaining insight on spray drying behavior of foods via single droplet drying analyses. Dry. Technol. 37(5), 525–534.

Seydel, P., Blömer, J., Bertling, J., 2006. Modeling particle formation at spray drying using population balances. Dry. Technol. 24(2), 137–146.

Shahidi, F., Han, X.Q., 1993. Encapsulation of food ingredients. Crit. Rev. Food Sci. Nutr. 33(6), 501–547.

Sharma, A., Jana, A.H., Chavan, R.S., 2012. Functionality of milk powders and milk-based powders for end use applications - A review. Compr. Rev. Food Sci. Food Saf. 11, 518–528.

Shishir, M.R.I., Chen, W., 2017. Trends of spray drying: A critical review on drying of fruit and vegetable juices. Trends Food Sci. Technol. 65, 49–67.

Shishir, M.R.I., Taip, F.S., Aziz, N.A., Talib, R.A., 2014. Physical properties of spray-dried pink guava (*Psidium guajava*) Powder. Agric. Agric. Sci. Procedia 2, 74–81.

Shishir, M.R.I., Taip, F.S., Aziz, N.A., Talib, R.A., Hossain Sarker, M.S., 2016. Optimization of spray drying parameters for pink guava powder using RSM. Food Sci. Biotechnol. 25(2), 461–468.

Shrestha, A.K., Howes, T., Adhikari, B.P., Wood, B.J., Bhesh R. Bhandari, 2007. Effect of protein concentration on the surface composition, water sorption and glass transition temperature of spray-dried skim milk powders. Food Chem. 104, 1436–1444.

Siemons, I., Politiek, R.G.A., Boom, R.M., van der Sman, R.G.M., Schutyser, M.A.I., 2020. Dextrose equivalence of maltodextrins determines particle morphology development during single sessile droplet drying. Food Res. Int. 131, 108988.

Sosnik, A., Seremeta, K.P., 2015. Advantages and challenges of the spray-drying technology for the production of pure drug particles and drug-loaded polymeric carriers. Adv. Colloid Interface Sci. 223, 40–54.

Subtil, S.F., Rocha-Selmi, G.A., Thomazini, M., Trindade, M.A., Netto, F.M., Favaro-Trindade, C.S., 2014. Effect of spray drying on the sensory and physical properties of hydrolysed casein using gum arabic as the carrier. J. Food Sci. Technol. 51(9), 2014–2021.

Sugiyama, Y., Larsen, R.J., Kim, J.W., Weitz, D.A., 2006. Buckling and crumpling of drying droplets of colloid-polymer suspensions. Langmuir 22, 6024–6030.

Sultana, A., Miyamoto, A., Lan Hy, Q., Tanaka, Y., Fushimi, Y., Yoshii, H., 2017. Microencapsulation of flavors by spray drying using *Saccharomyces cerevisiae*. J. Food Eng. 199, 36–41.

Takeiti, C.Y., Kieckbusch, T.G., Collares-Queiroz, F.P., 2010. Morphological and physicochemical characterization of commercial maltodextrins with different degrees of dextrose-equivalent. Int. J. Food Prop. 13(2), 411–425.

Tan, S.P., Kha, T.C., Parks, S.E., Stathopoulos, C.E., Roach, P.D., 2015. Effects of the spray-drying temperatures on the physiochemical properties of an encapsulated bitter melon aqueous extract powder. Powder Technol. 281, 65–75.

Tatar, F., Tunç, M.T., Dervisoglu, M., Cekmecelioglu, D., Kahyaoglu, T., 2014. Evaluation of hemicellulose as a coating material with gum arabic for food microencapsulation. Food Res. Int. 57, 168–175.

Tolun, A., Altintas, Z., Artik, N., 2016. Microencapsulation of grape polyphenols using maltodextrin and gum arabic as two alternative coating materials: Development and characterization. J. Biotechnol. 239, 23–33.

Tonon, R. V., Brabet, C., Hubinger, M.D., 2008. Influence of process conditions on the physicochemical properties of açai (*Euterpe oleraceae* Mart.) powder produced by spray drying. J. Food Eng. 88, 411–418.

Tonon, R. V., Brabet, C., Pallet, D., Brat, P., Hubinger, M.D., 2009. Physicochemical and morphological characterisation of açai (*Euterpe oleraceae* Mart.) powder produced with different carrier agents. Int. J. Food Sci. Technol. 44, 1950–1958.

Tonon, R. V., Freitas, S.S., Hubinger, M.D., 2011a. Spray drying of açai (*Euterpe oleraceae* Mart.) juice: Effect of inlet air temperature and type of carrier agent. J. Food Process. Preserv. 35, 691–700.

Tonon, R. V., Grosso, C.R.F., Hubinger, M.D., 2011b. Influence of emulsion composition and inlet air temperature on the microencapsulation of flaxseed oil by spray drying. Food Res. Int. 44, 282–289.

Tontul, I., Topuz, A., 2017. Spray-drying of fruit and vegetable juices: Effect of drying conditions on the product yield and physical properties. Trends Food Sci. Technol. 63, 91–102.

Tran, T.T.H., Avila-Acevedo, J.G., Tsotsas, E., 2016. Enhanced methods for experimental investigation of single droplet drying kinetics and application to lactose/water. Dry. Technol. 34(10), 1185–1195.

Tran, T.T.H., Jaskulski, M., Avila-Acevedo, J.G., Tsotsas, E., 2017. Model parameters for single-droplet drying of skim milk and its constituents at moderate and elevated temperatures. Dry. Technol. 35(4), 444–464.

Tsapis, N., Bennett, D., Jackson, B., Weitz, D.A., Edwards, D.A., 2002. Trojan particles: Large porous carriers of nanoparticles for drug delivery. Proc. Natl. Acad. Sci. U. S. A. 99(19), 12001–12005.

Tsapis, N., Dufresne, E.R., Sinha, S.S., Riera, C.S., Hutchinson, J.W., Mahadevan, L., Weitz, D.A., 2005. Onset of buckling in drying droplets of colloidal suspensions. Phys. Rev. Lett. 94(018302), 1–4.

Tze, N.L., Han, C.P., Yusof, Y.A., Ling, C.N., Talib, R.A., Taip, F.S., Aziz, M.G., 2012. Physicochemical and nutritional properties of spray-dried pitaya fruit powder as natural colorant. Food Sci. Biotechnol. 21(3), 675–682.

Ullum, T., Sloth, J., Brask, A., Wahlberg, M., 2010. Predicting spray dryer deposits by CFD and an empirical drying model. Dry. Technol. 28(5), 723–729.

Vakarelski, I.U., Li, E.Q., Thoroddsen, S.T., 2014. Soft colloidal probes for AFM force measurements between water droplets in oil. Colloids Surfaces A Physicochem. Eng. Asp. 462, 259–263.

Vehring, R., 2008. Pharmaceutical particle engineering via spray drying. Pharm. Res. 25(5), 999–1022.

Vehring, R., Foss, W.R., Lechuga-Ballesteros, D., 2007. Particle formation in spray drying. J. Aerosol Sci. 38, 728–746.

Verbeken, D., Dierckx, S., Dewettinck, K., 2003. Exudate gums: Occurrence, production, and applications. Appl. Microbiol. Biotechnol. 63, 10–21.

Vicente, J., Pinto, J., Menezes, J., Gaspar, F., 2013. Fundamental analysis of particle formation in spray drying. Powder Technol. 247, 1–7.

Vidović, S.S., Vladić, J.Z., Vaštag, Ž.G., Zeković, Z.P., Popović, L.M., 2014. Maltodextrin as a carrier of health benefit compounds in *Satureja montana* dry powder extract obtained by spray drying technique. Powder Technol. 258, 209–215.

Walton, D.E., 2000. The morphology of spray-dried particles a qualitative view. Dry. Technol. 18(9), 1943–1986.

Walton, D.E., Mumford, C.J., 1999a. The morphology of spray-dried particles: The effect of process variables upon the morphology of spray-dried particles. Chem. Eng. Res. Des. 77(Part A), 442–460.

Walton, D.E., Mumford, C.J., 1999b. Spray dried products-characterization of particle morphology. Chem. Eng. Res. Des. 77(Part A), 21–38.

Walzel, P., Furuta, T., 2011. Morphology and properties of spray-dried particles, in: Tsotsas, E., Mujumdar, A.S. (Eds.), Modern Drying Technology: Product Quality and Formulation (Volume 3). Wiley-VCH Verlag GmbH & Co. KGaA, Weinheim, Germany.

Wandrey, C., Bartkowiak, A., Harding, S.E., 2010. Materials for encapsulation, in: Nicolaas, J.Z., Viktor, A.M. (Eds.), Encapsulation Technologies for Active Food Ingredients and Food Processing. Springer, New York, USA.

Wang, S., Langrish, T., 2010. The use of surface active compounds as additives in spray drying. Dry. Technol. 28(3), 341–348.

Wang, S., Langrish, T., 2009. A review of process simulations and the use of additives in spray drying. Food Res. Int. 42, 13–25.

Wang, W., Dufour, C., Zhou, W., 2015. Impacts of spray-drying conditions on the physicochemical properties of soy sauce powders using maltodextrin as auxiliary drying carrier. CYTA - J. Food 13(4), 548–555.

Wang, W., Zhou, Q.T., Sun, S.P., Denman, J.A., Gengenbach, T.R., Barraud, N., Rice, S.A., Li, J., Yang, M., Chan, H.K., 2016. Effects of surface composition on the aerosolisation and dissolution of inhaled antibiotic combination powders consisting of colistin and rifampicin. AAPS J. 18(2), 372–384.

Wang, Y.-J., Wang, L., 2000. Structures and properties of commercial maltodextrins from corn, potato, and rice starches. Starch - Stärke 52, 296–304.

Williams, P.A., Phillips, G.O., 2009. Gum Arabic, in: Phillips, G.O., Williams, P.A. (Eds.), Handbook of Hydrocolloids. Woodhead Publishing, Cambridge, England.

Wu, W.D., Liu, W., Gengenbach, T., Woo, M.W., Selomulya, C., Chen, X.D., Weeks, M., 2014. Towards spray drying of high solids dairy liquid: Effects of feed solid content on particle structure and functionality. J. Food Eng. 123, 130–135.

Xu, W., Choi, C.H., 2012. Effects of surface topography and colloid particles on the evaporation kinetics of sessile droplets on superhydrophobic surfaces. J. Heat Transfer 134, 1–7.

Yu, Y.S., Wang, Z., Zhao, Y.P., 2012. Experimental and theoretical investigations of evaporation of sessile water droplet on hydrophobic surfaces. J. Colloid Interface Sci. 365, 254–259.

Zhang, C., Quek, S.Y., Fu, N., Liu, B., Kilmartin, P.A., Chen, X.D., 2019. A study on the structure formation and properties of noni juice microencapsulated with maltodextrin and gum acacia using single droplet drying. Food Hydrocoll. 88, 199–209.

Appendix A

Sessile single droplet drying of mixed gum Arabic and maltodextrin solutions

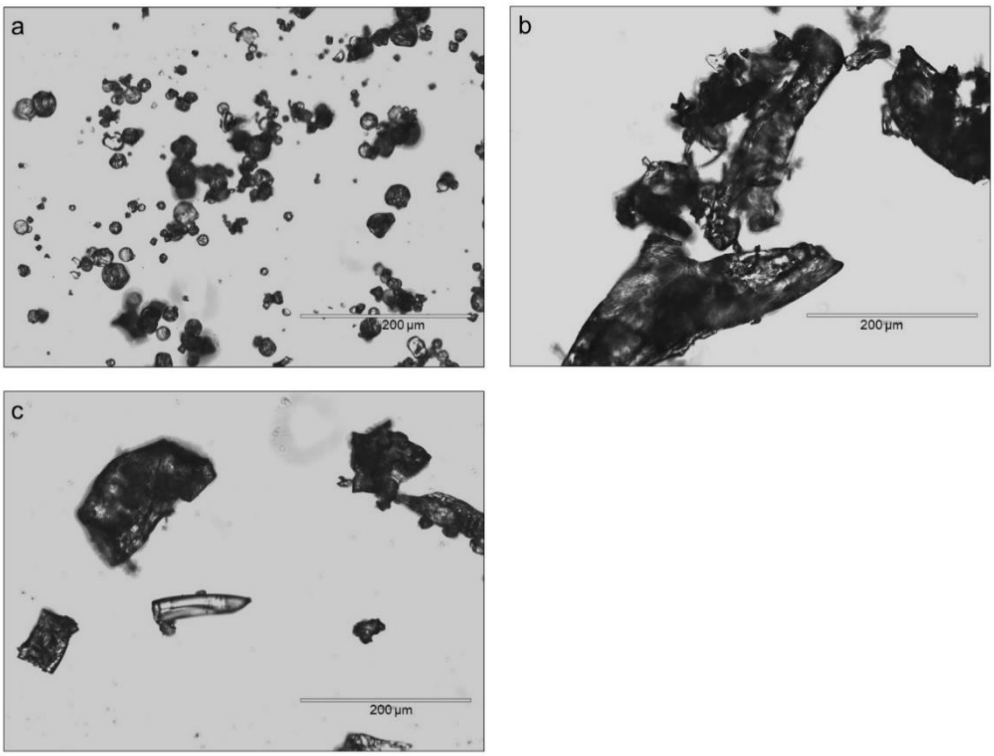

Figure A.1 Light microscopy images of a) GA, b) MD7 and c) MD12 that were used to prepare droplet solutions. Length of scale bar: 200 µm.

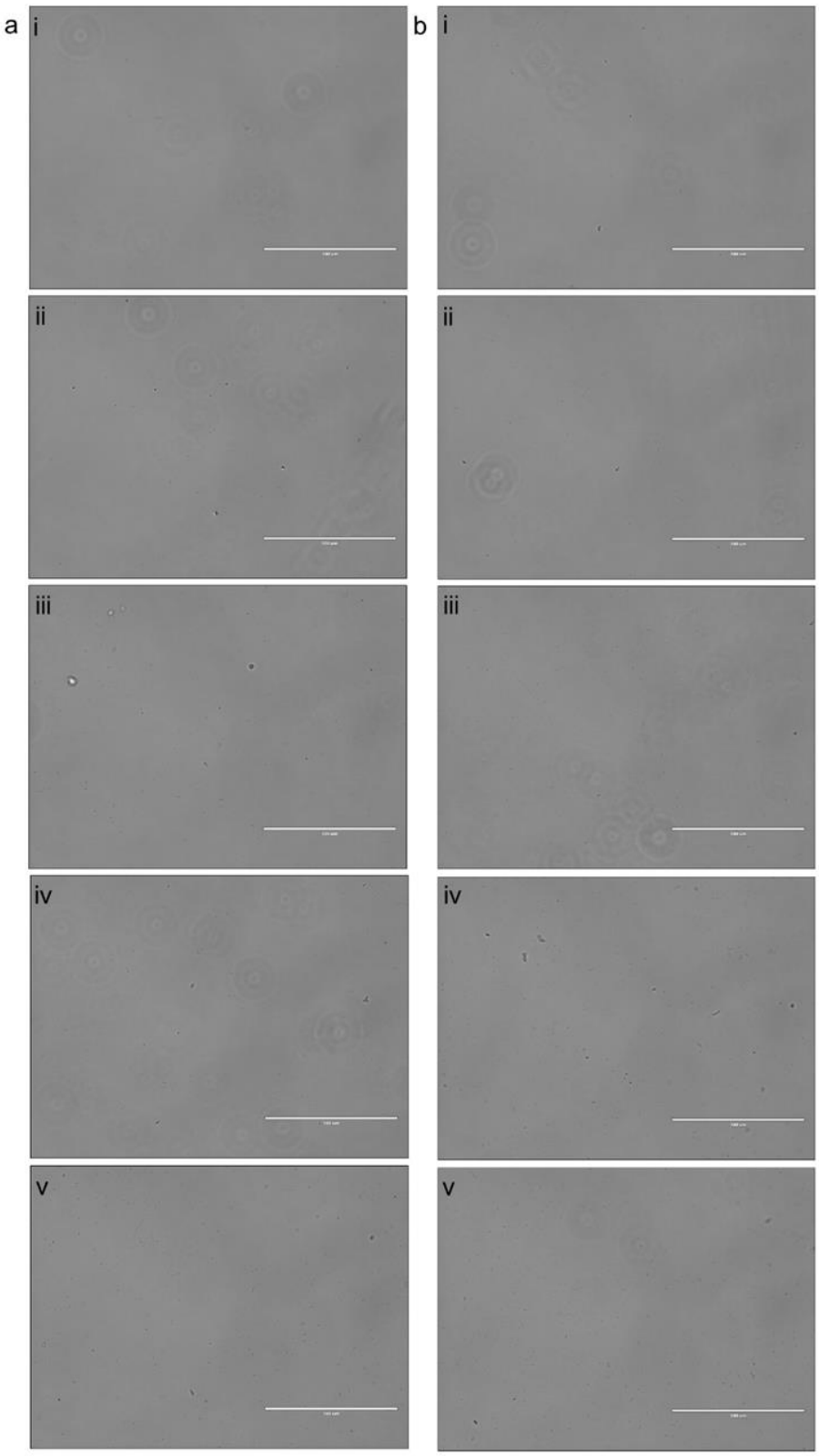

Figure A.2 Light microscopy images of solutions at initial, containing a) 20% and b) 40% w/v total solids with various compositions of GA:MD12; (i) 0:100, (ii) 25:75, (iii) 50:50, (iv) 75:25 and (v) 100:0. Length of scale bar: 100 µm.

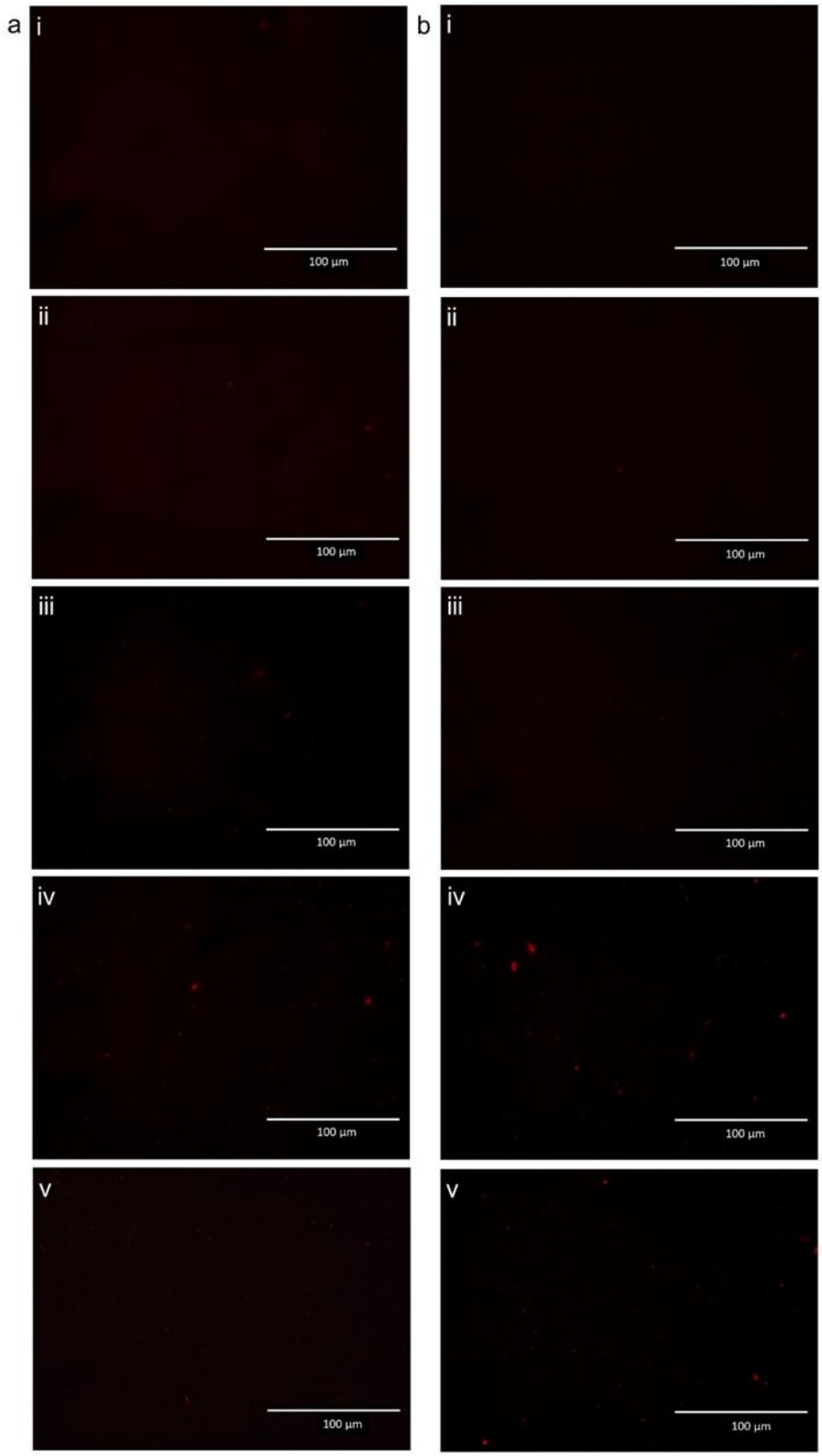

Figure A.3 Fluorescent images of solutions at initial, containing a) 20% and b) 40% w/v total solids with various compositions of GA:MD7; (i) 0:100, (ii) 25:75, (iii) 50:50, (iv) 75:25 and (v) 100:0.

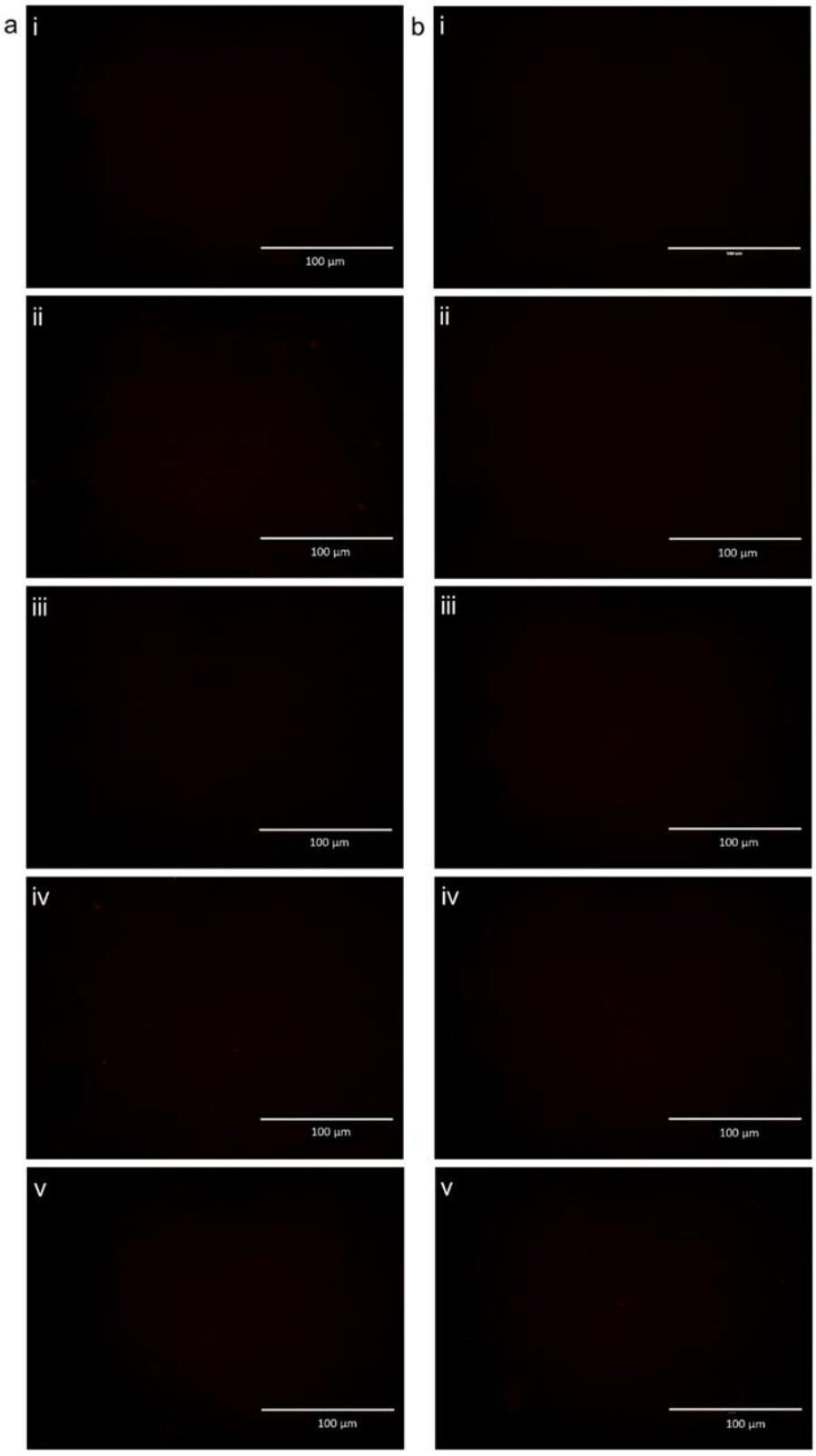

Figure A.4 Fluorescent images of solutions after centrifugation, containing a) 20% and b) 40% w/v total solids with various compositions of GA:MD12; (i) 0:100, (ii) 25:75, (iii) 50:50, (iv) 75:25 and (v) 100:0.

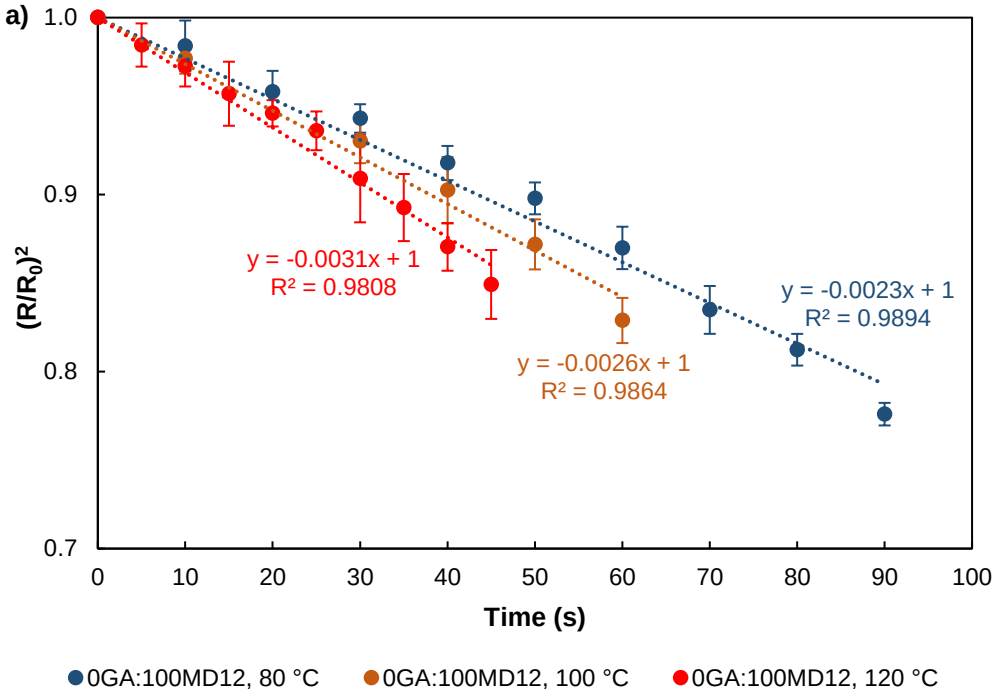

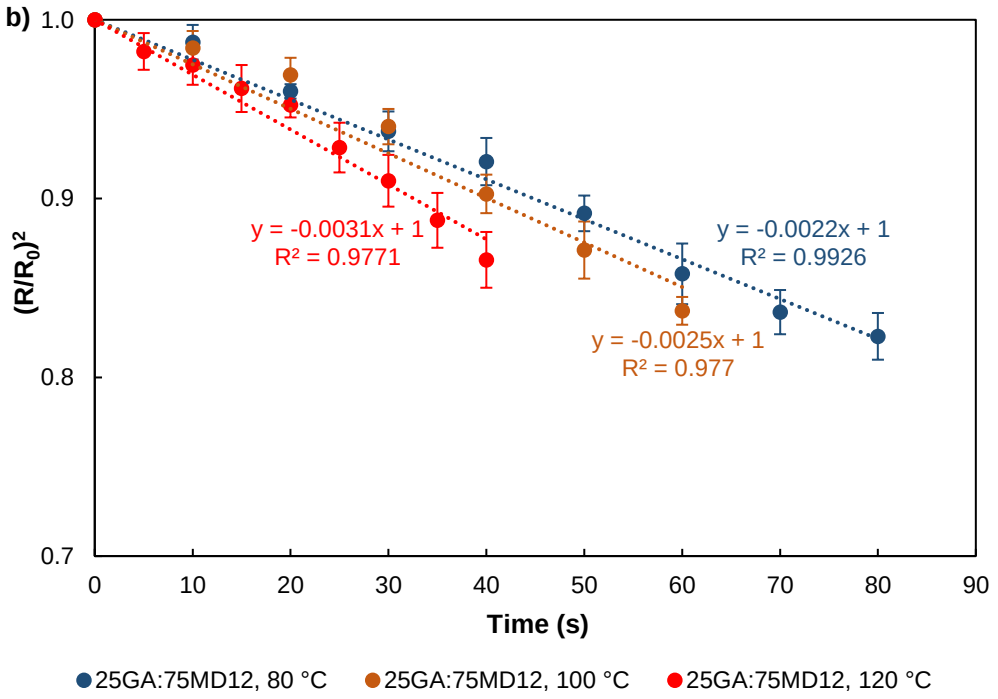

Figure A.5 Normalised radius squared of droplets containing various compositions of GA:MD12: a) 0:100, b) 25:75, c) 75:25, and d) 100:0, against time and dried at different temperatures. Blue: 80 °C, orange: 100 °C and red: 120 °C. Droplets had an initial total solids content of 30% w/v and an initial droplet volume of 2 µl. Lines were fitted to the experimental data.

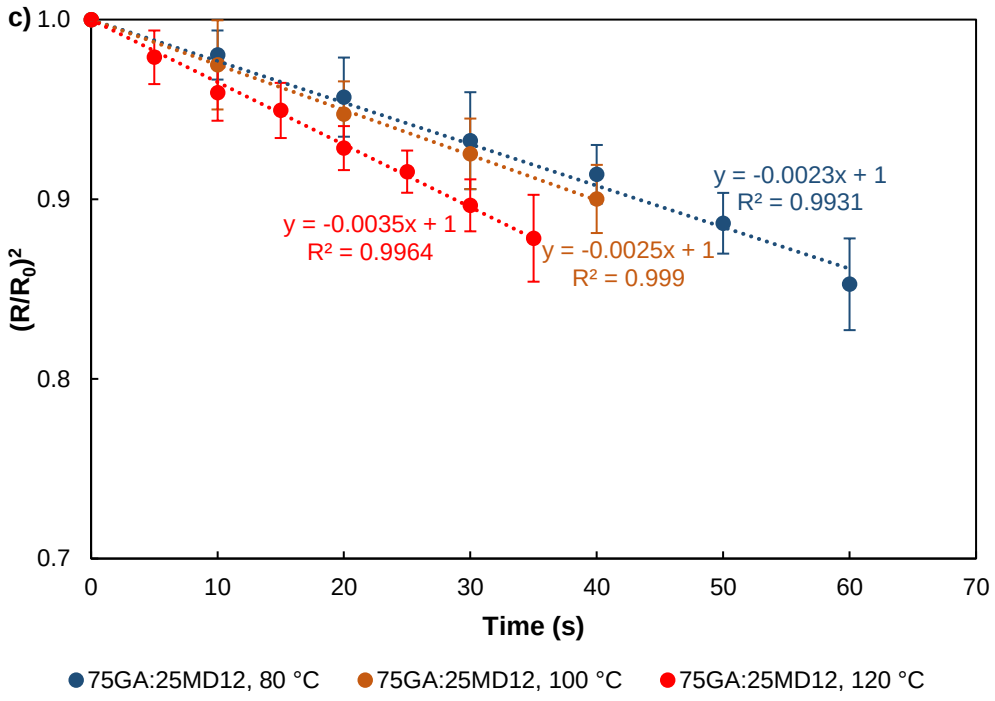

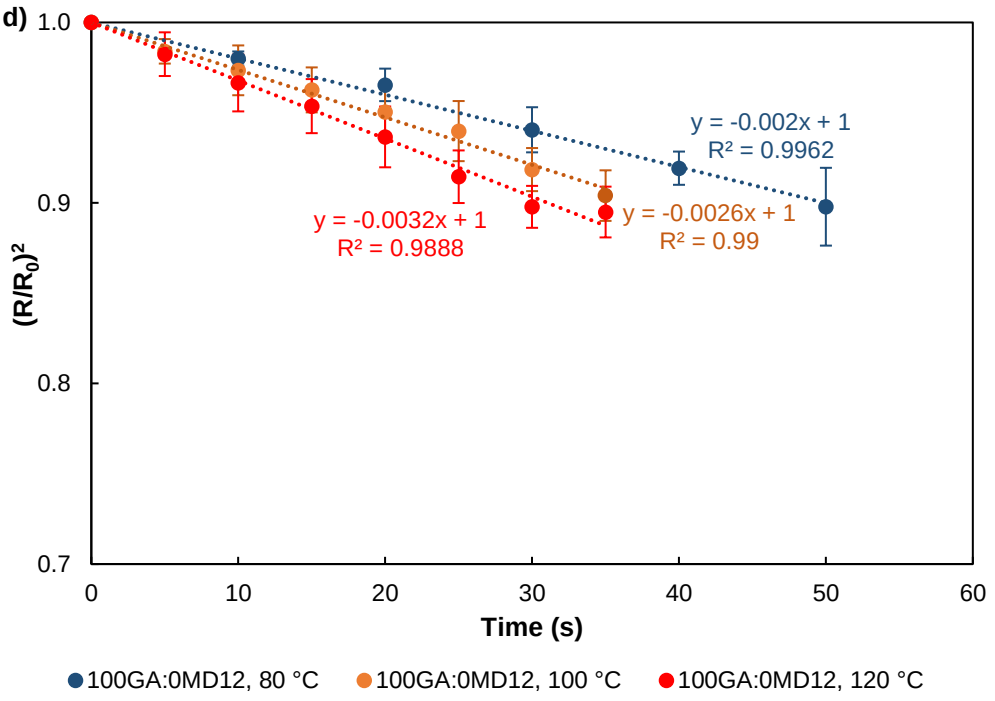

Figure A.5 (continued)

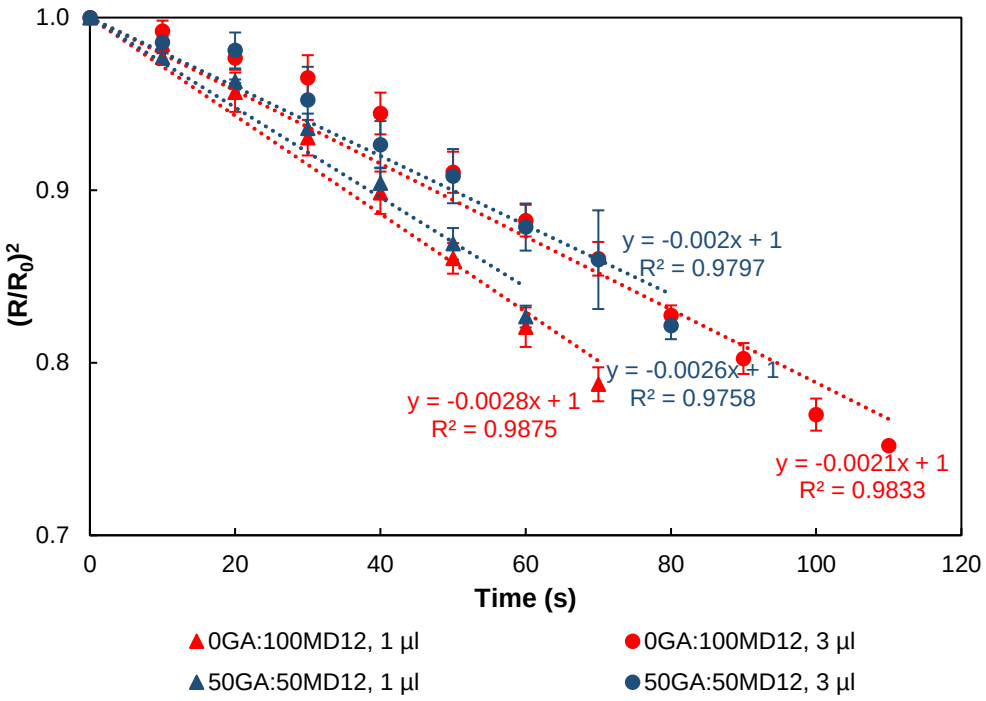

Figure A.6 Normalised radius squared of droplets containing various compositions of GA:MD12 and initial droplet volumes against time. Composition of GA:MD12: 0:100 (red) and 50:50 (blue); droplet volume: 1 µl (triangles:) and 3 µl (circles). Droplets had an initial total solids content of 30% w/v and were dried at 100 °C. Lines were fitted to the experimental data.

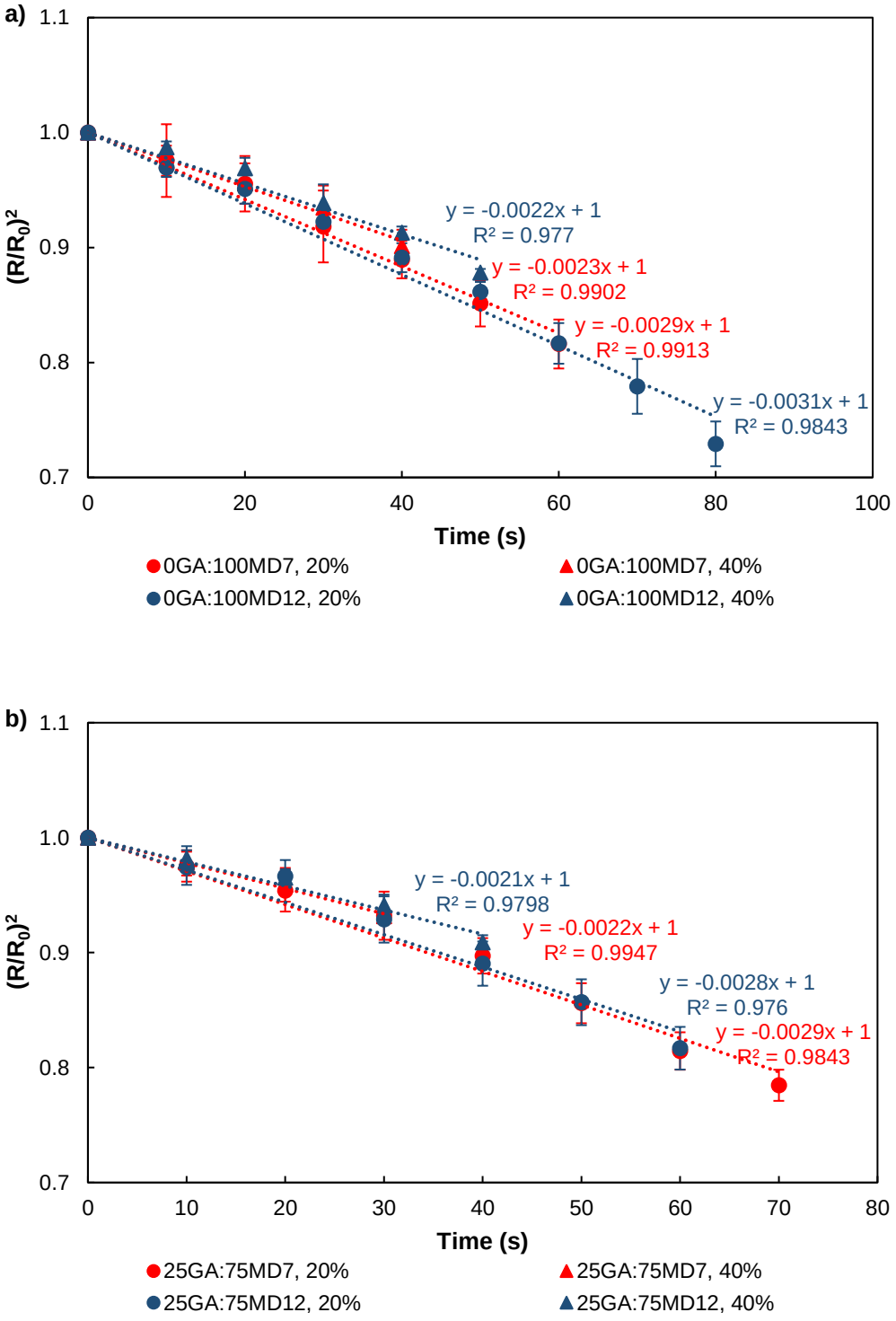

Figure A.7 Normalised radius squared of droplets containing various compositions of GA:MD, which prepared with different solids concentrations and DE-values of MD against time. Composition of GA:MD: a) 0:100, b) 25:75, c) 50:50, d) 75:25 and e) 100:0; solids concentration: 20% w/v (circles) and 40% w/v (triangles); DE-value of MD: MD7 (red) and MD12 (blue). Droplets had an initial volume of 2 µl and were dried at 120 °C. Lines were fitted to the experimental data.

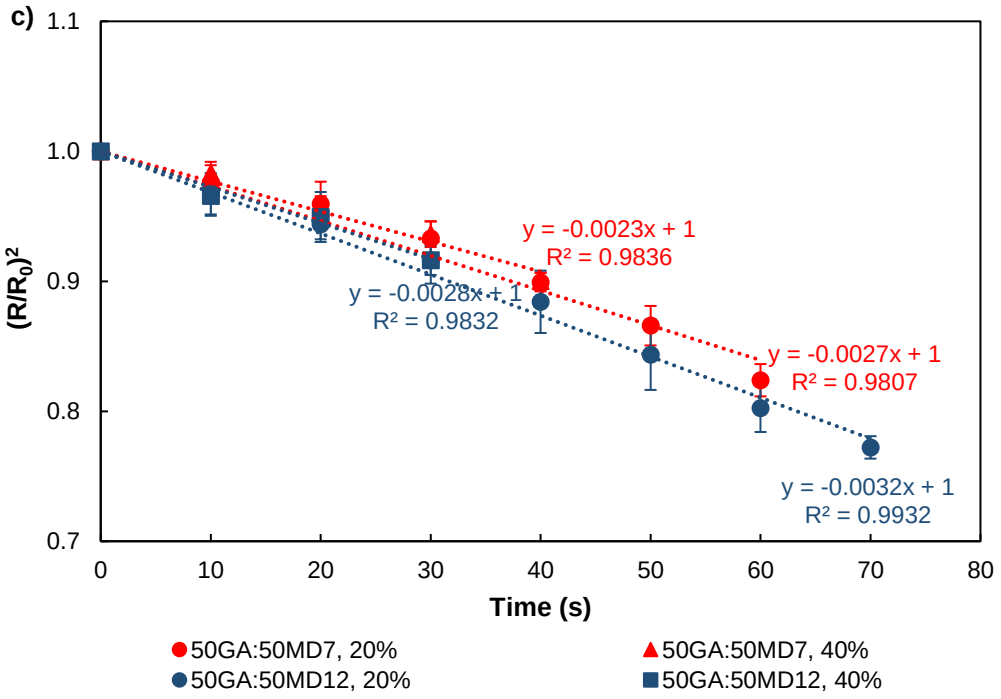

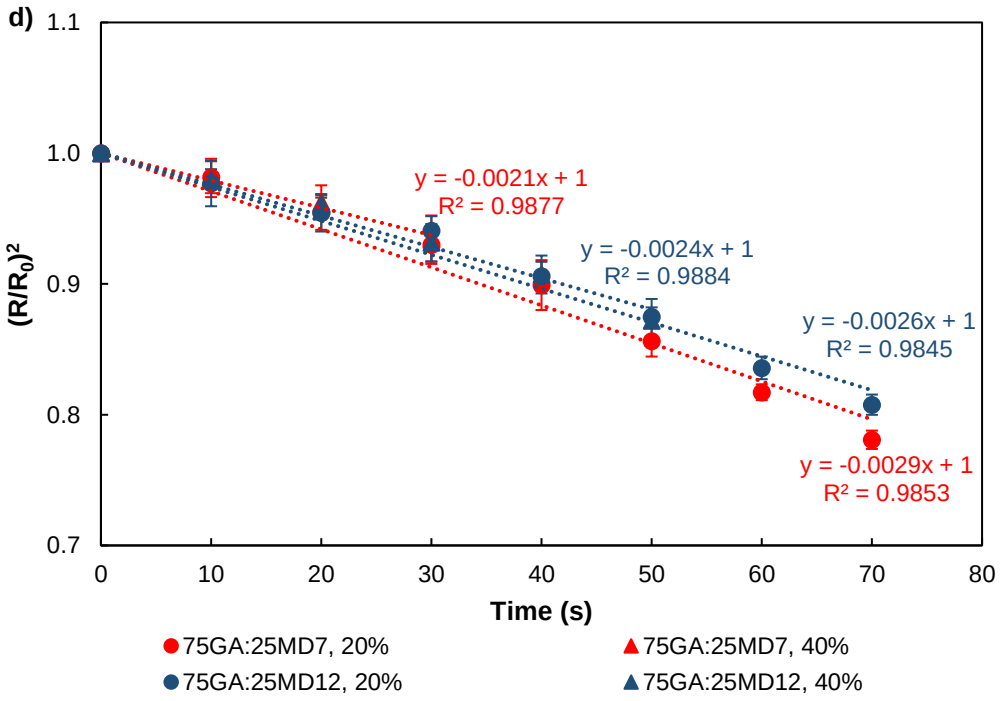

Figure A.7 (continued)

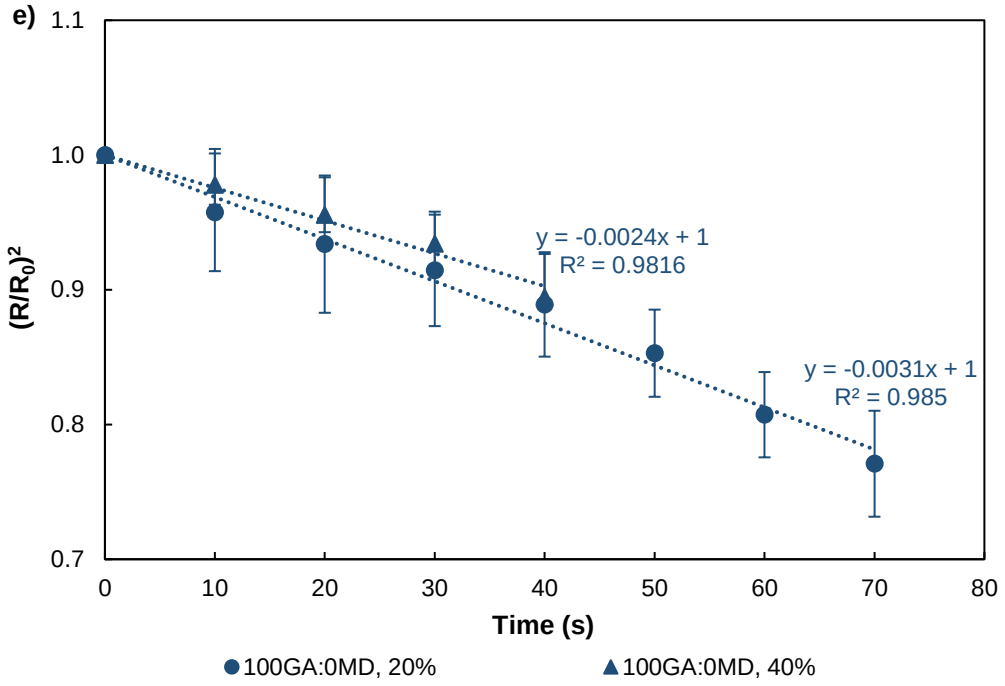

Figure A.7 (continued)

Appendix B

Wettability and dispersibility of spray dried powder (Turbiscan methodology)

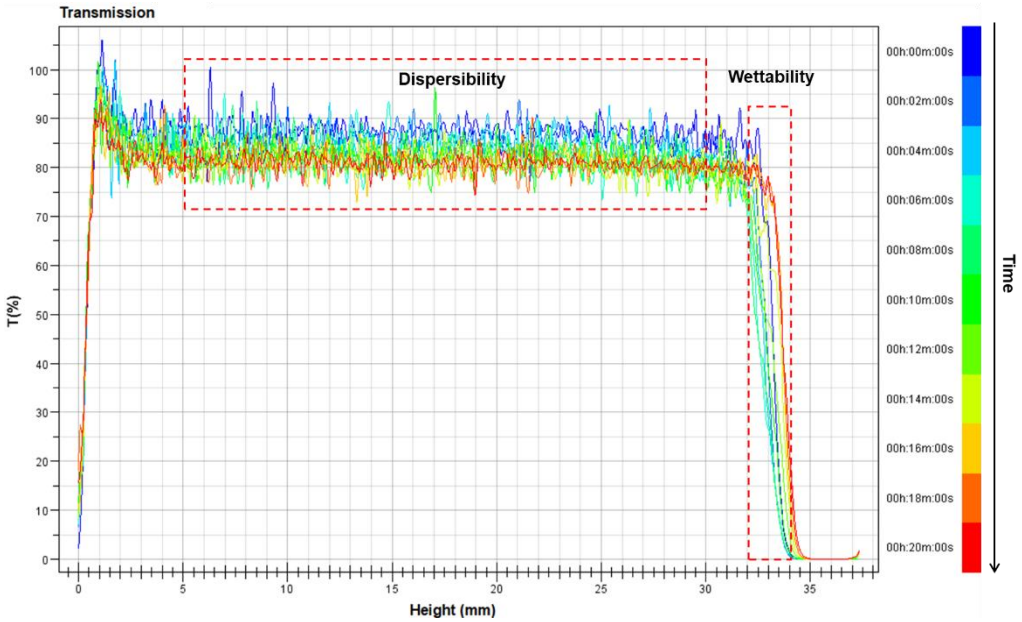

Figure B.1 An example of the evolution of the transmitted signal for one of the spray dried powders.

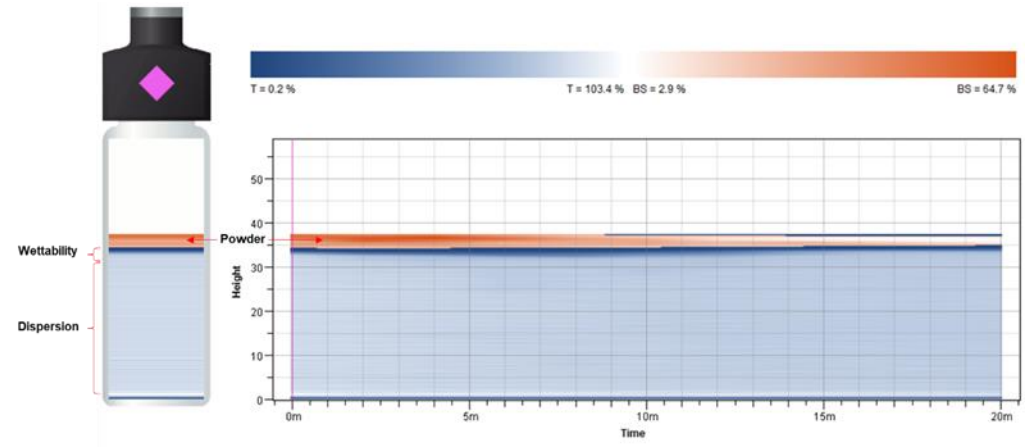

Figure B.2 Powder wettability and dispersibility measurements using Turbiscan.